SEARCH FOR WEAKLY INTERACTING MASSIVE PARTICLES WITH THE CRYOGENIC DARK MATTER SEARCH EXPERIMENT

A DISSERTATION
SUBMITTED TO THE DEPARTMENT OF PHYSICS
AND THE COMMITTEE ON GRADUATE STUDIES
OF STANFORD UNIVERSITY
IN PARTIAL FULFILLMENT OF THE REQUIREMENTS
FOR THE DEGREE OF
DOCTOR OF PHILOSOPHY

Tarek Saab
August 2002

© Copyright by Tarek Saab 2002
All Rights Reserved

I certify that I have read this dissertation and that in my opinion it is fully adequate, in scope and quality, as a dissertation for the degree of Doctor of Philosophy.

Blas Cabrera
(Principal Adviser)

I certify that I have read this dissertation and that in my opinion it is fully adequate, in scope and quality, as a dissertation for the degree of Doctor of Philosophy.

Patricia Burchat

I certify that I have read this dissertation and that in my opinion it is fully adequate, in scope and quality, as a dissertation for the degree of Doctor of Philosophy.

Giorgio Gratta

Approved for the University Committee on Graduate Studies:

Abstract

From individual galaxies, to clusters of galaxies, to in between the cushions of your sofa, Dark Matter appears to be pervasive on every scale. With increasing accuracy, recent astrophysical measurements, from a variety of experiments, are arriving at the following cosmological model : a flat cosmology ($\Omega_k = 0$) with matter and energy densities contributing roughly 1/3 and 2/3 ($\Omega_m = 0.35$, $\Omega_\Lambda = 0.65$). Of the matter contribution, it appears that only $\sim$10% ($\Omega_b \sim 0.04$) is attributable to baryons. Astrophysical measurements constrain the remaining matter to be non-realtivistic, interacting primarily gravitationally. Various theoretical models for such Dark Matter exist. A leading candidate for the non-baryonic matter are Weakly Interacting Massive Particles (dubbed WIMPS). These particles, and their relic density may be naturally explained within the framework of Super-Symmetry theories. Super-Symmetry also offers predictions as to the scattering rates of WIMPs with baryonic matter allowing for the design and tailoring of experiments that search specifically for the WIMPs. The Cryogenic Dark Matter Search experiment is searching for evidence of WIMP interactions in crystals of Ge and Si. Using cryogenic detector technology to measure both the phonon and ionization response to a particle recoil the CDMS detectors are able to discriminate between electron and nuclear recoils, thus reducing the large rates of electron recoil backgrounds to levels with which a Dark Matter search is not only feasible, but far-reaching. This thesis will describe in some detail the physical principles behind the CDMS detector technology, highlighting the final step in the evolution of the detector design and characterization techniques. In

addition, data from a 100 day long exposure of the current run at the Stanford Underground Facility will be presented, with focus given to detector performance as well as to the implications on allowable WIMP mass - cross-section parameter space.

Acknowledgements

It is almost impossible to express, within the scope of one or two pages, the immense debts of gratitude I owe to the numerous people who have, directly and indirectly, made *this* possible. By *this* I refer not just to the dissertation itself, but the entire Ph.D. process that began when I arrived at Stanford five years ago.

Let me begin by thanking Marcia Keating, Dawn Hyde, and Kathleen Guan who were extremely patient and helpful whenever I ran into their offices with the latest *emergency* regarding the progress of my degree or status of my student visa or (most important of all) my paycheck. Along with the rest of the physics department administerial staff; Rosenna Yau, Cindy Mendel, and Jennifer Conan-Tice, they made it possible for me to concentrate on my work here at Stanford rather than the logistics of my student status.

Of course, none of the research that I did would have been possible without the help and support of the Cabrera group. The groups administrative assistant, Linda Hubly, was instrumental in the acquisition of various experimental equipment, arranging for conference travel, and again quite importantly, getting reimbursed for said travel. From the senior graduate students at the time I joined the group, Sae Woo Nam and Roland Clarke, down through the likes of Aaron Miller, Tali Figueroa (who had a large part in my getting a job after graduating), Clarence Chang (who suffered for several years through my taste in music), David Abrams, Walter Ogburn, to the newest set of students, Jen Burney and Steve Leman it was a pleasure working with all of them. Sharing an office with Aaron Miller was a blast, if not the most

amenable situation with regards to productivity. If for nothing else, I am thankful for his teaching me his technique of picking locks, which permitted the occasional 3:00 a.m. raids on the physics department's cookie stash (yes the secret is out), and the less said about the scanner incident the better. I would be remiss not to mention Pat Castle, Astrid Tomada, Laura Baudis, and Betty Young who, though they weren't graduate student themselves, were very fun to work with and get to know. Paul Brink, once I became accustomed to his British accent, turned out be quite an interesting and intelligent person. I'm glad that I was able to expose him to American culture through the likes of *Dude, Where's My Car*, *Lara Croft : Tomb Raider*, and the *Austin Powers* movie series. Many thanks to Blas Cabrera. Blas provided me not only with the opportunity to work on a challenging and interesting experiment, but with a large degree of latitude to pursue research in my own style and manner. One of his many talents is his ability to communicate his knowledge and excitement about a subject quite effectively from which I learned significantly. Finally, I wish to thank the CDMS collaboration at large. I enjoyed working with everyone from the various institutions.

Outside of the laboratory, whenever the occasion arose, I managed to spend my time with a wonderful group of friends. At the risk of forgetting some names (for which I am truly sorry) I wish to mention Tim & Emily, Aaron & Holly, Tali & Barbara, Phil & Nicci, John & Danna, Tim & Danielle, Craig & Dani, Dave, Kanaka, Molly, Aron and the inexplicable George Marcus. They certainly managed to inject their own note of insanity into my symphony of madness.

Finally I wish to thank my family. I cannot express in words the support and inspiration they provided. Thanks again!!

Foreword

Well, here we are, 200 pages and five years later (well ten years if you start counting from the beginning of undergraduate studies) ...

Contents

Abstract **iv**

Acknowledgements **vi**

Foreword **viii**

1 Introduction **1**

1.1 The Cosmological Framework 2

1.2 Measuring the Cosmological Parameters 4

1.2.1 H_0 4

1.2.2 Ω_m and Ω_Λ 5

1.3 The Existence of Dark Matter 7

1.3.1 Mass-to-Light Ratio 7

1.4 Baryonic and Non-Baryonic Dark Matter 12

1.4.1 Big Bang Nucleosynthesis 12

1.4.2 Non-Baryonic Dark Matter 13

2 Supersymmetry and WIMPs **17**

2.1 Relic Abundance 17

2.2 Supersymmetry and WIMPs 20

2.2.1 WIMP-Nucleus Scattering 21

2.3 Recoil Energy Spectra 23

3 The Search for Dark Matter **27**

3.1 Direct Detection 30

3.1.1 Non-discriminating Detectors 30

3.1.2 Discriminating Detectors 31

3.1.3 Insensitive Detectors 35

3.2 Indirect Detection 35

4 ZIP Detector Technology **37**

4.1 The ZIP Detector 37

4.2 The Phonon Channel 40

4.2.1 Phonons in the Crystal 40

4.2.2 The QET 43

4.2.3 Transition Edge Sensors and Electrothermal Feedback 49

4.2.4 Tc Tuning 57

4.2.5 IV Characteristics of the TESs 60

4.3 The Ionization Channel 73

4.4 The Yield Parameter and Particle Identification 78

5 The CDMS Experiment 83

5.1 The SUF Facility 84

5.2 The Dilution Unit & Ice Box 85

5.2.1 The Tower 86

5.3 Event Rates and Shielding 89

5.4 Readout electronics and DAQ 91

5.4.1 The Front End electronics 91

5.4.2 Muon Veto 92

5.4.3 DAQ 93

5.5 Data Analysis 94

6 Establishing the Detector Response 95

6.1 Calibrating the Energy Scale 96

6.1.1 Neutralizing the Detectors 96

6.1.2 The Ionization Channel 97

6.1.3 The Phonon Channel 102

6.1.4 Energy Dependence of the Detector Noise 103

6.2 Position Dependence 107

6.3 Event Discrimination with the ZIPs 110

6.3.1 Determining the Electron and Nuclear Recoil Bands 112

6.3.2 Determining the Gamma Discrimination 126

6.4 Surface Electron Recoils and the Risetime Effect 130

6.4.1 Yield distribution of Betas 130

6.4.2 The Risetime Effect 139

6.5 Cut Efficiencies 140

6.5.1 Data Quality Cuts 140

6.5.2 Detector Cuts 142

6.5.3 Physics Cuts 147

6.6 Detector Stability 149

7 Contamination Levels 157

7.1 Surface Contamination 158

7.1.1 ^{210}Pb 159

7.1.2 ^{14}C 163

7.2 Bulk Contamination 163

8 Low Background Data 169

8.1 Defining the Data Set 169

8.2 Muon Coincident Data 170

8.3 Muon Anticoincident Data 176

8.3.1 Gammas & Betas 176

8.3.2 Anticoincident Nuclear Recoils 176

8.4 Statistical Tests 182

8.5 Determining the WIMP Exclusion Limit 189

9 Conclusion **193**

A Calculation of the Quasiparticle Collection Efficiency **195**

B Simulating IV Curves **199**

Bibliography **217**

List of Tables

4.1 Contribution of various resistances to the noise in the phonon channel. 56

6.1 Measured energies and widths of several lines in the ionization spectrum of a Ge detector (Z5). The *Width* column quotes the 1σ Gaussian line width, while the *Deviation* column quotes the difference between the actual and measured energy of the line in units of the line width. 101

6.2 Measured positions and widths of several lines in the phonon spectrum for one of the Ge detectors (Z5). The *Width* column quotes the 1σ Gaussian line width, while the *Deviation* column quotes the difference between the measured and actual position of the line in units of the line width. 103

6.3 Measured resolution of the ionization and phonon channels as a function of energy. 104

6.4 Fit parameters for the ionization and phonon channel energy dependent resolution. α and β have units of keV, while γ is unitless. Values of $\beta \sim 10^{-8}$–10^{-12} are not meaningful, they simply reflect the coarseness of the minimization algorithm and are consistent with zero. 106

6.5 Electron recoil discrimination, at 90% confidence level, in the ZIP detectors as a function of energy. Discrimination is defined as the fraction of electron recoil events that appear within the $\pm 2\sigma$ nuclear recoil band. The final column shows the discrimination obtained by summing up the events in the inner four detectors. Overall, the values listed in this table indicate that fewer than 1 electron recoil event out of 1000 is misidentified. 127

6.6 Number of surface β recoils expected to be misidentified as nuclear recoils, normalized to the number of events in the y=0.7 bin. The values are quoted in %. 135

8.1 Expected number of bulk and surface electron recoils leaking into the nuclear recoil band. 177

8.2 Kolmogorov-Smirnov test of the distribution of various parameters. . 184

List of Figures

1.1 Determination of the Hubble constant by the Hubble Space Telescope Key Project. 5

1.2 Determination of Ω_m with Type Ia supernovae data. 6

1.3 Mass-to-light ratio measurements as a function of scale. 8

1.4 Rotation curves of spiral galaxies. 10

1.5 Comparison of two methods for estimating the mass of galactic clusters. 11

1.6 Evolution of the light element abundances over time. 13

1.7 Light element abundances as a function of baryon density. 14

1.8 Power spectrum of density fluctuations. 15

1.9 Excluded Axion parameter space. 16

2.1 Relic density of a stable, massive particle. 19

2.2 Nuclear form factor and WIMP interaction rates for various target nuclei. 26

3.1 Annual modulation signal observed by the DAMA experiment and the resulting limits on WIMP mass and cross-section. 31

3.2 WIMP mass – cross-section upper limit by the ZEPLIN I experiment. 32

3.3 Exclusion limits obtained by the EDELWEISS experiment. 34

3.4 Exclusion limits obtained by the Super-Kamiokande experiment. . . . 36

4.1 A photograph of the CDMS ZIP detectors along with a schematic of the electronic readout channels. 38

4.2 Electronic band diagram of a QET. 44

4.3 Previous design of the CDMS ZIP QET. 46

4.4 One dimensional diffusion calculation of quasiparticle collection efficiency as a function of Al fin length and number of W elements per $(5\,\mathrm{mm})^2$ area. 48

4.5 Current geometry of a QET showing single TES element with Al quasiparticle collection fins. 49

4.6 $R(T)$ for a $\sim 220\,\mu\mathrm{m} \times 270\,\mu\mathrm{m}$ W square. 50

4.7 Thermal schematic of an ETF-TES. 51

4.8 Schematic of the SQUID readout circuit for the TES phonon sensors. 55

4.9 T_c dependence on dopant concentration. 59

4.10 Dependence of T_c suppression on dopant atom. 60

4.11 $R(T)$ curve pre- and post- ^{56}Fe implant. 61

4.12 Measured IV curves of an ideal TES. 64

4.13 Calculated TES power curves as a function of superconducting transition width. 66

4.14 Calculated TES power curves as a function of phase separation. . . . 67

4.15 Calculated TES power curves as a function of T_c uniformity 69

4.16 IV data showing ideal TES behavior. 72

4.17 IV data showing signs of phase separation. 72

4.18 IV data showing signs of a T_c gradient as well as phase separation. . 73

4.19 Schematic of the ionization readout circuit. 75

4.20 Schematic of the noise sources in the ionization readout circuit. . . . 78

5.1 Schematic diagram of the Stanford Underground Facility. 84

5.2 Mechanical drawing of the refrigerator and Ice Box assembly. 87

5.3 Mechanical drawing of a tower installed in the Ice Box. 88

5.4 Schematic of the CDMS I shield at SUF. 90

6.1 Detector neutralization as a function of LED bake. 98

6.2 Comparison of data and Monte Carlo ^{137}Cs ionization spectra. 99

6.3 10, 67, and 662 keV lines in the ionization spectra 100

6.4 22 keV peak in a Si ZIP ionization spectrum. 101

6.5 10 and 67 keV lines in the phonon spectra 102

6.6 Baseline noise resolution for the six detectors. 105

6.7 Phonon and ionization channel resolution as a function of energy. . . 107

6.8 Position determination with phonon delay and partition. 108

6.9 Event interaction position mapped onto a two dimensional manifold . 109

6.10 Phonon response as a function of position. 110

6.11 A 2D plot showing the ionization response as a function of phonon response for electron and nuclear recoils. 111

6.12 A y plot showing yield as a function of phonon response for electron and nuclear recoils. 112

6.13 Electron recoil yield histograms for a Si ZIP. 115

6.14 Electron recoil yield histograms for a Ge ZIP. 116

6.15 Yield mean, as a function of recoil energy, for electron recoils. 117

6.16 Yield band width, as a function of recoil energy, for electron recoils. . 117

6.17 Comparison of electron recoil bands for all six detectors. 118

6.18 y plots showing the electron recoil band for ^{60}Co data. 119

6.19 Nuclear recoil yield histograms for a Si ZIP. 121

6.20 Nuclear recoil yield histograms for a Ge ZIP. 122

6.21 Yield mean, as a function of recoil energy, for nuclear recoils. 123

6.22 Yield band width, as a function of recoil energy, for nuclear recoils. . 123

6.23 Comparison of nuclear recoil bands for all six detectors. 124

6.24 y plots showing the nuclear recoil band for ^{252}Cf data. 125

6.25 Electron recoil misidentification in a Si ZIP. 128

6.26 Electron recoil misidentification in a Gi ZIP. 129

6.27 Yield distribution of a β rich sample in a Si ZIP. 132

6.28 Yield distribution of a β rich sample in a Ge ZIP. 133

6.29 Yield-yield plots of ^{60}Co data. 134

6.30 y plots showing the distribution of the surface β's. 135

6.31 y distribution of surface electron recoils in a Si ZIP from a ^{60}Co calibration. 136

6.32 y distribution of surface electron recoils in a Ge ZIP from a ^{60}Co calibration. 137

6.33 Comparison of the low y distribution of surface electron recoil between data and Monte Carlo. 138

6.34 Risetime vs. yield plots for calibration data. 139

6.35 χ^2 as a function of ionization energy. 141

6.36 Ionization partition, illustrating the Qin cut 143

6.37 Efficiency of the Qin cut as a function of recoil energy. 144

6.38 Histogram of time between detector events and the most recent activity in the muon veto system. 146

6.39 Efficiency of the risetime cut for a Si and Ge detector. 147

6.40 Trigger efficiency as a function of phonon energy. 148

6.41 Stability of the phonon and ionization energy scales at 10 keV. 150

6.42 Stability of the ionization energy scales at 67 keV. 151

6.43 Stability of the electron recoil band. 152

6.44 Stability of the ionization baseline noise. 153

6.45 Stability of the muon coincident neutron rate. 155

7.1 Comparison of β spectra between data and ^{210}Pb Monte Carlo simulation. 160

7.2 2D plot and recoil histogram of α particles in the low background data. 161

7.3 Comparison of ^{210}Pb background rate estimates. 162

7.4 Comparison of β spectra between data and ^{14}C Monte Carlo simulation. 165

7.5 Radioisotopes created by cosmogenic activation in Ge. 166

7.6 Radioisotopes created by thermal and high-energy neutron activation in Ge. 166

7.7 Observation of the 11.4 day half-life of ^{71}Ge. 167

8.1 Accumulated livetime as a function of elapsed time for the 3V data set. 170

8.2 y plot of the muon coincident low background data. 172

8.3 Muon coincident bulk electron recoil spectra. 173

8.4 Muon coincident nuclear recoil spectra. 174

8.5 Muon coincident surface electron recoil spectra. 175

8.6 y plot of the muon anticoincident low background data. 178

8.7 Muon anticoincident bulk electron recoil spectra. 179

8.8 Muon anticoincident surface electron recoil spectra. 180

8.9 Muon anticoincident nuclear recoil spectra. 181

8.10 Kolmogorov-Smirnov test of the veto time distributions. 185

8.11 Kolmogorov-Smirnov test of the veto time distributions for Z1 186

8.12 Kolmogorov-Smirnov test of the y^* distributions. 187

8.13 Kolmogorov-Smirnov test of the cumulative livetime distribution. . . 188

8.14 Single scatter nuclear recoil efficiency in Ge ZIPs. 190

8.15 Comparison of the single scatter nuclear recoil spectrum in Ge ZIPs with the external neutron Monte Carlo spectrum. 191

8.16 Comparison of Monte Carlo predictions for the rate of multiple scatters, single scatters in Si, and single scatters in Ge with data. 191

8.17 WIMP mass – cross-section exclusion plots. 192

Chapter 1

Introduction

Astrophysics and cosmology are currently highly active and growing fields, spurred by the influx of a variety of precision measurements and a number of new and proposed experiments that are helping to answer some very old questions while creating many new ones.

A standard model of cosmology has emerged over the last several years in which some cosmological parameters like Ω_m, Ω_Λ, and H_0 have been measured to within an accuracy of 10%. The precision of these measurements is testing the consistency of the various methods by which the physical universe is described, with the emergence of a well constrained Dark Matter hypothesis as one example.

The remainder of this chapter will briefly describe the experimental and theoretical basis on which such a hypothesis is built. Subsequent chapters will go on to describe more detailed aspects of a favored Dark Matter candidate known as WIMPs (Weakly Interacting Massive Particles) and the methods by which they may be directly detected and identified.

1.1 The Cosmological Framework

In this section I will present the currently accepted cosmological model. The following discussion is based upon the standard cosmology texts [1] [2] [3] with more details being found therein.

We begin by invoking two (seemingly reasonable) assumptions:

Universal Isotropy We assume that the position of the Earth (or Milky Way) is not atypical in the Universe. Consequently, the observed isotropy (on large scales) leads to the conclusion that the Universe must appear to be isotropic from any arbitrary location. This in turns requires the Universe to be homogeneous.

The Equivalence Principle We assume that the laws of physics (as expressed within special relativity) hold in all local inertial frames.

The resulting metric must then obey the following form

$$ds^2 = -dt^2 + a(t)^2 \left[d\chi^2 + \Sigma^2(\chi) d\Omega^2 \right] \tag{1.1}$$

known as the Robertson-Walker metric. In the above equation χ is a dimensionless radial coordinate, $d\Omega$ is an infinitesimal solid angle element, and a is a scaling factor. Σ may be either $\sin(\chi)$ describing a closed, spheroidal universe, or $\sinh(\chi)$ describing an open, hyperboloid universe with a radius of curvature a. In the limit of $\chi \to 0$ or $a \to \infty$, $\Sigma(\chi)$ reduces to χ giving a flat, Euclidean universe.

To consider the evolution in time of the scale factor, a, a specific theory of gravitation must be invoked. General Relativity yields the following two equations:

$$H^2 \equiv \left(\frac{1}{a} \frac{da}{dt} \right)^2 = \frac{8\pi G}{3} \rho + \frac{\Lambda}{3} - \frac{k}{a^2} \tag{1.2}$$

and

$$\frac{1}{a} \frac{d^2 a}{dt^2} = -\frac{4\pi G}{3} (\rho + 3p) + \frac{\Lambda}{3} \tag{1.3}$$

where G is the Newtonian gravitational constant, Λ is the cosmological constant, and $k = \pm 1, 0$ for close/open or flat universes. ρ and p represent the density and pressure of the Universe's constituents.

Defining

$$\Omega_m \equiv \frac{8\pi G \rho_0}{3H_0^2} \tag{1.4}$$

$$\Omega_k \equiv \frac{-k}{a_0^2 H_0^2} \tag{1.5}$$

$$\Omega_\Lambda \equiv \frac{\Lambda}{3H_0^2} \tag{1.6}$$

as the normalized densities of the matter, curvature, and cosmological constant terms, where the 0 subscript denotes present day values, Equation 1.2 reduces to[1]

$$\Omega_m + \Omega_k + \Omega_\Lambda = 1 \tag{1.7}$$

For a Universe dominates by non-relativistic matter in the recent past, Equation 1.2 can be recast as

$$\left(\frac{H}{H_0}\right)^2 = \Omega_m \left(\frac{a_0}{a}\right)^3 + \Omega_k \left(\frac{a_0}{a}\right)^2 + \Omega_\Lambda \tag{1.8}$$

The time evolution of the scale parameter is then fully determined if three independent parameters, e.g. H_0, Ω_m, and Ω_Λ, can be measured. However, it can be seen that for small values of a the matter density dominates the expansion of the Universe, while for large values of a a non-zero cosmological constant drives the expansion.

[1] In a matter dominated universe, since the pressure of non-relativistic matter is zero.

1.2 Measuring the Cosmological Parameters

1.2.1 H_0

One of the most readily measurable astrophysical quantities is redshift[2]. Redshift, z, is related to the scale factor of the universe according to

$$1 + z = \frac{a_0}{a(t)} \tag{1.9}$$

For small values of redshift ($z \ll 1$) Equation 1.1 can be integrated to yield

$$z = H_0 a_0 \chi = H_0 d \tag{1.10}$$

which is the Hubble equation relating the distance to an astronomical object and its redshift.

Numerous experiments have made measurements of the Hubble constant H_0. I will refer, here, to the latest results of the Hubble Space Telescope (HST) Key Project [4]. Using Cepheid variable stars to calibrate distance scales over the range of 60–400 Mpc the HST Key Project arrives at a value for the Hubble constant of $H_0 = 72 \pm 8\,\mathrm{km\,s^{-1}\,Mpc^{-1}}$. Figure 1.1(a) shows the recession velocity of 23 galaxies as a function of distance determined directly from Cepheid variable stars. Distances to further galaxies (Figure 1.1(b)) are obtained by a variety of techniques that are calibrated to the Cepheids.

[2]Since the determination of redshift involves the measurement of a photon frequency (or wavelength) as it arrives at Earth and the knowledge of the photon's original frequency based on the physical process that led to its creation.

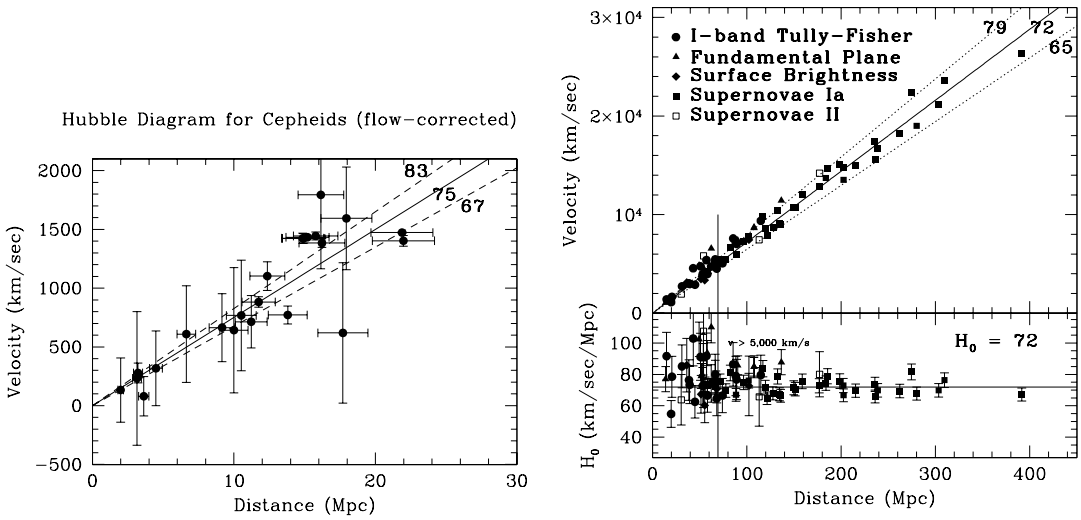

(a) (b)

Figure 1.1: Determination of the Hubble constant by the Hubble Space Telescope Key Project. (a) and (b) show a linear relationship between the observed recession velocity and distance of galaxies up to distances of 30 and 300 Mpc respectively. The slope of the data points yields a value for the Hubble constant of $H_0 = 72 \pm 8\,\mathrm{km\,s^{-1}\,Mpc^{-1}}$. Figures taken from [4].

1.2.2 Ω_m and Ω_Λ

The location of peaks in the cosmic microwave background (CMB) radiation angular anisotropy power spectrum is highly dependent on the sum of Ω_m and Ω_Λ. Measurements by experiments such as BOOMERANG [5], MAXIMA [6], and DASI [7] show that $\Omega_m + \Omega_\Lambda \approx 1$ to within a few percent. This implies (Equation 1.7) that $\Omega_k = 0$ and the Universe is flat.

Defining a deceleration parameter, q_0, as

$$q_0 \equiv \frac{-1}{H_0^2}\left(\frac{1}{a}\frac{d^2a}{dt^2}\right)_0 \tag{1.11}$$

Equation 1.3 can be expanded to yield

$$q_0 = \frac{1}{2}\Omega_m - \Omega_\Lambda \tag{1.12}$$

Thus q_0, a measurable parameter, determines a linear combination of Ω_m and Ω_Λ orthogonal to that measured by the CMB anisotropy. By measuring the the luminosity of Type Ia supernovae[3] as a function of redshift[4], up to redshifts of $z \sim 1$ (Figure 1.2(a)), [8] obtains values of $\Omega_m = 0.28 \pm 0.1$ (after applying the $\Omega_m + \Omega_\Lambda = 1$ constraint) as shown in Figure 1.2(b).

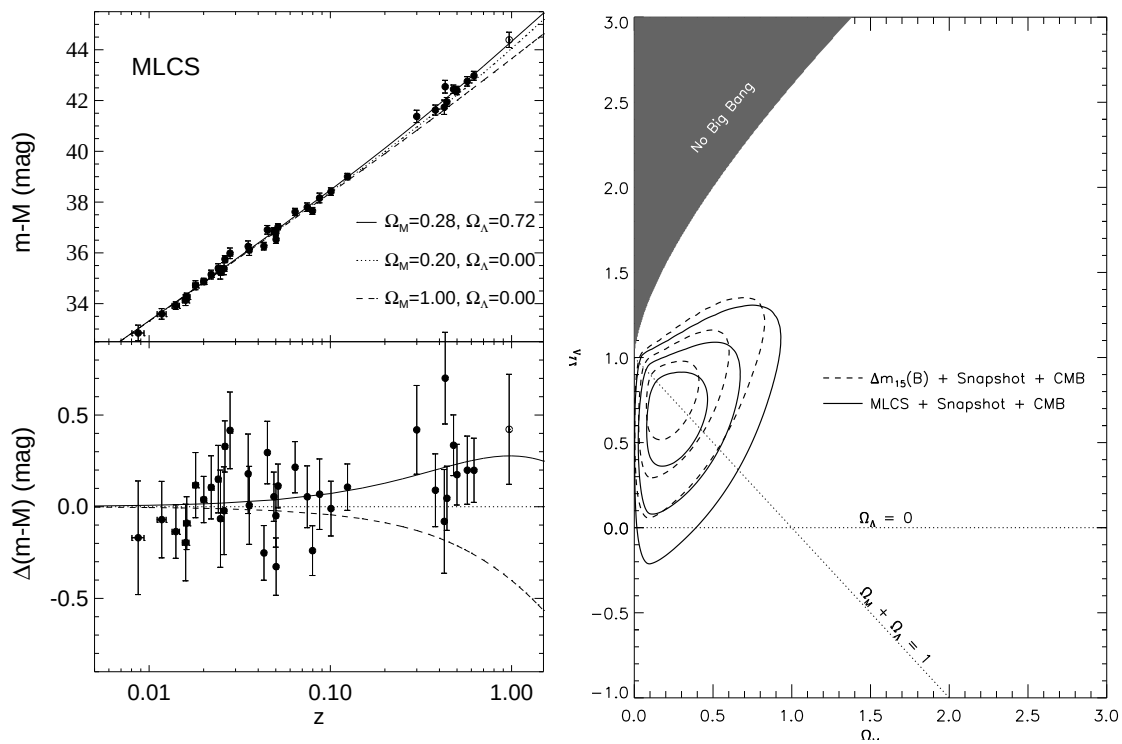

(a) (b)

Figure 1.2: Determination of Ω_m with Type Ia supernovae data. Measuring the luminosity of standard candles (Type Ia supernovae) as a function of redshift (a) results in a constraint on $\frac{1}{2}\Omega_m - \Omega_\Lambda$. Applying the further constraint of $\Omega_m + \Omega_\Lambda \sim 1$, based on CMB data, yields a value for Ω_m of ~ 0.28. Figures taken from [8].

There exist other techniques, based on large scale structure formation or the weak gravitational lensing effect, that are directly sensitive to Ω_m. The 2dF Galaxy Redshift Survey [9] reports a value of $\Omega_m h = 0.20 \pm 0.03$, where $h \equiv H_0/100$, based

[3]Type Ia supernovae can be used as standard candles

[4]This is a generalization of the Hubble constant measurement to much larger redshifts

on the distribution power spectrum of 160000 galaxies spanning the region $0.02 \leq k \leq 0.15\,h\,\mathrm{Mpc}^{-1}$.

1.3 The Existence of Dark Matter

1.3.1 Mass-to-Light Ratio

An illuminating way to arrive at the Dark Matter *problem* is to consider the mass-to-light ratio for various size scales. The luminosity density in the nearby Universe is measured to be [10]

$$j = 3.3 \times 10^8 h L_\odot/\mathrm{Mpc}^3 \tag{1.13}$$

where the $\odot$ subscript refers to the Sun. Given $\Omega_m \sim 0.3$ (or alternatively $\rho_m \sim 0.3 \times 10^{-29}\,\mathrm{g\,cm}^{-3}$) then the mass-to-light ratio for matter is roughly

$$\frac{M}{L} \sim 470\,h\,\frac{M_\odot}{L_\odot} \tag{1.14}$$

Since stars have a mass-to-light ratio that is typically $M_*/L_* < 10 M_\odot/L_\odot$ Equation 1.14 implies that a large fraction of the matter in the universe does not emit light[5], hence the name Dark Matter. On galactic scales mass-to-light ratios are observed to be $> 10\,h\,M_\odot/L_\odot$, while on the scale of galactic clusters the ratio is in the range $(250 - 450)\,h\,M_\odot/L_\odot$. This data is nicely summarized in Figure 1.3 [11] where it is seen that on size scales larger than 1 Mpc the mass-to-light ratio asymptotes close to the value in Equation 1.14.

Galactic Rotation Curves

In determining the mass-to-light ratio, luminosity is a directly measurable quantity. The mass, however, is determined indirectly by a variety of different techniques.

[5] At least not in the optical band

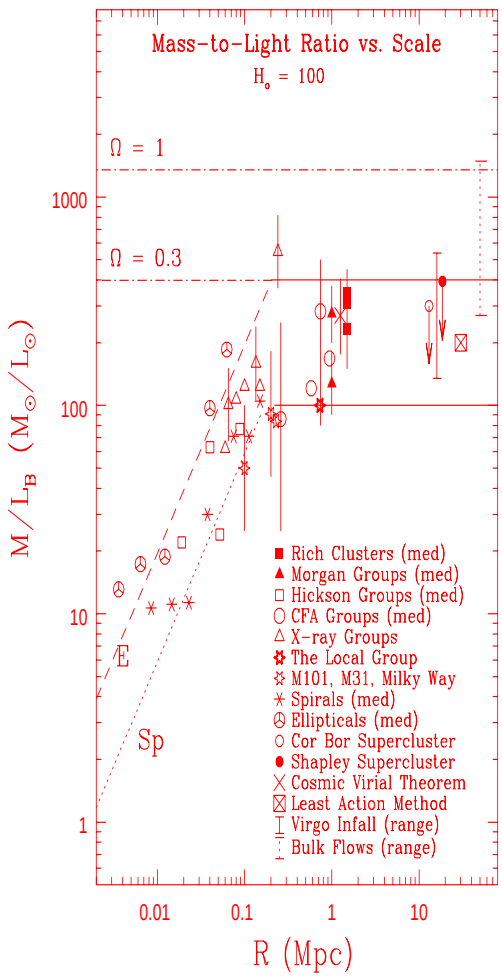

Figure 1.3: Mass-to-light ratio measurements as a function of scale. The evidence of an increasingly larger component of non-luminous matter is apparent up to scale of $\sim 1\,\mathrm{Mpc}$. Beyond $1\,\mathrm{Mpc}$ the mass-to-light ratio levels off at a value consistent with $\Omega_m \sim 0.3$ and $\Omega_{lum} \sim 0.001$. Figure taken from [11].

Galactic rotation curves are a well known example. The rotational velocity of galactic disks (in spiral galaxies) is determined from the redshift of various stellar absorption lines, or alternatively from the fine-structure line ($\lambda \sim 21\,\mathrm{cm}$) emission of interstellar atomic hydrogen. The mass within a certain radius, r, is given by Equation 1.15,

based on Newtonian mechanics.

$$\frac{v(r)^2}{r} = \frac{GM(r)}{r^2} \tag{1.15}$$

Rotation curves from ~ 1000 spiral galaxies presented in [12] indicate the presence of gravitating mass which cannot be accounted for by the luminous disk or the central bulge. The flattening of the rotation curves for large values of r are well fit by a matter density distribution of the form

$$\rho(r) = \frac{1}{r^2 + a^2} \tag{1.16}$$

where a is a constant defining a core radius so that the density of non-luminous matter does not diverge at small radii.

The Mass of Clusters

For clusters in dynamic equilibrium the mass of the clusters may be determined from a measurement of the peculiar velocities of the cluster's component galaxies [13]. According to the virial theorem, the kinetic and potential energies of a system are related according to

$$\langle T \rangle = -\frac{1}{2} \langle V \rangle \tag{1.17}$$

where $\langle T \rangle$, the average kinetic energy, is derived from the dispersion in the peculiar velocities, and $\langle V \rangle$ is the average value of the potential energy. The mass of the cluster is then estimated from the value of the gravitational potential $\langle V \rangle$.

Another method for measuring the potential well depth of galaxy clusters, also applicable to elliptical galaxies, is based on the X-ray emission of hot intracluster gas. Under the assumption of hydrostatic equilibrium, the measured X-ray profiles can be fit to models of temperature and density distributions in order to extract the cluster mass [14]. A comparison of mass-to-light ratios obtained with these two methods, done by [15], indicating good agreement is seen in Figure 1.5.

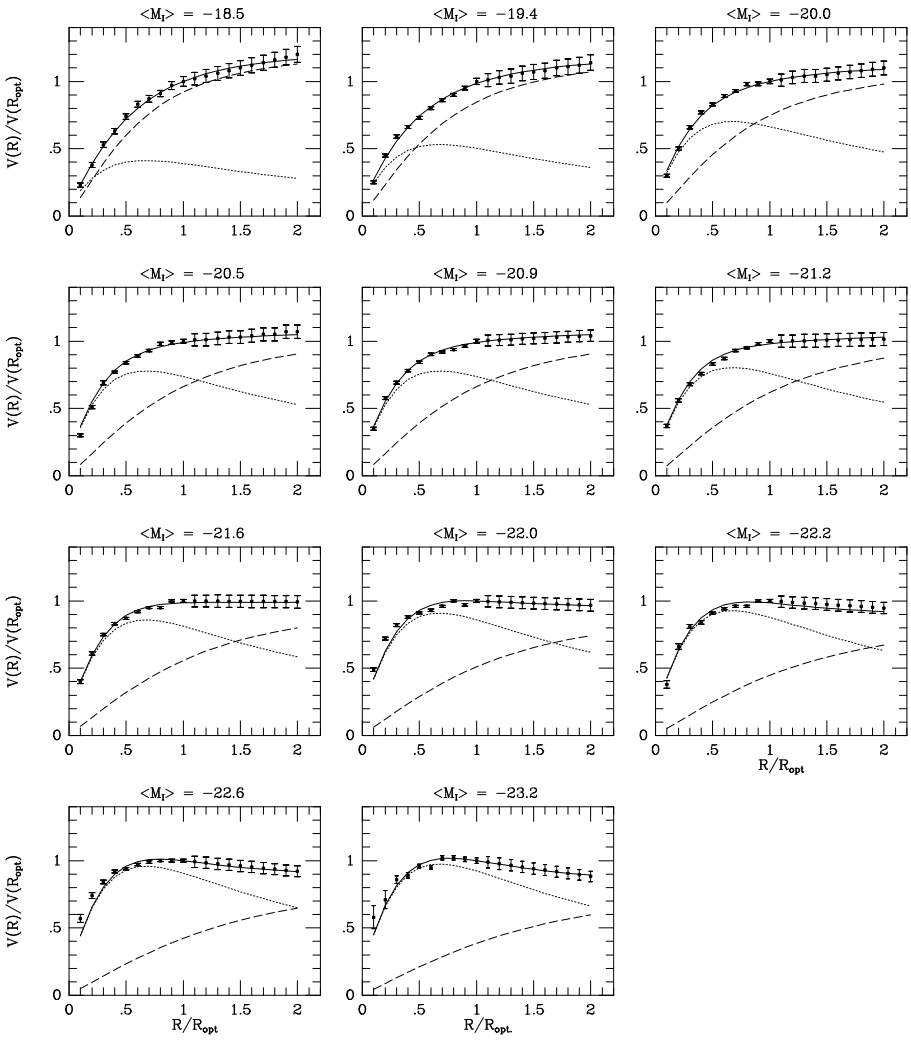

Figure 1.4: Rotation curves of spiral galaxies. Each panel represents an average taken over a collection of galaxies in a certain luminosity range. The points with error bars are the data while the solid, light and dashed lines represent the total, halo, and disk contributions respectively. Figure taken from [12].

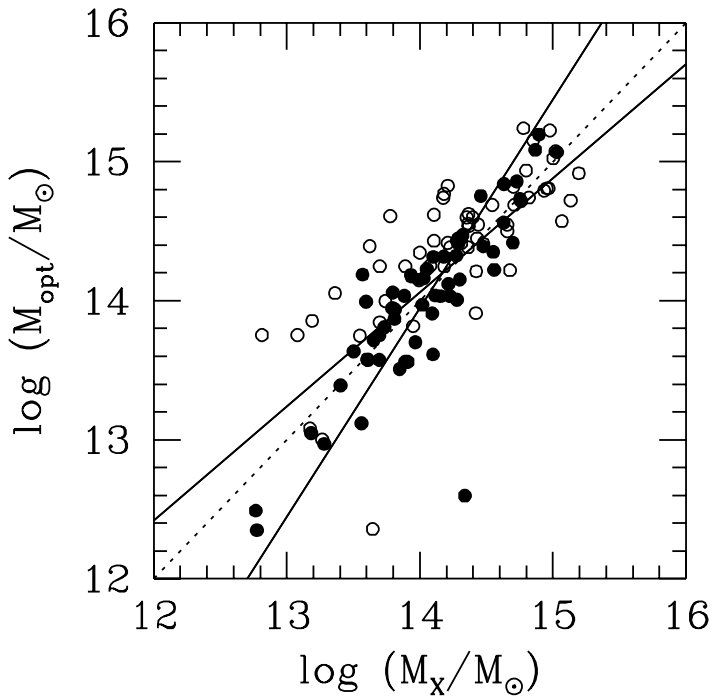

Figure 1.5: Comparison of two methods for estimating the mass of galactic clusters. The masses of galactic clusters as determined from measurements of the peculiar velocities and the Virial theorem (y-axis) agree well with those determined from measurements of X-ray emission of the intracluster gas (x-axis). Figure taken from [15].

1.4 Baryonic and Non-Baryonic Dark Matter

1.4.1 Big Bang Nucleosynthesis

Having established that a significant fraction of matter is *Dark* the question turns toward the nature of this matter. Big Bang Nucleosynthesis (BBN) is a term that refers to calculations of the light element (H, D, He, ^{3}He, and ^{7}Li) abundances within the framework of a hot Big Bang model. Details on this subject can be found in [16] [17] or textbooks such as [1] [3].

Formation of nuclei heavier than H begins once the temperature of the Universe drops such that the the number of photons with sufficient energy to photodissociate these nuclei is suppressed. The formation of the nuclei then proceeds until no free neutrons remain, as shown in Figure 1.6.

With most of the cross-sections involved in nucleosynthesis being well known, the primary uncertainty in the calculation is the baryon density ρ_b (or Ω_b). Measurements of the light element abundances can therefore place strong limits on the baryon density, as seen in Figure 1.7. Recent measurements [19] yield a value of Ω_b

$$0.018 < \Omega_b\, h^2 < 0.022 \tag{1.18}$$

accounting for less than 15% of the matter density Ω_m. While this measurement implies that the majority of Dark Matter is non-baryonic, it also suggests that the majority of baryonic matter is also dark, since $\Omega_{lum} \sim 0.004$.

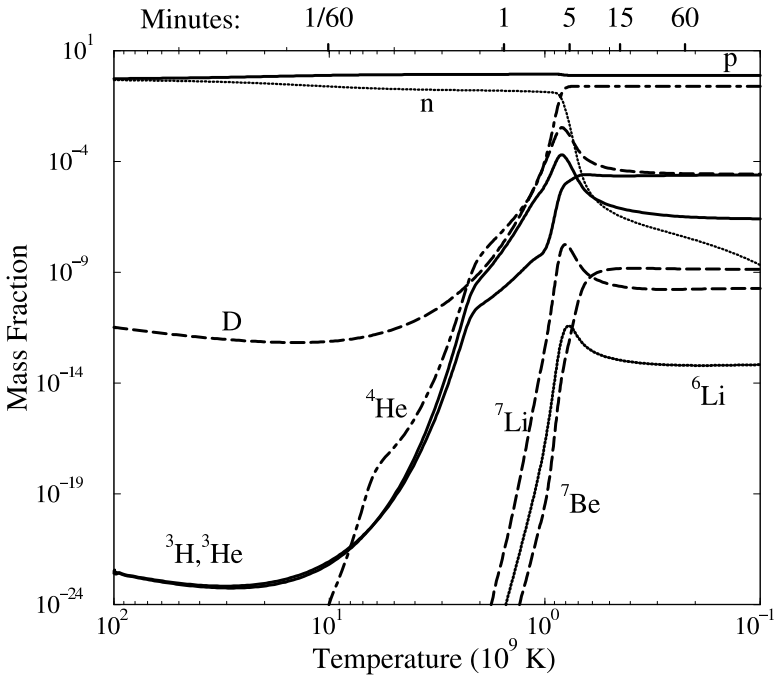

Figure 1.6: Evolution of the light element abundances over time (or temperature). When the Universe has cooled sufficiently that the light elements are no longer dissociated by energetic photons nucleosynthesis proceeds until the supply of free neutrons is exhausted. Figure taken from [18].

1.4.2 Non-Baryonic Dark Matter

Hot and Cold Dark Matter

A useful way of classifying Dark Matter candidates is based on their energy at the moment when they would have decoupled from the rest of the matter in the Universe. If a candidate is still relativistic at the time of decoupling it is referred to as *hot*, and alternatively if the candidate is non-relativistic it is referred to as *cold*. This classification is a useful one since there are measurable properties of the Universe which depend on the *hot/cold* nature of the Dark Matter. Recent results from the 2dF Galactic Redshift Survey [20], based on the power spectrum of density fluctuations,

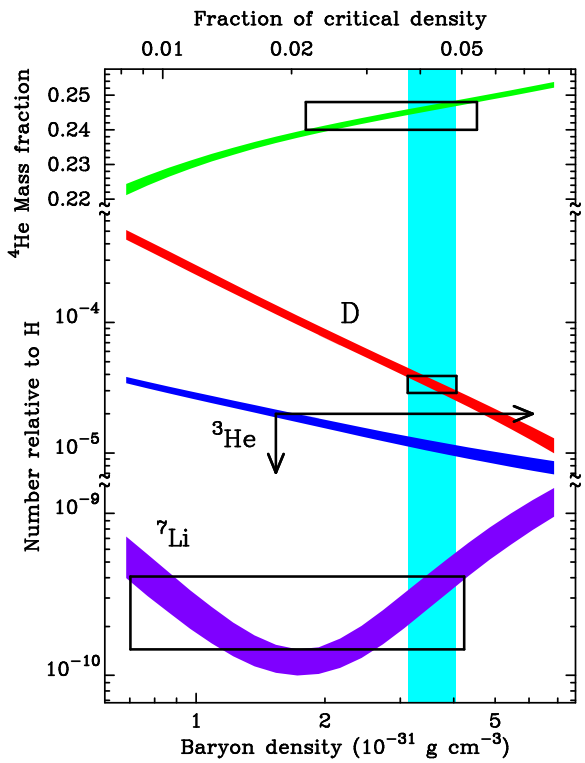

Figure 1.7: Light element abundances as a function of baryon density. The boxes and arrows indicate measured abundances. Good agreement between calculated and measured abundances is obtained for $\Omega_b\, h^2 \sim 0.02$. Figure taken from [18]

(shown in Figure 1.8) place an upper limit of the fraction of Hot Dark Matter of

$$f_\nu \equiv \Omega_\nu/\Omega_m < 0.13 \tag{1.19}$$

Axions & WIMPs

There currently exist two hypothetical particles which are favored candidates for the Dark Matter : Axions and WIMPs.

Originally motivated by particle physics to resolve the strong CP problem, Axions

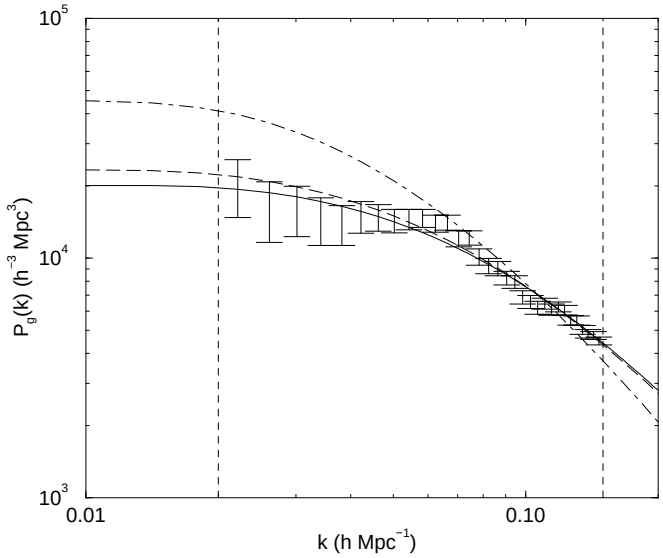

Figure 1.8: Power spectrum of density fluctuations. The solid, dashed, and dot-dashed lines represent power spectra for $\Omega_\nu = 0$, 0.01, and 0.05 respectively. The data support the conclusion that the fraction of Hot (relativistic) Dark Matter is less than 13% of the total matter density. Figure taken from [20]

are a good cold Dark Matter candidate [1]. Although the Axion mass is currently restricted to be within

$$10^{-6} < m_a < 10^{-2}\, eV \tag{1.20}$$

they are non-relativistic as a consequence of the method by which they are produced in the early Universe. Figure 1.9 shows the region of parameter space excluded by the U.S Cold Dark Matter Axion Search [21]

Weakly Interacting Massive Particles (WIMPs) are the other favored Dark Matter candidate. As with Axions, WIMPs have a natural explanation within particle physics, namely the Supersymmetric extentions to the Standard Model. A discussion of WIMPs and their properties is presented in Chapter 2.

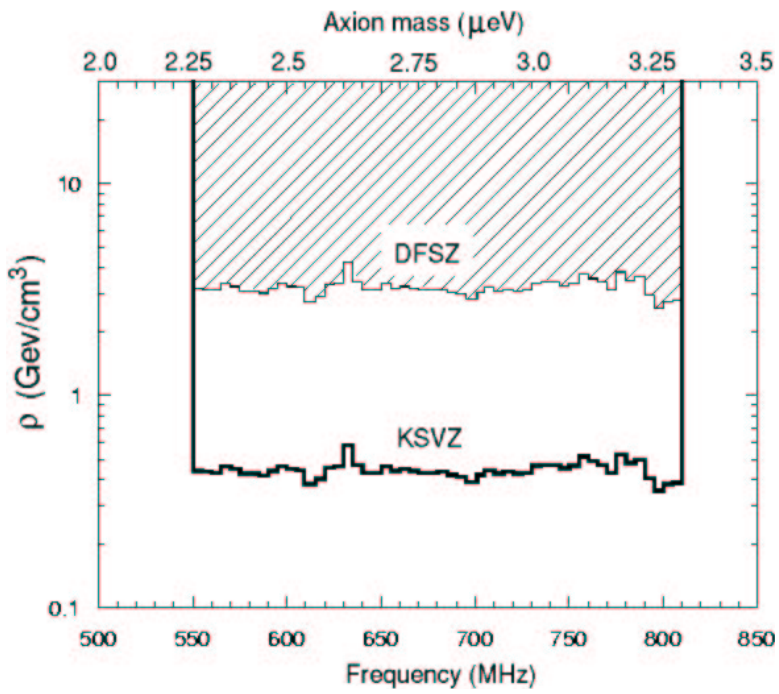

Figure 1.9: Excluded Axion parameter space. Figure taken from [21].

Chapter 2

Supersymmetry and WIMPs

2.1 Relic Abundance

Given the existence, in the early Universe, of a massive, stable particle, χ, that may annihilate into (or be created by) another particle, ℓ, according to the following interactions

$$\chi\overline{\chi} \rightarrow \ell\overline{\ell} \tag{2.1}$$

$$\ell\overline{\ell} \rightarrow \chi\overline{\chi} \tag{2.2}$$

it is possible to calculate the relic abundance[1] of the χ particle. The density of such a particle, in thermal equilibrium with the Universe, is given by

$$n_\chi \propto T^3 \quad , \quad m_\chi \ll kT \tag{2.3}$$

$$n_\chi \propto T^{3/2} \exp\left(\frac{-m_\chi}{kT}\right) \quad , \quad m_\chi \gg kT \tag{2.4}$$

It may naively be concluded that the relic density of the particle will approach zero

[1] The abundance of the particle at present times

(exponentially) as the Universe cools well below the temperature required to produce the χ ($kT \ll m_\chi$). The expansion of the Universe, however, causes the particle χ to fall out of equilibrium resulting in a finite relic density[2]. The evolution of the number density of χ over time ($n_\chi(t)$) is described by the Boltzmann equation [3] [22]

$$\frac{dn_\chi}{dt} + 3Hn_\chi = -\langle\sigma_A v\rangle \left[(n_\chi)^2 - (n_\chi^{eq})^2\right] \tag{2.5}$$

where H is the Hubble constant, $\langle\sigma_A v\rangle$ is the thermally averaged product of the annihilation cross section (σ_A) and relative velocity (v), and n_χ^{eq} is the number density of the particle in thermal equilibrium[3]. The second term on the left hand side of Equation 2.5 accounts for the expansion of the Universe, and in the the absence of any annihilation or creation of χ's, results in

$$n_\chi \propto a^{-3} \tag{2.6}$$

The first (second) term of right hand side of Equation 2.5 accounts for annihilation (creation) of χ's. The term describing the creation rate of χ's can be understood by noting that in thermal equilibrium, the creation and annihilation rates are equal. At early times, when the Universe is hot, the Hubble constant (H) scales as T^2, while the equilibrium density of χ's scales as T^3. Consequently, the expansion term is not very significant and the number density of χ's is given by the thermal equilibrium value (equations 2.3 and 2.4). As the Universe cools the creation rate of χ's approaches zero exponentially and becomes negligible. χ's remain capable of annihilating and their density drops rapidly until such time, referred to as the freezeout time, that the expansion and annihilation rates are equal ($Hn_\chi = \langle\sigma_A v\rangle (n_\chi)^2$). The temperature at which freezeout occurs (T_f) is roughly given by

$$T_f \approx \frac{m_\chi}{20} \tag{2.7}$$

[2]The comoving density approached a finite, constant value. The local density will decrease as a^3, where a is the scale factor of the Universe.

[3]The thermal equilibrium density depends on temperature (T) as shown in equations 2.3 and 2.4. The dependence of temperature (T) on time (t) depends on the details of the particular cosmological model.

After that time the expansion rate term dominates leading to the result given in Equation 2.6. Figure 2.1 illustrates the time evolution of χ number density based on the arguments mention above.

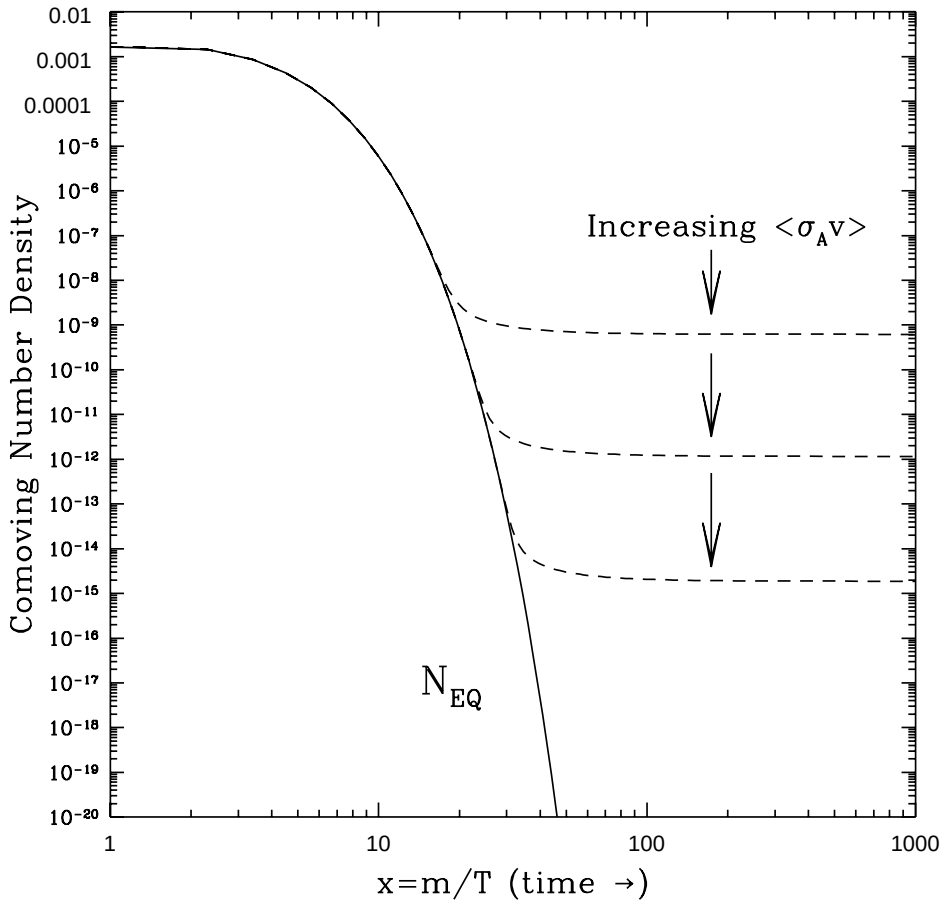

Figure 2.1: Relic density of a stable particle of mass m as a function the temperature (T) of the Universe. At early times, corresponding to temperatures $kT > m$, the annihilation and creation rates of the particle are sufficiently high to keep the number density in thermal equilibrium with the Universe. As the temperature drops the density of the particle is exponentially suppressed until the annihilation rate drops below the Universe's expansion rate. At the point, referred to as freezeout, the comoving number density becomes a constant that is largely determined by the particle's annihilation cross section.

The χ relic density is obtained by considering the conserved quantity n_χ/s, where s is the entropy density and scales as T^3. Using the freezeout criteria ($Hn_\chi = \langle\sigma_A v\rangle (n_\chi)^2$) the following relation is obtained

$$\left(\frac{n_\chi}{s}\right)_0 = \left(\frac{n_\chi}{s}\right)_f \propto \frac{H_f}{\langle\sigma_A v\rangle T_f^3} \propto \frac{1}{m_\chi \langle\sigma_A v\rangle} \tag{2.8}$$

The present day mass density of the χ can then be written as

$$\Omega_\chi h^2 = \frac{m_\chi n_\chi}{\rho_c} \approx \left(\frac{3\times 10^{-27}\mathrm{cm}^3\,\mathrm{s}^{-1}}{\langle\sigma_A v\rangle}\right) \tag{2.9}$$

2.2 Supersymmetry and WIMPs

It was argued in Chapter 1 that the density of Dark Matter in the Universe is roughly $\Omega_{DM}h^2 \sim 0.1$. According to Equation 2.9 if a stable, massive particle, as described above, were to constitute the Dark Matter in the Universe its annihilation cross section should be $\langle\sigma_A v\rangle \sim 10^{-28}\,\mathrm{cm}^2\,\mathrm{s}^{-1}$. A particle with interaction strengths characteristic of the Weak force, on the other hand, is expected to have an annihilation cross section on the order of $\langle\sigma_A v\rangle \sim 10^{-25}\,\mathrm{cm}^2\,\mathrm{s}^{-1}$. This remarkable agreement[4] suggests physics at the electroweak energy scale may result in a Dark Matter candidate. Supersymmetry provides such a candidate, generally referred to as a Weakly Interacting Massive Particle (WIMP). The subject of supersymmetric Dark Matter is covered in great detail in [22]. I will include just a brief overview.

Supersymmetry is an extension to the Standard Model of particle physics which requires that particles exist in multiplets, related by a supersymmetric transformation, which have a difference in spin of 1/2. Such a transformation turns fermions into bosons, and vice-versa. Thus for all the quarks (q) and leptons (l) there should exist bosonic partners referred to as squarks ($\overline{q}$) and sleptons ($\bar{l}$), while for all the bosons (photon, W, Z, Higgs) there exist fermionic partners referred to by the name

[4]Remarkable if one considers that the cross-sections associated with the other forces are many orders of magnitude larger.

of the boson with an "ino" suffix (e.g. photino). If R parity, the quantum number that distinguishes particles from their supersymmetric partners, is not broken then there exists a lightest supersymmetric particle which is stable[5] and is an ideal WIMP candidate. In most models, the lightest supersymmetric particle (LSP) is a linear combination of the partners of the photon, Z^0, and neutral Higgs bosons

$$\chi = N_{10}\tilde{B} + N_{20}\tilde{W}^3 + N_{30}\tilde{H}_1^0 + N_{40}\tilde{H}_2^0 \tag{2.10}$$

referred to as the lightest neutralino, with the mass of the neutralino (m_χ) determined by the coefficients N_{i0}. The coefficients N_{i0} also determine the interaction strengths of the neutralino and relate the elastic scattering cross sections to the annihilation cross section. This relationship allows the translation of the annihilation cross section, as determined from Ω_{DM} (Equation 2.9), into elastic scattering cross sections which are relevant for some detection experiments.

2.2.1 WIMP-Nucleus Scattering

With the WIMP-quark and WIMP-gluon scattering cross section in hand, the WIMP-nucleon scattering cross can be obtained. The differential cross section is given by

$$\frac{d\sigma}{d|\vec{q}|^2} = \frac{\sigma_0}{4m_r^2 v^2} F^2(Q) \tag{2.11}$$

where q is the momentum transfer, $m_r = m_\chi m_N/(m_\chi + m_N)$ is the WIMP-nucleus reduced mass, σ_0 the cross section in limit of zero momentum transfer, and $F(Q)$ the nuclear form factor. Q, the energy transferred to the nucleus, is related to the momentum transfer q according to

$$Q = \frac{|\vec{q}|^2}{2m_N} = \frac{m_r^2 v^2}{m_N}(1 - \cos\theta^*) \tag{2.12}$$

[5]Since there is no other supersymmetric particle it can decay into.

where θ^* is the scattering angle in the center of momentum frame. The zero momentum cross section (σ_0) is given by

$$\sigma_0 = \int_0^{4m_r^2 v^2} \left.\frac{d\sigma}{d|\vec{q}|^2}\right|_{q=0} d|\vec{q}|^2 = \frac{4m_r^2}{\pi}\left[Zf_p + (A-Z)f_n\right]^2 \sim \frac{4m_r^2}{\pi}\left[Af\right]^2 \tag{2.13}$$

where Z and A are the atomic and mass numbers, and f_p (f_n) are the coupling between the WIMP and the proton (neutron). Typically, $f_p \sim f_n$, resulting in the rightmost form of Equation 2.13. Equation 2.13 illustrates the strong (A^2) dependence of the cross section on the nucleus mass number. The form factor describes the coherence of the WIMP-nucleon interaction over the size of the nucleus. A common parametrization of the form factor, referred to as the Woods-Saxon form factor, is given by

$$F(Q) = \left[\frac{3j_1(qR_1)}{qR_1}\right] \exp\left[-(qs)^2/2\right] \tag{2.14}$$

where j_1 is a spherical Bessel function, $j_1(x) = \frac{\sin(x) - x\cos(x)}{x^3}$, and

$$\begin{aligned} R_1 &= \sqrt{R^2 + 5s^2} \\ R &\sim 1.2A^{1/3}\,\mathrm{fm} \\ s &\sim 1\,\mathrm{fm} \end{aligned} \tag{2.15}$$

Equations 2.13–2.15 are valid for spin independent interactions. The spin dependent equations are more complicated. However, in most models spin independent interactions dominate the cross section. A full treatment of the spin dependent case is given in [22].

2.3 Recoil Energy Spectra

For a unit mass of detector material, the differential event rate of WIMP interactions is given by

$$dR = \left[\frac{d\sigma}{d|\vec{q}|^2}\, d|\vec{q}|^2\right]\left[\frac{\rho_0}{m_\chi m_N}\, v f_1(v)\, dv\right] \tag{2.16}$$

where it can be seen that the first term describes the individual WIMP-nucleus interaction and is based on a particular theoretical model of the WIMP (i.e. one of the various Supersymmetric models). The second term describes the contribution of the local WIMP flux to the detection rate and is based on astrophysical measurements. $f_1(v)$ is the distribution of WIMP speeds[6] relative to the detector. By integrating over all WIMP velocities Equation 2.16 can be recast to give the differential event rate per recoil energy

$$\frac{dR}{dQ} = \frac{\sigma_0 \rho_0}{2 m_\chi m_r^2}\, F^2(Q)\, T(Q) \tag{2.17}$$

$$T(Q) = \frac{\sqrt{\pi}}{2}\, v_0 \int_{v_{min}}^{v_{max}} \frac{f_1(v)}{v}\, dv \tag{2.18}$$

where $v_{min} = \sqrt{(Q m_N)/(2 m_r^2)}$ is the minimum WIMP speed that can result in a recoil energy Q (Equation 2.12), and v_{max} is the maximum WIMP velocity. $f_1(v)$ is typically taken to be Maxwellian

$$f_1(v)\, dv = \frac{4 v^2}{\sqrt{\pi} v_0^3} \exp\left(-\frac{v^2}{v_0^2}\right) dv \tag{2.19}$$

with a velocity dispersion $v_0 \sim 220\,\mathrm{km\,s^{-1}}$. $v_{max} \sim 650\,\mathrm{km\,s^{-1}}$, the WIMP escape velocity at the Earth's position in the galaxy, is sufficiently larger than v_0 that it is typically taken to be ∞ in order to simplify the calculation of $T(Q)$. Integrating

[6] $f_1(v)$ is obtained by integrating the 3-dimensional velocity distribution over all angles, and is normalized such that $\int f_1(v)\, dv = 1$.

Equation 2.18, and assuming[7] $F(Q) \approx 1$, yields

$$T(Q) = \exp\left(-\frac{v_{min}^2}{v_0^2}\right) \tag{2.20}$$

$$\frac{dR}{dQ} = \frac{\sigma_0 \rho_0}{\sqrt{\pi} v_0 m_\chi m_r^2} \exp\left(-\frac{Q m_N}{2 m_r^2 v_0^2}\right) \tag{2.21}$$

$$R = \frac{2\sigma_0 \rho_0 v_0}{\sqrt{\pi} m_\chi m_N} \exp\left(-\frac{E_{Th} m_N}{2 m_r^2 v_0^2}\right) \tag{2.22}$$

Figure 2.2 illustrates the results of equations 2.17–2.20 for a hypothetical WIMP with mass $m_\chi = 100\,\mathrm{GeV}/c^2$ and a WIMP-nucleon cross-section of $\sigma_{\chi-n} = 10^{-42}\,\mathrm{cm}^2$ interacting with Si, Ge, and Xe nuclei (A = 28, 73, and 131 respectively). Heavier nuclei, such as Xe, benefit from the A^2 term in Equation 2.13 leading to higher interaction rates with WIMPs. However, the rapid drop in the nuclear form factor (Figure 2.2(a)) for recoil energies above $\sim 20\,\mathrm{keV}$ means that the majority of the WIMP interactions lie at low recoil energies, thus challenging any WIMP detection experiments to lower its detection threshold as much as possible. Figures 2.2(b) and 2.2(c) show the differential and integrated interaction rates, respectively. These figures highlight the fact that the choice of detector target material is strongly linked to the minimum recoil energy threshold achievable with that material since the light Si nuclei yield a higher interaction rate than the heavy Xe for sufficiently high energy thresholds.

The preceding calculation of $T(Q)$ did take not into account the motion of the Earth around the Sun. The variation in the speed of the Earth as it orbits the Sun, with respect to the WIMP halo, results in an annually varying WIMP flux as seen from the Earth. The component of the Earth's velocity in the plane of the Sun's orbit around the galactic center is given as function of time by

$$v_e = v_0 \left[1.05 + 0.07 \cos\left(\frac{2\pi(t - 152.5)}{365.25}\right)\right] \tag{2.23}$$

[7] A reasonable assumption for light nuclei or light WIMPs since the exponential suppression of the differential rate due to the $T(Q)$ term occurs before the form factor $F(Q)$ varies significantly from 1.

where $t = 0$ corresponds to January 1 of a given year. Assuming $v_{max} = \infty$ we obtain

$$f_1(v)\,dv = \frac{v\,dv}{\sqrt{\pi}v_e v_0}\left\{\exp\left[-\frac{(v-v_e)^2}{v_0^2}\right] - \exp\left[-\frac{(v+v_e)^2}{v_0^2}\right]\right\} \tag{2.24}$$

$$T(Q) = \frac{\sqrt{\pi}v_0}{4v_e}\left\{\mathrm{erf}\left[\frac{(v_{min}+v_e)}{v_0}\right] - \mathrm{erf}\left[\frac{(v_{min}-v_e)}{v_0}\right]\right\} \tag{2.25}$$

$$\tag{2.26}$$

with the differential and integral recoil rates being modified accordingly. The motion of the Earth around the Sun, thus, results in an annual modulation in both the amplitude as well as the shape of the WIMP recoil spectrum. The variation in the WIMP recoil rate is on the order of a few % and can be as much as 10% in the case of a $100\,\mathrm{GeV}/c^2$ WIMP, a Ge target, and a recoil threshold energy of $10\,\mathrm{keV}$.

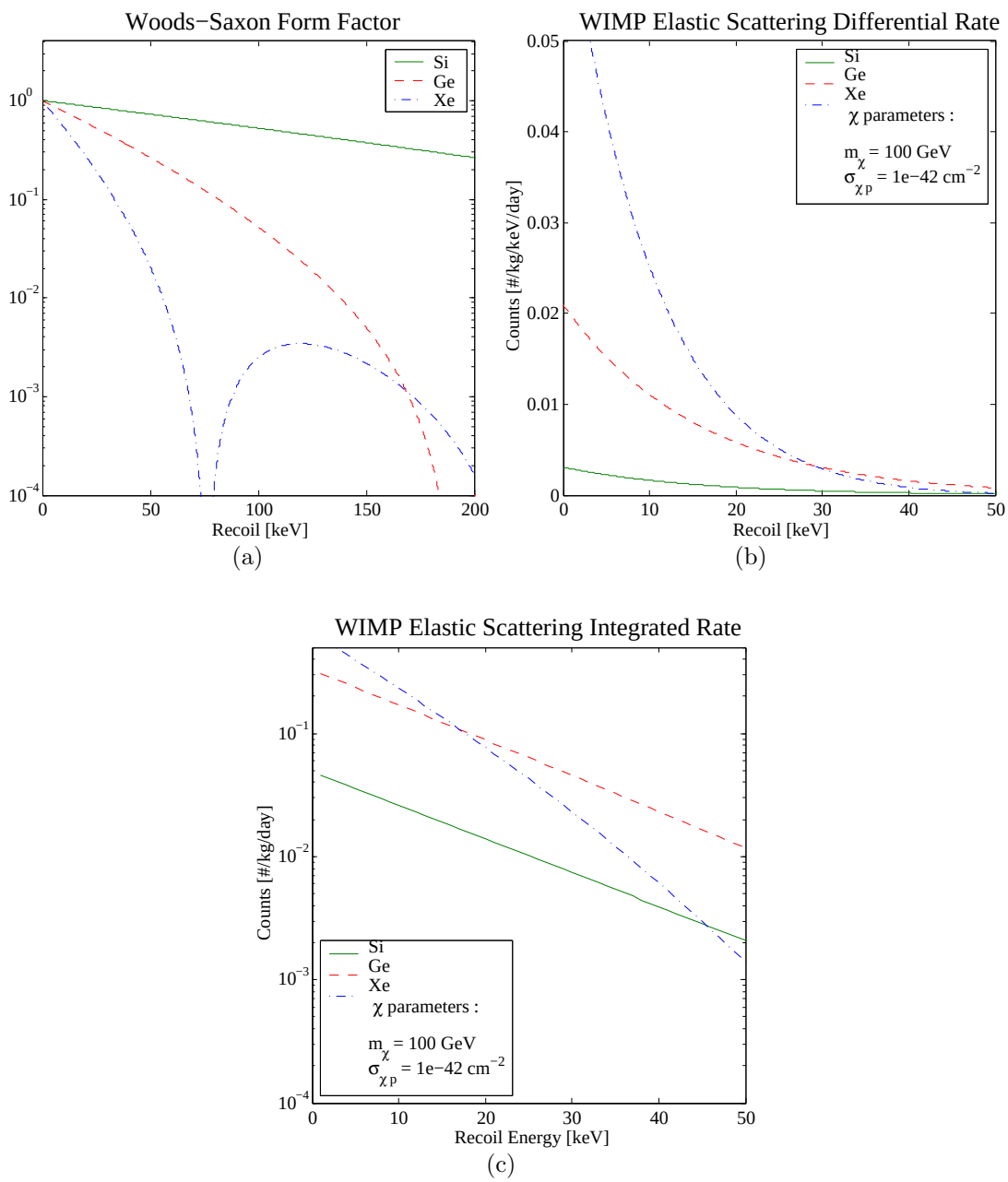

Figure 2.2: (a) Nuclear form factors for Si (solid line), Ge (dashed line), and Xe (dash dotted line). The form factors drop rapidly for the heavier nuclei as elastic scattering processes lose coherence due to the large size of the nucleus. (b) and (c) show the differential and integrated interaction rates for the same nuclei. It can be seen that a low recoil energy threshold is necessary to take full advantage of the A^2 cross-section scaling for heavier nuclei.

Chapter 3

The Search for Dark Matter

The search for Dark Matter in the form of the Weakly Interacting Massive Particles is an active field, with over two dozen experiments currently in operation or preparation. In this section I will briefly summarize a sample of these experiments, highlighting the variety of techniques being used.

A useful way of classifying the experiments is along the lines of whether or not the detectors are able to distinguish between a WIMP signal and a background event on an event by event basis. This is relevant because WIMP events rates (for some of the more optimistic SUSY models) will be ~ 0.01 events/kg/keV/day [22] [23] while background rates from naturally occurring radioactivity are order of magnitude higher. The reach, or sensitivity, of an experiment can be quantified as a function of three parameters : the background rate (B), the background misidentification fraction [1] (β), the signal acceptance fraction α, and the exposure MT, where M is the mass of the detectors and T is the duration of the experiment. For experiments which do not distinguish between signal and background events $\beta = 1$, while α may assume any value between 0 and 1. The sensitivity of such experiments, in the case of no observed events, is given by

$$S_{90} \propto \frac{2.3}{\alpha MT} \tag{3.1}$$

[1] Also referred to as the background leakage term

where 2.3 is the 90% confidence level (CL) upper limit on 0 observed events, and S_{90} is proportional to the 90% CL upper limit exlcuded cross-section. It can be seen from equation 3.1 that the sensitivity of such an experiment will improve linearly with exposure as long as no events are observed. In the case that events are observed, which are believed to be due to a background source the sensitivity of the non-discriminating experiment becomes [24]

$$S_{90} \propto \frac{N_{bkg} + 1.28\sqrt{N_{bkg}}}{\alpha MT} \tag{3.2}$$

where $N_{bkg} + 1.28\sqrt{N_{bkg}}$ is the 90% CL upper limit on N_{bkg} observed background events. Equation 3.2 reduces to

$$\begin{aligned} S_{90} &\propto \frac{BMT + 1.28\sqrt{BMT}}{\alpha MT} \\ &\propto \frac{B}{\alpha} + \frac{1.28}{\alpha}\sqrt{\frac{\beta B}{MT}} \end{aligned} \tag{3.3}$$

since the expected observed background rate $\langle N_{bkg} \rangle \equiv BMT$. It can be seen from equation 3.3 that as soon as a background is encountered, and the exposure is sufficiently large enough to accurately measure the background, the sensitivity stops improving. Although large efforts have been undertaken to reduce background levels down to a fraction ($\sim$0.04) of an event/kg/keV/day [25] a large fraction of WIMP parameter space are inaccessible to such experiments.

If an experiment is able to distinguish between signal and background events, based on the value of a particular, continuous, event parameter (η) then the sensitivity of the experiment will depend on the value of that parameter chosen as the discrimination criterion[2]. In the limit that the systematic errors on $\alpha(\eta)$ and $\beta(\eta)$ are significantly smaller that the statistical error on the observed number of events the sensitivity is given by [26]

$$S_{stat} = \sqrt{\frac{\beta(1-\beta)}{(\alpha-\beta)^2}}\sqrt{\frac{B}{MT}} \tag{3.4}$$

[2]i.e. The value of the *cut* using that parameter.

Defining

$$\mathcal{Q} = \frac{\beta(1-\beta)}{(\alpha-\beta)^2} \tag{3.5}$$

the value of η is chosen that will minimize $\mathcal{Q}$. It can be seen from equation 3.4 that the sensitivity of the experiment, once a background is encountered, will continue to improve as the square root of the exposure until the systematic errors on α and β become significant. It is useful to note that values of $\mathcal{Q}$ as low as 10^{-3} are achievable, leading to a significant increase in WIMP sensitivity.

The main physical handle for discriminating between a WIMP signal and background events on an event by event basis is the nature of the interaction, i.e. whether it is an electron recoil, in which the incoming particle interacts with an atomic electron, or a nuclear recoil, in which the interaction occurs with the nucleus. The main difference between the two types interactions is the 'track energy density' which can be exploited by various measurement techniques to distinguish electron from nuclear recoils. The distinction between electron and nuclear recoils is relevant since a potential WIMP interaction will consist of a nuclear recoil, while the predominant radioactive backgrounds, such as gammas, betas, and muons result in electron recoils. Neutrons interacting with the detector , however, will result in nuclear recoils, and thus cannot on this basis alone be distinguished from a WIMP signal. Naturally occurring neutron backgrounds, however, are significantly lower than gamma and beta backgrounds such that most experiments are not currently limited by neutrons.

Another important technique for discrimination between backgrounds and a WIMP signal, on statistical basis however, takes advantage of the interaction kinematics. Observation of an annual modulation in the even rate, as described in section 2.3, is one such method in which the sinusoidally modulated WIMP interaction rate is used to distinguish it from a potentially constant background. A similar effect exists on a diurnal scale, where the strong directionality of WIMP recoils, due to the overall motion of the Earth at $\sim 230\,\mathrm{km\,s^{-1}}$ through the WIMP halo, can be used to distinguish them from an isotropic background.

3.1 Direct Detection

3.1.1 Non-discriminating Detectors

There exists several experiments which rely on scintillation or ionization in the detector material to determine the energy of an interaction. Although the pulse shape may differ somewhat for electron and nuclear recoils the effect is typically small enough such that it cannot be used to distinguish between the two types of recoils on an event by event basis, but can be exploited on a statistical basis. For that reason I list such experiments in this section.

DAMA

The DAMA (DArk MAtter) experiment is one of a number of experiments using NaI(Tl) crystals as Dark Matter detectors. With a detector mass of $\sim 100\,\mathrm{kg}$ (consisting of 9 individual crystals) and a total exposure of $\sim 58000\,\mathrm{kg}$-days the DAMA experiment has the largest sensitivity of the various NaI experiments.

In addition to background rejection with pulse shape discrimination, the DAMA exposure is sufficiently large to be sensitive to the WIMP annual modulation signature. Figure 3.1(a) shows the annual modulation signal that has been observed over a period of four years. If this signal were to be interpreted as being due to galactic halo WIMPs it would correspond to a WIMP mass of $\sim 52\,\mathrm{GeV/c^2}$ and a spin independent nucleon cross-section of $7.2 \times 10^{-42}\,\mathrm{cm}^2$ (as shown in Figure 3.1(b)) [27].

ZEPLIN I

The ZEPLIN I detector consists of a volume of 3.7 kg of liquid Xe, with three photomultiplier tubes used to measure the scintillation signal produced within the Xe. Pulse shape is also used to determine, on a statistical basis, the rate of electron recoil

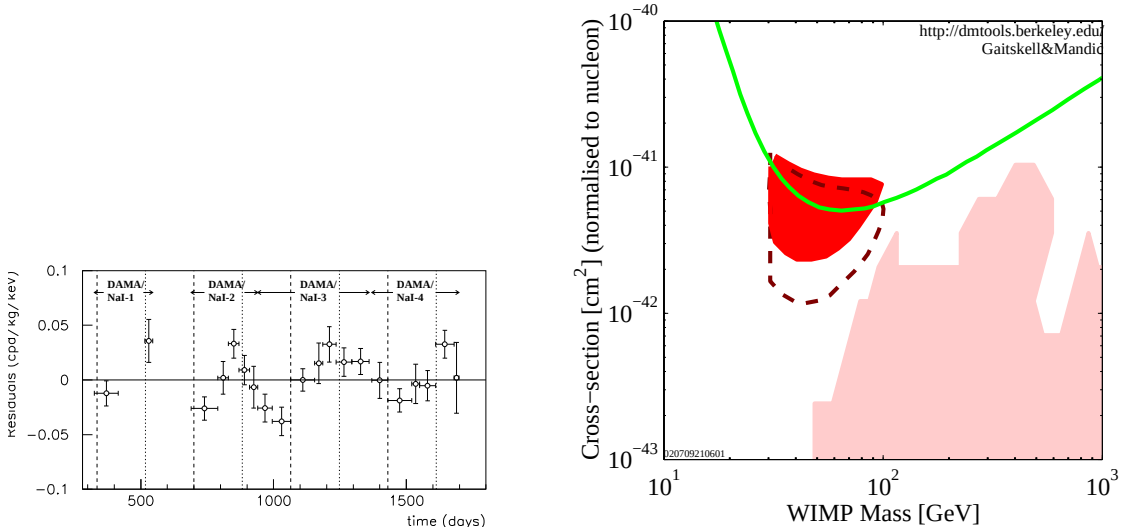

(a) (b)

Figure 3.1: Annual modulation signal observed by the DAMA experiment (a) and the resulting limits on WIMP mass and cross-section (b). The light solid line (in (b)) is the upper limit determined with the DAMA pulse shape discrimination techniques, while the solid (dashed) closed regions are the 3σ CL contours without (with) taking into account the pulse shape discrimination limit. The solid region toward the bottom right of the figure represents allowed WIMP mass – cross-section parameter space according to some SUSY models. Panel (a) taken from [27] and panel (b) taken from [28].

backgrounds. Data obtained from an ongoing run result in the Dark Matter limit shown in Figure 3.2 [29].

3.1.2 Discriminating Detectors

The list of Dark Matter experiments which use event by event discrimination techniques includes a number of cryogenic experiments such as CRESST, EDELWEISS, ZEPLIN, and CDMS.

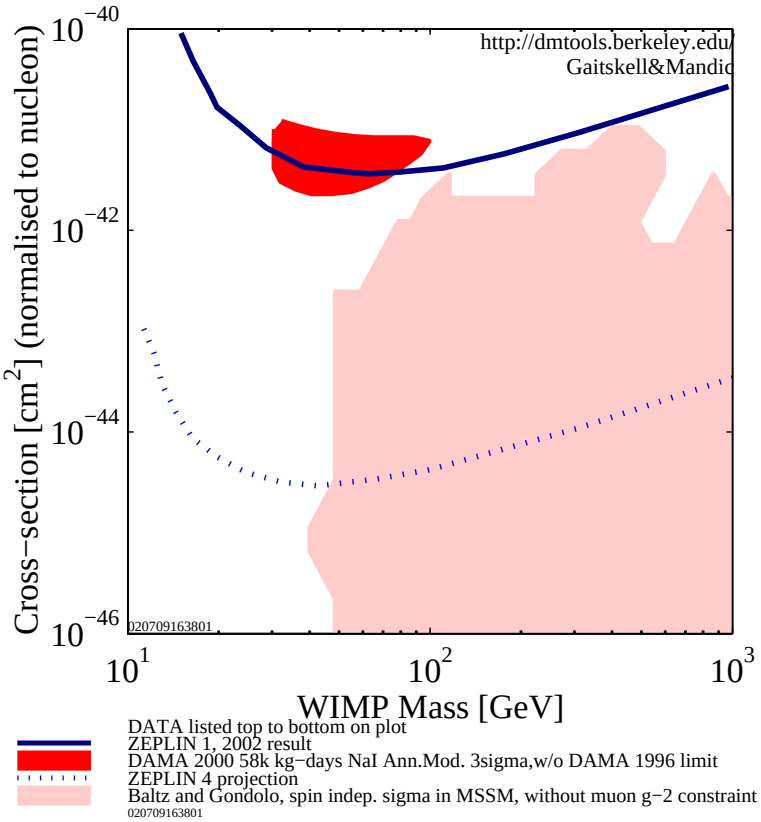

Figure 3.2: WIMP mass – cross-section upper limit by the ZEPLIN I experiment. The solid line corresponds to the current limit obtained with ZEPLIN I experiment. Included for comparison are the DAMA contour and the SUSY parameter space shown in Figure 3.1. The dotted line corresponds to the projected sensitivity of next generation Xe experiment, ZEPLIN IV. Figure taken from [28].

CRESST

The first generation of the CRESST (Cryogenic Rare Event Search with Superconducting Thermometers) experiment utilized a 262 g sapphire (Al_2O_3) crystal as a target material. The energy deposited by a recoiling particle is determined by measuring the change in temperature of the crystal with a superconducting W film. While these

detectors were not able to perform event by event discrimination, the background levels were reduced to as low as a few counts/kg/keV/day, a level competitive with other cryogenic experiments [30].

Discrimination with the CRESST detectors is achieved by measuring the scintillation light produced by an interaction in addition to the temperature change of the crystal. The current generation of CRESST detectors use 300 g $CaWO_4$ crystals as absorbers, instrumented with superconducting W thermometers. The scintillation light is absorbed by a sapphire wafer, instrumented with a superconducting W thermometer, adjacent to the $CaWO_4$ crystal [31]. The CRESST detectors are sensitive to spin dependent WIMP interactions, and are located in the same underground laboratory as DAMA.

EDELWEISS

Of the various Dark Matter direct detection experiments, the EDELWEISS (Expérience pour Detecter Les WIMPs en Site Souterrain) experiment resembles CDMS the most. The EDELWEISS experiment is based on the measurement of the ionization and bolometric responses of a germanium crystal to a recoiling particle. The detectors are cylindrical in shape, 70 mm in diameter, 20 mm thick and weigh $\sim$320 g each. Electrodes on the top and bottom surfaces are used to measure the amount of excited charge carriers created by a recoiling particle (ionization response), while NTD thermistors[3] measure the temperature rise ($\sim$tens of μK) of the entire crystal (bolometric or heat response). The combination of the two channels provides information on the energy as well as the nature of the recoil allowing the detectors to discriminate between a WIMP signal and the majority of background sources.

Operating at a depth of 4800 m.w.e.[4] in the Laboratoire Souterrain de Moudane beneath the French-Italian Alps the EDELWEISS experiment is well shielded from

[3]Neutron Transmutation Doped germanium crystals

[4]Meter Water Equivalent is a measure of depth used to compare amongst sites with different rock/soil compositions.

undiscriminated background sources resulting from the flux of cosmic ray muons at the surface. An 11.7 kg-day exposure with one of the detectors, based on a combination of data taken in the years 2000 and 2002, resulted in no observed WIMP candidate events [32] [33]. Based on these results the EDELWEISS experiment is able to establish the 90% C.L. WIMP exclusion limit shown in Figure 3.3. This limit is incompatible with the results reported by the DAMA experiment [27] at more than a 99.8% C.L., for the standard halo and WIMP assumptions.

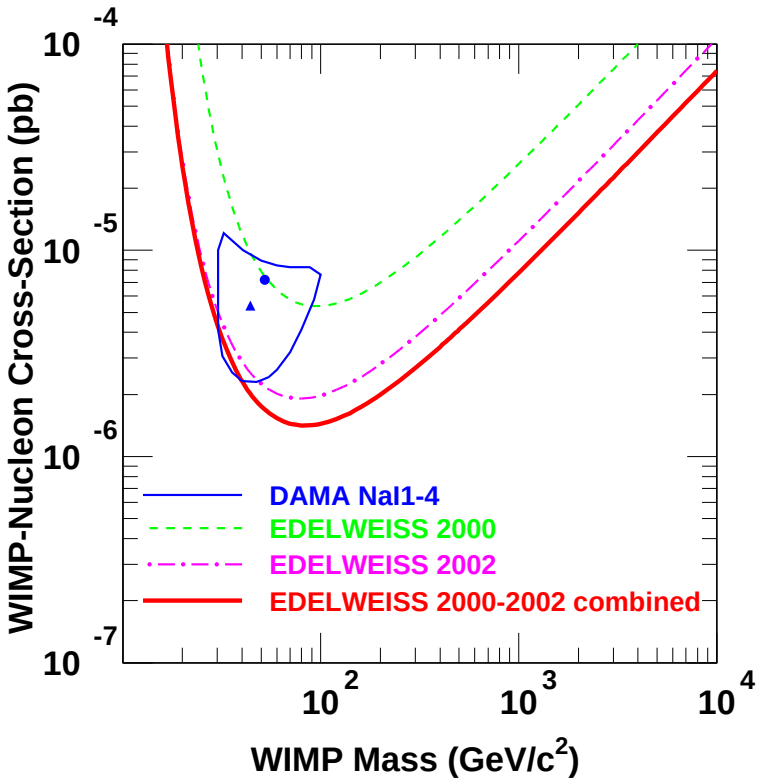

Figure 3.3: Dark Matter exclusion limits obtained by the Edelweiss experiment. The thick solid line shows the results of an 11.7 kg-day exposure from one detector. The EDELWEISS results are inconsistent with the DAMA measurement (closed contour and square/triangular points) under the standard halo and WIMP interaction models.

ZEPLIN

The ZEPLIN II – IV experiments implement event by event discrimination by applying an electric field across a liquid Xe target. The electric field suppresses the recombination of the ionized electrons resulting in a prompt and a delayed signal. The relative sizes of the two signals is a powerful discrimination parameter between electron and nuclear recoils. The ZEPLIN IV detector proposes to instrument up to 1 Ton of Xe, allowing for sensitivities to cross-sections down to $10^{-45}\,\mathrm{cm}^2$ [34] [35] [36].

3.1.3 Insensitive Detectors

An interesting technique in discriminating against electron recoil backgrounds is the use of detectors that are sensitive to nuclear recoils while being insensitive to electron recoils. Such is the case of the DRIFT [37] and PICASSO [38] experiments.

The DRIFT experiment employs a time projection chamber with Xe gas as a target material. DRIFT has good directional resolution, for the recoiling nuclei, and will be sensitive to the diurnal variation in WIMP recoils. PICASSO, on the other hand, is a threshold detector. The high track energy density of nuclear recoils causes superheated liquid droplets to vaporize into bubbles which are detected acoustically. PICASSO uses fluorine as a target material and is thus highly sensitive to spin dependent interactions.

3.2 Indirect Detection

Other experimental searched for WIMPs are based on the detection of WIMP annihilation products such as high energy cosmic rays, photons, or neutrinos. Such experiments exploit the fact WIMPs, after having elastically scattered within the cores of the Earth, Sun, or Galactic bulge, may become trapped in their gravitational wells.

Such an effect will lead to the accumulation of WIMPs until equilibrium is achieved when the rate of infalling WIMPs is balanced by the rate of WIMP annihalation.

The Super-Kamiokande experiment [39] searched for an excess of energetic upward going muons[5] which would result from ν_μ arising from WIMP annihilation. The lack of a muon flux in excess of that due to atmospheric neutrinos allowed the Super-Kamiokande experiment to set the WIMP exclusion limit shown in Figure 3.4. This results demonstrates that indirect detection techniques can be competitive and complementary to direct detection experiments in the search for WIMPs.

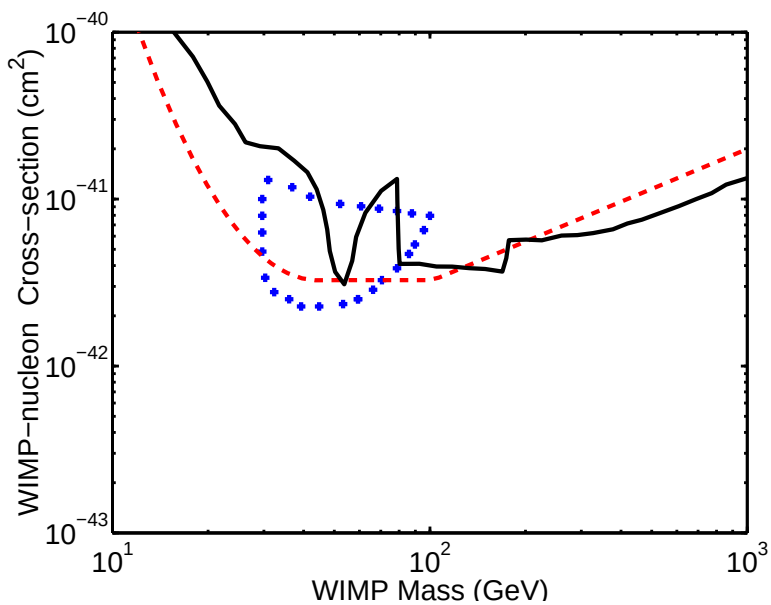

Figure 3.4: Dark Matter exclusion limits (solid line) obtained by the Super-Kamiokande experiment. The dotted line is the limit obtained by the CDMS experiment in 2000 [40] and the dotted closed region is the DAMA result [27] shown in previous figures. Figure taken from [39]

[5]Muons created by neutrinos traversing the Earth and interacting in the rock beneath the Super-Kamiokande detector

Chapter 4

ZIP Detector Technology

4.1 The ZIP Detector

The CDMS experiment uses crystals of germanium or silicon as detectors in its Dark Matter search. The cylindrical crystals are 1 cm thick, 7.62 cm (3 in) in diameter[1], and weigh 250 g and 100 g for Ge and Si respectively. Figure 4.1 shows a picture and schematic of the detectors.

The detectors, known as ZIPs (Z-dependent Ionization and Phonon) are amongst the first generation of cryogenic detectors to be developed for Dark Matter detection experiments. Although one of the primary reasons for pursuing cryogenic detector technology is the promise of excellent energy resolution (on the order 1 keV for kg scale detectors) the true potential of these detectors lies in their ability to perform particle identification on an event by event basis. As mentioned in Chapter 3, Dark Matter searches tend to be dominated by γ and x-ray backgrounds with rates orders of magnitude higher than the expected WIMP rates. The ability to identify and reject events due to these backgrounds can significantly increase the reach of a Dark Matter search.

[1]Roughly the size of a hockey puck.

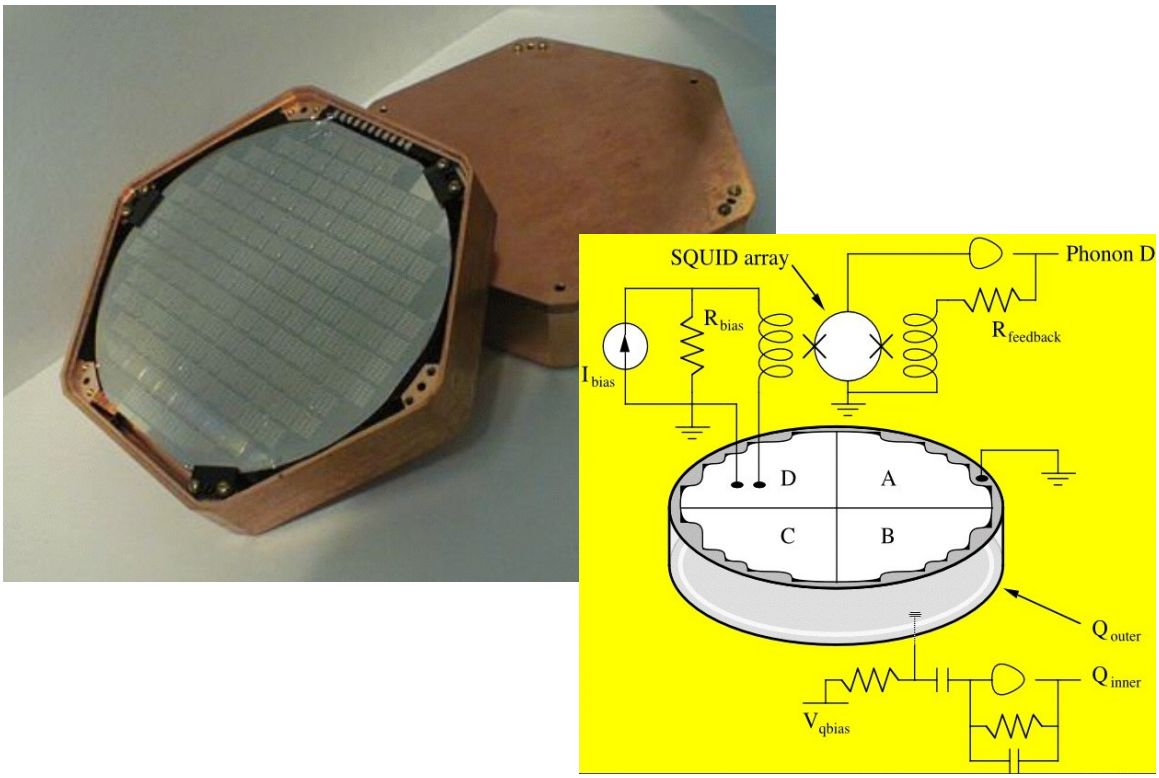

Figure 4.1: The top left image shows a photograph of a CDMS ZIP detector in its copper housing. The lower right image is a schematic of the detector, showing the four phonon and two ionization channels along with their readout electronics.

The CDMS ZIP detectors achieve this identification by taking advantage of the nature of the recoil that a given particle undergoes with the detector. Electromagnetic interactions, which photons and charged particles undergo, result in electron recoils, namely a recoil off of the atomic electrons of the detector. Nuclear or weak interactions, on the other hand, result in recoils off of the detector's nuclei. While it is expected that WIMP recoils will be nuclear in nature, the majority of radioactive backgrounds, such as those due to photons and electrons, result in electron recoils. Particle identification[2] is then reduced to distinguishing between electron and nuclear recoils.

[2]Also referred to as discrimination

In order to understand discrimination one must consider the solid state physical processes that occur as a consequence of a recoil. The Ge (Si) crystals are semiconductors. This means that there exists, at room and cryogenic temperatures ($\sim 20\,\mathrm{mK}$ for the CDMS experiment), a gap in the electronic band structure. An electron recoil in the crystal results in the creation of electron-hole pairs in direct proportion to the energy deposited (ionization response). Not all of the deposited energy, however, goes into creating the charge carriers. The remainder of the deposited energy will be expressed as a spectrum of high energy (THz), athermal phonons (phonon response). As the charge carriers ultimately recombine, whether in the bulk of the crystal or at the surfaces, the energy stored in them is released as phonons. Consequently, an interaction in the detector will eventually result in the creation of populations of athermal phonons which carry the entire recoil energy of the event as well as a number of excited charge carriers in proportion to the total energy. Nuclear recoil events behave in very much the same manner. Where they differ from electron recoils is in the number of charge carriers created for a given energy deposition. Nuclear recoils are less efficient at creating charge carriers and on average create roughly one third the number of carriers as a same-energy electron recoil. It is important to note that the phonon system continues to contain the total energy of the recoil. More details on nuclear recoils can be found in [41] [42] [43].

Measuring both the phonon and ionization response of the detector allows for the construction of two orthogonal variables describing a given recoil : the type and the energy, thus allowing for event by event discrimination.

The following sections describe in some detail the physics behind the two measurements as well as the electronic circuits that were developed to read out the respective channels.

4.2 The Phonon Channel

As mentioned earlier, the ZIP detectors consist of 250 g crystals of Ge or 100 g crystals of Si. On one surface of the crystals aluminum (Al) and tungsten films (W) are deposited and patterned into the structures that form the phonon sensors. These structures are known as **Q**uasiparticle-Assisted **E**lectrothermal-Feedback **T**ransition-Edge-Sensors (QETs) and are described in section 4.2.2. Aluminum and tungsten films are also deposited on the opposite surface, but are patterned into an electrode for use in the ionization measurement described in section 4.3. The cylindrical sides of the crystal are left bare.

A particle recoil in a detector creates a population of phonons at the interaction point. The phonons propagate through the detector until they interact with the surface films by breaking up Cooper pairs[3] in the Al creating long lived quasiparticles[4]. In this manner, roughly half the energy of the interaction is transferred from the phonon system in the crystal's bulk into the quasiparticle system in the Al films. The quasiparticles diffuse in the Al film until they encounter a region of W metal. Since the W has lower T_c than Al, the overlap forms a proximitized region with an intermediate T_c and bandgap. Once the quasiparticles scatter within that region they become trapped and eventually transfer their energy to the W electron system. The phonon channel measurement is thus reduced to determining the amount of heat deposited in the W electron system as is described in section 4.2.3.

4.2.1 Phonons in the Crystal

A particle recoil in a detector creates a population of phonons at the interaction point with a spectrum peaked near the Debye frequency (~ 3 THz for Ge, and ~ 6 THz for Si). These phonons then travel through the crystal while undergoing anharmonic

[3]The detectors, operated at 20 mK are well below the aluminum superconducting T_c of 1.2 K.

[4]The energy gap and quasiparticle excitations in a superconductor are analogous to the bandgap and excited electron-hole pairs in a semiconductor.

decay and subsequently, isotopic scattering. Anharmonic decay is a process in which one phonon spontaneously splits into two lower frequency phonons. Energy and momentum conservation are obeyed by considering the recoil of the crystal[5]. Isotopic scattering on the other hand, is a process by which a phonon scatters off of a Ge (Si) isotope[6] elastically, resulting in a change of the phonon's direction, but no loss of energy. Both isotopic scattering and anharmonic decay are strongly frequency dependent, with cross sections given by Equation 4.1

$$\sigma_{IS} \propto \left(\frac{f_{ph}}{1\ \mathrm{THz}}\right)^4, \sigma_{AD} \propto \left(\frac{f_{ph}}{1\,\mathrm{THz}}\right)^5 \tag{4.1}$$

Consequently, high frequency phonons will rapidly undergo many scatterings and decays before they get a chance to travel significant distances. From this behavior emerges a quasidiffuse propagation in which the initial population of phonons moves away from the interaction point with a velocity $\sim 1/3$ that of the speed of sound in the crystal ($\sim 1\,\mathrm{cm}/\mu\mathrm{s}$) [44]. When the phonon frequencies drop sufficiently (0.6 THz in Ge and ~ 1 THz in Si) their mean free path becomes larger than the dimensions of the crystal. At that point the phonons are considered ballistic and propagate in a straight line at the speed of sound, until a surface is encountered. Phonons encountering a bare, unmetallized, portion of the surface will simply be reflected back into the crystal, with no change in energy. Phonons which encounter Al films on the surface, however, have a finite probability (roughly 0.3 averaged over all phonon frequencies) of being absorbed. The quasidiffuse propagation of the initial phonon population determines a time scale of $\sim$ few μs over which the energy from the phonon system is injected into the Al films.

The charge carriers created by the recoil drift across the crystal within several

[5]The analogous process of a photon in vacuum splitting into two does not occur due to the nature of the continuous vacuum as opposed to the discretized crystal. The periodic nature of the crystal also results in a non-linear dispersion relation and a minimum phonon wavelength defined by the inter-atomic spacing.

[6]Natural isotopic abundances for Ge are : ^{70}Ge 20.5%, ^{72}Ge 27.4%, ^{73}Ge 7.8%, ^{74}Ge 36.5%, ^{75}Ge 7.8%, while those for Si are : ^{28}Si 92.2%, ^{29}Si 4.7%, ^{30}Si 3.1%. Consequently, isotopic scattering is more dominant in Ge crystals.

hundred nanoseconds due to an applied electric field of several Volts/cm (this is described in more detail in section 4.3). When the charge carriers recombine at the surface electrode they release their energy in the form of high frequency phonons which, through interaction with the surface metallic films, are rapidly converted into ballistic phonons. As the charge carriers drift through the crystals they also shed ballistic phonons. The details of this process, known as the Neganov-Luke effect, are described in [45]. Simply put, these phonons are the manifestation of the work done by the electric field in moving the charge carriers. The energy injected into that phonon population is given simply by $E_{ph} = QV$, where V is the voltage across the crystal and Q is the amount of charge created by the recoil[7].

It can be seen from the above discussion that there are two populations of phonons arriving at the Al films, one with a time scale of several (10–15) μs and one with a timescale of a few (2–4) μs. The fraction of an interaction's energy that is present in the two phonon populations depends largely on the electric field applied across the crystal (the Neganov-Luke effect) and to some extent on the nature of the recoil (through the dependence on the number of charge carriers created by electron vs. nuclear recoils). Barring those two variables, events within the bulk of the crystal will have a similar fraction of the two phonon populations and will exhibit a characteristic time scale of energy injection into the Al quasiparticle system.

One class of events, however, has a significantly larger fraction of prompt, ballistic phonons. For events occurring sufficiently near the surfaces of the crystal, the interaction between the initial quasi-diffuse phonon population and the metal films result in a very rapid down conversion of the phonons into the ballistic regime. The time scale of energy injection into the Al quasiparticle system is measurably faster for surface events than for bulk events. This phenomenon is well described in [46]. The implication for the CDMS experiment is significant since the risetime of the phonon

[7]The process by which the Neganov-Luke phonons are created is analogous to that of Cerenkov light creation. Namely, once the speed of a drifting charge carrier exceeds that of the phonons in the crystal it will spontaneously emit a phonon and, consequently, slow down.

pulse provides information about the depth of an interaction within the crystal, allowing for the identification and elimination of some backgrounds arising from surface contamination.

Finally, the inefficiency of the Al films at fully absorbing phonons, in a given pass, gives rise to another time scale associated with the reflection from and subsequent revisiting of the surface several μs later[8]. A time scale of tens of μs arises as the number of unabsorbed phonons exponentially decreases. Note that the times scales are roughly twice as long in Ge than in Si due largely to the slower speed of sound.

4.2.2 The QET

The purpose of the QET is to collect the interaction's energy from the phonon system and transfer it to the sensing element. The QET consists of 300 nm thick Al films, covering macroscopic areas, connected to 35 nm thick W films at discrete locations throughout the surface of the detector. The W films form the energy sensing elements and are fully described in section 4.2.3. Details of QET fabrication are described in [47] and [48].

The deposition and patterning of the QET structure are done with photolithographic processes similar to those used in CMOS technology. One surface of the detector is divided into four phonon channels, as shown in Figure 4.1. Each channel consists of 37 repeated, electrically connected $(5\,\mathrm{mm})^2$ cells. Each cell contains identical QET structures. Since the 37 cells form a single channel an electrical short in a single cell will disable the entire channel. Consequently, the demands on fabrication yield, as well as inspection and repair procedures, are quite stringent.

The connection between the Al and W films is accomplished via a $4\,\mu$m wide overlap region. Figure 4.2 shows a schematic of the resulting electronic band structure. The size of the superconducting energy gap in Al is $2\Delta_{Al} = 340\,\mu\,\mathrm{eV}$. This energy corresponds to a phonon frequency of 84 GHz. Phonons with higher frequencies are

[8]Thickness of the crystal divided by speed of sound.

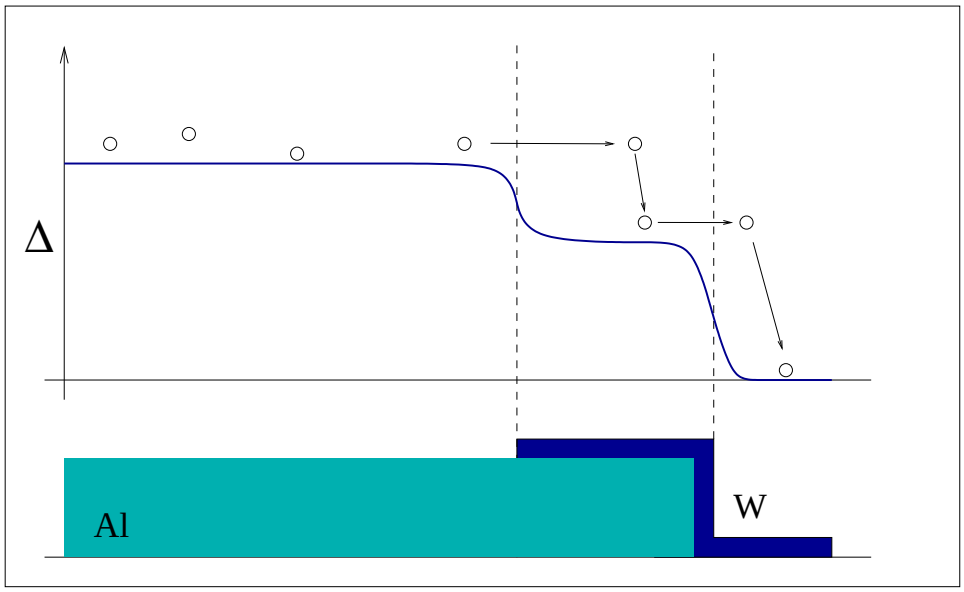

Figure 4.2: Electronic band diagram of a QET, showing the region of Al (leftmost), W (rightmost) and the Al/W overlap (middle). Once quasiparticles inelastically scatter in the overlap region they become trapped due to the lower energy gap. Subsequently, they are funneled into the W film where they transfer their energy to the W electron system.

able to break Cooper pairs in the Al film, creating 2 quasiparticles. Since phonons become ballistic at frequencies of 0.6–1 THz the average energy that they'll impart to the quasiparticles will be $\sim 2-4$ meV. These initial quasiparticles then decay down to the gap edge by shedding phonons which are able to create other quasiparticles. This process, known as a cascade, transforms a single quasiparticle with energy $\sim 10\times 2\Delta_{Al}$ into a collection of quasiparticles with energy Δ_{Al}. During this process, however, approximately half the initial energy is lost to phonons with energies less than the Al energy gap[9]. As these phonons are unable to create further quasiparticle they are undetectable, and thus pose an unavoidable energy collection loss. Similarly, a small fraction of the initial phonon spectrum will be sub-gap, contributing an additional $\sim 10\%$ inefficiency for Ge ($\sim 5\%$ for Si).

[9]These are known as sub-gap phonons.

Measurement of the quasiparticle diffusion length in 150 nm thick Al films has yielded a result of $l_{diff} \sim 180\,\mu$m[10] [49]. Consequently, quasiparticles created more than a few diffusion lengths from a TES will unlikely be able to reach and deposit their energy in the TES.

Previous generations of the ZIP detectors [46] used 150 nm thick Al films with nearly 100% surface coverage as shown in Figure 4.3. A $(5\,\text{mm})^2$ cell consisted of a 6×2 array of the QET units. With that design, phonons from the crystal interact with the Al film and create quasiparticle pairs homogeneously across the detector's surface. This means, however, that the average distance between the quasiparticles and the nearest TES is $\sim 625\,\mu$m, significantly larger than the diffusion length. Diffusion simulations of such a design indicate that only 6.4% of all quasiparticles are able to reach a TES. Quasiparticle loss is thus a major component of energy inefficiency in the phonon channel. Consequently, an attempt was made to redesign the QETs with the aim of eliminating as much of that inefficiency as possible.

Quasiparticle diffusion length is determined roughly by two factors : the diffusivity ($\mathcal{D}$) and lifetime[11] (τ_{qp}) of the quasiparticles (Equation 4.2)

$$l_{diff} \sim \sqrt{\mathcal{D}\,\tau_{qp}} \tag{4.2}$$

with the diffusivity and lifetime, in turn, being determined by the quasiparticle mean free path and film thickness respectively. If the quasiparticle mean free path is limited by the Al film thickness then increasing the thickness would result in a linear increase of the diffusion length. If, on the other hand, the mean free path is limited by a feature smaller than the film thickness the diffusion length will only increase as the square root of the film thickness. Unfortunately, we cannot take advantage of this mechanism by arbitrarily increasing the Al film thickness due to step coverage issues. Namely, the connection between the W and Al film becomes less reliable as the thickness of the

[10] Although the quasiparticles eventually will recombine with each other, such a process scales as n^2, where n is the quasiparticle number density. We believe that the main loss mechanism of quasiparticle is due to interactions with trapping sites, a mechanism that is dependent linearly on n.

[11] Alternatively referred to as the trapping time.

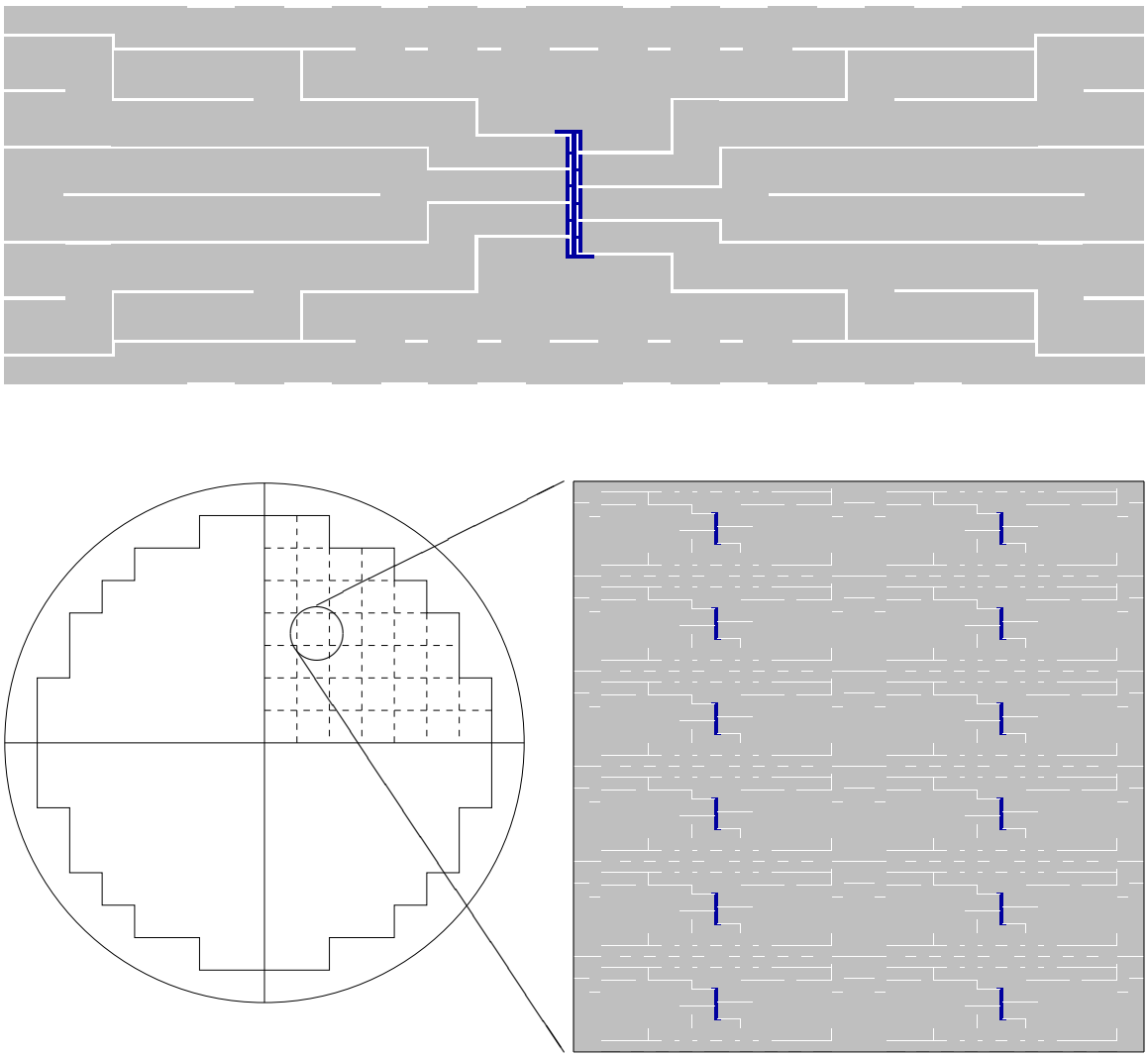

Figure 4.3: Previous design of the CDMS ZIP QET. $2352 \times 770\,\mu\text{m}^2$ of Al collector fins funnel quasiparticles toward the $250 \times 2\,\mu\text{m}^2$ W TES at the center. A 6×2 array of these structures forms a 5 mm unit cell.

Al film increases to over 10× that of W. The most recent generation of ZIP detectors uses 300 nm thick Al films.

By reducing the amount of Al film coverage we can take advantage of the fact that the phonons undergo very little down conversion at the bare crystal surface. Consequently, phonons will keep reflecting off the detector's surfaces until they are

eventually absorbed in a region of the Al film close to a TES. The collection efficiency can be calculated as a function of the Al film coverage. Figure 4.4 shows the dependence of the quasiparticle collection efficiency on the Al coverage and number of TESs. The features of the quasiparticle collection efficiency as a function of Al fin length can be understood as follows :

Large Al fin lengths The quasiparticle collection efficiency asymptotes to a constant value. For Al fin lengths corresponding to 100% area coverage, quasiparticles are generated uniformly over the detector surface. Only those quasiparticle within several diffusion lengths of the TESs are collected, corresponding to a fixed fraction of all quasiparticles. As the surface Al coverage is decreased slightly, the fraction of quasiparticles within several diffusion length of the TES increases slowly.

Intermediate Size Fins As the area of Al surface coverage is further reduced, the length of the fins becomes comparable with the quasiparticle diffusion length and the fraction of collected quasiparticle increases rapidly with diminishing Al fins length.

Short Al Fins In principle, decreasing the Al fin length to zero should result in the quasiparticle collection efficiency approaching 100%. This is not the case due to an unavoidable loss mechanism. Metallic layers, both Al and W, on the surface of the detector making up the ionization electrodes and the electrical connectivity among the individual phonon sensor cells, as well as providing features necessary for the fabrication of the detectors, cover $\sim 6\%$ of the detector surface area. Phonons are absorbed in these uninstrumented films as readily as in the Al fins. Consequently, as the total area of the Al fins begins to drop a larger fraction of phonons, and thus quasiparticles, are lost to the uninstrumented films.

Details of the calculation are shown in Appendix A. The current design of the QETs uses 28 TESs, per $(5\,\mathrm{mm})^2$ cell, connected to ten $380\,\mu\mathrm{m} \times 60\,\mu\mathrm{m}$ Al fins, each as

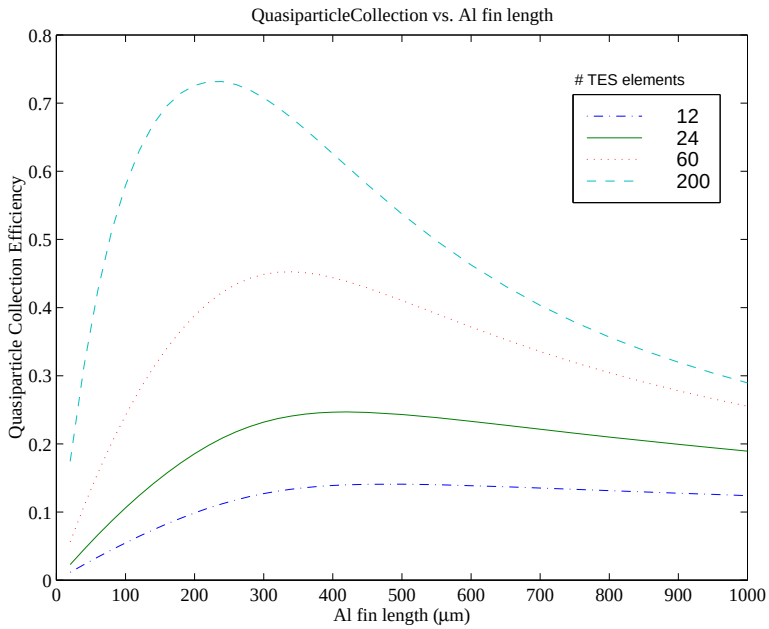

Figure 4.4: One dimensional diffusion calculation of quasiparticle collection efficiency as a function of Al fin length and number of W elements per $(5\,\mathrm{mm})^2$ area. The maximum collection efficiency depends strongly on the number of TESs and the Al fin length.

shown in Figure 4.5. This configuration is expected to have a quasiparticle collection efficiency of 24%. Increased efficiency can be achieved by a combination of more TESs and shorter Al fins. However, details of the TES readout circuit impose an operational upper limit to the number of TESs in a single channel [47].

It is important to note that the improvements in quasiparticle collection result in a direct increase in the phonon measurement's signal to noise ratio. This is due to the fact that the signal is linearly dependent on the number of collected quasiparticles, while the dominant noise terms in the measurement are independent of the area of the Al film.

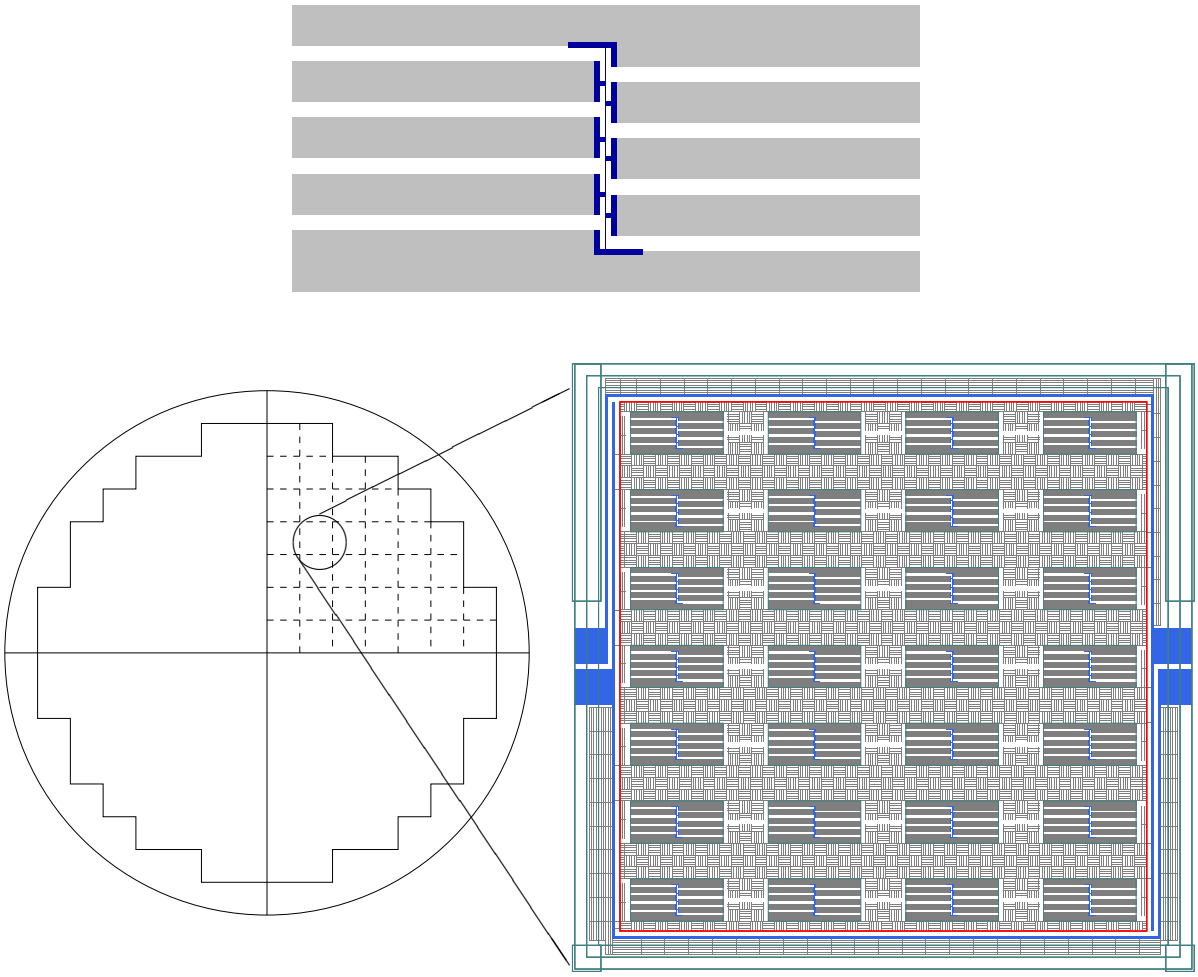

Figure 4.5: Current geometry of a QET showing single TES element with Al quasiparticle collection fins. The 380 μm long and 50 μm wide Al fins funnel quasiparticles toward the $250 \times 1\,\mu\text{m}^2$ W TES at the center. A 7×4 array of these structures forms a 5 mm unit cell.

4.2.3 Transition Edge Sensors and Electrothermal Feedback

Principles of Operation

The energy sensing elements in the ZIP detectors are the **T**ransition **E**dge **S**ensors (TES). Voltage biased TESs were first developed back in 1994 by Kent Irwin and

Blas Cabrera [50] [51]. Many developments and improvements have since ensued, the description of which can be found in the theses of Sae Woo Nam [47] and Aaron Miller [52]. I will present here a brief discussion of the properties of TESs in addition to highlighting those important and relevant to the CDMS experiment.

The transition edge sensor is essentially a very sensitive thermometer. By maintaining a piece of tungsten at its critical temperature[12], T_c, a small change in the W temperature causes a large change in its resistance, as shown in Figure 4.6.

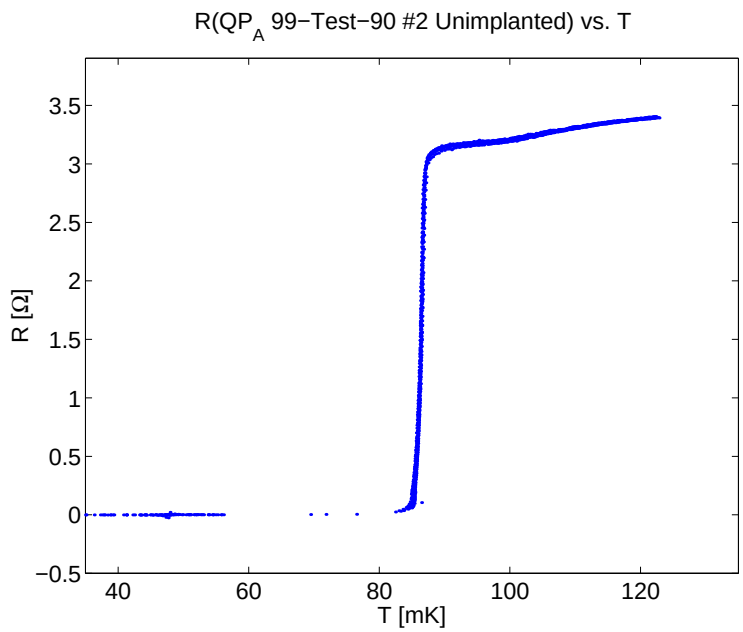

Figure 4.6: $R(T)$ for a $\sim$ 220 μm $\times$ 270 μm W square. This value of T_c and transition width is characteristic of the W films used for the ZIPs

Figure 4.7 illustrates schematically the thermal circuit that the TES forms with its surroundings. The thermal conductivities g_{sub} and g_{W-Xtal} are sufficiently large such that the thermal link between the phonons in the W and the refrigerator is strong. Consequently, the W phonons and the detector substrate are considered to be at the

[12]For the W we produce, T_c lies in the range : 50 mK $< T_c <$ 150 mK, and has a transition width $\sim$ 1 mK.

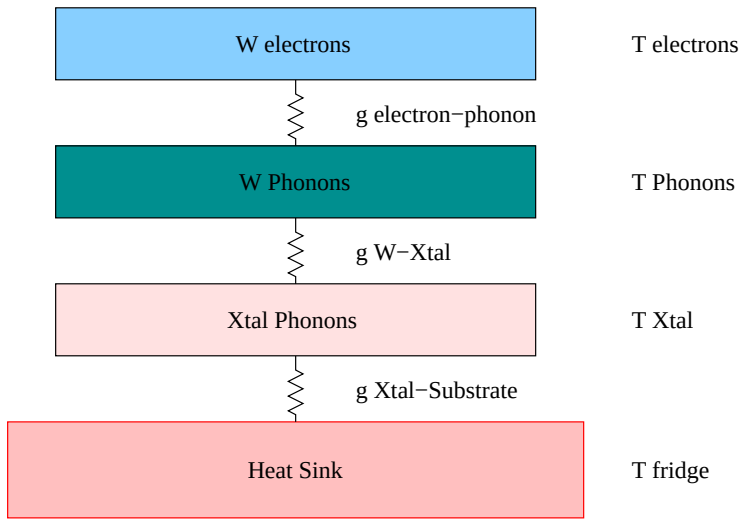

Figure 4.7: Thermal schematic of an electrothermal feedback (ETF) TES illustrating the various thermal sources, sinks, and impedances. The thermal path between the W phonons and the heat sink is sufficiently low that the phonons can be considered to be at the refrigerator temperature.

refrigerator's base temperature[13]. If the temperature of the W electron system (T_e) is higher than the base temperature then it will experience cooling as described by Equation 4.3.

$$P_{cool} = g_{e-ph}(T_e - T_{sub}) \tag{4.3}$$

According to electron-phonon decoupling theory at low temperatures [53], the thermal conductivity, g_{e-ph}, takes on the form

$$g_{e-ph} = n\kappa T_e^{n-1} \tag{4.4}$$

where n, a constant[14], is equal to 5 and $\kappa = \Sigma V$. Σ is the electron-phonon coupling parameter and V is the volume of the W element. For the W films we produce, n has been measured to be $\sim$ 5.0 [52]. Based on equations 4.3 and 4.4 the cooling power

[13]Subsequent references to T_{sub} implicitly apply to the W phonon temperature T_{phonon}.

[14]For thermal impedances due to electron-phonon decoupling $n = 5$, while $n = 4$ for impedances due to Kaptiza boundary resistance for example.

that the W electron system experiences can be rewritten as

$$P_{cool} = \kappa(T_e^n - T_{sub}^n) \tag{4.5}$$

In order to keep the TES at its T_c the net power flow must equal zero. This is accomplished by applying a voltage bias across the TES which, through joule heating, allows the TES to maintain an equilibrium temperature at T_c. The equilibrium point achieved in this manner is stable, and underlies the mechanism by which the TESs measure energy. The power balance equation can be expressed as

$$c_v \frac{dT_e}{dt} = \frac{V_{bias}^2}{R_{TES}(T_e)} - \kappa(T_e^n - T_{sub}^n) \tag{4.6}$$

The TES's reaction to a δ-function energy deposition can be seen by considering a small temperature excursion (ΔT_e) from the equilibrium point. A first order expansion of Equation 4.6 yields the following :

$$c_v \frac{d\Delta T_e}{dt} = -\frac{V_{bias}^2}{R_\circ^2}\frac{dR}{dT_e}\Delta T_e - g\Delta T_e \tag{4.7}$$

which has a solution of the form

$$\Delta T_e = \Delta T_\circ \exp\left(t/\tau_{\mathrm{ETF}}\right) \tag{4.8}$$

where $\Delta T_\circ = E/C_V$, and the time constant τ_{ETF} is given by

$$\tau_{\mathrm{ETF}} = \frac{\tau_\circ}{1 + \frac{\alpha}{n}\left(1 - \frac{T_{sub}^n}{T_\circ^n}\right)} \tag{4.9}$$

$\tau_\circ = c_v/g$ is the intrinsic thermal decay time, $\alpha = \frac{1}{R/T}\frac{dR}{dT}$ is a (unitless) measure of the slope of the resistance curve at the superconducting transition, and $T_\circ$ is the equilibrium temperature of the TES electron system. For the W films we produce

$\alpha \approx 100$ when loaded[15] and $T_\circ \gg T_{sub}$ therefore Equation 4.9 reduces to

$$\tau_{\mathrm{ETF}} = \frac{\tau_\circ n}{\alpha} \ll \tau_\circ \tag{4.10}$$

The reduction of Joule heating on the time scale of τ_{ETF}, measured to be $\sim$ 40 μs, means that the energy deposited in the TES is measured before much can escape into crystal.

For a voltage biased TES the current flow is given by $I_{TES} = V_{bias}/R_{TES}(T_e)$. The current response to an energy deposition is then given by

$$\Delta I_{TES} = -I_\circ \alpha \frac{\Delta T_e}{T_\circ} \tag{4.11}$$

producing a signal of 0.040 μA per keV to be measured. This sets the scale of the signal to be measured and defines the maximum amount of measurement noise that can be tolerated.

Noise Performance of a TES

The noise response of a TES to a δ-function energy deposition is given by [50]

$$\Delta E_{rms} = \sqrt{4k_b T_c P_o \tau_{\mathrm{ETF}}} \tag{4.12}$$

This is determined by temperature fluctuations in the TES due to thermal fluctuations in the W phonon system across the electron-phonon impedance. Using equations 4.3, 4.4, and 4.9 the noise can be recast as

$$\Delta E \propto \sqrt{4k_b T_c^6 \tau_{\mathrm{ETF}}} = \sqrt{4k_b C_V n \alpha^{-1} T_c^2} \propto T_c^2 \tag{4.13}$$

[15]This refers to the value of α with a finite current flowing through the TES. The value of α will be somewhat different in the limit of zero current since the the resistance of a superconductor does depend on both the temperature and current, $R = R(T, I)$.

For energy depositions that occur over time scales $\tau_{phon} > \tau_{ETF}$, however, the resolution becomes

$$\Delta E \propto \sqrt{4k_b T_c^6 \tau_{ETF}} \sqrt{\frac{\tau_{phon}}{\tau_{ETF}}} = \sqrt{4k_b T_c^6} \propto T_c^3 \tag{4.14}$$

The strong dependence of the noise on the tungsten's critical temperature favors lower T_cs. However, since electrothermal feedback requires $T_{sub} \ll T_\circ$, W T_cs of $\sim$70–80 mK are preferable. Since thermal fluctuation in the TES are an irreducible noise source it is desired that other elements of the phonon readout circuit, as described in the following section, have a smaller noise contribution.

SQUID Readout and TES Bias Circuit

SQUIDs (**S**uperconducting **Qu**antum **I**nterference **D**evices) are high bandwidth, low impedance, low noise devices, ideally suited for use with TESs. The TESs are inductively coupled to the SQUIDs as shown in Figure 4.8. Current flowing through the TES induces magnetic flux in the SQUID which results in a voltage change across its terminals. This change in voltage drives an amplifier which feeds a current back into the feedback coil in order to cancel the change in magnetic flux through the SQUID. An input to feedback coil ratio of 10:1, and a feedback resistor of $R_{feedback} = 1\text{k}\Omega$ convert the TES current into an output voltage given by $V_{out} = 10 * I_{TES} * 1\text{k}\Omega$. The CDMS SQUIDs are characterized by a modulation depth of 5 mV, flux quantum of 25 μA, and a nominal noise performance of 2 pA/$\sqrt{\text{Hz}}$ (both referenced to the input coil). A more complete description of the SQUID characteristics and details can be found in [54]. The bias resistor R_{bias} and bias current I_{bias} provide the TES bias voltage. $R_{bias} = 20\,\text{m}\Omega$ provides a stiff voltage source for TES resistances above $\sim 200\,\text{m}\Omega$.

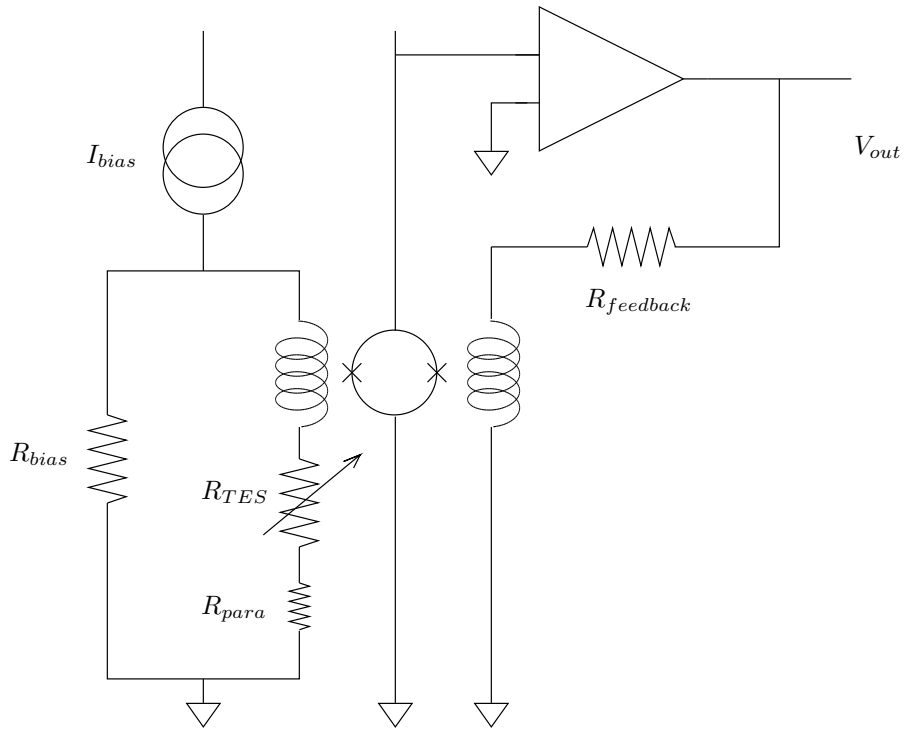

Figure 4.8: Schematic of the SQUID readout circuit for the TES phonon sensors.

Additional contributions to the readout circuit noise, arising from the Johnson electrical noise of the TES, bias, and parasitic resistors are given by

$$\begin{aligned} i_n^2(\omega) &= \frac{4k_bT_{TES}}{R_{TES}}\left(\frac{R_{TES}}{R_{TES}+R_{para}+R_{bias}}\right)^2 + \frac{4k_bT_{para}}{R_{para}}\left(\frac{R_{para}}{R_{TES}+R_{para}+R_{bias}}\right)^2 \\ &+ \frac{4k_bT_{bias}}{R_{bias}}\left(\frac{R_{bias}}{R_{TES}+R_{para}+R_{bias}}\right)^2 \end{aligned} \tag{4.15}$$

with i_n^2 being independent of frequency. The phonon noise contribution (Equation 4.12) expressed in terms of current noise is [47]

$$i_n^2(\omega) = \frac{4k_bT_{TES}}{R_{TES}}\left[\frac{\frac{n^2}{\alpha^2}+\omega^2\tau_{eff}^2}{1+\omega^2\tau_{eff}^2} + \frac{\frac{n}{2}}{1+\omega^2\tau_{eff}^2}\right] \tag{4.16}$$

Table 4.1 breaks down the estimated noise contributions of the various resistances. It can be seen that a significant noise contribution is due to the Johnson noise of

Element	R [mΩ]	T [mK]	Noise [pA/$\sqrt{\text{Hz}}$]
R_{para}	4	4000	4.2
R_{bias}	20	600	3.6
R_{TES}	$\sim$ 200	$\sim$ 80	4.2
Total Noise			7.2
Phonon Noise (f = 1 kHz)			7.4

Table 4.1: Contribution of various resistances to the noise in the phonon channel. The total noise includes the SQUID contribution of 2 pA/$\sqrt{\text{Hz}}$.

the parasitic resistance at 4 K. The parasitic resistance arises from pressure contacts (Millmax pins), while the rest of the circuit consists of superconducting wiring. The total electrical noise, however, is comparable with that from the phonon thermal fluctuations so that eliminating the electrical noise entirely will only improve the energy resolution by a factor of $\sqrt{2}$.

4.2.4 Tc Tuning

W films have two crystalline phases, referred to as α and β. The α phase has a T_c of $\sim 15\,\mathrm{mK}$ and a resistivity of $0.2\,\Omega\,\mu\mathrm{m}$, while the β phase has a T_c of $\sim 1\,\mathrm{K}$ and a resistivity of $1\,\Omega\,\mu\mathrm{m}$. The W films we produce are predominantly α phase[16]. The T_c values vary between different depositions, but tend to lie in the range of 100–150 mK. In addition, the W films exhibit a T_c variation, on the order of 20–40 mK, across the surface of an individual detector. As mentioned in section 4.2.3 the noise performance of the TESs depends strongly on the W T_c. Just as important as the value of T_c, however, is its uniformity within a single detector, across many TESs. A T_c gradient across the surface of a detector causes, in addition to varying noise contributions, a variation in pulse shape, as a function of position. This results in a position dependent systematic uncertainty in the energy measurement as well as a degradation in the ability to perform particle identification based on pulse shape.

In order to reduce the effect of the T_c variations a method of tuning the W T_c was developed [55]. The mechanism behind the tuning lies in the dependence of the critical temperature on the concentration of magnetic impurities (dopants) in the film. The theory behind this effect is described in [56] and [57], however, I will briefly present it in this section.

According to the Abrikosov-Gor'kov (AG) model [56], the presence of dilute magnetic impurities in a superconductor leads to an interaction between the spins of the electrons in a Cooper pair and those of the magnetic dopants. This interaction can be represented by a perturbing Hamiltonian of the form :

$$H_{pert} = K(\vec{r}_e - \vec{r}_i)\vec{S}_e \cdot \vec{S}_i \tag{4.17}$$

where $\vec{r}_e$ and $\vec{r}_i$ are the positions of a Cooper pair electron and a magnetic dopant atom respectively, $\vec{S}_e$ and $\vec{S}_i$ are the spin vectors, and K is a coupling constant. This

[16] β phase tungsten is catalyzed by O_2. Approximately one year ago a residual gas analyzer was installed on the W sputtering system which allowed us to measure trace amounts of O_2 present during a W deposition and correlate that information with the W T_c.

Hamiltonian leads to a variation of the critical temperature with magnetic dopant concentration given by :

$$\ln\left(T_c/T_{c0}\right) = \psi\left\{1/2\right\} - \psi\left\{(1/2) + (1/4)(e^{-\gamma})(x/x_c) \times \left(T_c/T_{c0}\right)\right\} \tag{4.18}$$

where ψ is the digamma function[17], γ is the Euler-Mascheroni constant ($\gamma \sim 0.577\cdots$), x is the magnetic dopant concentration and x_c is the critical concentration[18].

As the dopant concentration grows, self interactions (either antiferromagnetic or ferromagnetic) need to be considered. The Roushen-Rouvalds model [57] extends the AG model by including the effect of the nearest-neighbor magnetic interaction between the dopant atoms. The dependence of the critical temperature with magnetic dopant concentration becomes :

$$\begin{aligned}\ln\left(T_c/T_{c0}\right) = \psi\left\{1/2\right\} - \psi\{&(1/2) + (1/4)(e^{-\gamma})(x/x_c)\\ &\times \left(T_c/T_{c0}\right)\left[1 + \alpha(x/x_c)(T_{c0}/T_c)\right]\}\end{aligned} \tag{4.19}$$

where α is a parameter that describes the ferromagnetic ordering ($\alpha > 0$) or antiferromagnetic ordering ($\alpha < 0$) of the dopant spins.

Figure 4.9 shows a plot of the T_c of a W film as a function of dopant concentration. Concentrations of as much as 70 parts per million (ppm) of ^{56}Fe atoms were implanted in the 35 nm thick W films resulting in T_c suppression of up to 90 mK. It can be seen that for low Fe concentration, the variation in T_c is linear, deviating from the AG model for concentrations above [Fe] $\sim$45 ppm. The RR model, however, successfully fits the data to the highest tested concentrations. The validity of the RR model is further supported by its ability to correctly fit T_c suppression data from a variety of dopant atoms such as Ni and Co, in addition to Fe. The data shown in Figure 4.10 allows the determination of the strength of magnetic coupling between the dopant and Cooper pair electron spins.

[17]The digamma function is defined, in terms of the gamma function, as $\psi(z) \equiv \frac{d}{dz}\ln\Gamma(z)$

[18]Defined in this model as the concentration at which the superconductivity vanishes.

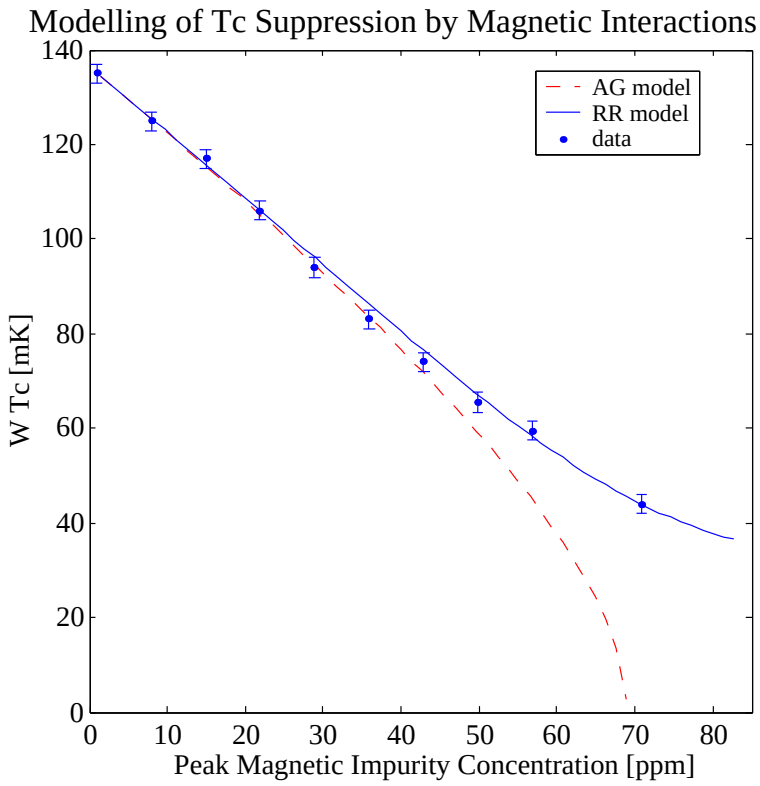

Figure 4.9: T_c dependence on dopant concentration. The data is well fitted by the AG model at low dopant (^{56}Fe) concentration. At higher concentration the AG model fails while the RR model successfully describes the data over a range of $\sim 100\,\mathrm{mK}$ suppression.

One concern with T_c suppression in this manner is its effect on the width of the superconducting transition. Since the slope of the resistance curve is relevant to the operation of the TES is it desirable that the width of the superconducting transition remain unchanged. Figure 4.11 shows a pre- and post-suppression resistance curve. It can be seen that while the T_c has decreased by the desired amount the width of the transition is unaffected.

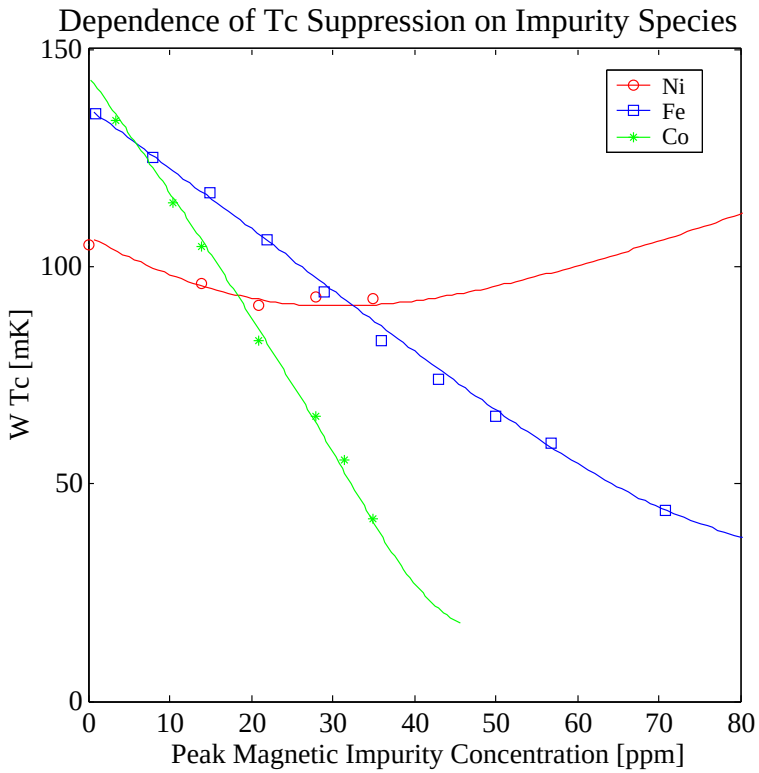

Figure 4.10: Dependence of T_c suppression on dopant atom. Fe, Ni, and Co, all ferromagnetic atoms, couple to the W electrons with different strengths, resulting in different T_c suppressions as a function of concentration.

4.2.5 IV Characteristics of the TESs

A very important tool in characterizing the parameters and performance of a TES is the IV measurement. IV measurements, in combination with critical current (I_c) measurements [58] [59], are especially useful in determining the extent of a T_c gradient for a collection of TESs, unlike a standard T_c measurement which is only sensitive to the elements with the highest T_c. IV measurements are also very useful in determining the width of the superconducting transition as well as the presence of the phase separation phenomenon (described later in this section).

In order to explain the IV data, I will briefly describe the behavior of a TES in

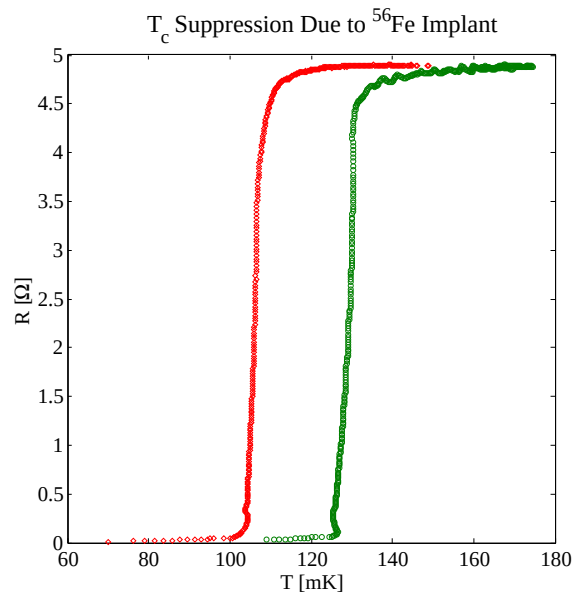

Figure 4.11: $R(T)$ curve pre- and post-^{56}Fe implant. It can be seen that the width of the superconducting transition is not affected.

three regimes : normal, biased, and superconducting. The regime is determined by the voltage bias[19] applied to the TES.

1. Normal : If the voltage across the TES, and consequently the current through it (I_s), is sufficiently large, the W will revert to its normal state with a resistance of $\sim 1\,\Omega$. Since the normal state resistance is much larger than R_{bias} the TES is voltage biased and I_s is given by the linear relation

$$I_s = (R_{bias}/R_{TES})I_b \tag{4.20}$$

   where I_b is the bias current as shown in Figure 4.8

2. Biased : Once I_b drops sufficiently, the Joule heating generated in the W TES

[19]There is a one to one correspondence between the bias current applied to the TES circuit (as shown in Figure 4.8), and the bias voltage across the TES, hence these terms may be used interchangeably.

equals the power lost to the cold substrate (through electron-phonon interactions). It is in this regime that electrothermal feedback occurs and the sensors can be operated at an arbitrary point in their superconducting transition. Equation 4.5 gives the temperature dependence of the power dissipation into the substrate. Since the superconducting transition is only a few mK wide it is a good approximation that the power dissipation is constant throughout the transition. Therefore, from the relationships

$$P = VI = V^2/R \tag{4.21}$$

we see that the resistance of the TES will decrease quadratically with bias voltage while I_s will vary inversely.

3. Superconducting : Once I_b drops below a value such that R_{TES} is comparable to R_{bias}, the TES will cease to be voltage biased and will become current biased. In such a case, Joule heating will decrease with the bias current and the TES will quickly cool (*snap*) becoming fully superconducting. In this state one would expect I_s to be equal to I_b, however, due to small parasitic resistances, $\sim$few mΩ, I_s will be slightly smaller but linearly dependent on I_b. The TES will remain superconducting as the sensor current is increased, until I_s exceeds the critical current (I_c), at which point the sensor quickly becomes normal.

For all three cases, the exact dependence of I_s on I_b is given by the following equation

$$I_s = \frac{R_{bias}}{(R_{TES} + R_{para} + R_{bias})} I_b \tag{4.22}$$

The three states of the TES can be seen in Figure 4.12. The top plot shows I_s as a function of I_b; the two linear regimes, corresponding to the superconducting and normal can be easily distinguished from the biased regime ($|I_b| < 110\,\mu$A) with its characteristic inverse relationship. Similarly, the middle plot shows the constant resistances, with $R_{TES} = R_N$ and $R_{TES} = 0$, in the normal and superconducting regions respectively. The bias region shows a quadratic dependence of R_{TES} on I_b. Finally, the third plot shows the P vs. I_b curve. The bias regions shows the characteristic

constant power dissipation; while in the normal region it is quadratically dependent on I_b.

The characteristics of the IV curve described above are qualitatively correct, and quantitatively accurate to first order. The diagnostic utility of IV curves, however, lies in the strong dependence of the curves on any deviations from ideal behavior.

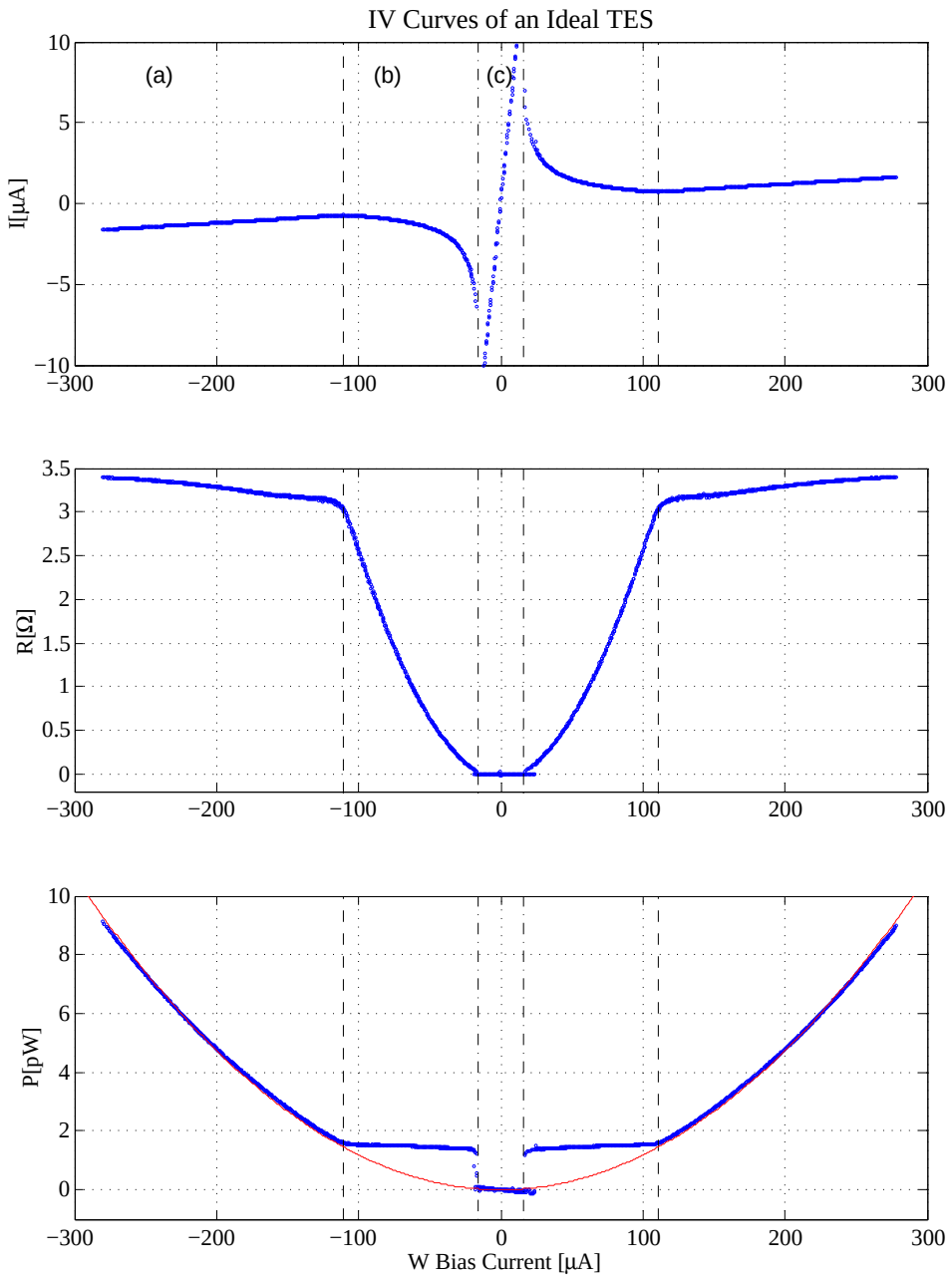

Figure 4.12: Measured IV curves of an ideal TES. The top, middle, and bottom panels show respectively the dependence of the current through the sensor (I_s), the resistance of the sensor (R_{TES}), and the power dissipated by the sensor (P) on the bias current (I_b). A parabolic line, in the bottom panel indicates the power dissipated by a normal resistor. The normal (a), superconducting (c), and biased (b) regions can be identified with the descriptions in the text.

Finite Transition Width

W films produced by a Balzers magnetron sputtering system[20], both patterned and bulk, have superconducting transition widths $\sim$2–3 mK. This means that the power dissipated by the TES when in the bias regime is not actually constant. If we consider Equation 4.5 for $T_c \sim$ 60 mK, $T_{sub} \sim$ 40 mK, and a transition width of 2 mK then there will be a 10% decrease in power dissipated at the lower end of the superconducting transition with respect to the higher end. The slope of the P vs I_b plot in the bias regime is then a measure of the width of the TES's superconducting transition. Figure 4.13 shows the P vs. I_b plot for TESs with a T_c of 60 mK, referenced to the center of the transition, with widths of 2 and 4 mK.

Phase Separation

Another phenomenon that can affect the shape of the IV curve, in addition to impacting the performance of the TES, is phase separation. This refers to a superconducting - normal phase separation in which a portion of the TES is normal (resistive) while the remainder is fully superconducting. In comparison, the treatment given so far has assumed that the entire length of the TES is at the same temperature and in the same phase.

The mechanism behind phase separation in a TES is the balance of heat flow along the TES with that of heat flow into the substrate. The general idea is that the equilibrium power balance between the Joule heating (at a given I_b (or V_b), and a T_c) can be satisfied by having a fraction of the TES being normal, with $T > T_c$. Equation 4.23 gives the necessary criterion for phase stability and is a consequence of the solution of the heat flow equations along the TES [47].

$$\frac{g_{wf}}{g_{ep}} \geq \frac{\alpha/n}{\pi^2} \tag{4.23}$$

[20]Referred to as Balzers.

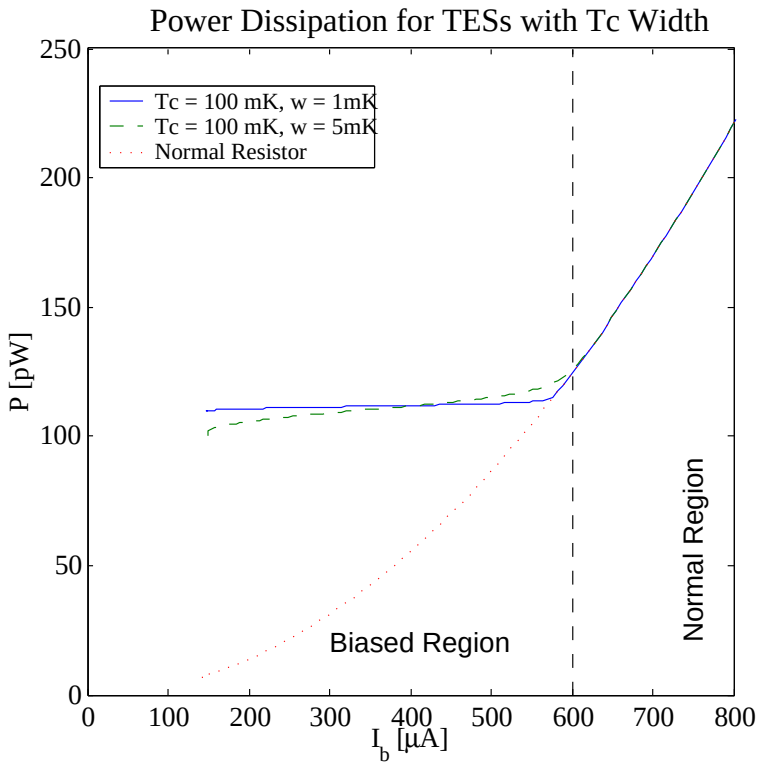

Figure 4.13: Calculated TES power curves as a function of superconducting transition width. The solid line corresponds to a 2 mK wide transition while the dashed line corresponds to 4 mK.

Here, g_{ep} is the thermal conductivity into the substrate due to electron-phonon interactions, g_{wf} is the Wiedeman-Franz thermal conductivity along the TES, $\alpha = \frac{1}{R/T}\frac{dR}{dT}$, and $n = 5$.

The equilibrium point (in the limit of an infinitely sharp transition, i.e. $\alpha_0 = \infty$) is given by the solution to the following two equations [60]

$$-K_N \frac{d^2T}{dx^2} + \frac{\beta}{d}(T - T_{ph}) = \left(\frac{I}{Wd}\right)^2 \rho \tag{4.24}$$

$$-K_S \frac{d^2T}{dx^2} + \frac{\beta}{d}(T - T_{ph}) = 0 \tag{4.25}$$

where Equation 4.24 refers to the normal portion of the TES and Equation 4.25 refers

to the superconducting portion. K_N and K_S are the thermal conductivities along the length of the TES for the normal and superconducting phases respectively. β is the heat transfer coefficient[21] (per unit area) into the substrate, and d is the thickness of the TES W film. The solutions of equations 4.24 and 4.25 yield the current and voltage across the TES as a function of the size of the normal region (x_0). From this information, IV curves can be calculated. Figure 4.14 compares the power curves of two TESs with the same $T_c = 100\,\mathrm{mK}$ for the phase separated and non-phase separated cases. Since phase separation is dependent on heat flow from the TES into

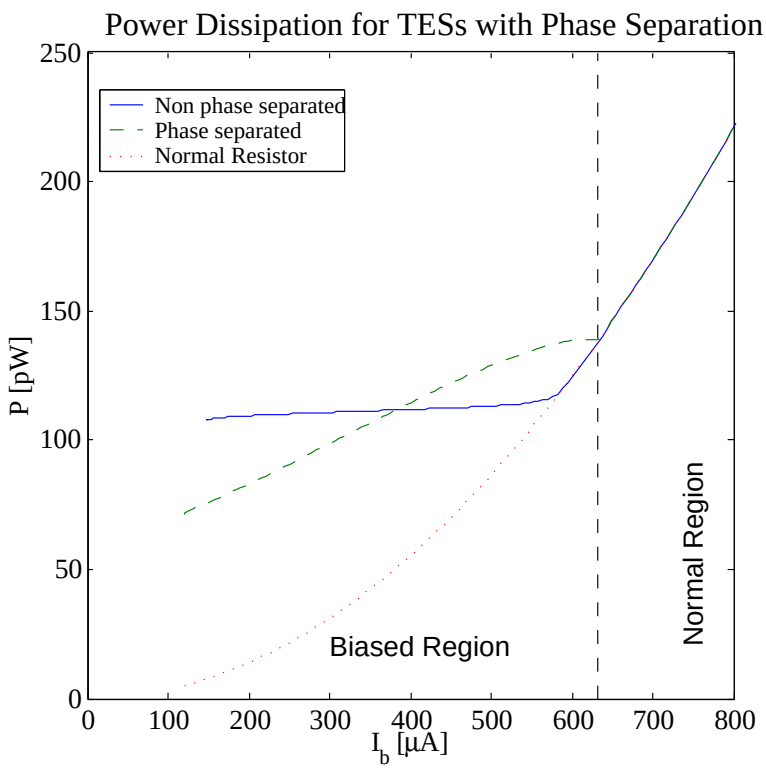

Figure 4.14: Calculated TES power curves as a function of phase separation. The solid line corresponds to a non phase separated TES, while the dotted line shows the effects of phase separation.

the substrate, raising the temperature of the substrate and thereby decreasing the

[21] In the cited reference the heat transfer coefficient is referred to as α, I renamed the variable β in order to avoid confusion with the other use of α in the chapter.

heat flow makes the TES less likely to phase separate.

Equations 4.24 and 4.25 refer to a TES with an infinitely sharp transition. Consequently, the criterion for phase separation is independent of the length of a TES. Using Equation 4.23, however, the phase separation stability criterion can be rewritten in terms of the various TES parameters as follows [47] :

$$l_{max}^2 = \frac{\pi^2 \mathcal{L}_{Lor}}{\alpha \Sigma T_c^3 \rho_n} \tag{4.26}$$

where l_{max} is the maximum length of a phase stable TES, $\mathcal{L}_{Lor}$ is the Lorentz constant $\sim$ 25 nWΩ/K^2, α is $\frac{1}{R/T}\frac{dR}{dT}$ and is $\sim$100 when loaded for the W we produce and ρ_n is the normal state bulk resistivity, $\sim$ 0.2 $\Omega\,\mu$m. With the aforementioned constants, and for a T_c of 80 mK, a maximum phase stable TES length of $\sim$ 245 μm is obtained. Empirically, phase stable TES lengths of 250 μm for $T_c \leq 80$ mK have been observed.

Non Uniform T_c

Recent W films produced by the Balzers appear to have non-uniform T_c across the wafer surface. This T_c non-uniformity affects the TES performance as well as the shape of the IV curve. Figure 4.15 shows the power curve for two TESs of equal area and resistance, but with T_c's of 80 and 110 mK, connected in parallel. It can be seen that if the TESs are biased with a sufficiently low bias current, I_b, their net behavior will be equivalent to a TES with a single T_c of

$$T_{c-eqv} = \left(\frac{1}{2}\left(T_{c1}^5 + T_{c2}^5\right)\right)^{\frac{1}{5}} \tag{4.27}$$

such that the power dissipation is equal to the average of the two different TESs. If three TESs with different temperatures are connected in parallel, one sees that although the general behavior of the power curve is similar, it has acquired an extra *kink* corresponding to the point where a TES enters its bias region. As the T_c distribution becomes continuous the kinks merge into a smooth curve. Nonetheless, the

flat portion of the power curve is still determined by the TES with the lowest T_c, while the first deviation from a normal resistance power curve is determined by the highest T_c element.

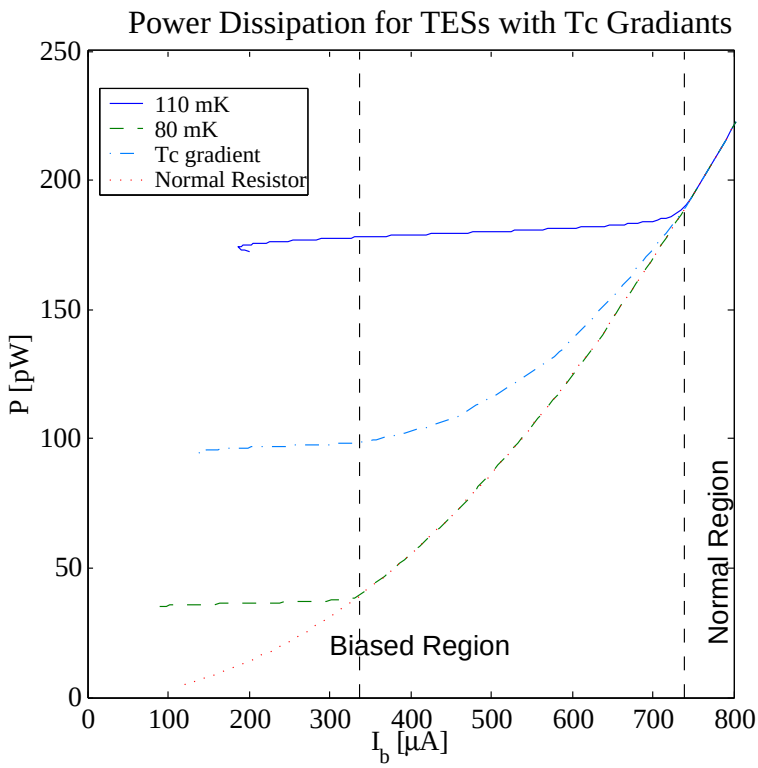

Figure 4.15: Calculated TES power curves as a function of T_c uniformity. The solid and dashed lines correspond to TESs with uniform T_c of 110 and 80 mK respectively. The dash-dotted line in between the two extremes shows the effect of a 30 mK T_c gradient.

Simulating IV Curves

A simulation has been developed, based on the principles described above, that calculates theoretical IV curves, as well as signal to noise ratios, for a given configuration of TESs. The parameters required for the calculations are listed below.

For a non-phase separated calculation all the following input parameters are required :

- T_c: The upper limit on the T_c is obtained experimentally by measuring a bulk W sample or a TES.
- ρ_n: The resistance per square for the W films has historically been $\sim$ $5\,\Omega/$ square. This corresponds to a normal state bulk resistivity of $\sim$ $0.2\,\Omega\,\mu$m.
- κ: The electron-phonon coupling for a TES is given by the product of the electron-phonon coupling constant ($\Sigma \sim$ $0.4 \times 10^{-9}\,\mathrm{W/K^5}\mu\mathrm{m}^3$) and the volume of the TES ($V = 1036 * (250 \cdot 1 \cdot 0.04\,\mu\mathrm{m}^3)$). Σ is determined empirically using Equation 4.5 and a measured value of T_c. For the CDMS ZIP TESs we need to multiply the ΣV product by an additional factor of 7 to get the correct value of κ. This correction is needed in order to take into account the additional volume of W that connects the quasiparticle traps on the Al fins to the W TES.
- w : The width of the superconducting transition has been measured to be 1–2 mK.

For a phase separated calculation the following additional parameters are required :

- K_N : The normal thermal conductivity along the TES is given by

$$K_N = \frac{\mathcal{L}_{Lor}\,T_c}{4\rho_n} \tag{4.28}$$

- K_S: The superconducting thermal conductivity is approximately equal to $K_N/3$.
- β : The heat transfer coefficient into the substrate is calculated from the electron-phonon coupling constant.

$$\beta = \frac{g_{ep}}{(T_c - T_{ph})} = \Sigma \cdot \frac{(T_c^5 - T_{ph}^5)}{(T_c - T_{ph})} \tag{4.29}$$

R vs. T Curves

In the absence of phase separation, a TES's R vs. T curve can be calculated from the power curve. This simply makes use of Equation 4.5 to calculate the temperature associated with every data point based on the dissipated power. The TES resistance is then calculated from the IV curve by inverting Equation 4.22 resulting in

$$R_{TES} = \left(\frac{I_b}{I_s} - 1\right) \cdot R_{bias} - R_{para} \tag{4.30}$$

Figure 4.6 shows an R vs. T curve obtained in such a manner. The usefulness of this technique arises from the ability of the TES to regulate its temperature, while in electrothermal feedback, rather than having to temperature regulate a dilution refrigerator to the precision necessary for measuring R vs. T in a more conventional manner.

IV Curves : Device performance diagnostic

Figure 4.16 is an example of ideal TES behavior, exhibiting a flat P vs. I_b region. The simulated data was based on a T_c of 84 mK and a transition width of 4 mK.

A good example of a phase separated TES is shown in Figure 4.17, with good agreement between the calculation (line) and the data (dots). The parameters used to produce the calculated IV curves were $T_c = 90\,\mathrm{mK}$, $\Sigma = 3.77\,\mathrm{nW/K\mu m^3}$, and the assumption of phase separation. The measured T_c for this device, in the low excitation current limit, was 93 mK.

Finally, Figure 4.18 shows the power curve of a TES with a T_c gradient. The top and bottom curves are those of ideal TESs with $T_c = 70$ and 95 mK respectively, corresponding to the limits of the modeled T_c range. The dots and superimposed curve correspond to the measured and calculated data. In addition to a T_c gradient of 70–90 mK, the model assumed phase separation.

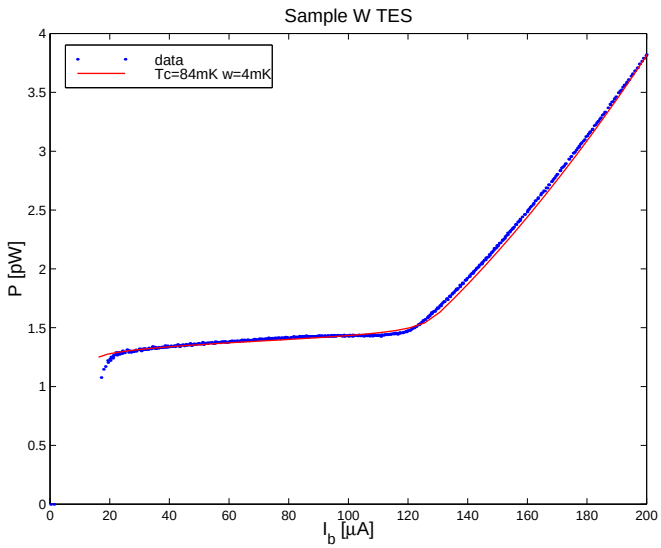

Figure 4.16: IV data showing ideal TES behavior. The data is well fitted by the IV model.

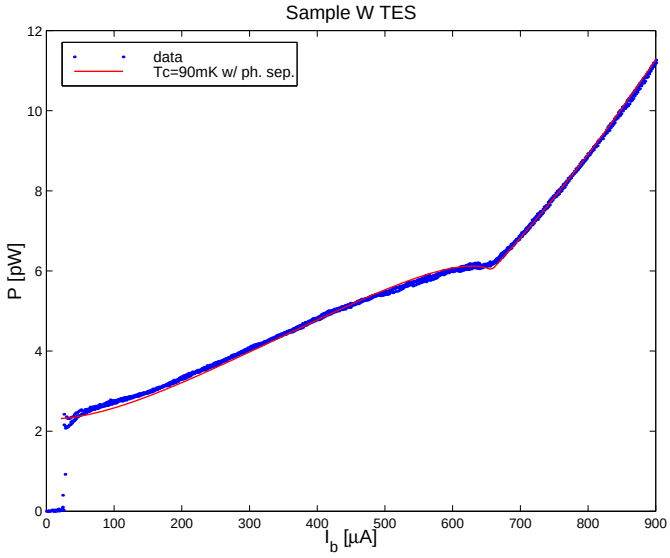

Figure 4.17: IV data showing signs of phase separation. The data is well fitted by the IV model.

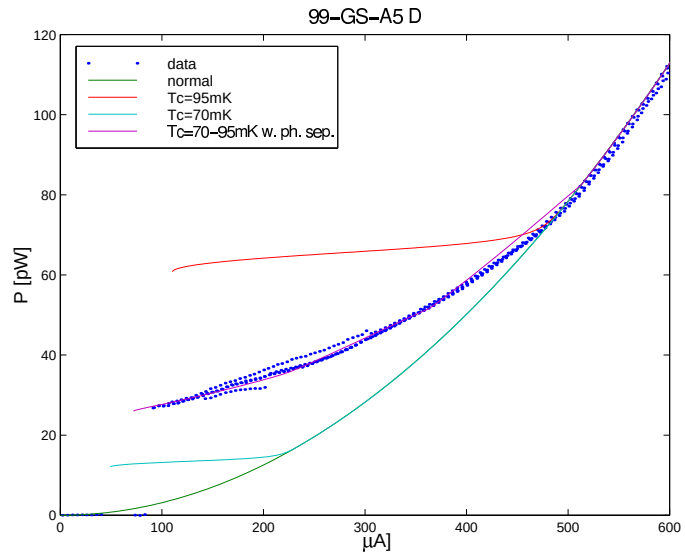

Figure 4.18: IV data showing signs of a T_c gradient as well as phase separation. The data is well fitted by the IV model.

The utility of IV characterization, along with critical current measurements, lies in determining the T_c distribution across the surface of a ZIP detector. Fe ion implantation can then be tailored to reduce the gradient in T_c, in addition to the mean value, to within the 70–80 mK target. This will reduce the position dependence of both the phonon channel response and TES noise, resulting in a more uniform detector response.

4.3 The Ionization Channel

The ionization signal is read out by a charge amplifier as shown schematically in Figure 4.19. A recoil event in the detector will create a number of electron hole pairs given by

$$N_Q = E_r/3.0\,(3.82) \tag{4.31}$$

with

$$Q = N_Q/1.6 \times 10^{-19} \tag{4.32}$$

where E_r is in eV and the 3.0 (3.82) refer to Ge (Si) crystals. An electric field of a few Volts/cm is applied across the detector via the V_{bias} line, causing the electrons and holes to drift to their respective electrodes. As the drifting electrons begin to develop a voltage across C_d, the amplifier responds by lowering its output voltage in order to attract the charge carriers onto the feedback capacitor, maintaining the JFET gate voltage at virtual ground. The size of the signal that appears at the output of the amplifier is given by $V_f = Q/C_f \propto E_r$. The feedback capacitor is allowed to discharge through the feedback resistor, R_f with a time constant of $\tau = R_f C_f \sim 40\mu s$. This charge amplifier circuit, thus produces voltage pulses in which pulse height depends linearly on the recoil energy. The coupling capacitor C_c serves to isolate the JFET gate from the ionization DC bias voltage, allowing it to remain at virtual ground. The presence of the coupling capacitor results in a fraction of the charge carriers, $C_d/(C_c + C_d)$, not appearing on the feedback capacitor, resulting in a suppressed signal. This effect is minimized by using a coupling capacitor with a large capacitance. Empirically, a value of 300 pF was chosen to avoid breakdown of the capacitors when operated at cryogenic temperatures.

For a subset of recoils that occur within a depth of several μm of the surface the charge carriers have the opportunity to diffuse, against the electric field, into the incorrect electrode[22]. This results in fewer charge carriers reaching the feedback capacitor and, consequently, a smaller output signal for a given recoil. Since an electron recoil event with a suppressed ionization signal has the potential to mimic a nuclear recoil event it is important to minimize the magnitude of the surface effect. The deposition of a thin layer ($\sim$ 40 nm) of amorphous Si (α-Si) between the bulk crystal and the metallic electrodes as discovered to minimize the signal suppression effect [61]. The larger bandgap of α-Si ($\sim$1.2 eV), compared to Ge ($\sim$0.74 eV) and Si ($\sim$1.17 eV), results in a potential barrier which minimizes the diffusion of charge

[22]Referred to henceforth as the surface effect

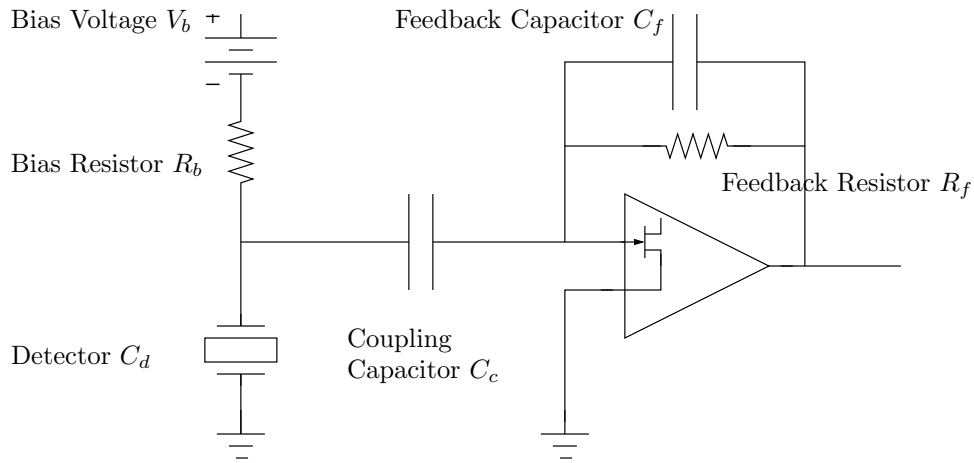

Figure 4.19: Schematic of the ionization readout circuit. The detector is represented as a capacitor C_d, and the active element of the charge amplifier, a JFET, is highlighted.

carriers into the incorrect electrode. Note, however, that the application of the ionization voltage bias allows the charge carriers to overcome the potential barrier and pass into the correct electrode.

A similar degradation in the measured signal occurs if charge carriers are trapped within the bulk of the detector at shallow impurity sites. Impurities (acceptors/donors) in the detector bulk create shallow energy levels just above/below the valence/conduction bands. The depth of these impurity levels is $\sim 10\,\mathrm{meV}$, and at room temperature ($kT_{rm} = 25\,\mathrm{meV}$) they are fully ionized (filled with holes/electrons respectively). As the detectors are cooled to $20\,\mathrm{mK}$ ($kT_{base} = 2\,\mu\mathrm{eV}$) the occupation of the acceptor/donor states goes to zero, leaving ionized impurity sites throughout the bulk of the crystal ($\sim\ 10^{11}\,\mathrm{cm}^{-3}$ (Ge), $\sim\ 10^{14}\,\mathrm{cm}^{-3}$ (Si)). Such sites are quite efficient at trapping drifting electrons/holes, especially if the electric field is $\sim$few volts/cm. Given the impurity density of our Ge (Si) detectors, and that a 1 keV recoil creates ~ 330 (260) electron-hole pairs in Ge (Si), electron-hole trapping poses a significant challenge to the ionization measurement.

Since the the thermal energy of the charge carriers at $20\,\mathrm{mK}$ ($kT_{base} = 2\,\mu\mathrm{eV}$) is

$\sim$1000 times smaller than the trap potential well depth, a configuration in which the impurity sites are filled is stable as long as the temperature of the detectors remains below 1 K. Such a metastable state is desirable since the probability of a charge carrier being trapped by a neutralized impurity site is reduced by several orders of magnitude, allowing an accurate measurement of the ionization signal to be performed at a low bias voltage. Neutralizing the detectors is achieved by exposing them to light from LEDs. Photons from the LED, with energies $\sim$the band gap of the Ge (Si) crystals create electron-hole pairs throughout the detector volume. In the absence of an electric field the electrons and holes diffuse throughout the bulk detector and fall into the impurity traps, neutralizing them. Such a procedure, referred to as an *LED Bake*, is performed for several hours after the detectors are first cooled down. Subsequently, minute long LED *flashes* every few hours, with the ionization electrodes grounded[23], suffice to keep the detectors neutralized. The periodic flashing is necessary since the detectors' continual exposure to radiation, even at the low rates of the CDMS experiment, result in an accumulation of space charge near the detectors' surfaces over time. A thorough explanation of the microscopic mechanism behind the ionization measurement can be found in [24].

The performance of the ionization readout circuit is ultimately determined by the noise in that channel. The noise contributions of the ionization readout circuit falls into two categories : thermal fluctuations of the voltage across the various capacitors in the circuit, and noise due to the charge amplifier components. Voltage fluctuations in a capacitor (C) at a temperature (T) are given by

$$V_{rms} = \sqrt{4k_B T/C} \tag{4.33}$$

[23]The presence of an electric field during the LED flash accelerates the charge carriers sufficiently that they do not get captured at the trapping sites. In fact, if the charge carriers have sufficient energy they may scatter off of a trapped quasiparticle causing it to leave the trap, effectively de-neutralizing the crystal. As such, we are extremely careful to ensure that the ionization electrodes are grounded during an LED flash.

the resulting equivalent charge fluctuations are then given by

$$Q_{rms} = \sqrt{4k_B TC} \tag{4.34}$$

As shown in Figure 4.20 the detectors can be treated as capacitances with $C_d = 100\,\mathrm{pF}$ [24]. Given that the detectors are operated at a temperature of 20 mK, a noise contribution of 66 electron-hole pairs arises from the thermal fluctuations. This translates into a 1σ noise resolution of $\sim 200\,\mathrm{eV}$ for electron recoils in Ge detectors ($\sim 250\,\mathrm{eV}$ in Si). For a more accurate calculation one must consider, in addition to the detector capacitance the various other elements that can contribute thermal fluctuations. Namely, the coupling capacitor C_c (which adds in series to the detector capacitance) and the parasitic capacitance $C_p = 10\,\mathrm{pF}$ which adds in parallel to the detector/coupling capacitance combination.

The charge amplifier noise is usually quantified by the voltage fluctuations at the gate of the FET which is $\sim 1\mathrm{nV}/\sqrt{\mathrm{Hz}}$. It should be noted that optimal noise performance of the FET is obtained when the FET is operated at a temperature of 130 K. This is accomplished by isolating the FET on a membrane which is heat sinked to the 4 K bath and allowing it to self heat to 130 K. The rest of the components shown in Figure 4.20 are at the refrigerator's base temperature of 20 mK. If one considers the FET voltage fluctuations from the perspective of the detector capacitance, it can be calculated that its contribution to the noise is ~ 250 electron-hole pairs, $\sim 750\,\mathrm{eV}$ ($\sim 955\,\mathrm{eV}$) for electron recoils in Ge (Si). The FET and detector capacitance noise terms are independent of the recoil energy and determine the minimum resolvable ionization signal.

The calculations described above are a first order approach and do not properly take into account the full spectral behavior of the noise[25], however, they are a very good first order approximation, and serve to illustrate qualitatively and quantitatively

[24] The value of 100 pF is determined empirically.

[25] Since this circuit is composed of various resistance and capacitances the circuit bandpass is not constant over all of frequency space. However, it is a very good approximation to assume that the noise is white (flat) in the bandwidth of the signal.

the expected noise performance.

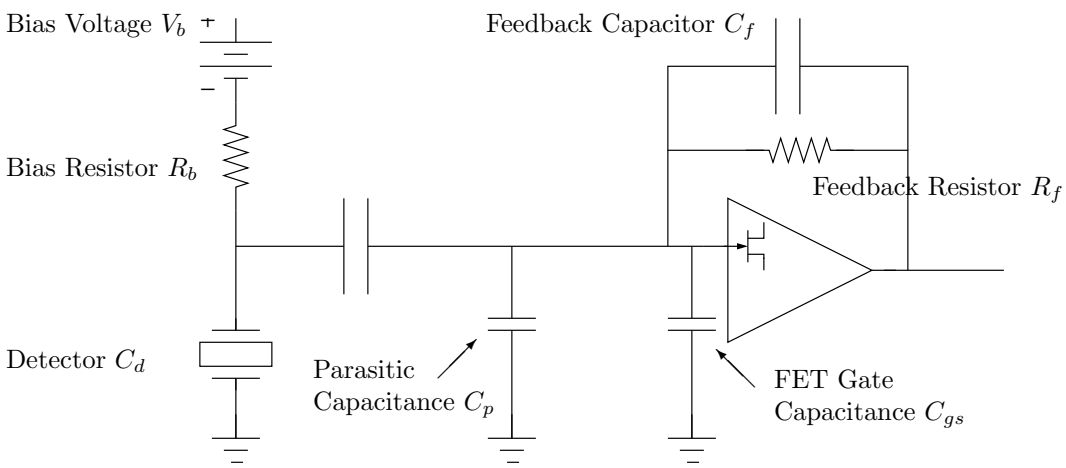

Figure 4.20: Schematic of the noise sources in the ionization readout circuit. The various capacitances contribute thermally induced voltage fluctuations in addition to those due to the FET.

4.4 The Yield Parameter and Particle Identification

The preceding sections discussed in some detail the principles behind the phonon and ionization channel measurements. These two pieces of information can be combined to determined the recoil energy of the interaction and the type of recoiling particle[26].

As mentioned in section 4.2.1, Neganov-Luke phonons generated by the charge carriers, have a total energy proportional to the number of charge carriers and the ionization bias voltage. This energy, in addition to the recoil energy is measured by

[26]Particle identification is limited to distinguishing electron recoils (charged particles and photons) from nuclear recoils (neutral particles such as neutrons and WIMPs)

the phonon channel. We, therefore we have

$$P_{Tot} = R + \frac{V}{\epsilon}Q \tag{4.35}$$

where P_{Tot} is the energy measured by the phonon channel, Q is the energy measured by the ionization channel, V is the ionization bias voltage, and $\epsilon = 3.0$ (3.82) is the average amount of energy in eV required to create an electron-hole pair in Ge (Si). From these variables a parameter, known as ionization yield[27] is constructed :

$$y \equiv \frac{Q}{R} = \frac{Q}{P_{tot} - \frac{V}{\epsilon}Q} \tag{4.36}$$

The yield serves as the discrimination parameter, since according to [43] the ionization signal of nuclear recoils is suppressed with respect to electron recoils by a factor of ~ 3. More accurately, the suppression of the ionization signal is energy dependent and can be parametrized as

$$\frac{Q_{NR}}{Q_{ER}} = aR^{b-1} \tag{4.37}$$

with values of a and $b \sim$ 0.2 and 0.14 respectively.

An important operation parameter for the ZIP detectors is the choice of ionization bias voltage. As described in section 4.3 the *surface effect* degrades the ability to distinguish surface electron recoils from bulk nuclear recoils, rendering the experiment vulnerable to those events arising primarily from low energy electron backgrounds. Increasing the ionization bias voltage reduces the severity of the surface effect by increasing the potential barrier against which charge carriers must diffuse to pass into the incorrect electrode. While it may appear from the preceding argument that arbitrarily high bias voltages are favorable, there is an upper limit imposed by the requirement to distinguish between *bulk* electron and nuclear recoils. The uncertainty in the value of the yield parameter arises from the noise in the phonon and ionization

[27] Or simply *yield*

measurements. This uncertainty is quantified as follows :

$$\left(\frac{\Delta y}{y}\right)^2 = \left(\frac{\Delta Q}{Q}\right)^2 + \left(\frac{\Delta R}{R}\right)^2 \tag{4.38}$$

$$(\Delta R)^2 = (\Delta P_{Tot})^2 + \left(\frac{V}{\epsilon}\right)^2 (\Delta Q)^2 \tag{4.39}$$

It can be seen that increasing the ionization bias voltage results in an increase in the noise of the reconstructed recoil energy and yield parameter, and thus an overall decrease in the ability to identify and reject bulk electron recoils. Choosing the operating ionization bias voltage becomes a matter of balancing the rejection of surface electron recoils against that of bulk electron recoils.

Increasing the ionization bias voltage also has the disadvantage of reducing the surface recoil risetime effect, which is used to identify surface electron recoils. Higher bias voltages result in an increased fraction of prompt ballistic phonon, reducing the contrast in phonon pulse risetime between bulk and surface recoils. This can be seen quantitatively by considering the ratio of prompt (few μs) to delayed ($\sim$ 10 μs) phonons. It was argued in section 4.2.1 that a large fraction of the phonons due to a surface interaction event are prompt. I will assume that the fraction is 100% for the sake of simplicity. The ratio of prompt to delayed phonons for an interaction in the bulk of the crystal is given by

$$E_{\text{Delayed}} = R - \frac{\delta}{\epsilon} Q \tag{4.40}$$

$$E_{\text{Prompt}} = \frac{1}{\epsilon}(V + \delta) Q \tag{4.41}$$

$$f_{bulk} = \frac{V + \delta}{V + \epsilon \frac{R}{Q}} \tag{4.42}$$

where δ is the crystal bandgap. It can be seen from Equation 4.42 that as the ionization bias voltage is increased, the fraction of prompt phonons for bulk events approaches 100% reducing the contrast with surface events. For this experimental run, half the data was taken at an ionization bias of 3V for Ge and 3.8V for Si (known as the 3V data set). The remainder of the run used a bias of 6V (for both types of

detectors). The data presented in this thesis (Chapters 6–8) is primarily from the 3V data set.

Chapter 5

The CDMS Experiment

The **C**ryogenic **D**ark **M**atter **S**earch II (CDMS II) experiment is preparing to begin operation at the Soudan mine in Minnesota toward the end of the year 2002. The low rate of cosmic-ray muons and related particles, due to a rock overburden of $\sim$2400 feet, will allow the experiment to probe new regions of the WIMP mass – cross-section parameter space. In the meantime, the CDMS experiment has been operating at a site on the Stanford University campus for the past few years. The experimental run which began in the fall of the year 2001 (known as Run 21) deployed a set of 6 ZIP detectors (4 Ge and 2 Si) with the purpose of extending the sensitivity of the experiment that was established in 1999 [40] [62]. This run would also serve as the final testing grounds for the detectors which will go into the first run at the deep site. Precision measurements of the detectors' background rates are a very important goal of the run.

In following sections I will describe the facility and infrastructure that was required to operate the experiment. Most of the information presented is summarized from the great work done by other members of the CDMS collaboration. The reader is directed to the following references [63] [64] [65] [62] for further details.

5.1 The SUF Facility

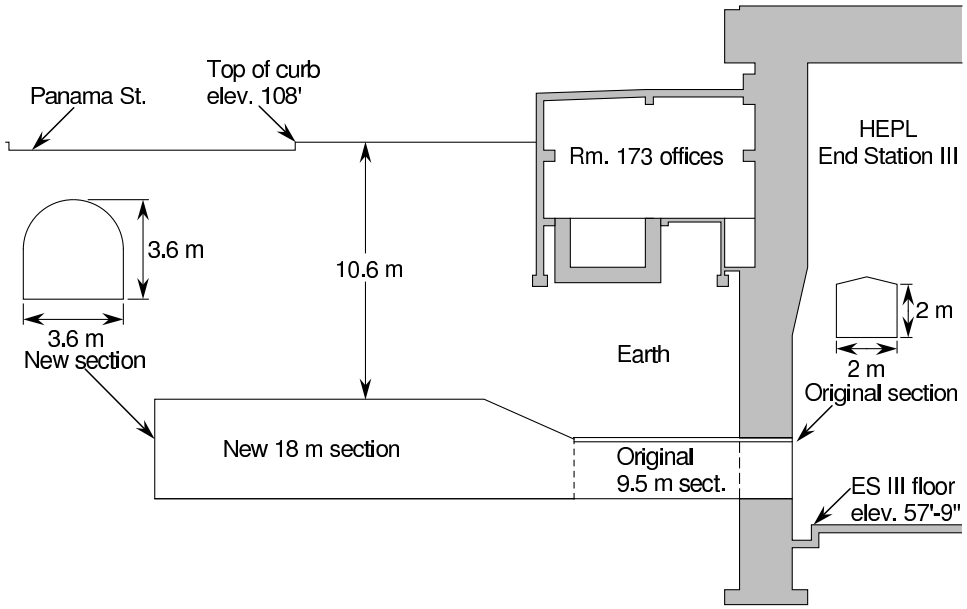

Figure 5.1: Schematic diagram of the Stanford Underground Facility. The experiment is housed in a tunnel at the end of the Hansen Experimental Physics Laboratory, 10.6 meters underground.

Interaction rates from the hadronic and muonic components of cosmic rays, at the earth's surface, are too high[1] to allow for a Dark Matter search which looks for a signal event rate of a few events per year. The construction of an underground laboratory facility on the Stanford campus (known as the **S**tanford **U**nderground **F**acility or SUF), at a depth of 10.6 m of soil (equivalent to ~ 16 m of water) provides an environment in which the hadronic component of cosmic rays is eliminated, while the muonic component is suppressed by $\sim$ a factor of 5. The site (shown schematically in Figure 5.1) also provides the necessary facilities for cryogenic operation.

The SUF facility consists of three tunnels at the end of the Hansen Experimental Physics Laboratory endstation III[2]. The first, and largest, tunnel houses the cryostat

[1] ≥ 10 Hz for the CDMS detectors.

[2] The cavern was first constructed in $\sim$1971 to house fixed target experiment for the Mark I

and experimental volume, another houses the pumps necessary for operation of the dilution refrigerator, and the third one serves as a clean room for long term storage of detector materials. Underground storage is necessary to reduce the activation of the detector materials due to the large rate of cosmogenic interactions at the surface. The clean room is of class 10000, and contains benches of class 1000, in order to minimize the amount of radioactive material in airborne dust which may be deposited on the detectors. In addition, the materials are stored in cabinets purged with the liquid nitrogen boil off in order to minimize radon plate-out[3].

5.2 The Dilution Unit & Ice Box

An Oxford KelvinOx 400-S dilution refrigerator provides the cooling necessary to bring the detectors and their surrounding experimental volume down to a temperature of $\sim 20\,\mathrm{mK}$. The cooling power of the refrigerator, nominally $400\,\mu\mathrm{W}$ at $100\,\mathrm{mK}$, decreases quadratically with temperature. At a base temperature of $20\,\mathrm{mK}$, therefore, the fridge provides a cooling power of $\sim\ 16\,\mu\mathrm{W}$. The power budget is dominated primarily by black body radiation from the $600\,\mathrm{mK}$ thermal shields surrounding the detector volume. Other power demands on the fridge come from heat sinking the FETs at 4K. The FET power load of $54\,\mathrm{mW}$, combined with conduction along the electronic readout wiring (from room temperature to 4K) results in the consumption of 40 liters of liquid He per day.

Most experiments requiring a dilution refrigerator locate the experimental payload beneath the mixing chamber, attached via a short, vertical cold finger in order to improve the heat sinking. The CDMS refrigerator, however, is modified from the standard design. The thermal and mechanical connection between the mixing chamber and the experimental volume is accomplished by a horizontal cold finger (at 90 degrees to the mixing chamber) $\sim 1\,\mathrm{m}$ long (known as a dog leg). While this complicates

accelerator.

[3]Radon decays to ^{210}Pb, a long-lived β emitter which has the potential of being a limiting background for the experiment.

the mechanical engineering somewhat, there are two main advantages. First, space considerations at SUF dictated the need for modification of the standard configuration. Secondly, and more importantly, the material from which dilution refrigerators are constructed cannot conform to the strict radioactivity cleanliness limits required by the experiment. Having the dog leg allows for the construction of an experimental volume with no line of sight path to the refrigerator's interior. It also allows for the construction of a $\sim 4\pi$ coverage shield around the detector volume. This is important given the shallowness of the SUF site and is further described in section 5.3.

The detectors are housed in a unit known as the *Ice Box*. The Ice Box consists of 6 cans made of OFHC copper, heat sunk to the 20 mK, 50 mK, 600 mK, 4 K (LHe), 77 K (LN), and room temperature stages respectively. This provides the mechanical support (designed to account for the differential contraction at all temperatures) and the necessary heat sinking to the refrigerator. The innermost can of the Ice Box consists of a volume of $\sim 1\,\mathrm{ft}^3$ and is designed to hold an ultimate payload of 18 ZIP detectors and ~ 8 kg of polyethylene neutron moderator[4]. Figure 5.2 shows a mechanical drawing of the refrigerator and Ice Box assembly.

5.2.1 The Tower

The tower is the mechanical structure which holds the detectors together and anchors them to the various thermal levels within the Ice Box, as shown in Figure 5.3. Though the primary function of the tower is to provide mechanical support for the detectors, cryogenic electronics, and wiring, it also serves the important function of thermally isolating the various layers of the icebox while being mechanically connected to them. This was necessary because since the heat dissipation and thermal noise requirements of the various cryogenic electronic components could not be satisfied by heat sinking them to a single thermal stage. The optimal noise performance of the FETs is obtained by operating them at a temperature of $\sim$ 130 K. This is accomplished by

[4]The Ice Box at the Soudan deep site is designed to hold 42 ZIP detectors and no polyethylene moderator.

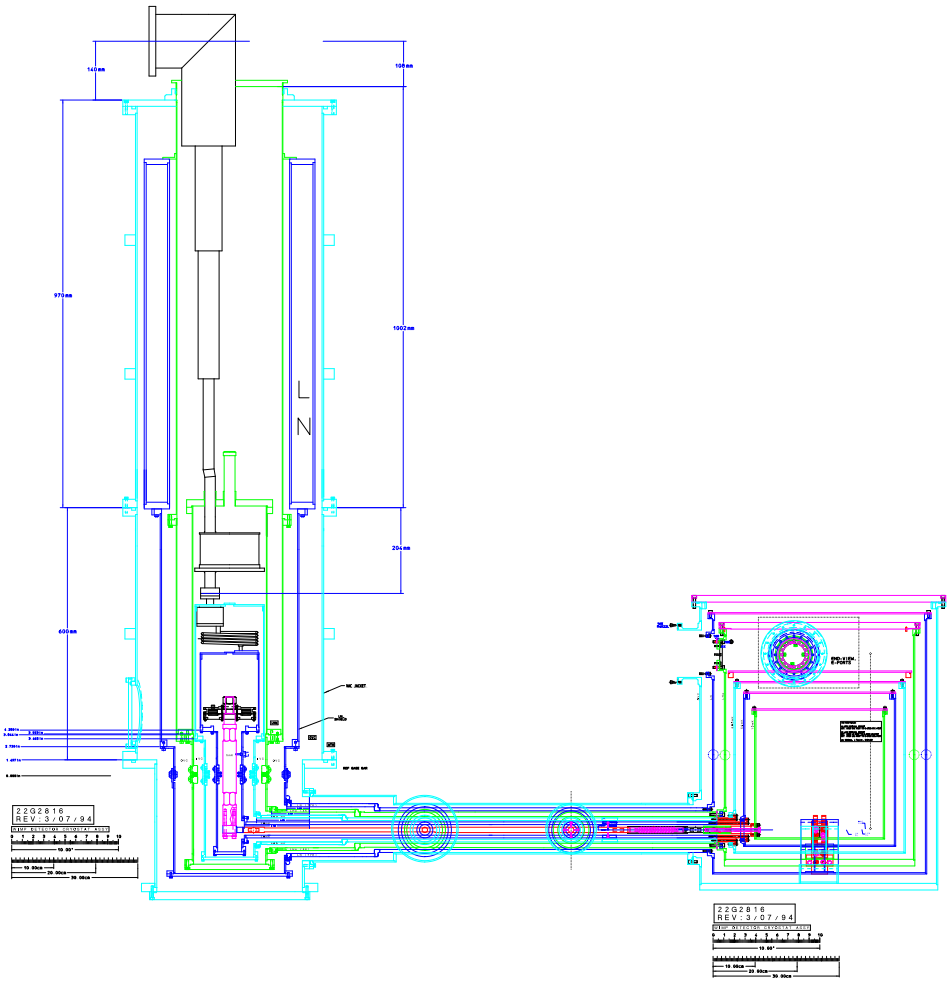

Figure 5.2: Mechanical drawing of the dilution refrigerator and Ice Box assembly.

isolating them on a membrane with the appropriate thermal conductance to allow the FETs to self heat to that temperature. The 4K thermal stage is the only one capable of sinking the tens of mW of power dissipated by the FETs. SQUIDs, on the other hand, dissipate only a few hundred nW and can thus be heat sunk to the 600 mK stage resulting in lower SQUID noise.

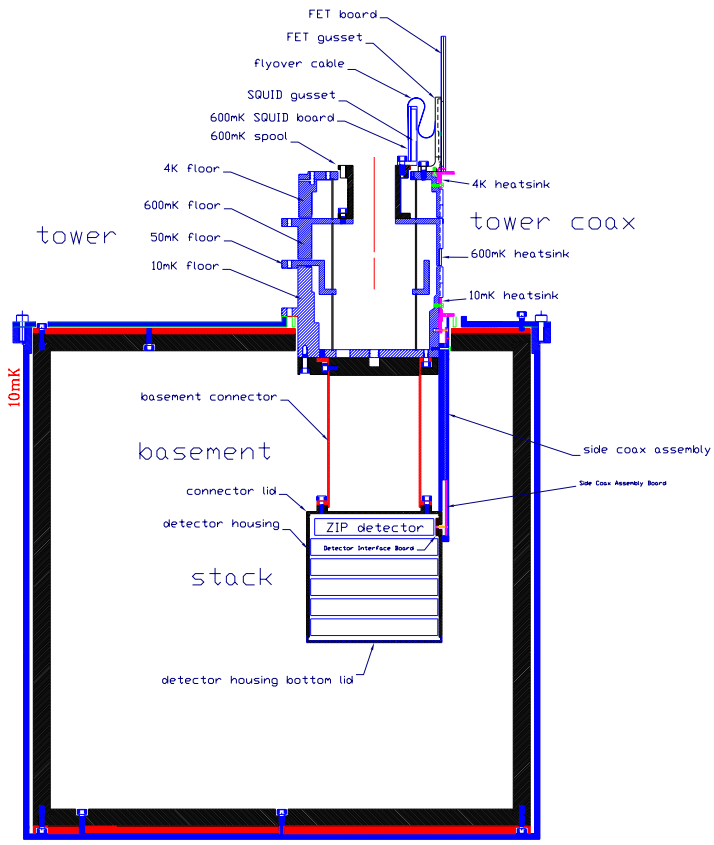

Figure 5.3: Mechanical drawing of a tower installed in the Ice Box. Only the 20 mK Ice Box can is shown, but the figure indicates the location of the other thermal connections. Portions of electronics card at the top of the tower are heat sunk to the 4 K stage, while others are sunk at 600 mK.

The original use of the term *tower* referred to the functional unit described above; however, it has also come to refer to a unit of 6 detectors, arranged vertically as shown in Figure 5.3. Detectors within the Run 21 tower are numbered from one to six in descending vertical order, and will be referred to as Z#, throughout the following sections, when a particular detector is identified. A hexagonal arrangement of seven such towers will form the ultimate payload of the CDMS II experiment of 42 detectors at the Soudan deep site.

5.3 Event Rates and Shielding

At the SUF depth, one expects a significant background event rate (as compared to the rate of WIMPS). These events fall into several classes :

- Gammas from natural radioactivity : Such gammas originate within the rock of the SUF walls from radionucleides of the ^{238}U and ^{232}Th decay chains as well as from ^{40}K.
- Betas from natural radioactivity : Radionucleides such as ^{210}Pb, ^{40}K, ^{63}Ni, and ^{14}C are β emitters and may be found in the SUF environment. 9
- Neutrons from natural radioactivity : Neutron production from (α,n) interactions in the rock are expected to produce ~ 30 neutrons/day/kg. These neutrons have an energy spectrum that is predominantly below 2 MeV [63].
- Muon induced neutrons : There are several mechanisms by which neutrons can be generated via the interaction of muons passing through material. An excellent description is provided in [63] and [64]. A total rate of ~ 60 neutrons/day/kg of rock is estimated at the SUF depth. The total rate can be broken down into three categories : slow (thermal) neutrons with energies well below 1 MeV constitute $\sim 67\%$ of the total rate (or ~ 40 neutrons/day/kg of rock); fast neutrons ($E \sim$ few MeV) constitute a further 25% (or ~ 15 neutrons/day/kg of rock); and finally highly energetic neutrons ($E >$ tens of MeV) contribute the remaining few events/day/kg of rock.
- Muon interactions with the detectors : Such events are clearly identified by the large amount of energy deposited in the detectors ($\sim$ 5–10 MeV).

In response to these event rates, a shield was designed consisting of passive layers of lead and copper[5] to shield the γ flux in addition to polyethylene used to moderate the neutrons [62]. Additionally, an active plastic scintillator is used to identify and

[5]The Cu used in the shielding is simply that of the Ice Box.

veto muons or muon related events. Such a veto system is important in eliminating the flux of gammas due to muon interactions with the shield material, which dominate the trigger rate at SUF, in the offline analysis. Figure 5.4 shows a schematic of the shield with the various Pb, Cu, and polyethylene layers indicated. Such a shielding configuration is expected to reduce the γ and neutron rates to $\sim$ 1 event/keV/kg/day and $\sim$ 0.01 event/keV/kg/day within the energy range $\sim$5–100 keV, respectively .

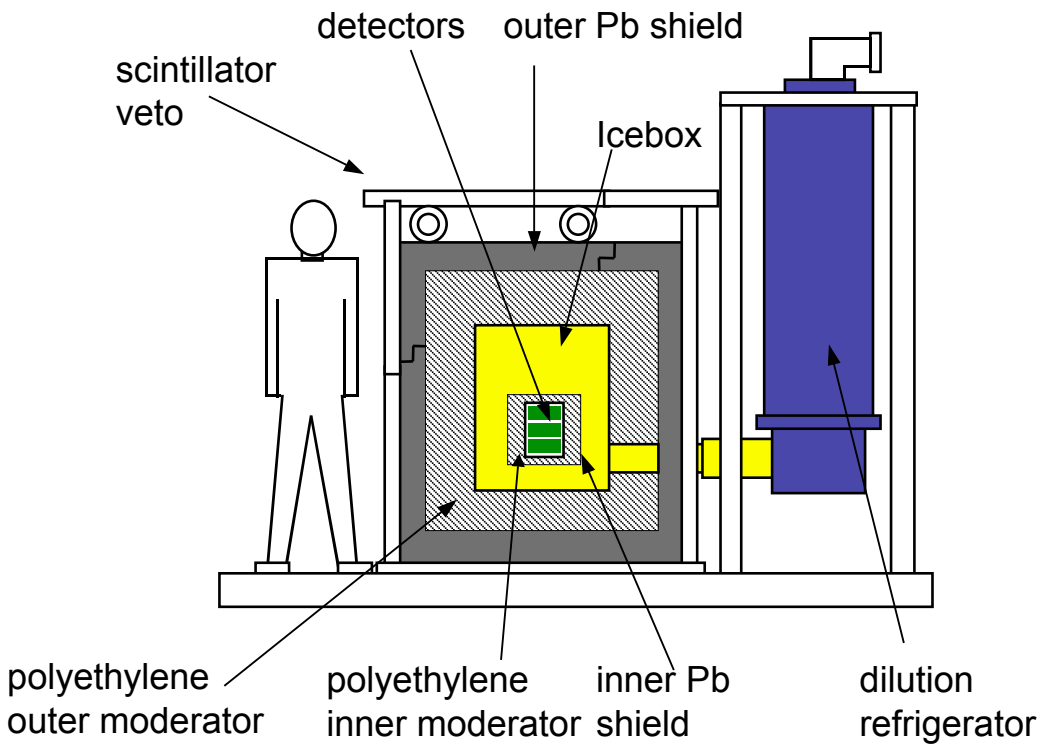

Figure 5.4: Schematic of the CDMS I shield at SUF. The various layers of Pb, Cu, and polyethylene, intended to moderate the rate of gammas and neutrons, are indicated.

5.4 Readout electronics and DAQ

The data acquisition system (DAQ) and readout electronics are an important part of the experiment. The readout electronics fall into 2 major categories : room temperature (warm) and cryogenic (cold). Cold electronics refer to the SQUID and FET circuits that are located inside the fridge and are operated at cryogenic temperatures. These have been described in chapter 4. The warm electronics are described in the following section.

5.4.1 The Front End electronics

The electronics chain can best be understood by following the path of the analog signals from the detectors to the digital information stored on hard drives. Signals from the cold electronics are transmitted outside the refrigerator via strip lines. These are $\sim 3\,\mathrm{m}$ long, $2.5\,\mathrm{cm}$ wide strips of kapton on which a thin copper layer ($0.018\,\mathrm{mm}$ thick) has been etched to form 50 distinct conductors. This design was adopted to minimize the heat load on the 4K stage since the strip lines, by necessity, connect the 4K stage to room temperature. The room temperature end of a strip line is connected to an electronics board known as the **F**ront **E**nd **B**oard (FEB). The FEBs are the room temperature portion of the detector readout circuits. They contain such elements as the feedback amplifiers, which dissipate too much power to be installed inside the fridge, but are robust enough to be well separated from the detectors and cold portions of the circuit (with respect to noise and impedance considerations). A FEB contains all the electronics required to read out and operate a single detector, namely four phonon channels and two ionization channels. It also contains various control electronics, such as digital to analog converters (DACs) that supply the bias currents and voltages, amplifiers for providing further gain stages, and digital logic circuits to allow remote communication with and control of the boards and detectors.

The detector signals, after amplification upon reaching the FEB, are large enough ($\sim 1\,\mathrm{V}$) that they're unlikely to suffer degradation while being transmitted over cables

for a distance of $\sim 15\,\mathrm{m}$. In other words, any further noise that might be acquired will be smaller that the amplified, resolution limiting, noise determined by the cryogenic components of the circuit. Leaving the FEBs, the signals are transmitted to **R**eceiver-**T**rigger-**F**ilter (RTF) boards. The main purpose of the RTF boards is to determine whether there exists a pulse of sufficient amplitude to issue a trigger. The RTFs are programmable, allowing a selection of trigger levels on the scale of mV, corresponding to fractions of a keV. It is important to have a low trigger level in order to identify and record any recoils with energies down to the detector noise limit[6]. The trigger level, however, cannot be set arbitrarily low such that the trigger rate is dominated by random noise. Therefore, the signals are filtered with a high pass ($f_{pole} = 400\,\mathrm{Hz}$) and a low pass ($f_{pole} = 5\,\mathrm{kHz}$) filter to remove as much noise as possible, while preserving the maximum signal[7].

Leaving the RTF boards, the detector signals are fed into high-speed, high-resolution digitizers. The signals are continuously digitized at 1.25 MHz with 12 bit resolution and a dynamic range of 4 V. When a trigger is issued, a 2048 bin long trace (corresponding to 1.6 ms) is recorded by the DAQ.

5.4.2 Muon Veto

The muon veto counters cover a surface area of $\sim 20\,\mathrm{m}^2$ [8] with panels of 4.1 cm thick NE-110 plastic scintillator. The panels are grouped into functional units representing the six sides (or *faces*) of the cube formed by the Pb shield. Each panel is read out by photomultiplier tubes, one to four depending on the size and location of the panel, connected to the panels via wavelength shifter bars and light guides. The photomultiplier tube signals from each panel are then summed and digitized in one

[6] This is particularly important for Dark Matter searches since the theoretical interaction rates rise exponentially with decreasing energy thresholds

[7] The best way to do this, of course, is to use optimal filtering. Optimal filtering, however, is not a real-time process and hence cannot be constructed from inactive electronic components. Once the data time traces are acquired they can be processed with a digital optimal filter to obtain the best energy determination.

[8] Corresponding to the surface area of the outermost Pb shield.

μs time bins. A continuous record of the digitized muon veto information is then sent into a memory buffer to be accessed whenever an event related trigger is issued.

5.4.3 DAQ

The DAQ consists of a combination of custom built electronic hardware and software modules written in the LabView programming language. The DAQ is an umbrella name for a system that performs various tasks, only one of which is recording the actual detector signals.

Signals from the RTF boards and muon-veto logic, along with their timing information, are continuously collected and stored in a memory buffer. When an event occurs that satisfies the triggering criteria a command is issued to download the contents of the digitizers as well as the contents of the memory buffer. This provides information about the activity in the detectors and the muon veto immediately preceding, during, and following the event in question; allowing the determination of whether the event was associated with particles originating within or without the shield.

In addition to recording the data, the DAQ handles the task of controlling the detectors and coordinating among several activities that occur during data taking. Data is taken in a 240 minute cycle, after which the detectors' ionization channels are grounded and the LEDs are flashed (see section 4.3). During this time, data acquisition is stopped. This opportunity is taken to monitor the refrigerator's temperature and pressure sensors, which are otherwise disabled in order to avoid contaminating the detector signals with pickup noise. Additionally, quantities such as trigger and veto rates, as well as various detector diagnostics are continuously monitored (approximately once a minute) to ensure that the experiment is operating within acceptable parameters. In the event that any of the monitored parameters, whether detector or refrigerator related, are outside of the acceptable range the DAQ is capable of issuing e-mail and pager alarms to alert the operators.

5.5 Data Analysis

A first pass data analysis is run offline on a cluster of PCs running the Linux operating system. The purpose of this analysis, known as *DarkPipe*, is to transform the digitized pulse information from a digitizer bin vs. time format into rudimentary physical quantities such as pulse integrals, start times, and rise times. The analysis is automated such that as soon as a data file (usually 500 or 1000 events) becomes available it is promptly sent to the first available CPU. In normal (background) running the trigger rate is $\sim$ 0.7 Hz, and a single CPU[9] is sufficient to keep up with the data rate. When calibration data is taken, trigger rates can be as high as 3–4 Hz, which can be handled in real time by the 10 CPU cluster. DarkPipe takes as input an 80 Mb file (per 500 events) and produces an output of 7 Mb. A typical day of background data consists of $\sim$50000 events, corresponding to $\sim$8 Gb raw and 700 Mb processed data.

A second pass data analysis (known as *PipeCleaner*) is then run on the output of DarkPipe. This consists primarily of applying calibration constants to produce quantities with meaningful units (such as keV) and of calculating derived quantities, such as the x-y coordinates of an event. The second pass analysis takes a few minutes for one days' worth of data; therefore, the final processed version of the data (known as RRQs - Relational Reduced Quantities) is available almost immediately at the end of the acquisition of a data series. During background running, data sets (series) are divided into convenient day-long periods. This is done, primarily, because the DAQ is turned off daily for a period of $\leq$ 1 hour during cryogenic transfers. It is convenient, however, to divide the data into day-long sets since this provides a natural time scale for monitoring detector stability.

Higher level analysis of the data (i.e. searching for a Dark Matter signal) is done with software packages built upon the Matlab programming language.

[9] A CPU refers to a Pentium III 850 MHz processor.

Chapter 6

Establishing the Detector Response

Between the time when a detector is fabricated and when it is installed in the Ice Box at the beginning of the current run, it undergoes numerous tests and calibrations. One purpose of these calibrations is to determine and select the six best available detectors to be used. Consequently, the behavior of a detector is reasonably well understood by the time it is installed at SUF for a Dark Matter experiment. Nonetheless, it remains extremely desirable and compelling to perform in-situ calibrations. The SUF offers a background radiation environment that cannot be reproduced by the above ground test facilities[1]. Additionally, other subtle effects may result in a slightly different detector performance between the test facilities and SUF.

This chapter will explain, in some detail, the various tests and calibrations performed at SUF at the beginning of, and throughout the experimental run.

[1]The event rate is more than 10^4 times lower.

6.1 Calibrating the Energy Scale

6.1.1 Neutralizing the Detectors

The first task, after the detectors have reached base temperature, is to establish the energy scale for both the ionization and phonon channels. As described in section 4.3, the pulse height to energy conversion for the ionization channel has no free parameters. This is only true, however, once the detectors have been fully neutralized. The ionization energy calibration therefore becomes, in essence, a determination of whether the detectors are properly neutralized.

An ideal way to establish if a detector is neutralized is to expose it to an external monochromatic radiation source and determine whether the shape and position of the spectral peak are as expected. Sources that produce a gamma line in the energy range of interest, $1 < E_\gamma < 100$ keV would be ideal. However, gamma rays of that energy are quite efficiently absorbed by the Cu cans of the Ice Box, with the resulting flux reaching the detectors being extremely attenuated and dominated by continuum Compton gamma rays. Consequently, a ^{137}Cs source is used for the initial calibrations. ^{137}Cs produces 662 keV γ rays[2] which can penetrate the copper cans (absorption length ~ 1.5 cm). Unfortunately, 662 keV gammas can also pass through the Si and Ge detectors easily; however, a sufficient number of gammas are absorbed to provide the needed information.

Figure 6.1 shows the ionization channel spectra taken during a ^{137}Cs calibration. The various lines show the spectra taken during a given day, after an LED bake was performed the previous night. It can be seen that the Ge detectors exhibit no variation, indicating that they were properly neutralized after the first night's baking. In fact, the last data set shown, taken with only the standard LED flashing regimen (see section 5.4.3) rather than a full night bake, indicates that no deterioration has occurred. The Si detector Z4, can also be seen to have been successfully neutralized

[2] Actually, ^{137}Cs beta decays into ^{137m}Ba, which then relaxes and emits the γ.

after the first night's LED bake, whereas the other Si detector Z6 required three nights. It is believed that this behavior arises from the confluence of two effects : (1) the detector, at the bottom of the stack, is only exposed to one set of LEDs (its own, from above), and (2) the LEDs themselves may have been mounted incorrectly in the detector housing, resulting in a diminished photon flux at the detector. Once the detectors have been neutralized, they remain so as long as their temperature doesn't rise above 1 K. No evidence of a deterioration was seen throughout the run.

6.1.2 The Ionization Channel

662 keV

Once the 662 keV peak is seen in the ionization spectra the calibration constants that transform pulse height to energy can be determined. For the Ge detectors, those constants are in good agreement (to within a few percent) with their expected, theoretical, values. The Si detectors pose a somewhat larger challenge since their low photoabsorption cross-section at 662 keVdoes not allow for the observation of an actual spectral peak. Comparison of the ionization spectrum with a detailed Monte Carlo simulation [66] becomes the primary means of confirming the calibration constants. Figure 6.2 shows the ^{137}Cs calibration data for both a Ge and a Si detector along with their respective Monte Carlo spectra. The agreement between simulation and data is quite good, and the features seen in the Si (due to Compton edges both in the detectors and the surrounding material) allow the determination of the Si ionization energy scale to within a few percent.

Low energy lines - 10 & 67 keV

Nature is kind enough to provide us with two more handles on the Ge detectors' ionization energy calibration. These handles come in the form of two photon peaks

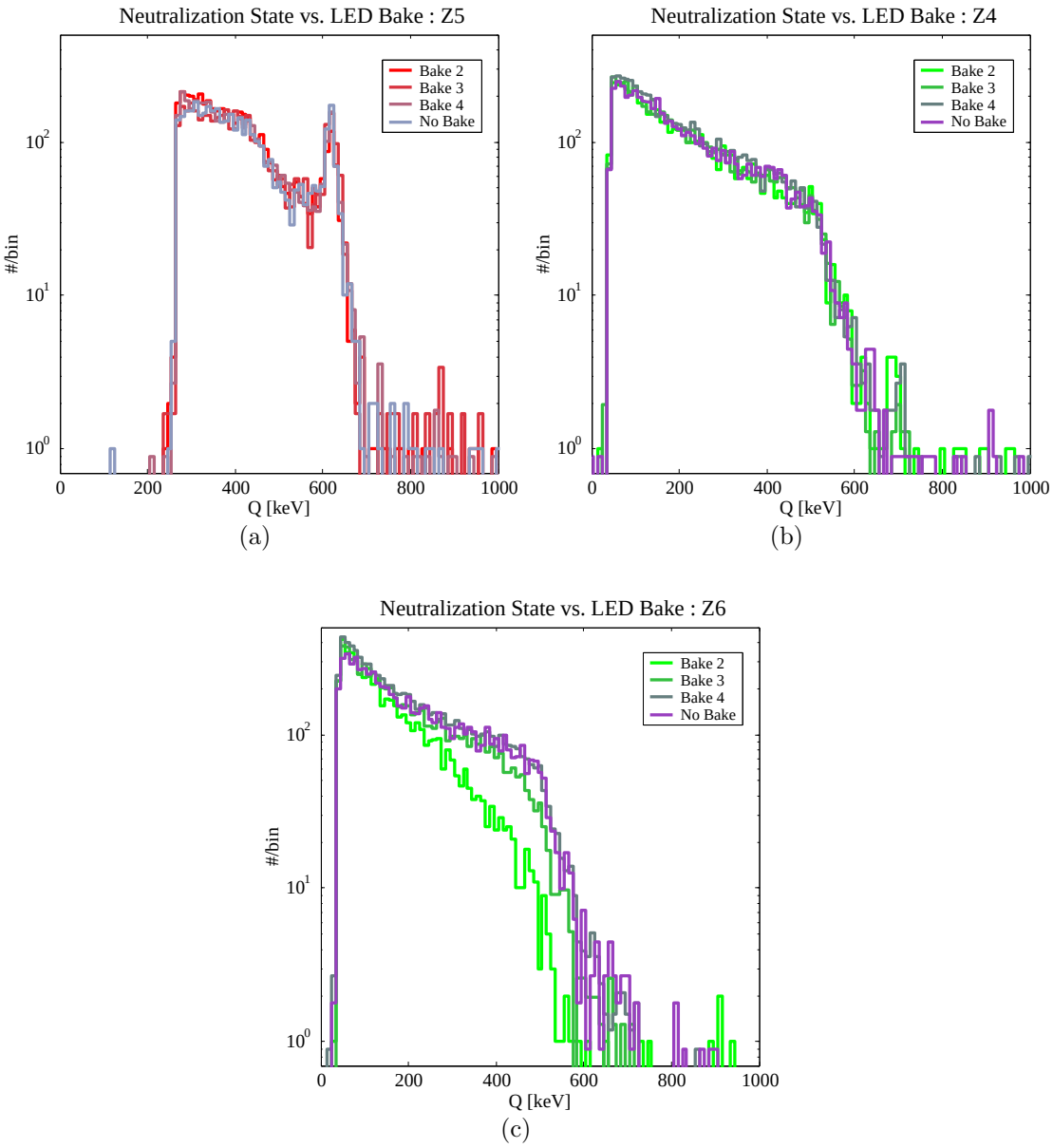

Figure 6.1: Detector neutralization as a function of LED bake. One of the 4 Ge detectors is shown in (a) and its behavior is typical of the others. Plot (b) shows one of the two Si detectors (Z4) which was successfully neutralized after one night of LED baking. It took three nights to properly neutralize Z6 (c).

at 10 and 67 keV[3], in the heart of the relevant energy range. As mentioned above,

[3]The 10 keV peak is an x-ray peak due to electronic transitions in a Ga atom, while the 67 keV peak is due to a γ-ray from a nuclear transition of ^{73}Ge

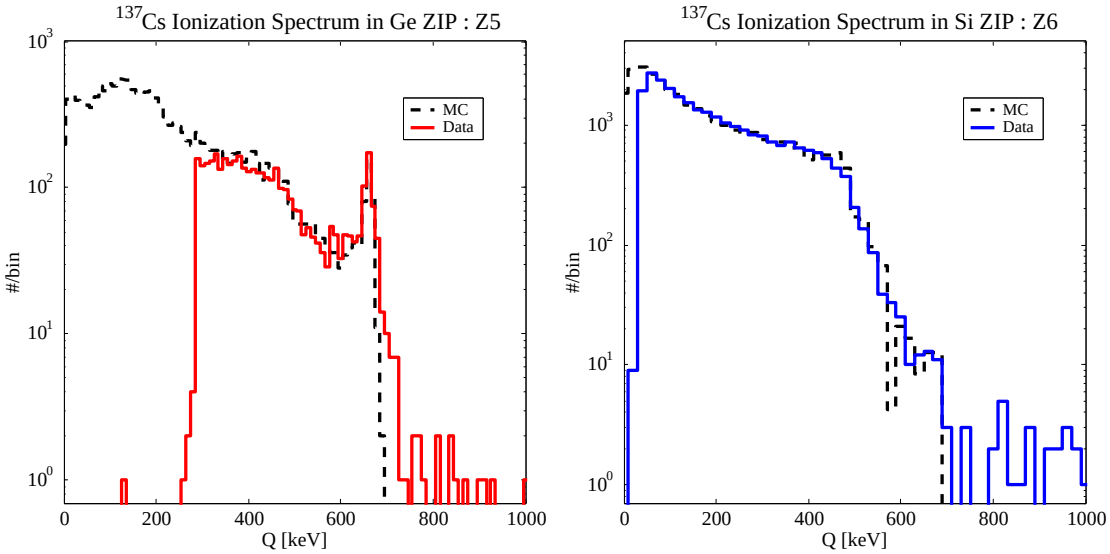

(a) (b)

Figure 6.2: Comparison of data and Monte Carlo ^{137}Cs ionization spectra. A 662 keV peak is clearly seen in the Ge detectors (a), while one is limited to features such as Compton edges in the Si detectors (b). Monte Carlo spectra from [66].

these energies are too low to penetrate the Ice Box, and are in fact generated within the detectors themselves. The lines are due to the activation of some of the Ge intrinsic isotopes and are generated uniformly throughout the detectors (the origin of this activation will be described in Chapter 7)[4].

Figure 6.3 shows the 10, 67, and 662 keV peaks in a Ge ZIP. It is worthwhile to note that the low energy shoulder seen in Figure 6.3(a) does not indicate misbehavior of the ionization channel. Rather, it shows the presence of two gamma lines at 8.98 and 9.65 keV at a somewhat lower rate[5]. The measured positions and widths of the lines, listed in Table 6.1, reveal excellent linearity (better than 2%) from 0 to $\sim$ 700 keV for the Ge detectors.

Unfortunately, none of the isotopes present in Si the detectors provide similarly

[4]Ordinarily, the presence of a long-lived line source at low energy is a source of concern for rare event experiments such as Dark Matter searches. As demonstrated later in this chapter, the excellent ability of the CDMS ZIP detectors at discriminating between electron and nuclear recoils transforms this liability into a very useful asset by providing calibration information at low energies.

[5]The three gamma lines are from the same source and are described in section 7.2

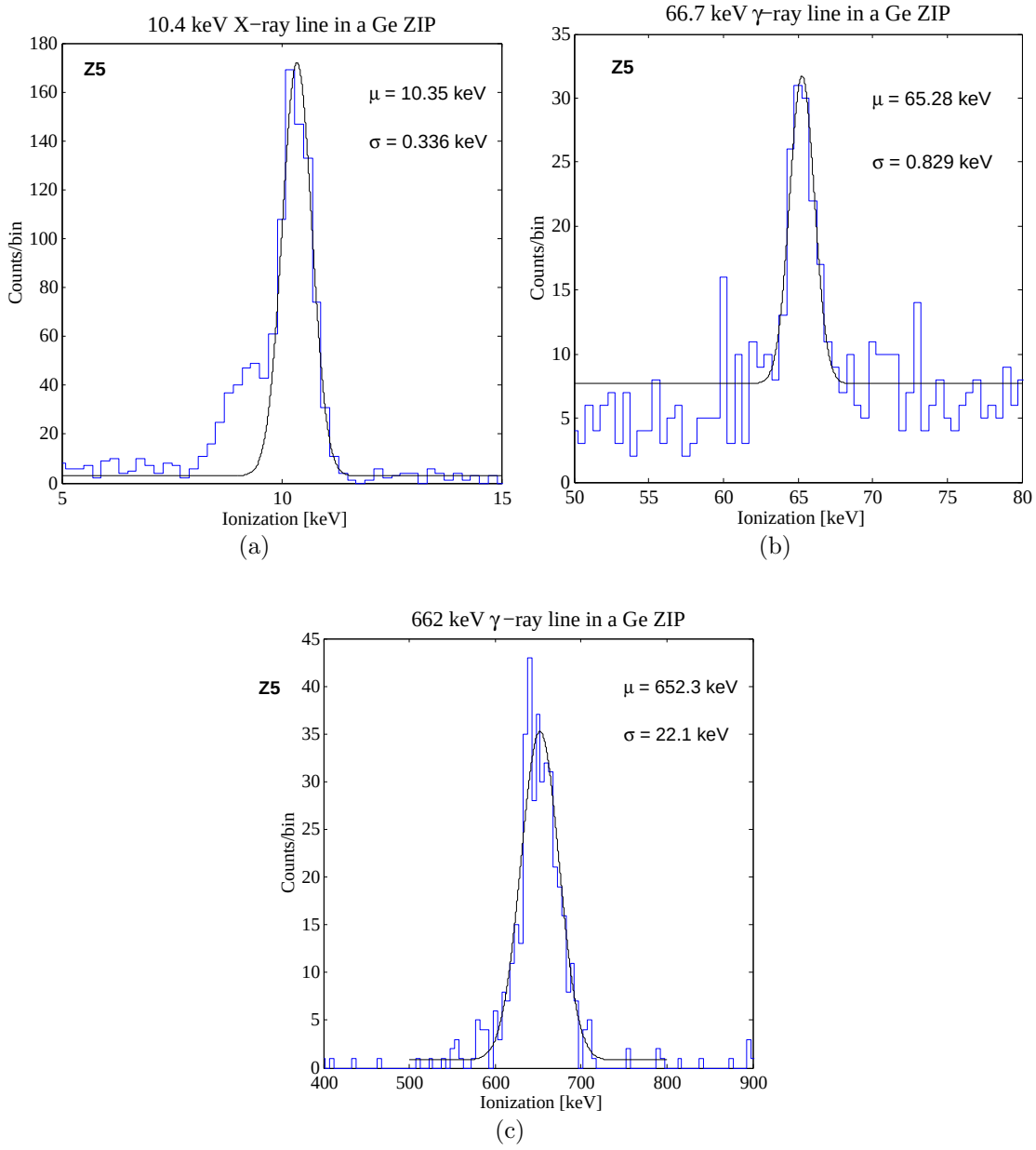

Figure 6.3: The lines in the ionization spectra at (a) 10 keV, (b) 67 keV, and (c) 662 keV establish the absolute energy scale in that channel as well as determining the linearity of ionization response.

convenient features. One must therefore continue to rely upon Monte Carlo simulations of the high energy sources, as well as measurements made at test facilities

Gamma Line [keV]	Measured Position [keV]	Width [keV]	Deviation [σ]
0	0	0.28	–
10.36	10.35	0.34	0.029
66.7	65.3	0.83	1.67
662	652	22	0.45

Table 6.1: Measured energies and widths of several lines in the ionization spectrum of a Ge detector (Z5). The *Width* column quotes the 1σ Gaussian line width, while the *Deviation* column quotes the difference between the actual and measured energy of the line in units of the line width.

where it is possible to expose the detectors to monochromatic gamma rays with energies in the range $\sim 20 < E_\gamma < 120\,\text{keV}$, as shown in Figure 6.4. Such calibrations demonstrate the absence of non-linear behavior in the ionization response of the Si detectors, allowing the calibration the energy response at SUF with the ^{137}Cs data to a high degree of accuracy.

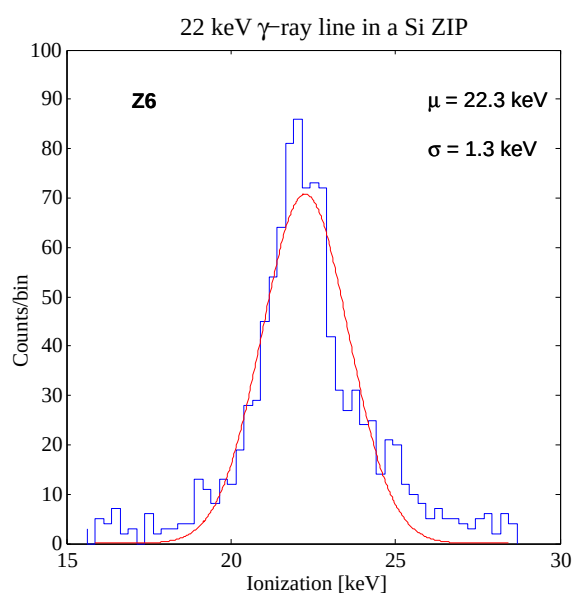

Figure 6.4: 22 keV peak in a Si ZIP ionization spectrum. This data was taken at a test facility where it is feasible to place a ^{109}Cd calibration source in close proximity to the detector.

6.1.3 The Phonon Channel

Unlike the ionization channel, the phonon channels are quite saturated, displaying some non-linearity by 662 keV. Consequently, they cannot be calibrated on their own merits at the beginning of the run. The calibration constants are obtained by normalizing the phonon response to the ionization channels, at low energies ($<$ 100 keV). As the run progressed, the 10 and 67 keV peaks became available in the Ge detectors and a direct calibration of the phonon channels became possible as is shown in Figure 6.5. Table 6.2 shows the equivalent quantities for the phonon

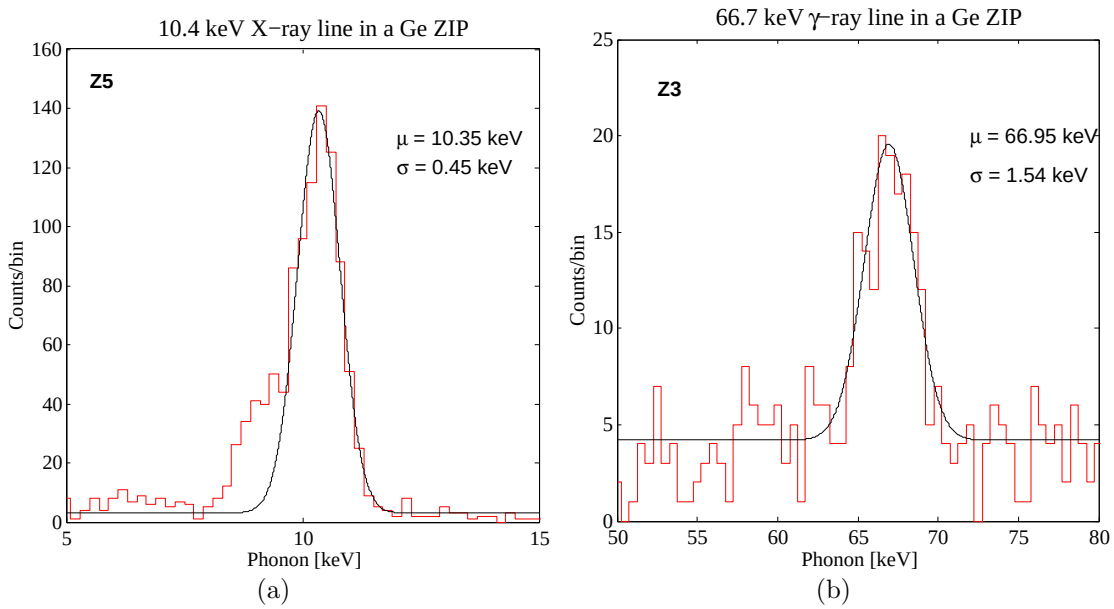

Figure 6.5: The lines in the phonon spectra at (a) 10 keVand (b) 67 keV establish the absolute energy scale in that channel as well as determining the linearity of phonon response.

channels as shown in Table 6.1

As with the ionization channel, directly calibrating the Si detectors remains elusive due to the lack of spectral lines. Instead we have to rely on equating the phonon response to the ionization response for electron recoil events from an extensive γ calibration. This can be done quite precisely with large statistic. The dominant error

Gamma Line [keV]	Measured Position [keV]	Width [keV]	Deviation [σ]
0	0	0.13	–
10.36	10.35	0.45	0.022
66.7	66.9	3.9	0.051

Table 6.2: Measured positions and widths of several lines in the phonon spectrum for one of the Ge detectors (Z5). The *Width* column quotes the 1σ Gaussian line width, while the *Deviation* column quotes the difference between the measured and actual position of the line in units of the line width.

on the phonon energy calibration, for the Si detectors, comes from the ionization energy calibration.

6.1.4 Energy Dependence of the Detector Noise

Figure 6.6 shows the baseline noise resolution[6] of the six detectors to be within 300–600 eV FWHM ($\sigma \sim$ 130–250 eV) for the phonon channels and $\sim$ 1 keV FWHM ($\sigma \sim$ 400 eV) for the ionization channels. As in most detectors, the noise in the phonon and ionization channels is energy dependent with a behavior as described in Equation 6.1 :

$$\Delta E_{rms} = \sqrt{\alpha^2 + \beta E + (\gamma E)^2} \tag{6.1}$$

Equation 6.1 reflects the fact that three independent sources contribute to the noise, and are thus added in quadrature :

- α : The baseline noise contribution arises from a combination of detector thermal fluctuations and readout circuit response.
- β : This term reflects Poisson counting fluctuations and thus scales as the square root of the relevant quantity, such as number of charge carriers.

[6]The baseline noise is the noise in the limit of zero deposited energy in the detector. It determines the smallest possible measurable signals and acceptable trigger thresholds.

- γ : This term, due to a systematic error in estimating a quantity such as a position dependent signal height, scales linearly with signal size.

Table 6.3 summarizes the measured detector resolutions at low energy ($E < 100\,\text{keV}$) for the ionization and phonon channels. The parameters α, β, and γ are obtained by fitting Equation 6.1 to the data, and are summarized in Table 6.4[7].

	Energy [keV]					
	0		10.4		66.7	
Detectors	Q	P	Q	P	Q	P
Z1	0.273	0.33	0.412	0.70	1.72	3.66
Z2	0.249	0.12	0.379	0.61	1.69	3.31
Z3	0.285	0.15	0.313	0.47	1.14	1.54
Z4	0.359	0.27	–	–	–	–
Z5	0.280	0.13	0.300	0.45	0.884	3.93
Z6	0.433	0.24	–	–	–	–

Table 6.3: Measured resolution of the ionization and phonon channels as a function of energy.

The dependence of the ionization and phonon channel resolution on energy is shown graphically in Figure 6.7. It can be seen that while the phonon channels have a lower baseline noise than the ionization channels, they have a stronger linear dependence on energy, performing slightly worse than the ionization resolution at energies above 10 keV. Although the variation of the W T_c over the surface of the detector would result in a strong linear dependence of the phonon resolution on energy, this effect is largely removed by the position dependent correction (as described in section 6.2). The remaining linear dependence of the resolution may arise from highly localized phenomena such as disconnected TESs and physical scratches on the detector surface or from a residual position dependence beyond the resolution of the

[7]The values are a result of a fit that only included the 0–67 keVpoints. The 662 keVdata point was ignored since its large *lever arm* effect would dominate the fit resulting in a fit that is only sensitive to the value of γ. This poses a problem since the gain setting used while taking the 662 keV data was different from that used for the low energy lines, and the absolute value of the gains are not known to within a few percent.

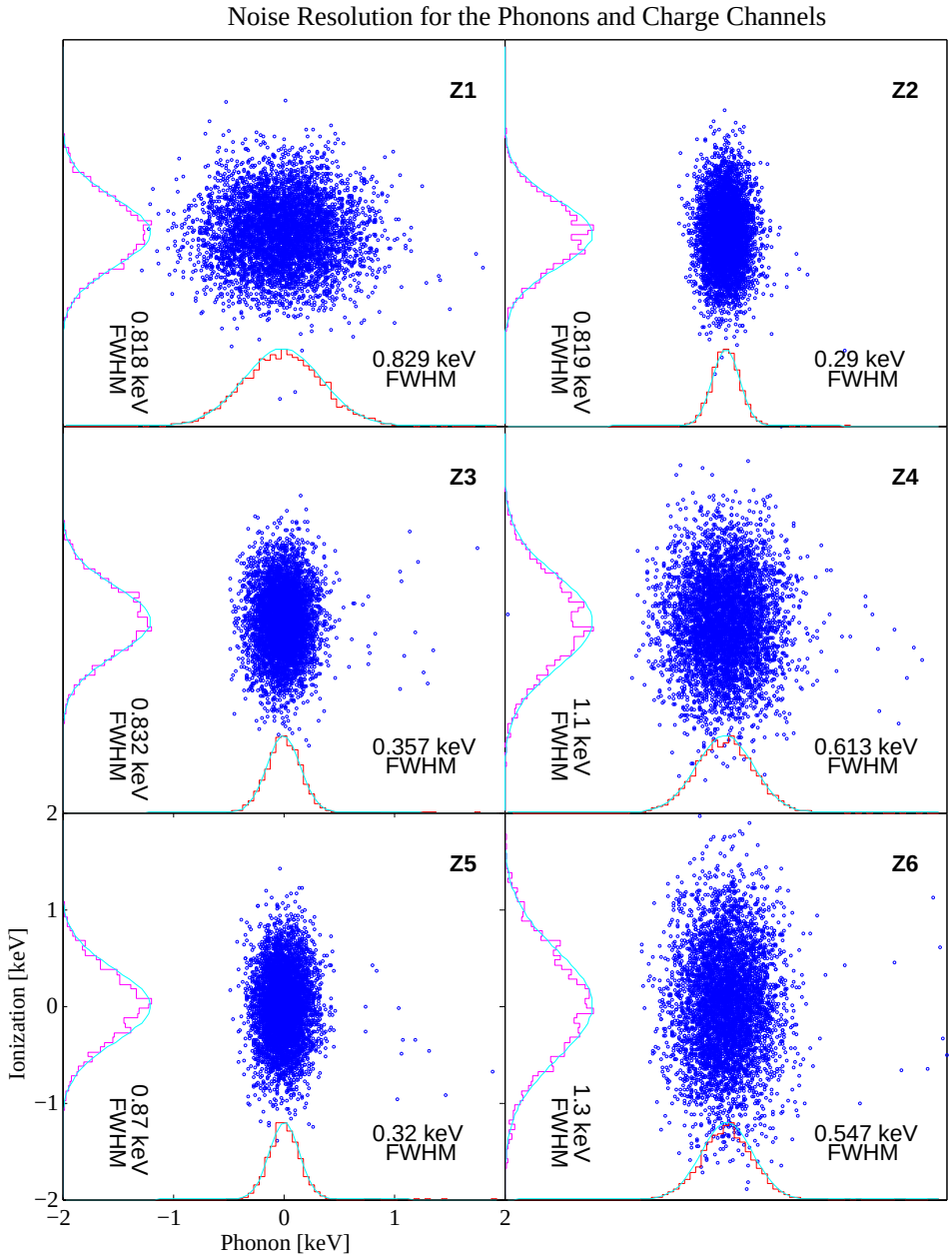

Figure 6.6: Baseline (or zero energy) noise resolution for the six detectors. The phonon and ionization responses are plotted on the x and y axes respectively. A projection onto either axis is fitted to a Gaussian shape in order to obtain the noise resolution.

	Ionization			Phonon		
Detectors	α	β	γ	α	β	γ
Z1	0.27	2.85×10^{-3}	2.5×10^{-2}	0.35	4.6×10^{-3}	5.4×10^{-2}
Z2	0.25	1.56×10^{-3}	2.5×10^{-2}	0.12	1.0×10^{-2}	4.8×10^{-2}
Z3	0.28	2.1×10^{-8}	1.6×10^{-2}	0.15	1.0×10^{-2}	2.4×10^{-2}
Z4	–	–	–	–	–	–
Z5	0.28	6.1×10^{-12}	1.2×10^{-2}	0.13	2.8×10^{-10}	5.3×10^{-2}
Z6	–	–	–	–	–	–

Table 6.4: Fit parameters for the ionization and phonon channel energy dependent resolution. α and β have units of keV, while γ is unitless. Values of $\beta \sim 10^{-8}$–10^{-12} are not meaningful, they simply reflect the coarseness of the minimization algorithm and are consistent with zero.

position dependence correction. The presence of a non-zero square root energy dependence for some of the phonon channels (Table 6.4) is somewhat puzzling since the number of individual participants in the phonon signal[8] is extremely large and thus the effects of statistical fluctuations is expected to be relatively small.

The magnitude of the three terms in the ionization noise are consistent with predictions based on understanding of the behavior of the ionization response and readout circuit. The baseline resolution is determined by the JFET gate noise, amplified by the various circuit elements (as shown in Figure 4.20). The β term is given theoretically by the following equation:

$$E_{rms} = \sqrt{\omega \epsilon E} \tag{6.2}$$

$$\beta = \omega \cdot \epsilon \tag{6.3}$$

where $\epsilon = 3.0$ (3.8) eV is the average energy required to create an electron-hole pair in Ge (Si) and $\omega \sim 0.1$ is the Fano factor, a term which quantifies the statistical fluctuations inherent in the creation of the charge carriers. Equation 6.3 predicts a value of $\beta = 0.3 \times 10^{-4}$, for E in keV. It is difficult to make a claim about the validity

[8] i.e. the phonons and quasiparticles which transfer the energy from the crystal to the sensor.

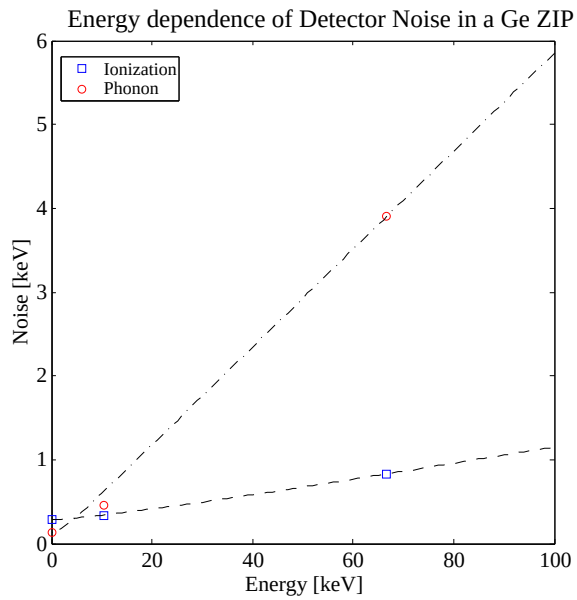

Figure 6.7: Phonon and ionization channel resolution as a function of energy.

of extrapolating the Fano factor[9] to temperatures of 20 mK due to the apparent variation of the value of β between the four Ge detectors. Finally, there appears to be a component to the ionization resolution that is linearly dependent on energy with a scaling factor of $\sim 1\%$.

6.2 Position Dependence

Most of the detectors in this run had T_c gradients across their surface of ~ 10 mK, with some as large as 30–40 mK. Such a variation in T_c results in a position dependent phonon signal height and a systematic error in the determination of an event's recoil energy and ionization yield. Other event parameters, such as the reconstructed position and energy partition, which are based on the phonon pulse start times and relative energy distributions are less sensitive to T_c variation than the pulse height and may be used, in conjunction with the ionization signal, to correct the phonon

[9]Traditionally not investigated below the temperature of liquid Nitrogen ($T = 77$ K).

energy response on an event by event basis. A method of correcting the phonon response as a function of event position , known as the phonon correction was developed and implemented by Blas Cabrera and Clarence Chang during Run 21. I will briefly describe the principles behind the technique since all of the data shown hereafter makes use of the phonon correction.

For each event the following variables are calculated :

X Delay / Y Delay These variables describe the x/y position of the interaction based on the arrival times (start times) of the phonon pulses. Figure 6.8(a) shows the reconstructed position from a uniformly illuminating γ-ray source.

X Partition / Y Partition These variables describe the energy partition amongst the four phonon channels. Figure 6.8(b) shows the partition distribution for the same events shown in Figure 6.8(a).

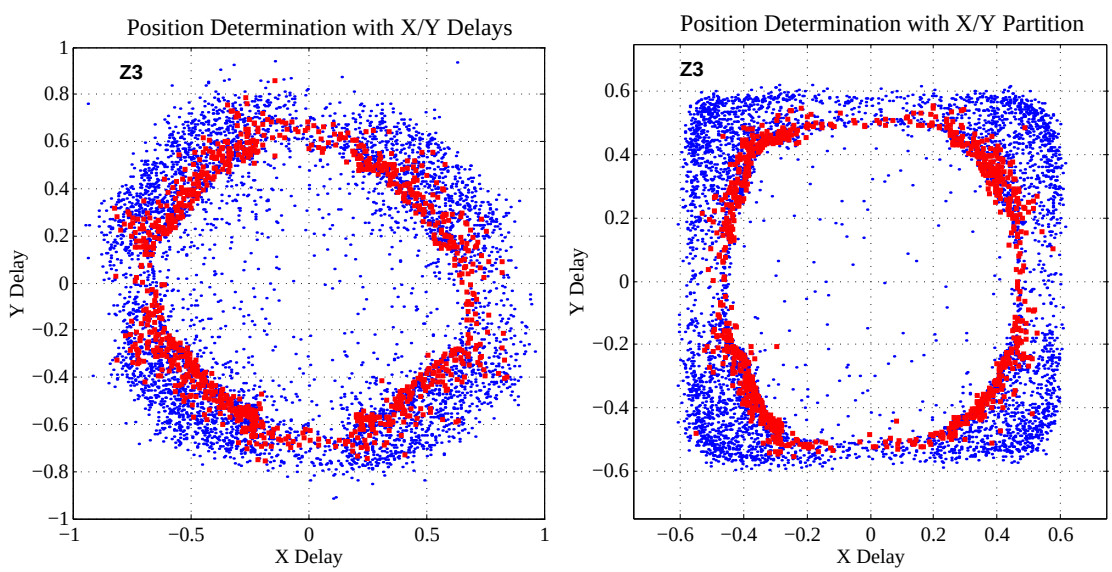

(a) (b)

Figure 6.8: Position determination with phonon delay (a) and partition (b).

Individually, both delay and partition space show a slight degeneracy in reconstructed event position (i.e. interactions at two different locations within a detector

may result in the same value of delay or partition. This degeneracy can be broken, however, by combining information from both the delay and partition parameters. Using the partition values as coordinates in an x-y plane and the magnitude of the delay values (i.e. $\sqrt{x_{del}^2 + y_{del}^2}$) as a z coordinate, the data points are mapped into a two dimensional manifold embedded in a three dimensional space. Figure 6.9 shows one slice of this *position* manifold. The degeneracy is evident by projecting the points onto the x-axis. Equally evident is the manner in which the manifold breaks the degeneracy that is present in the delay or partition parameters individually. Figure 6.10 shows a similar manifold for which the z coordinate corresponds to the phonon response (normalized to the ionization signal). The large spread in the z-axis shows the effect of T_c variation on the phonon signal response. It should be noted that the data shown in Figure 6.10 is taken from the detector with the worst T_c gradient. The variation in phonon response for the other five detectors is considerably less dramatic.

A correction value is then associated with each position in the manifold and ap-

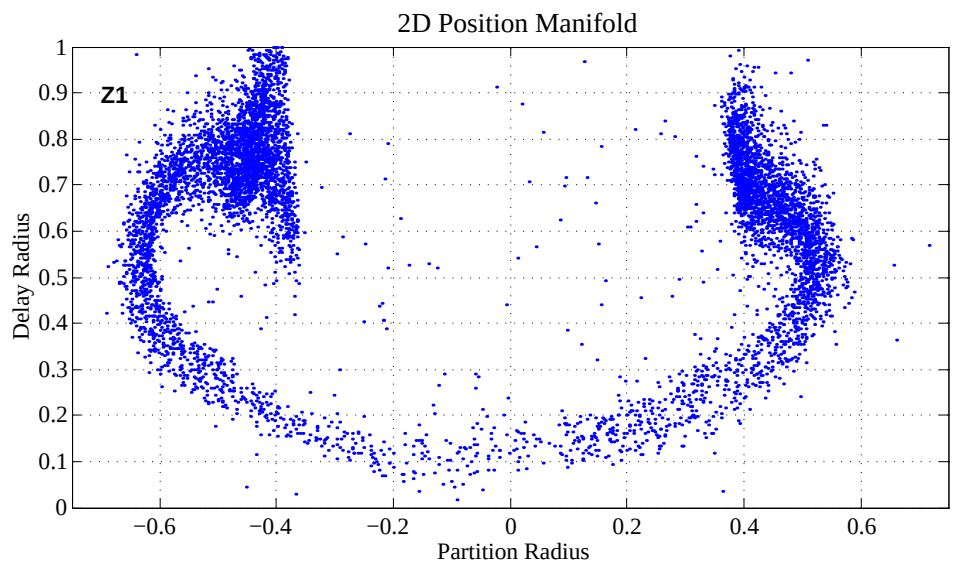

Figure 6.9: Event interaction position mapped onto a two dimensional manifold. The x-y coordinates are given by the phonon partition parameters while the z coordinate is the delay radius ($\sqrt{x_{del}^2 + y_{del}^2}$). Shown in this Figure is a slice of the manifold perpendicular to the x-y plane.

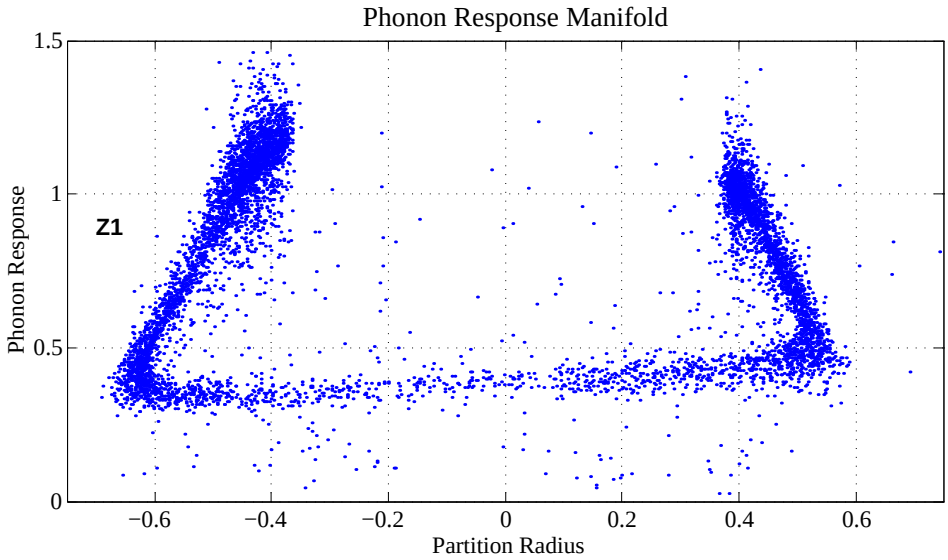

Figure 6.10: Phonon response as a function of position. The x-y coordinates are given by the phonon partition parameters while the z coordinate is the normalized phonon response. The large spread in the z-axis indicates the severity of the T_c gradient effect on the phonon response. The Figure shows data from the same slice shown in Figure 6.9.

plied on an event by event basis, resulting in a uniform phonon response. A similar procedure is applied to the phonon risetimes to remove any x-y position dependence in that variable.

6.3 Event Discrimination with the ZIPs

Once the phonon and ionization energy scales have been established, we proceed to determining the particle identification/discrimination as a function of energy. This is best demonstrated in Figure 6.11 which shows the ionization signal plotted against the phonon signal (referred to as 2D plots). The data points fall into two distinct populations, each of which lies along a line through the origin, but with different slopes. Simply put, event by event discrimination is determined by the ability to

identify to which population a particular event belongs. From Figure 6.11 it can be seen that event by event discrimination can easily be performed down to energies $\leq 10\,\text{keV}$.

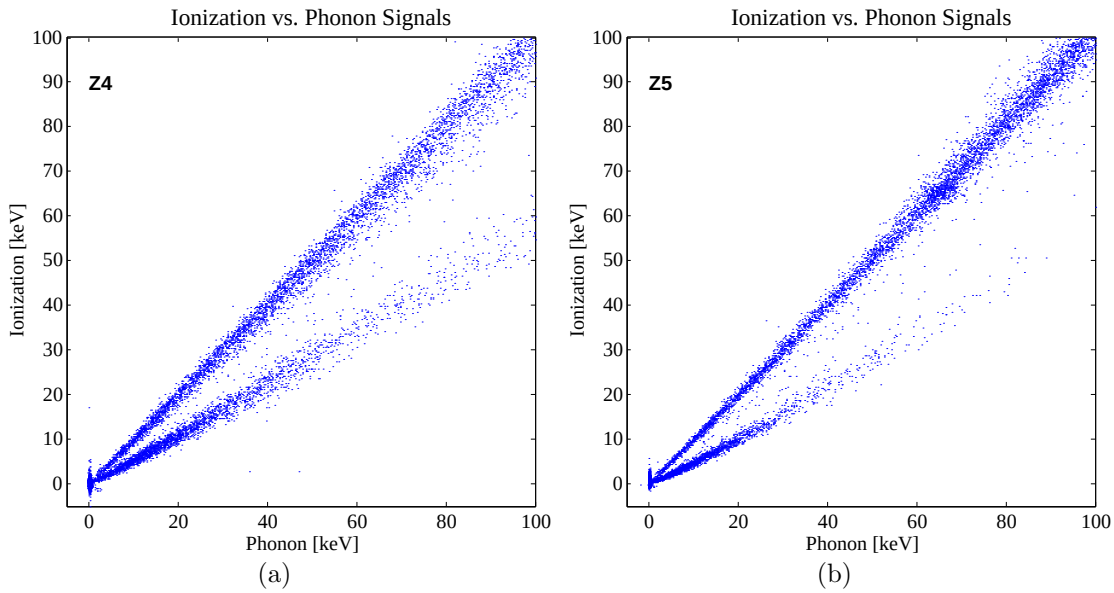

Figure 6.11: A 2D plot showing the ionization response as a function of phonon response for electron and nuclear recoils. Data taken with a Si detector is shown in (a), and a Ge detector in (b). The two populations, distinguishable to below 10 keV, are due to electron (steep slope) and nuclear (shallow slope) recoils.

An equally informative way of presenting the data is to plot the yield, defined as the ratio of ionization to recoil, as a function of recoil energy (referred to as a y plot). This is shown in Figure 6.12 for the same data presented in Figure 6.11. In this format, the data produces two populations with a roughly constant, but different value of yield as a function of recoil energy. This way of presenting the data allows an easier visual determination of the point (in recoil energy) at which discrimination starts to fail.

The following section describes how the performance of the discrimination parameter, and the energy range over which it is usable, is quantified.

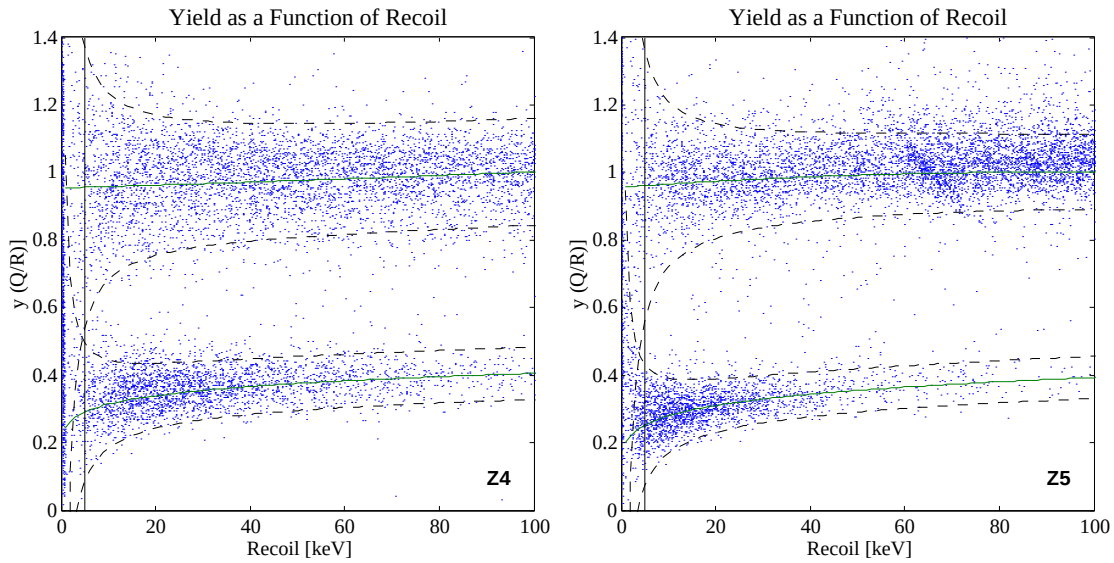

(a) (b)

Figure 6.12: A y plot showing yield as a function of phonon response for electron and nuclear recoils. Data taken with a Si detector is shown in (a), and a Ge detector in (b). In this representation, the electron recoil ($y \sim 1$) and nuclear recoil ($y \sim 0.3$) populations are seen to be distinct above $E_r \sim 5\,\text{keV}$, the position of the vertical solid line.

6.3.1 Determining the Electron and Nuclear Recoil Bands

The Electron Recoil Band

The behavior of the discrimination parameter (yield) for electron recoils is determined from extensive γ calibration data sets taken at the beginning, middle, and end of the experimental run. A ^{60}Co source produces 1.2 and 1.3 MeV γ's which result, after Compton scattering in the shielding and material surrounding the detectors, in a spectrum with a significant number of low energy (i.e. $E < 100\,\text{keV}$) events. Since we are primarily concerned with the energy region below 100 keV the data acquisition trigger was configured to reject event with energy larger than $\sim 100\,\text{keV}$. This allows us to collect events at roughly twice the normal rate since no DAQ deadtime is incurred by triggering on events of little interest.

Determination of the electron recoil band is made by slicing up the ^{60}Co calibration data into recoil energy bins. For each such slice the yield parameter is then histogrammed and fitted to a Gaussian as shown in Figures 6.13 and 6.14. In order to obtain an accurate representation of the behavior of the yield parameter it is necessary to apply some cuts to the data to remove spurious events and misleading populations of events. The cuts that were used to obtain Figures 6.13 and 6.14 are summarized below: full description given in section 6.5.

1. **Good Event** : A generic cut on variables such as χ^2 and baseline standard deviation, intended to remove pile-up events as well as those associated with periods of unstable electronics.

2. **Inner Electrode** : Defines a fiducial volume away from the edges of the crystal to ensure uniform ionization response.

3. **Muon Veto Anticoincident** : Rejects events associated with activity in the muon veto scintillators. This cut removes possible genuine nuclear recoil events whose presence would be mistaken for an artificially low discrimination performance.

4. **Single Scattered Event** : Requiring that no energy deposition is present in other detectors removes the possible effects of signal cross talk as well as eliminating a large fraction ($\geq 50\%$) of the population of surface β's which have a suppressed yield relative to bulk electron recoils.

The position of the electron recoil band mean is then parametrized as a second order polynomial in recoil:

$$y_{ER} = a + bE_r + cE_r^2 \tag{6.4}$$

with the parameters a, b, and c determined by a fit as shown in Figure 6.15 The 1σ width of the band is also parametrized as a function of recoil energy by fitting the product of the 1σ width and recoil to a first order polynomial as shown in Equation 6.5 (Figure 6.16)

$$\sigma(y_{ER})E_r = cE_r + d \tag{6.5}$$

Figure 6.17 shows the behavior of the electron recoil band mean of all six detectors. The actual errors on the mean are too small to be seen on this scale. Instead, the error bars shown in the figure correspond to the $\pm 1\sigma$ width of the Gaussian and are meant to give an impression of band edges. Finally, Figure 6.18 shows a y plot of the above mentioned data with the dashed lines representing $\pm 2\sigma$ limits.

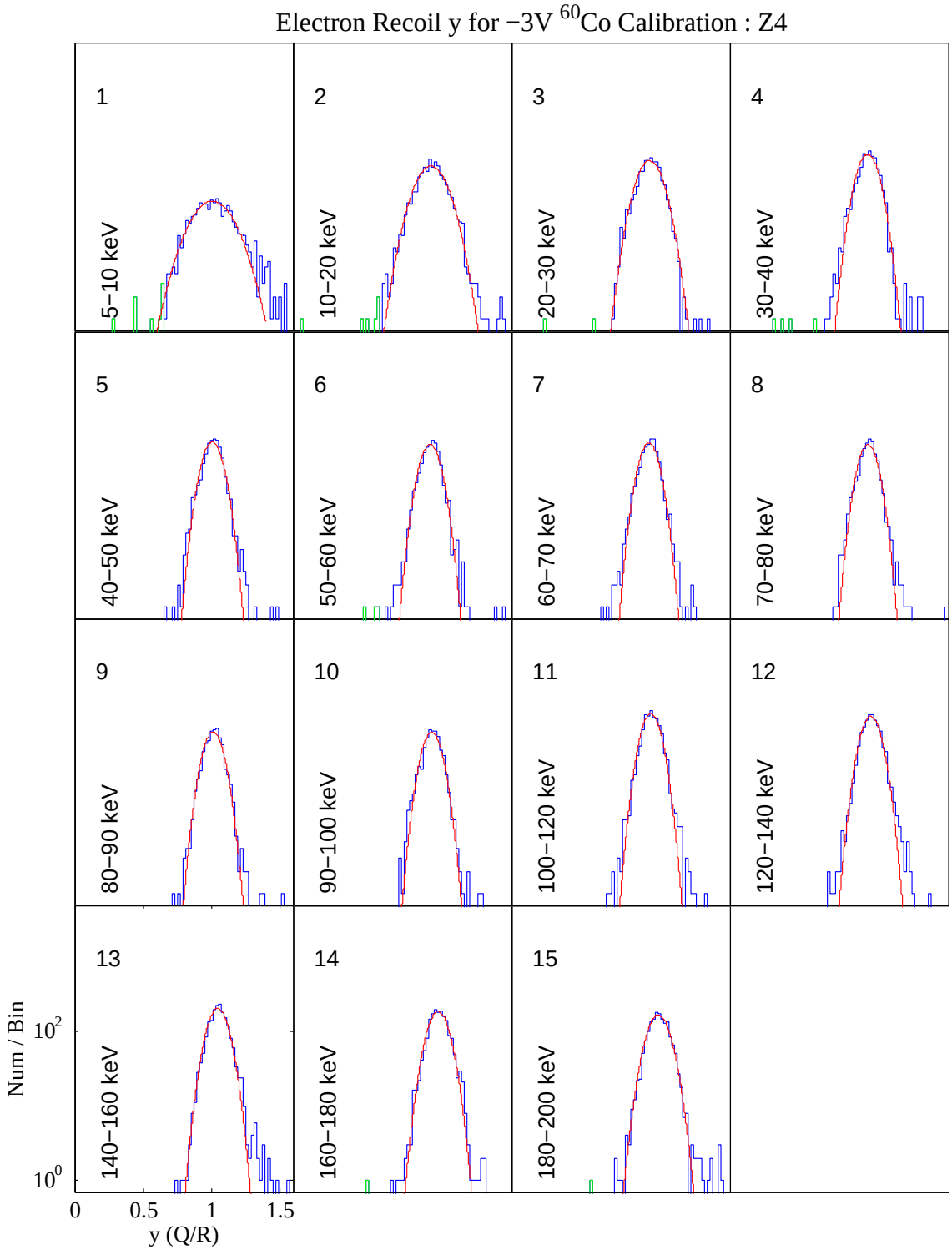

Figure 6.13: Electron recoil yield histograms for a Si ZIP from an external ^{60}Co calibration. The figure shows the yield parameter in various energy bins, histogrammed and fitted to a Gaussian.

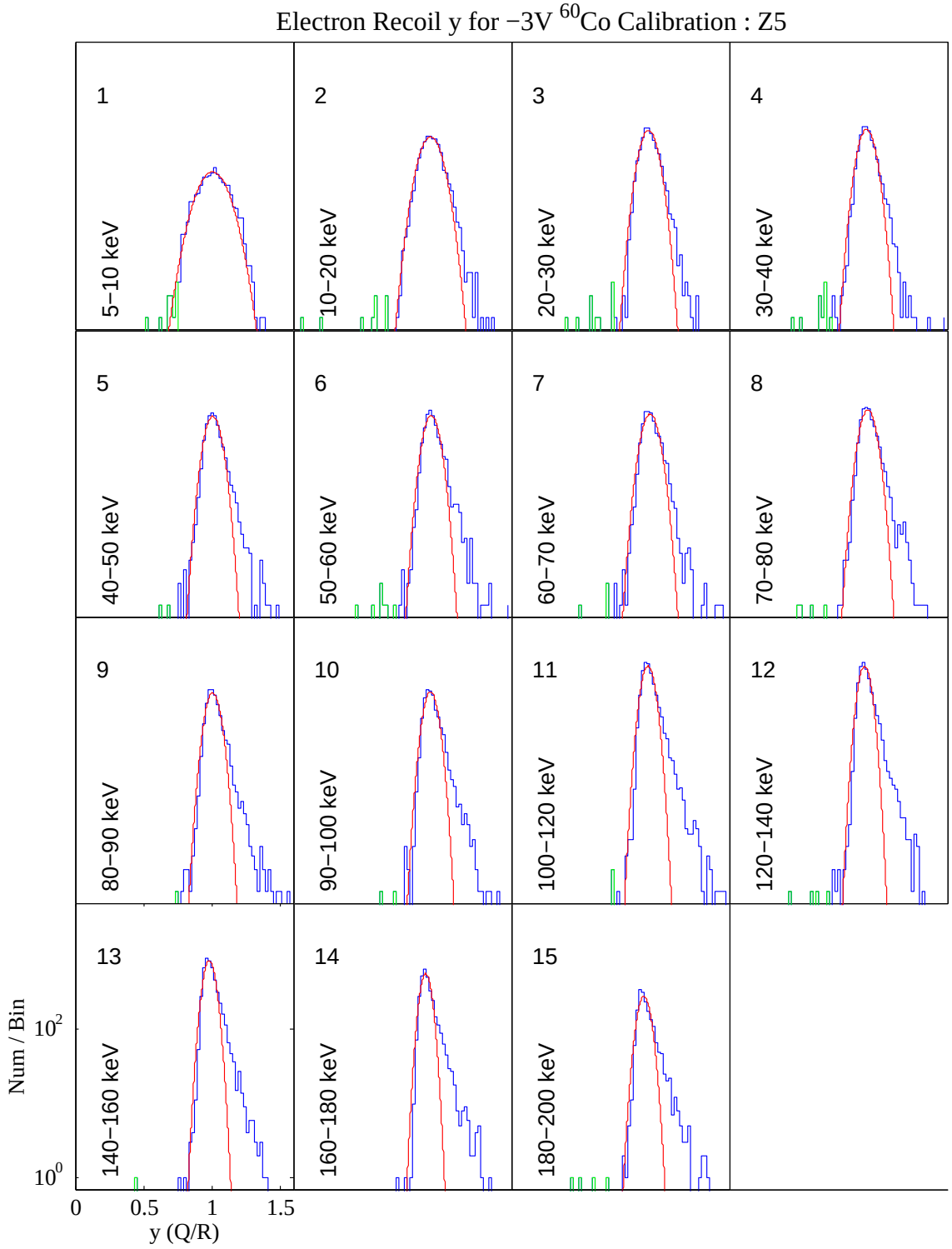

Figure 6.14: Electron recoil yield histograms for a Ge ZIP from an external ^{60}Co calibration. The figure shows the yield parameter in various energy bins, histogrammed and fitted to a Gaussian.

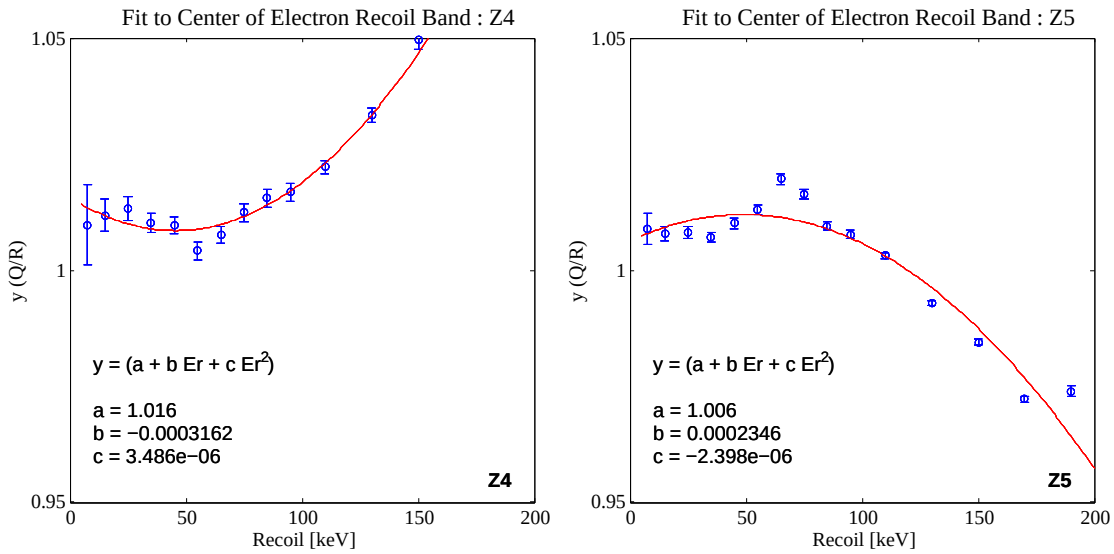

(a) (b)

Figure 6.15: Yield mean, as a function of recoil energy, for electron recoils. The electron recoil band is parametrized as a second order polynomial in recoil. Data from a Si ZIP are shown in (a) and a Ge ZIP in (b).

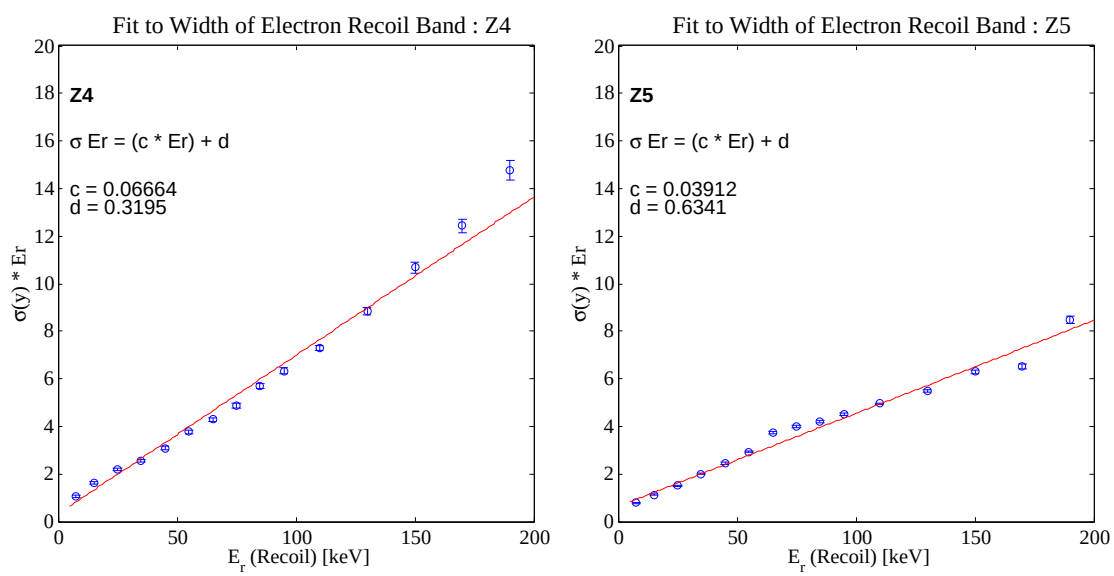

(a) (b)

Figure 6.16: Yield band width, as a function of recoil energy, for electron recoils. The product of band width and recoil energy is parametrized as a first order polynomial in recoil. Data from a Si ZIP are shown in (a) and a Ge ZIP in (b).

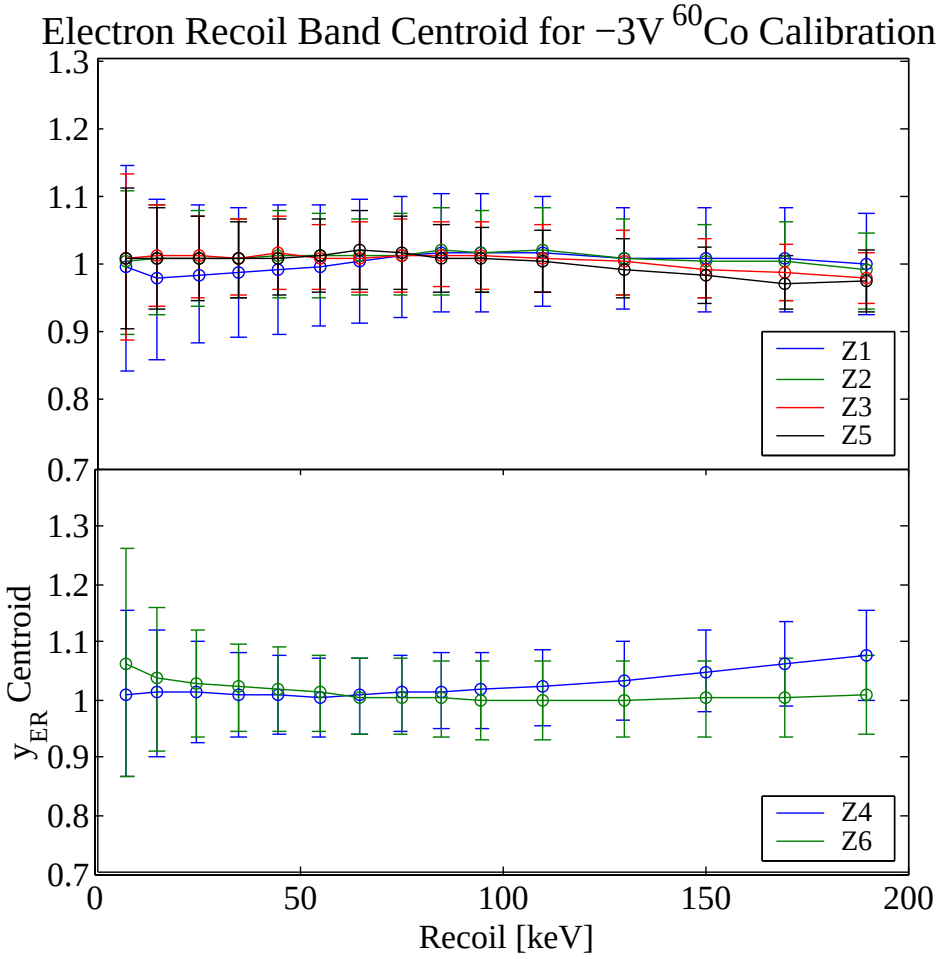

Figure 6.17: Comparison of electron recoil bands for all six detectors. Since the errors on the mean are too small to be seen on this scale the error bars are taken to indicate the 1σ width of the band. The top panel shows the four Ge detectors, while the bottom panel shows the two Si detectors.

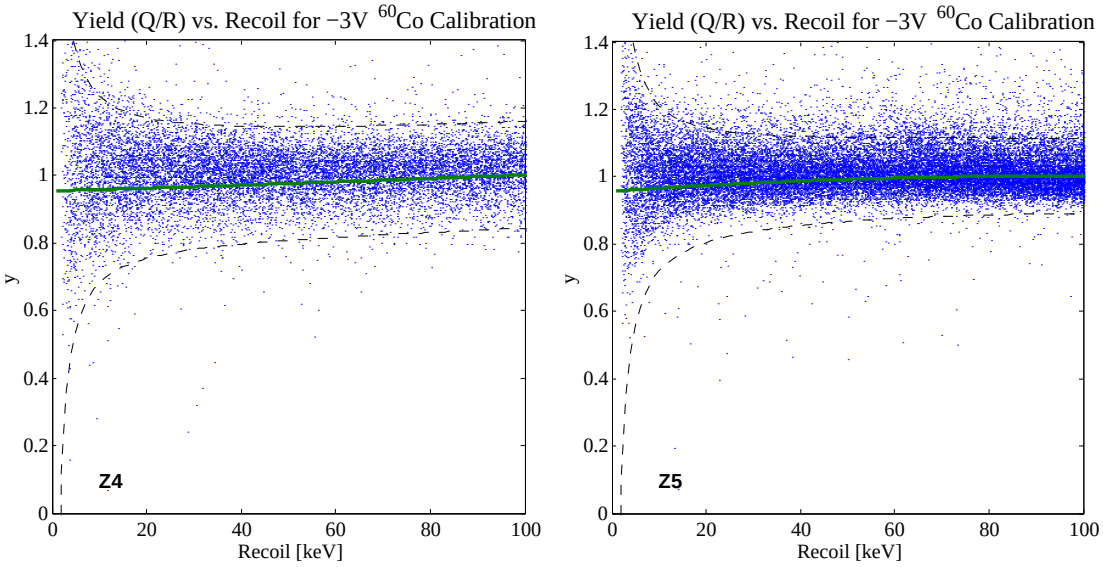

(a) (b)

Figure 6.18: y plots showing the electron recoil band for ^{60}Co data. The solid line indicates the mean of the band, while the dashed lines indicate the $\pm 2\sigma$ limits. Data from a Si ZIP is shown in (a) and from a Ge ZIP in (b).

The Nuclear Recoil Band

A similar procedure was used to determine the yield distribution for nuclear recoils. Two calibrations with a ^{252}Cf source were performed, one at the beginning of, and one at the end of the run. Figures 6.19 and 6.20 show the yield parameter for a Si and a Ge detector histogrammed and fitted to a Gaussian in various energy bins. The same cuts were used on this data as for the ^{60}Co calibration with the exception of the muon veto cut, which was relaxed. Since the ^{252}Cf calibration is performed with the source outside the muon scintillator perimeter a large fraction of the desired events trigger the muon veto. Rejecting events on this basis results in a $\sim 50\%$ depletion of the collected statistics.

The position of the nuclear recoil band mean is parametrized as a two parameter power law, according to [43] [42], as shown in Equation 6.6 and Figure 6.21

$$y_{NR} = \left(aE_r^b\right)/E_r \tag{6.6}$$

The 1σ width of the band is parametrized as a function of ionization signal by fitting the product of the 1σ width and recoil to a first order polynomial as shown in Equation 6.7 and Figure 6.22

$$\begin{aligned} \sigma(y_{NR})E_r &= c(aE_r^b) + d \\ &\equiv cQ + d \end{aligned} \tag{6.7}$$

As for the electron recoil band, the mean of the histogram is plotted as a function of recoil in Figure 6.23. The error bars shown in the figure correspond to the 1σ width of the Gaussian and are meant to give an impression of edges of the band since the errors on the mean are too small to be seen on this scale. Finally, Figure 6.24 shows a y plot of the above mentioned data with the dashed lines representing $\pm 2\sigma$ limits.

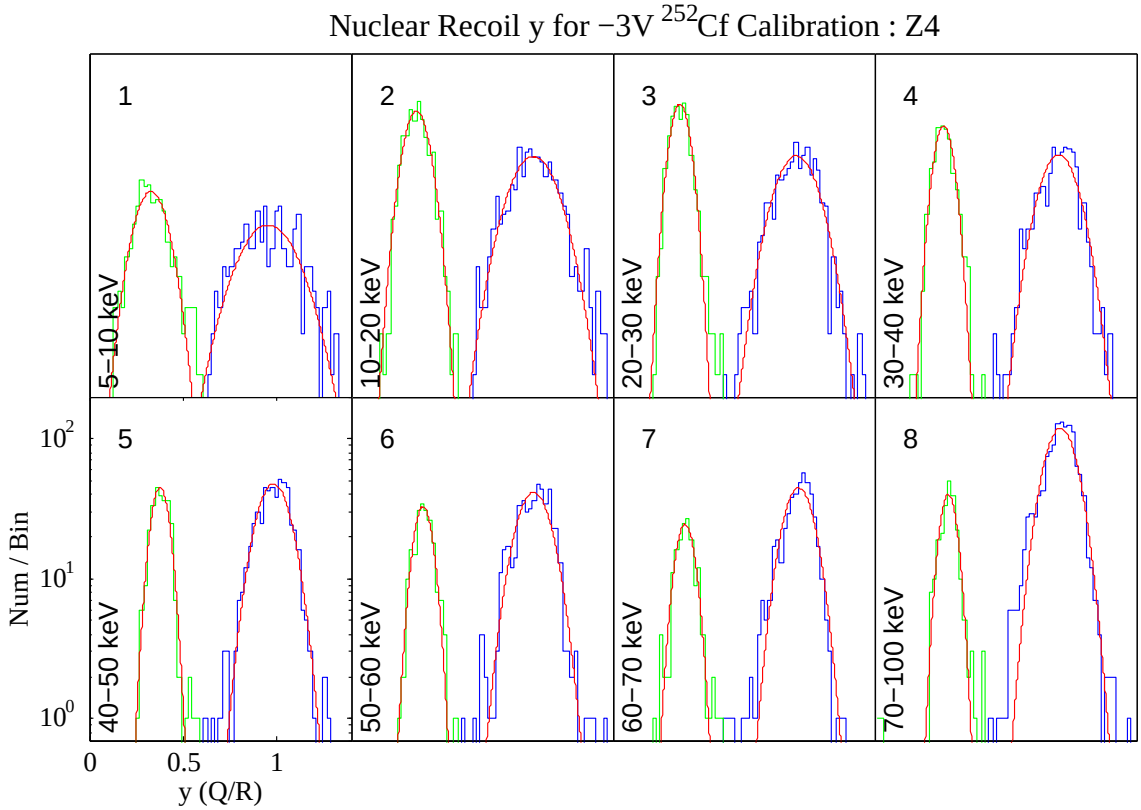

Figure 6.19: Nuclear recoil yield histograms for a Si ZIP. The figure shows the yield parameter in various energy bins, histogrammed and fitted to a Gaussian. Two peaks are seen, the left (low y) corresponding to nuclear recoils and the right (high y) to electron recoils.

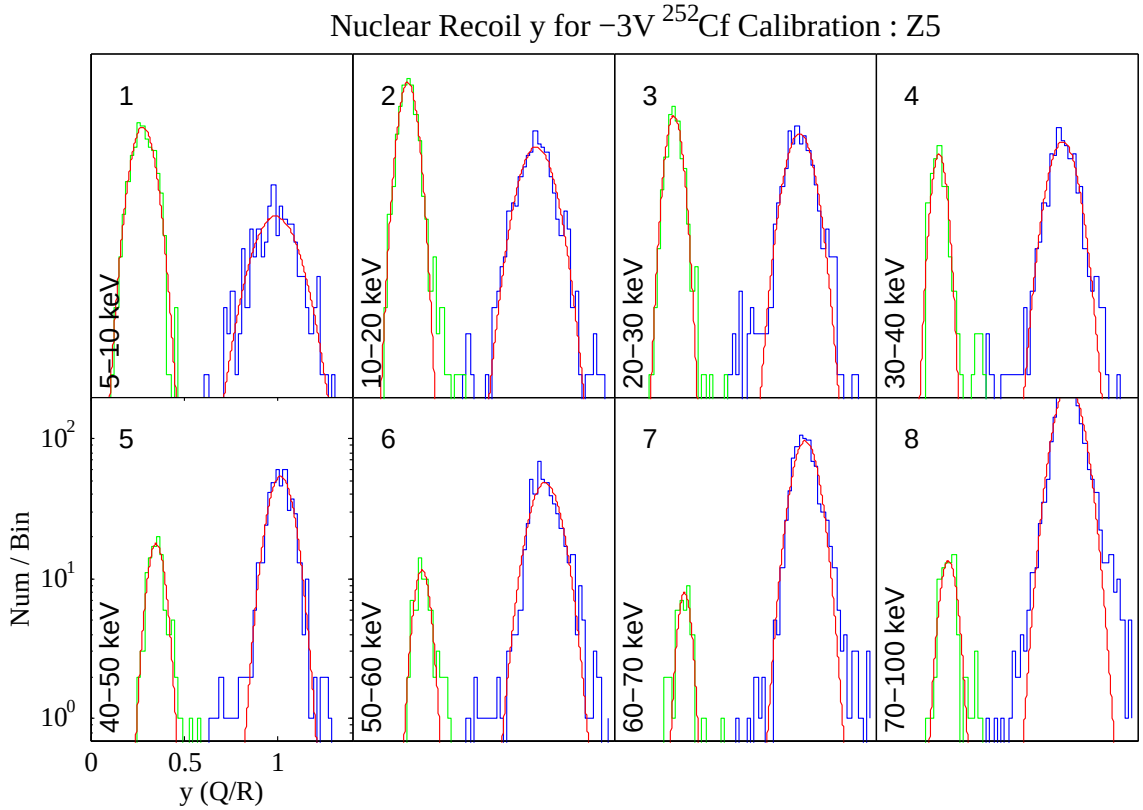

Figure 6.20: Nuclear recoil yield histograms for a Ge ZIP. The figure shows the yield parameter in various energy bins, histogrammed and fitted to a Gaussian. Two peaks are seen, the left (low y) corresponding to nuclear recoils and the right (high y) to electron recoils.

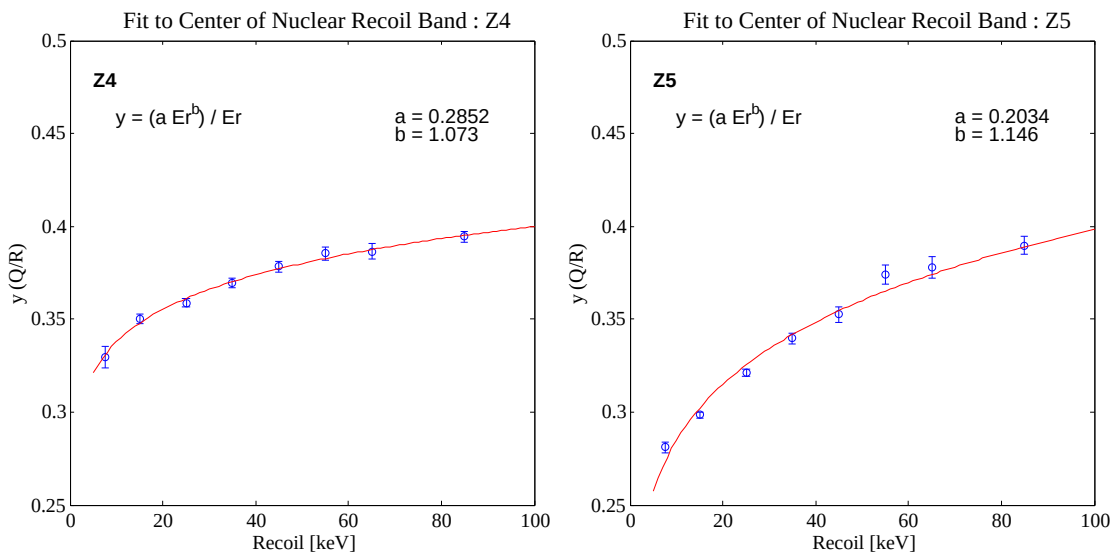

(a) (b)

Figure 6.21: Yield mean, as a function of recoil energy, for nuclear recoils. The nuclear recoil band is parametrized as a power law in recoil. Data from a Si ZIP are shown in (a) and a Ge ZIP in (b).

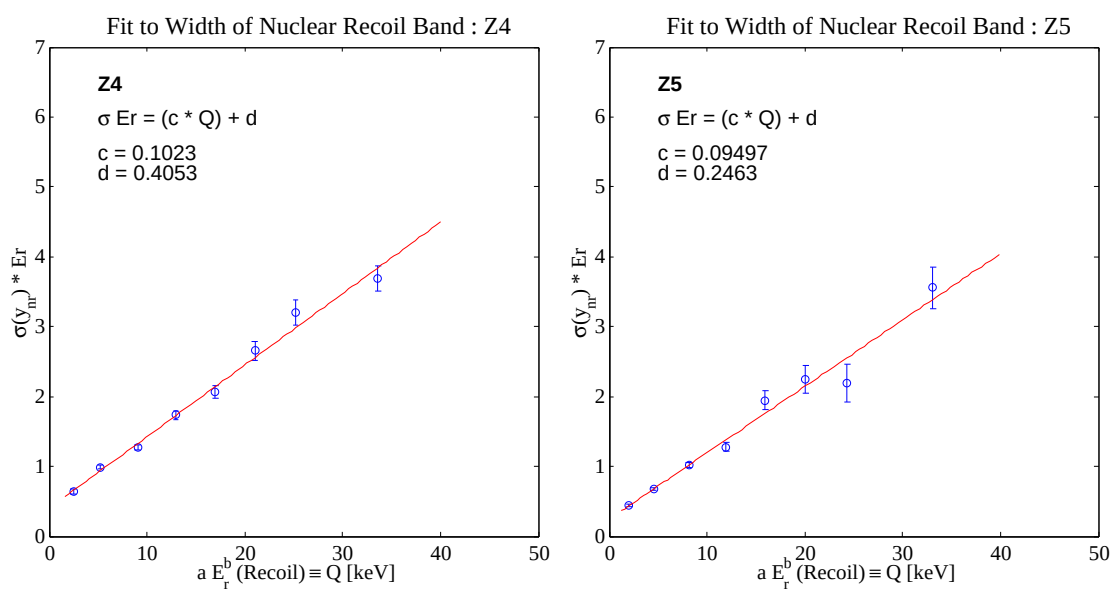

(a) (b)

Figure 6.22: Yield band width, as a function of recoil energy, for nuclear recoils. The product of band width and recoil energy is parametrized as a first order polynomial in ionization. Data from a Si ZIP are shown in (a) and a Ge ZIP in (b).

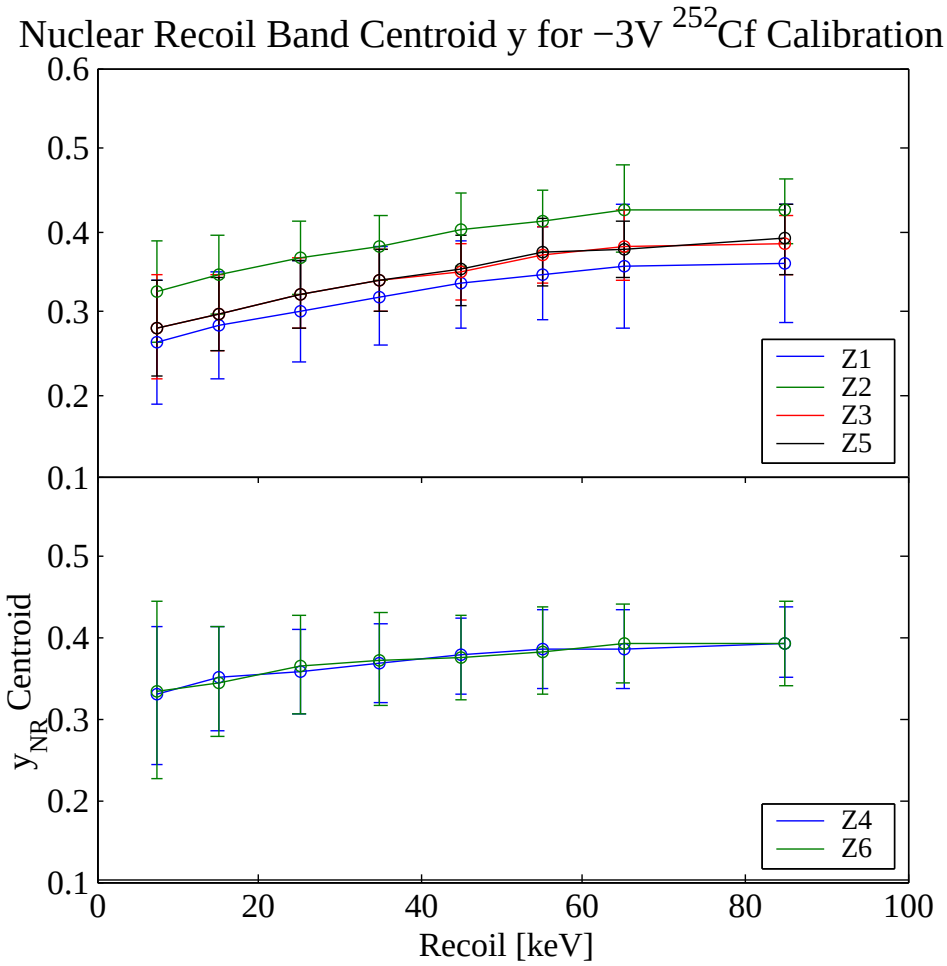

Figure 6.23: Comparison of nuclear recoil bands for all six detectors. Since the errors on the mean are too small to be seen on this scale the error bars are taken to indicate the 1σ width of the band. The top panel shows the four Ge detectors, while the bottom panel shows the two Si detectors.

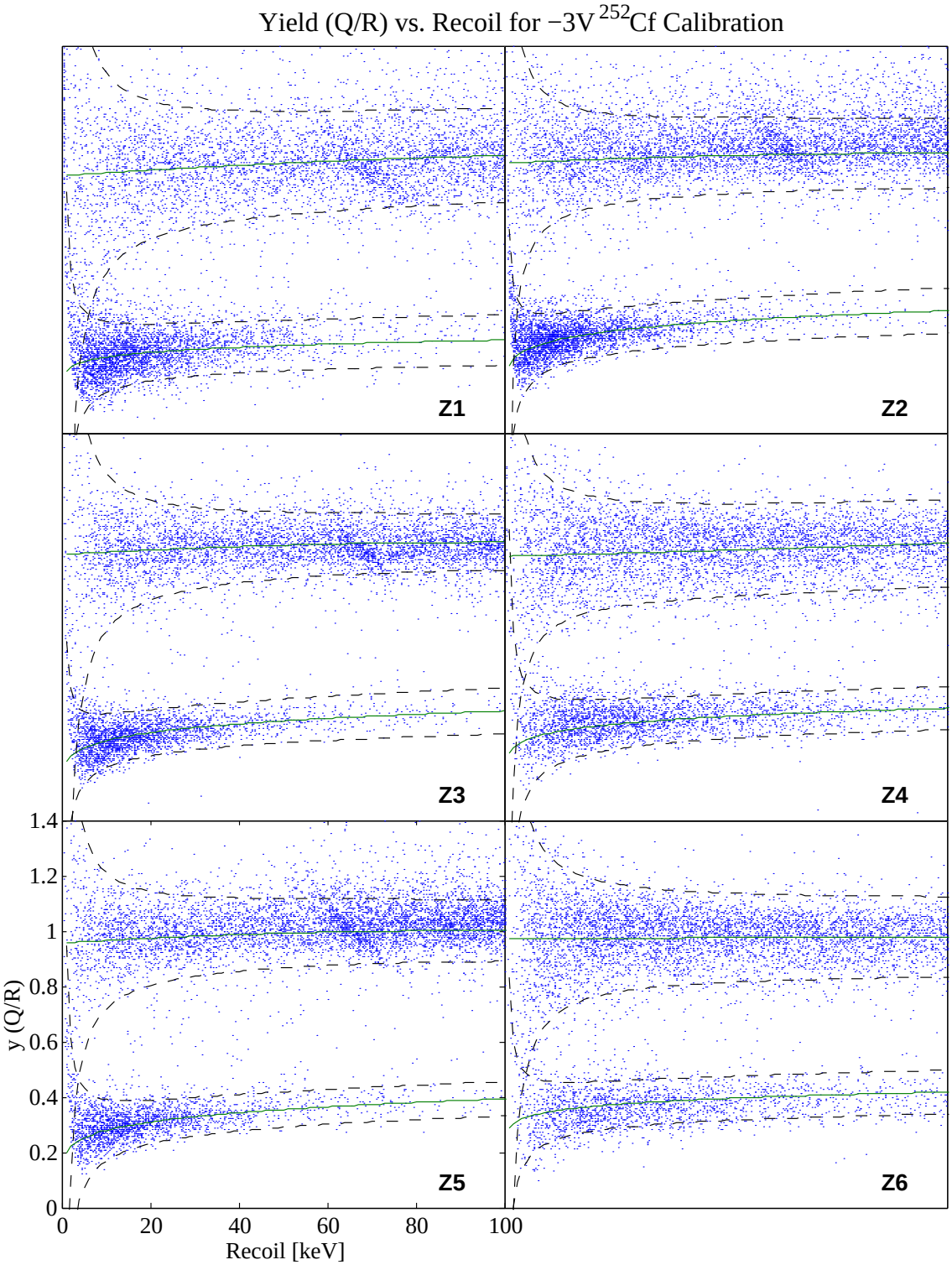

Figure 6.24: y plots showing the nuclear recoil band for ^{252}Cf data. The solid line indicates the mean of the band, while the dashed lines indicate the $\pm 2\sigma$ limits.

6.3.2 Determining the Gamma Discrimination

Electron recoil discrimination (also referred to as γ leakage) is defined as the fraction of electron recoils with sufficiently low yield as to fall within the 2σ bounds of the nuclear recoil band. Figures 6.25 and 6.26 show yield histograms, for different slices in energy, of the ^{60}Co calibration data after application of the cuts described in section 6.3.1. The number of events within the nuclear recoil 2σ region are summed up and a 90% confidence level, lower limit of the electron recoil rejection value is estimated according to Equation 6.8

$$1 - \text{Rejection} = \frac{\text{N90(\# of misidentified events)}}{\text{Total \# of events}} \tag{6.8}$$

where N90(x) refers to the 90% confidence level upper bound on x observed events.

The discrimination values in each energy bin for the six detectors are given in Table 6.5. It is important to note that the majority of the energy bins represented in Table 6.5 did not contain a single misidentified electron recoil. The finite value quoted for the discrimination is simply a result of the fact that the 90% confidence level upper bound on zero observed events, for a Poisson process, is 2.3 possible events. As the size of the calibration data set increases (and thus the denominator in Equation 6.8), the measured value of the discrimination will improve (as long as no misidentified events are observed) since the value of possible leaked events will remain fixed at 2.3. This is the reason why the discrimination value of the 5–100 keV bin appears to be significantly better than that of the individual energy bins.

	Detector						
Energy [keV]	**Z1**	**Z2**	**Z3**	**Z4**	**Z5**	**Z6**	**Z2-Z5**
0–5	2.68%	1.50%	1.84%	1.56%	0.95%	1.23%	0.36%
5–10	2.21%	0.47%	0.82%	0.90%	0.19%	0.66%	0.30%
10–20	0.66%	0.13%	0.28%	0.15%	0.088%	0.30%	0.053
20–30	0.44%	0.13%	0.16%	0.16%	0.088%	0.25%	0.032
30–40	0.17%	0.13%	0.17%	0.35%	0.090%	0.13%	0.072
40–50	0.14%	0.13%	0.17%	0.16%	0.090%	0.15%	0.033
50–60	0.12%	0.14%	0.29%	0.17%	0.089%	0.18%	0.057
60–70	0.14%	0.13%	0.17%	0.17%	0.080%	0.15%	0.033
70–80	0.10%	0.13%	0.16%	0.18%	0.075%	0.12%	0.032
80–90	0.16%	0.13%	0.16%	0.18%	0.072%	0.13%	0.031
90–100	0.066%	0.12%	0.15%	0.18%	0.071%	0.14%	0.030
5–100	**0.23%**	**0.023%**	**0.060%**	**0.069%**	**0.0087%**	**0.12%**	**0.022**

Table 6.5: Electron recoil discrimination, at 90% confidence level, in the ZIP detectors as a function of energy. Discrimination is defined as the fraction of electron recoil events that appear within the $\pm 2\sigma$ nuclear recoil band. The final column shows the discrimination obtained by summing up the events in the inner four detectors. Overall, the values listed in this table indicate that fewer than 1 electron recoil event out of 1000 is misidentified.

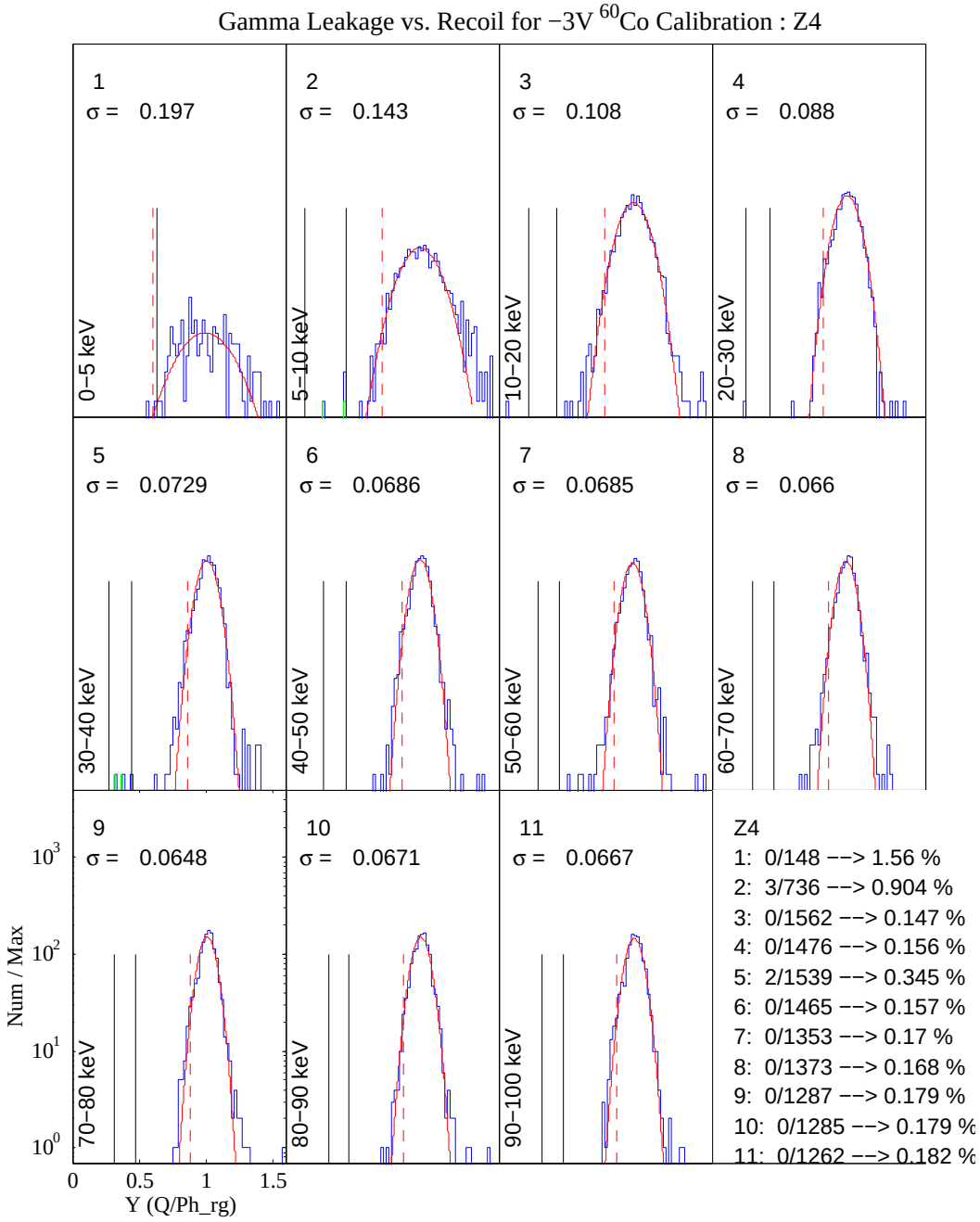

Figure 6.25: Electron recoil misidentification in a Si ZIP. Histograms of yield are shown for various energy bins. The solid vertical lines denote the nuclear recoil $\pm 2\sigma$ region, while the vertical dashed line denotes the electron recoil -2σ limit. Electron recoil discrimination is given by the number of misidentified events that fall within the nuclear recoil region. The electron recoil discrimination values are shown in the lower right corner

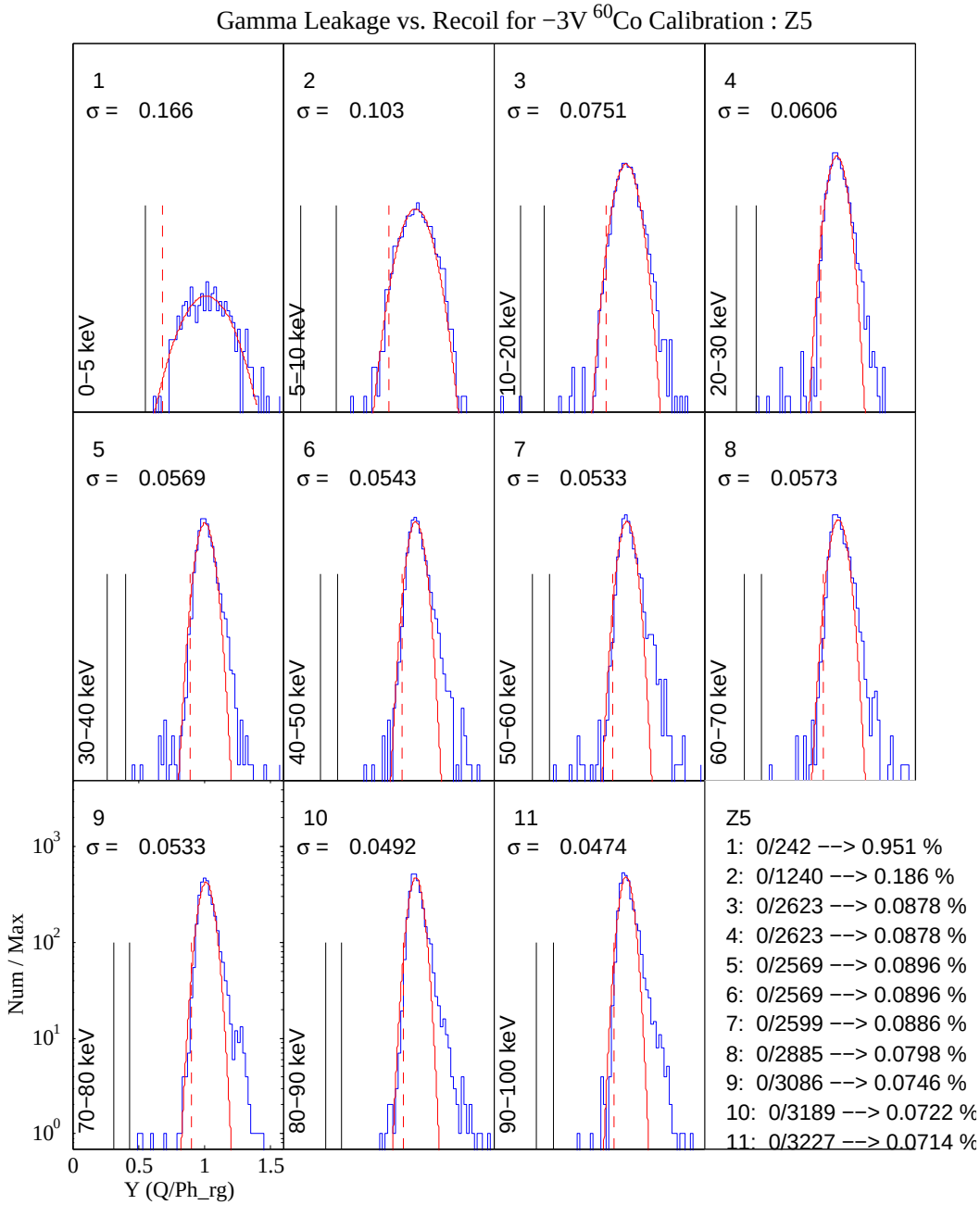

Figure 6.26: Electron recoil misidentification in a Ge ZIP. Histograms of yield are shown for various energy bin. The solid vertical lines denote the nuclear recoil $\pm 2\sigma$ region, while the vertical dashed line denotes the electron recoil -2σ limit. Electron recoil discrimination is given by the number of misidentified events that fall within the nuclear recoil region. The electron recoil discrimination values are shown in the lower right corner

6.4 Surface Electron Recoils and the Risetime Effect

6.4.1 Yield distribution of Betas

As described in section 4.3, events occurring near the surface of a detector suffer from a suppressed ionization signal. As a result there is a larger probability for such electron recoils to be misidentified than there is for bulk recoils. Although gammas have a non-zero chance of interacting sufficiently close to the surface, the fraction of such events is small. There is a class of electron recoils, however, that occurs predominantly at the surface, namely incident electron (β) interactions.

Calibrating the detector response to β's is a very challenging task because β's are not penetrating particles[10]. Therefore, it is required that the β calibration source be placed alongside the detector, within the cryogenic volume. Such a setup has the possibility of contaminating the detectors with the radioactive atoms, due to the response of the source to the stresses of vacuum and cryogenic cycling. An ideal β calibration source would then be external to the cryogenic volume and capable of being inserted and removed at will (the same requirements as for a γ source). It was discovered that such a source does exist in the form of the ^{60}Co calibration. After the first extensive ^{60}Co calibration was performed it became apparent that a small number of events ($\sim 0.7\%$) were due to surface β interactions. These events are generated by electrons ejected from the surface of a detector (or surrounding material such as Cu) by an interacting γ. The β's then impinge on the nearest detectors and, due to the large probability of back scattering, may bounce bounce back and forth several times, depositing energy in two neighboring detectors. This mechanism suggests that the subset of events characterized by nearest neighbor multiple scatters should contain a significantly larger fraction of β's, and thus low yield events, than the subset of single scatter events.

[10] In the energy range of interest : $E_r < 100\,\mathrm{keV}$

Figures 6.27 and 6.28 show the yield distribution for the following three classes of events :

1. **All** : All events from the ^{60}Co calibration passing a set of minimal cuts.
2. **Nearest Neighbor** : Events in which there was a simultaneous interaction in a detector immediately above/below the detector in question.
3. **Single Scatter** : Events in which the only measurable interaction occurred in the detector in question.

All three event classes had the following cuts in common : **Good Event**, **Inner Electrode**, and **Muon Anticoincident**. It is clear from Figures 6.27 and 6.28 that the prominent low yield tail is present primarily in the Nearest Neighbor data set. Further evidence that these low yield events are due to β's rather than a non-Gaussian tail in the electron recoil band is presented in Figure 6.29. This figure shows the yield of an event in a given detector versus the yield observed in a second detector. This manner of plotting the data necessarily selects multiple-scatter events, but without a nearest neighbor requirement. The same set of cuts mentioned above are made, with the added requirement that the energy of the event fall within $10 < E_r(\,\mathrm{keV}) < 100$ in both detectors.

The data plotted in Figure 6.29 can be divided into three classes based on their position in the plot : events with high yield in both detectors (top right corner), events with high yield in one detector and low yield in the other (forming a horizontal or a vertical line from the top right corner), and events with low yield in both detectors (along the diagonal, toward the bottom left corner). The tell-tale sign that the low yield events are due to β's is the disappearance of the mid-y – mid-y population in non- neighboring detectors. Empirically, betas are defined as events with a yield more than 3σ away (to the lower side) from the electron recoil band and 2σ above the nuclear recoil band. Figure 6.30 highlights, in a y plot, the distribution of the ^{60}Co betas and graphically illustrates the concern that they pose with regards to contributing to the nuclear recoil background.

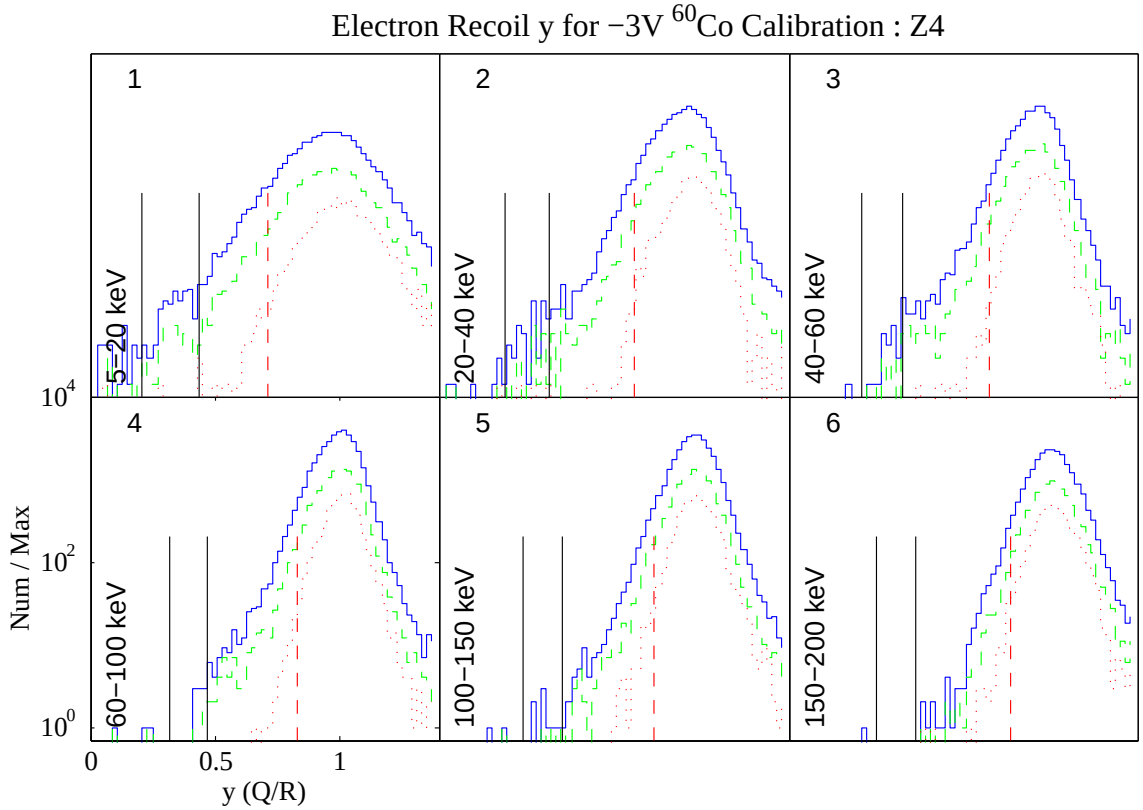

Figure 6.27: Yield distribution of a β rich sample in a Si ZIP. The solid line is a histogram of yield for all ^{60}Co events passing cuts. The dashed line corresponds to events for which there was a simultaneous interaction in a neighboring detector and is representative of a β population. The dotted line corresponds to events in which no interaction is seen in any other detector.

Given that there may exist a β population in the Dark Matter data set against which discrimination is less effective that for bulk electron recoils, the ability to estimate the resulting number of misidentified events becomes quite important. Figures 6.31 and 6.32 show one such attempt at quantifying the rate of these *leaked* events. The low yield tail due to the β population appears to be well described by an exponential function in yield. With a functional form for the β distribution in hand the number of events expected in the nuclear recoil band can be calculated as a function of the number of events in a given yield bin (chosen to be sufficiently distant

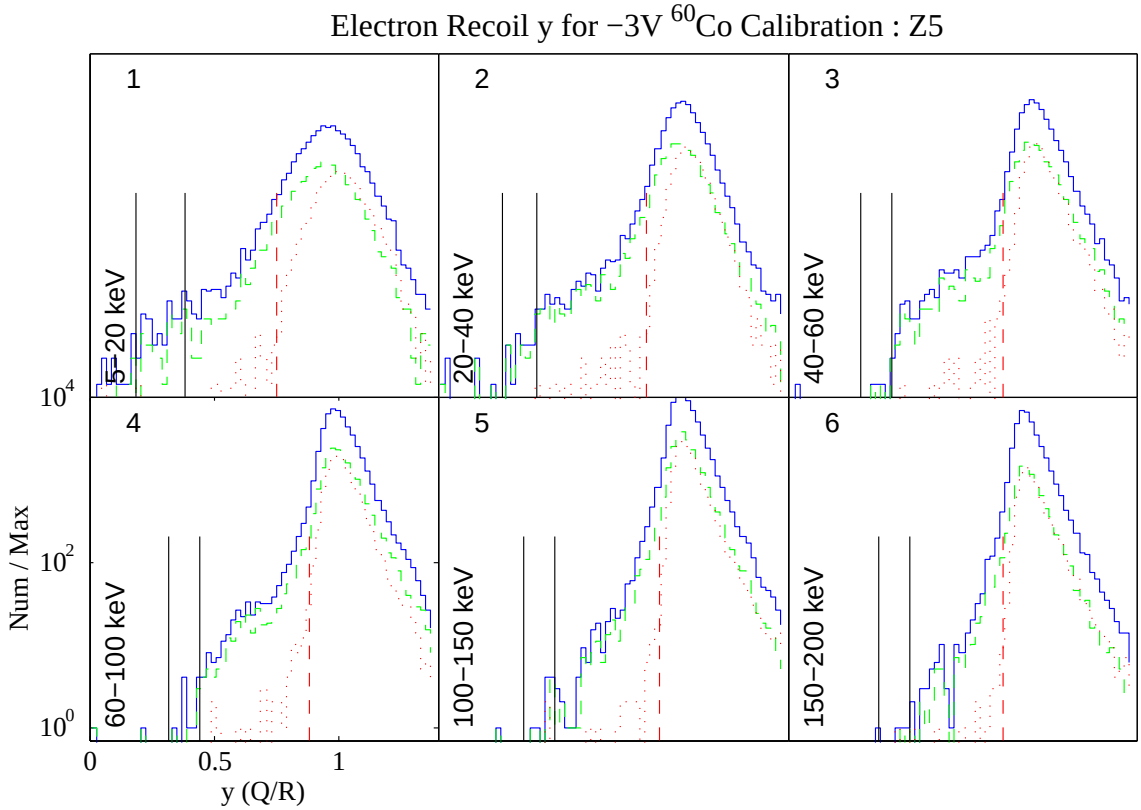

Figure 6.28: Yield distribution of a β rich sample in a Ge ZIP. The solid line is a histogram of yield for all ^{60}Co events passing cuts. The dashed line corresponds to events for which there was a simultaneous interaction in a neighboring detector is representative of a β population. The dotted line corresponds to events in which no interaction is seen in any other detector.

from the electron or nuclear recoil bands). These results are summarized in Table 6.6, where the entries reflect, in percent, the number of leaked events, normalized to the y=0.7 bin.

Recent results (shown in Figure 6.33) from a Monte Carlo simulation of a ^{60}Co calibration show remarkable agreement with the data on the shape of the low y tail from surface electron recoils. As these studies are pursued further, our understanding of the yield distribution of various populations of events will reduce the sensitivity of the Dark Matter search to unexpected backgrounds.

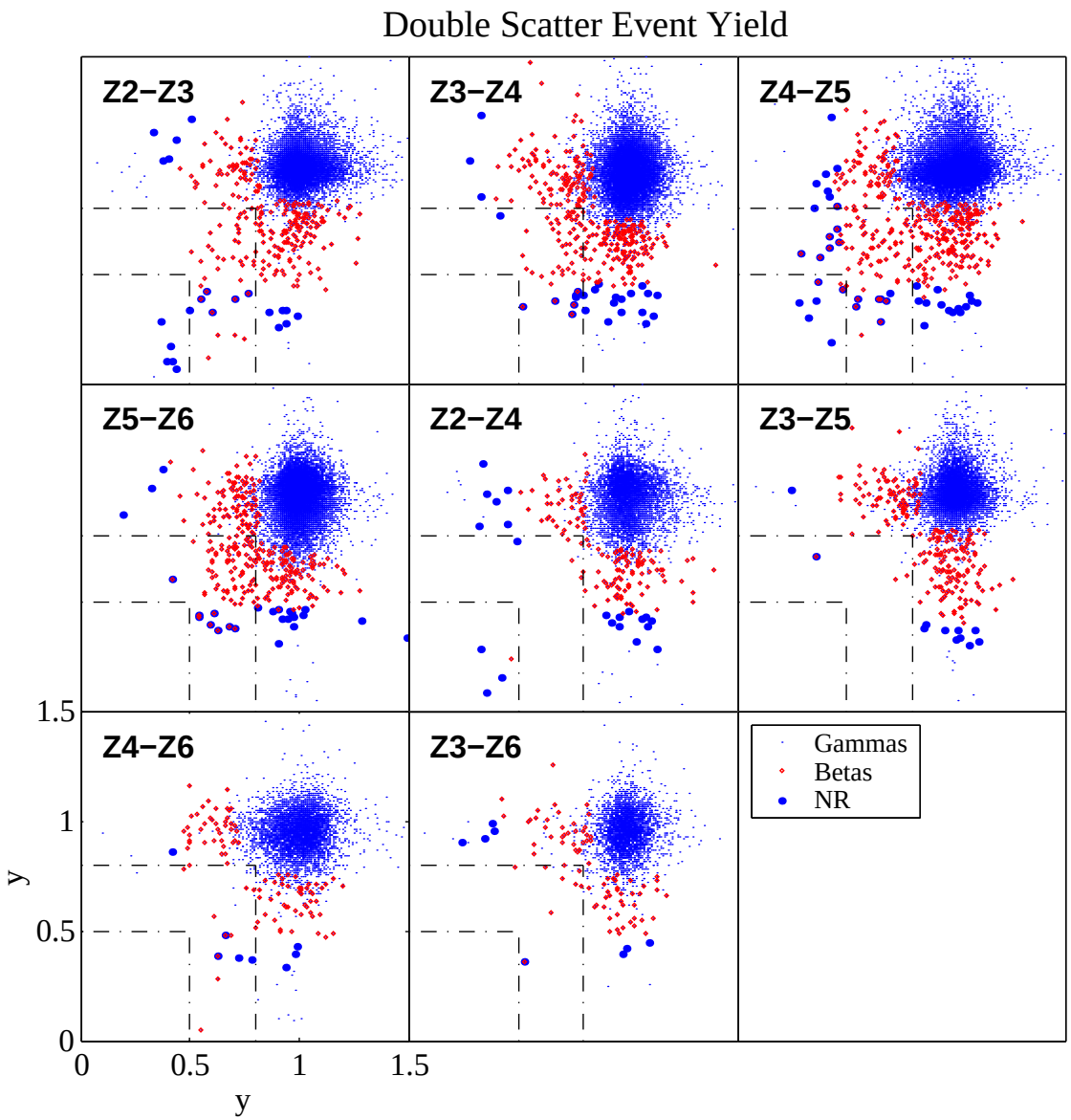

Figure 6.29: Yield-yield plots of ^{60}Co data. The dashed lines roughly indicate the top edge of the nuclear recoil band (lower left) and the bottom edge of the electron recoil band (top right). The significant reduction of events along the lower right portion of the diagonal in non-neighboring detectors supports the hypothesis that these events are due to surface β.

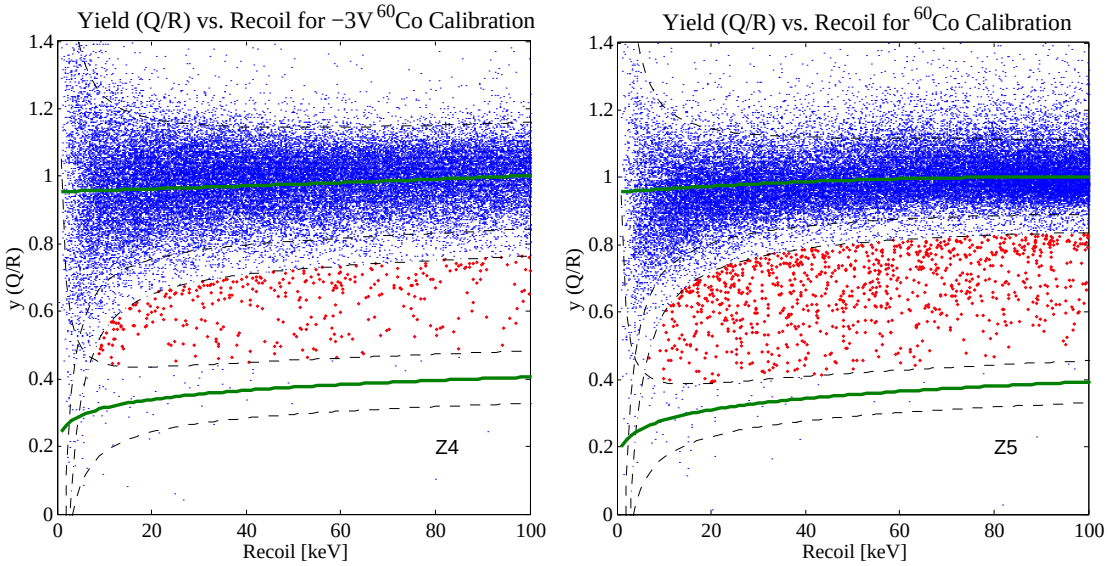

(a) (b)

Figure 6.30: y plots showing the distribution of the surface β's. β's are empirically defined as those events which lie beneath the electron recoil 3σ line and above the nuclear recoil 3σ line.

	Detector					
Energy [keV]	**Z1**	**Z2**	**Z3**	**Z4**	**Z5**	**Z6**
5–20	3.3	1.5	0.57	2.4	1.1	2.6
20–40	0.73	1.4	1.8	3.1	2.1	1.7
40–60	0.63	1.3	3.7	1.9	2.3	1.8
60–100	0.74	2.6	2.5	1.5	2.7	1.5
100–150	1.3	6.0	1.9	1.2	1.6	1.0
150–200	1.5	5.3	1.9	8.7	1.6	0.44

Table 6.6: Number of surface β recoils expected to be misidentified as nuclear recoils, normalized to the number of events in the y=0.7 bin. The values are quoted in %.

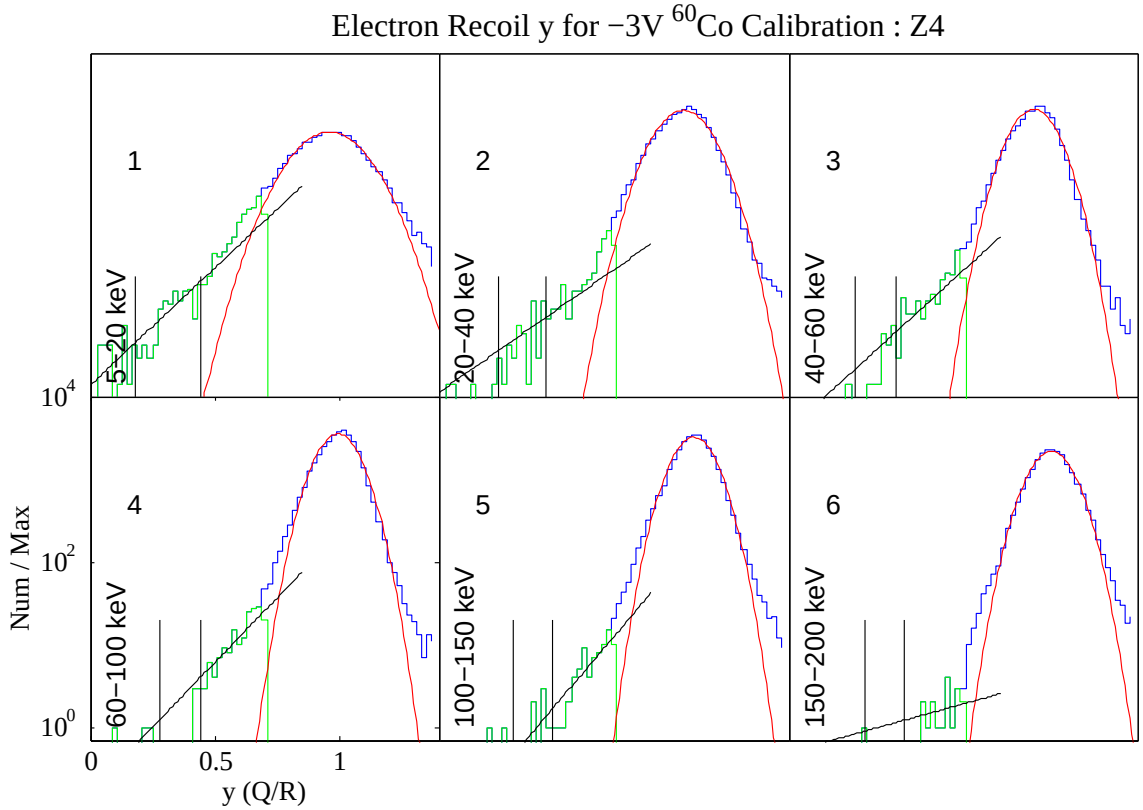

Figure 6.31: y distribution of surface electron recoils in a Si ZIP (Z4) from a ^{60}Co calibration. By selecting multiple scatter events an enhanced low yield tail appears next to the bulk electron recoil Gaussian. The solid diagonal lines are the results of fitting an exponential to the low y tail.

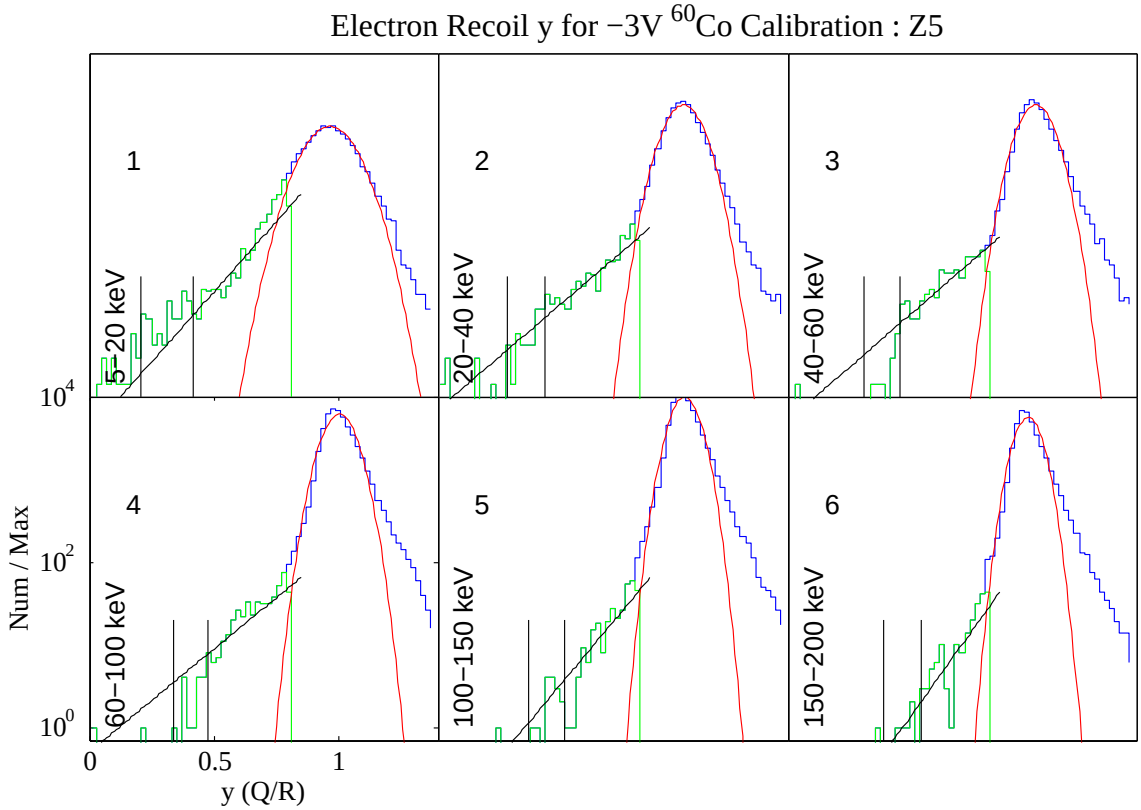

Figure 6.32: y distribution of surface electron recoils in a Ge ZIP (Z5) from a ^{60}Co calibration. By selecting multiple scatter events an enhanced low yield tail appears next to the bulk electron recoil Gaussian. The solid diagonal lines are the results of fitting an exponential to the low y tail.

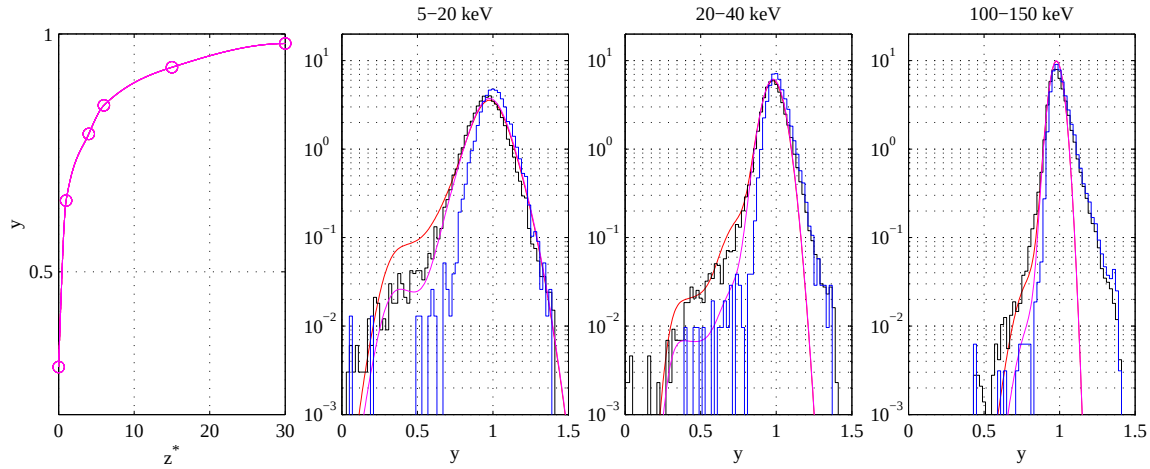

Figure 6.33: Comparison of the low y distribution of surface electron recoil between data and Monte Carlo. The histograms, corresponding to the nearest neighbor and single scatter data sets are well reproduced by a Monte Carlo simulation using the ionization loss profile shown in the first panel. Figure taken from [67].

6.4.2 The Risetime Effect

With their suppressed yield, surface electron recoils, namely β contamination, have the potential to dominate the background event rate in the nuclear recoil band. As described in section 4.2.1, the phonon pulse shape dependence on event depth offers a mechanism by which surface electron recoils may be identified and rejected.

Figure 6.34 shows the phonon risetime plotted as a function of yield for the ^{252}Cf and ^{60}Co calibration data. It can be seen that the data form three distinct populations : one with low values of yield corresponding to the ^{252}Cf nuclear recoil data, one with high values of yield corresponding to the ^{60}Co bulk electron recoils (as identified by the single scatter requirement described above), and finally one at intermediate values of y, but with low values of risetime corresponding to surface electron recoils (as identified by the nearest neighbor multiple scatter requirements described above). A combination of cuts in yield and risetime can, therefore, eliminate a large fraction

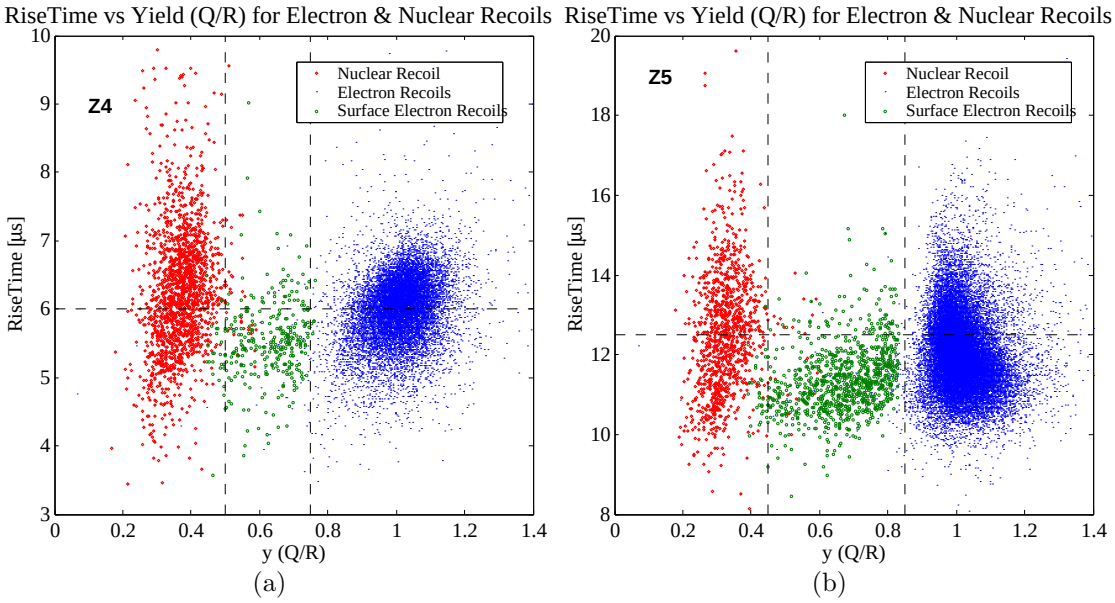

Figure 6.34: Risetime vs. yield plots for calibration data. In the risetime–yield plane three distinguishable population are attributed to nuclear recoils (left most blob), surface electron recoils (middle blob), and bulk electron recoils (right blob). Data from a Si ZIP is shown in (a) and from a Ge ZIP in (b).

of the surface electron recoil, while maintaining a significant fraction of the nuclear recoils.

6.5 Cut Efficiencies

The preceding sections mentioned some of the cuts used in analyzing the calibration data. A comprehensive list of cuts used in the analysis, as well as a determination of their efficiencies where applicable, will be presented in some detail here. The cuts are classified into the following three general categories according to their function :

Data Quality Cuts These cuts operate on properties of the raw data traces and attempt to reject events in which the behavior of digitized data renders it unacceptable. Such cuts do not have any dependence on the nature of the recoil, and generally have efficiencies very close to 100%.

Detector Cuts These cuts operate on more physical parameters, such the energy or risetime in a given channel. The purpose of these cuts is to identify the class of events relevant for the Dark Matter analysis.

Physics Cuts These cuts operate on the highest level physical parameters, and are not necessarily restricted to the behavior of individual detectors. They tend to be defined more by the requirements of the Dark Matter search rather than the performance of the detectors.

6.5.1 Data Quality Cuts

χ^2

Figure 6.35 shows the distribution of χ^2 of the ionization channel as a function of energy in the ionization channel. The χ^2 is calculated by comparing the data pulse to

that of a template constructed from several hundred data pulses in the energy range $\sim 50\,\mathrm{keV}$. The ionization χ^2 cut is defined as a second order polynomial in ionization energy :

$$\chi^2 < \alpha Q^2 + \beta \tag{6.9}$$

where α, and β differ for each detector. Such a form for the cut is motivated by the fact that a small deviation between the shape of the template and the true pulses will lead to a quadratic dependence of χ^2 on pulse height.

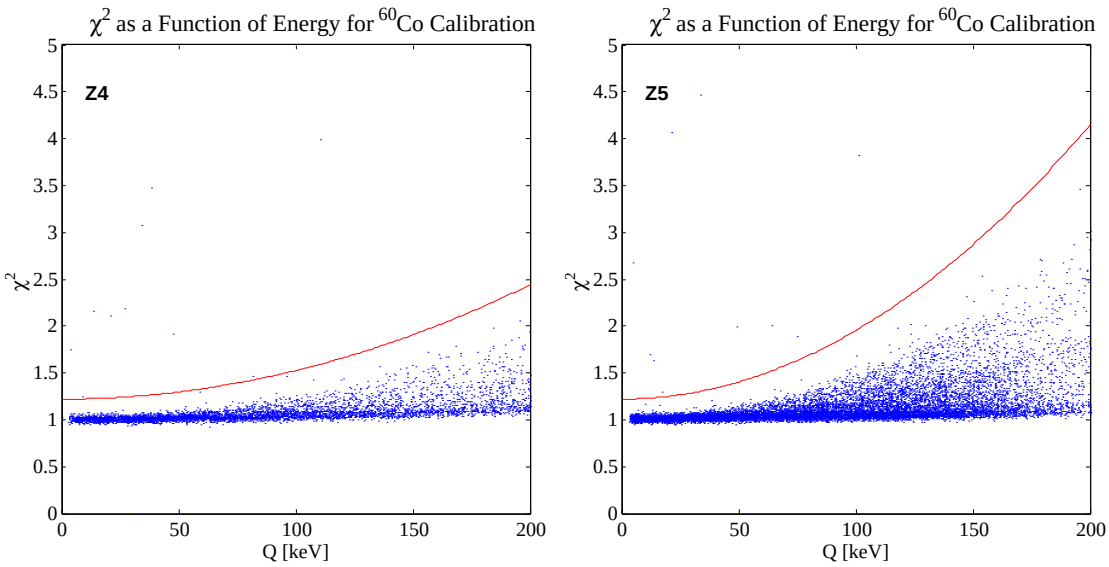

(a) (b)

Figure 6.35: χ^2 as a function of ionization energy. The solid line indicates the boundary of the χ^2 cut. At high energies, the χ^2 distribution flares due to small differences between the template and actual pulses. Data from a Si ZIP is shown in (a) and from a Ge ZIP in (b).

No such cut is applied to the phonon pulses as there is a fair amount of variability in the pulse shapes, rendering such a cut of limited use.

Baseline Standard Deviation

A cut is made on the standard deviation of the pre-trigger baseline. The purpose of this cut is to remove events in which there was significant activity in the time period just prior to the trigger, such as would be caused by electronic noise bursts or a still decaying pulse. Phonon and ionization baseline standard deviations are required to be within 5σ of their nominal value, as defined by traces in which no pulses exist.

Pileup

Events in which more than one interaction occurs within a single trace (2 ms) will suffer from incorrect energy reconstruction, among other mis-calculated quantities. Thus, it is desirable to have a cut which removes such events. The pileup cut is defined to be the logical sum of the χ^2 and baseline standard deviation cuts.

6.5.2 Detector Cuts

Inner Electrode Cut

The inner electrode cut (also referred to as *Qin*) is the workhorse cut of this analysis. In fact, hardly any quantity is examined without having first applied a minimum of the Qin cut. The reason this is important arises from the behavior of the ionization signal near the edge of the detectors. The bare, relatively unpolished edges of the crystal result in a non-uniform electrical field as well as the presence of a large number of trapping sites, leading to incomplete charge collection. Since electron recoils with incomplete charge collection may be mistaken for nuclear recoils, the Qin cut is always employed to ensure that the interaction point is sufficiently within the bulk of the detector (radially) as to result in nominal behavior.

Figure 6.36(a) shows a histogram of the ionization partition, defined as

$$Q_{part} = \frac{Qi - Qo}{Qi + Qo} \tag{6.10}$$

where Qi and Q_o are the inner and outer ionization signals respectively. The two peaks at $Q_{part} = \pm 1$ represent events that are fully beneath the inner/outer electrode, while the continuum of events between the two peaks is due either to scatters beneath the electrode gap, or to multiple scatters within the same detector. Another way of presenting this data is shown in Figure 6.36(b), in which the signal in the inner and outer electrodes, normalized to the total phonon signal, are plotted against each other. The two diagonal populations represent electron and nuclear recoils. The necessity of implementing the Qin cut is seen by the continuous distribution of events between the two populations along the Qo axis.

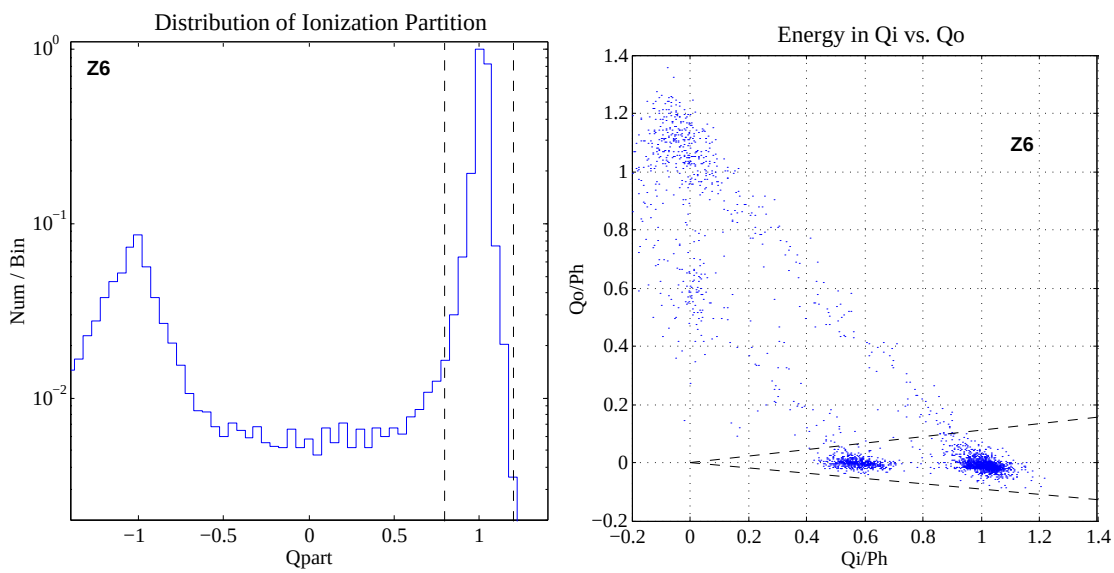

(a) (b)

Figure 6.36: A histogram of the ionization partition (a) shows two peaks at ± 1 corresponding to events beneath the inner/outer electrode. A plot of the normalized signals in the inner vs. outer electrode (b) shows a lack of clear separation between electron and nuclear recoils beneath the outer electrode. The dashed lines denote the accepted region of the Qin cut.

It is important, in calculating the efficiency of the Qin cut, that the detector be uniformly illuminated[11]. As such, the ^{252}Cf nuclear recoil calibration data is used rather than the ^{60}Co data because the mean free path of neutrons in Si/Ge is $\sim$ a few cm. Figure 6.37 shows the efficiency of the Qin cut as a function of recoil energy for one of the detectors. The decrease in efficiency below 20 keV is due to the increasing significance of the ionization noise in determining the partition. At higher energies the efficiency plateaus at a value close to 85%, the geometrical area of the inner electrode.

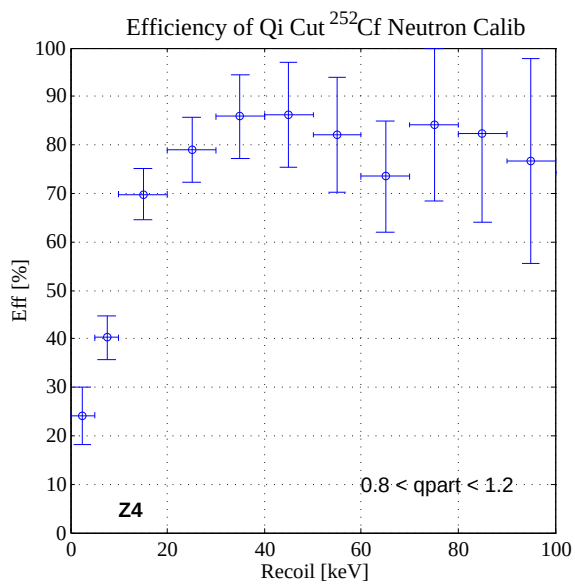

Figure 6.37: Efficiency of the Qin cut as a function of recoil energy. The high energy plateau $\sim$85% is in agreement with the geometrical area of the inner electrode. The decrease in efficiency at $E_r < 20$ keV is due to the increasing significance of the ionization noise.

[11] As would be the case for WIMP interactions.

Muon Anticoincidence

Of the ~ 50000 events recorded daily, more than 80% are a direct or indirect consequence of muons passing near the detectors. Of these events, there are typically ~ 10 events in the nuclear recoil band with $E_r < 100\,\text{keV}$. Such a rate is orders magnitude larger than any possible WIMP interaction rate and would thus mask any such signal, if it exists. The muon anticoincidence cut (referred to as the *anticoincidence* cut) is meant to remove all events associated with muons passing through the experimental volume[12]. This is done by measuring the time between an event in the detectors and the preceding activity in the muon veto scintillators. Figure 6.38 shows a distribution of such times. Two structures are observed in the figure : the sharp peak near zero is a result of events correlated with the muon passage through the veto scintillators, and the exponential tail is due to random coincidences between a detector event and activity in the muon veto. The slope of the exponential tail is $\sim$ 190 μs, corresponding the a total muon veto rate of 5.2 kHz. The anticoincidence cut accepts all events for which the time to the most recent muon veto is more that 40 μs, namely events to the left of the dashed vertical line in Figure 6.38. The efficiency of such a cut is given by $\epsilon = \exp(-40/\tau) = 0.80$, where $\tau = 190\,\mu$s, is the slope of the exponential distribution. This efficiency is also obtained by observing the number of randomly triggered events containing a muon veto hit.

Nuclear Recoil Selection

The nuclear recoil band cut is the cut by which discrimination is performed and the potential WIMP candidates identified. The cut is defined to accept events within $\pm 2\sigma$ of the nuclear recoil band mean (as defined in section 6.3.1 and Figures 6.23 and 6.24 . Since the cut, in terms of σ, is independent of energy, the efficiency is simply 95% over the whole recoil energy range.

[12] i.e. the detectors, cryogenics shells, and radiation shielding.

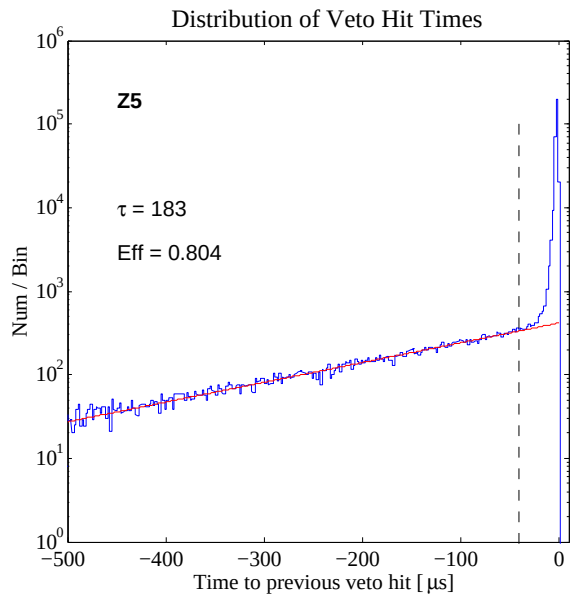

Figure 6.38: Histogram of time between detector events and the most recent activity in the muon veto system.

Phonon Risetime

The risetime cut is intended to remove the small fraction of surface events that may be misidentified as nuclear recoils. The mechanism behind the correlation of risetime and interaction depth is described in section 4.2.1, with Figure 6.34 demonstrating the effect in calibration data. The risetime cut is defined to accept events with a phonon pulse risetime larger than 12 μs (6 μs) for the Ge (Si) detectors.

Figure 6.39 shows the efficiency of the risetime cut on the surface electron and nuclear recoil event populations. Up to 80% of surface electron recoils are rejected over a broad energy range while retaining a nuclear recoil acceptance of over 50%.

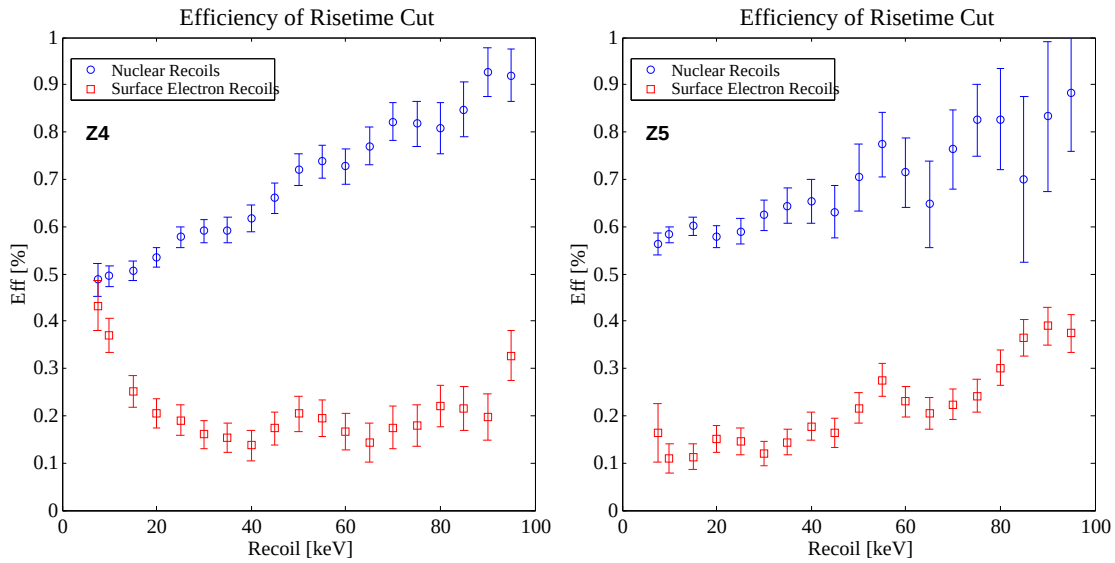

(a) (b)

Figure 6.39: Efficiency of the risetime cut for a Si (a) and Ge (b)detector. The cut is more than 50% efficient for nuclear recoils (circles) at all energies while suppressing surface electron recoils (squares) by up to 80% above 20 keV.

6.5.3 Physics Cuts

Phonon and Ionization Thresholds

Figure 6.40 shows the phonon trigger efficiency as a function of the energy in the phonon channel. It can be seen that above 3 keV full efficiency is achieved for all detectors, with the exception of Z1. The phonon threshold cut was chosen to lie at 5 keV in recoil energy. This value was chosen in order to satisfy the following three criteria : the threshold must be in a region where the trigger efficiency is well understood and slowly varying; it must be sufficiently low so as to allow for as large a sensitivity to WIMP recoils as possible, yet must be high enough for highly effective electron/nuclear recoil discrimination.

An ionization energy threshold of 1.5 keV is also imposed to ensure that the signals are sufficiently large to be inconsistent with noise fluctuations. In addition, determining the ionization partition and yield for events with sub-threshold ionization signals

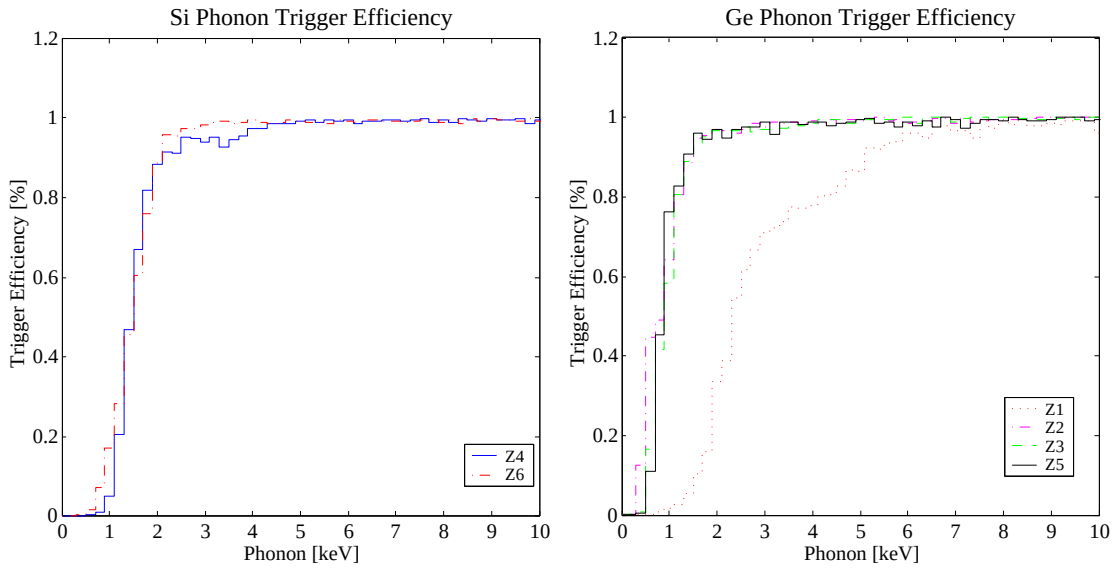

(a) (b)

Figure 6.40: Trigger efficiency as a function of phonon energy. The efficiency reaches 100% by 3 keV for all detectors but Z1.

is quite uncertain.

Single & Multiple Scatters

The class of events due to neutron scatters is indistinguishable from WIMP interaction on an event-by-event basis. As such, a measurement of this background, in the absence of a WIMP signal, would provide a good means of extracting the size of the WIMP signal from the actual data. Such an experiment can be performed by considering the subset of the data in which a particle scatters in more than one detector. Since the fraction of WIMPs that will multiply scatter is vanishingly small we are able to confidently determine the rate of multiply scattered neutrons in the data. The rate of neutron multiple scatters, in combination with a Monte Carlo prediction for the ratio of neutron single to multiple scatters allows for a determination of the single scatter neutron background and remaining WIMP signal in the data.

The definition of single and multiple scattered events are rigidly defined as follows

in order to allow for an unambiguous comparison with the Monte Carlo predictions.

Single Scatter These events are identified by the absence of a phonon trigger, in any of the other detectors, within 50us of the event trigger.

Multiple Scatter These events are defined as follows: the pulses in all 6 detector must pass the data quality cuts. At least two detectors must pass the Qin and phonon threshold cuts. With regards to the risetime cut, if any of the detectors which satisfy the recoil threshold and Qin criteria also satisfies the risetime cut, the entire event is considered to pass the risetime cut.

6.6 Detector Stability

Since Dark Matter searches need to operate on a timescale of years, it is very important to ensure detector stability, in terms of energy linearity, noise performance, discrimination, etc ... over the duration of the run. This section will highlight the stability of a few key parameters over the 100 day running period.

The Energy Scale

The Ge detectors have a nice feature which allows the monitoring of the energy scale over time, namely the presence of lines at 10.4 and 67 keV, as shown Figures 6.41 and 6.42. The data are divided into three roughly equal time periods and the position of the peaks is seen to remain stable in both the phonon and ionization channels at 10 keV. At 67 keV, the combination of degrading phonon resolution and decreasing statistics does not allow for a direct fit to be performed in the phonon channel. Instead, the stability at higher energies is determined by monitoring the behavior of the yield over time, as described in the following section.

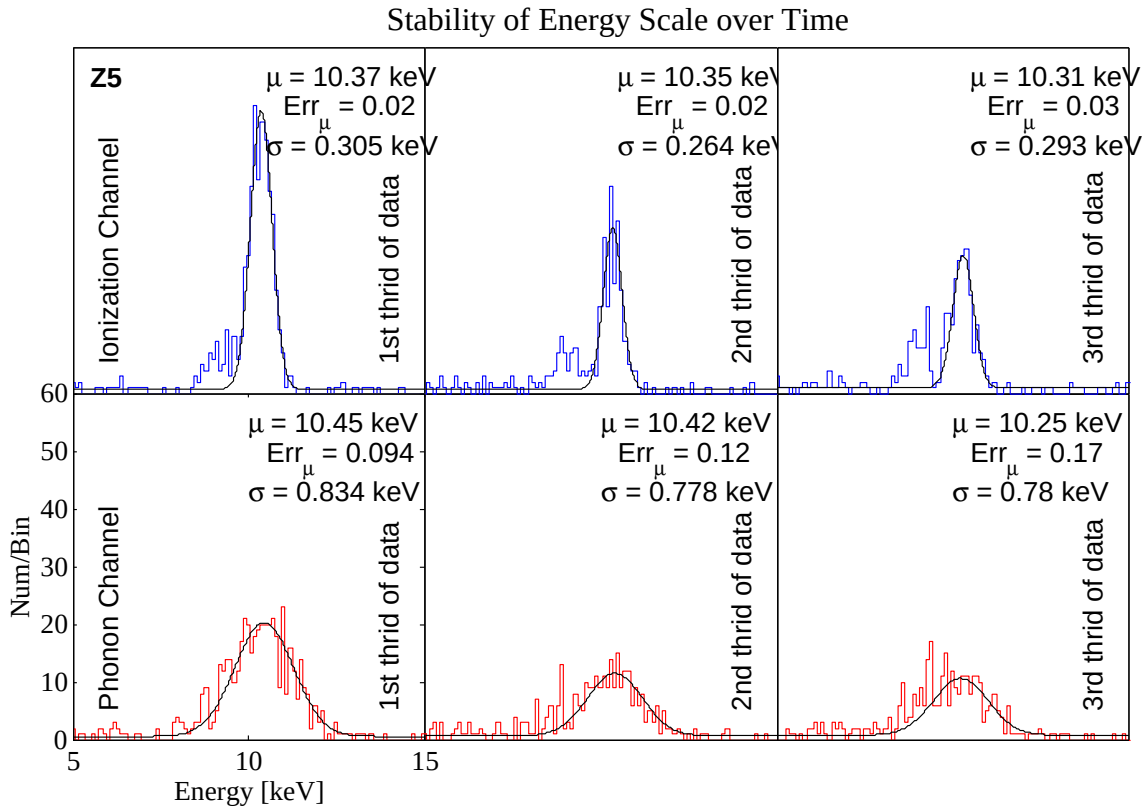

Figure 6.41: Stability of the phonon and ionization energy scales at 10 keV. The top (bottom) row shows behavior of the ionization (phonon) channel over three roughly equal periods. The fitted position of the peaks are listed at the top of each panel.

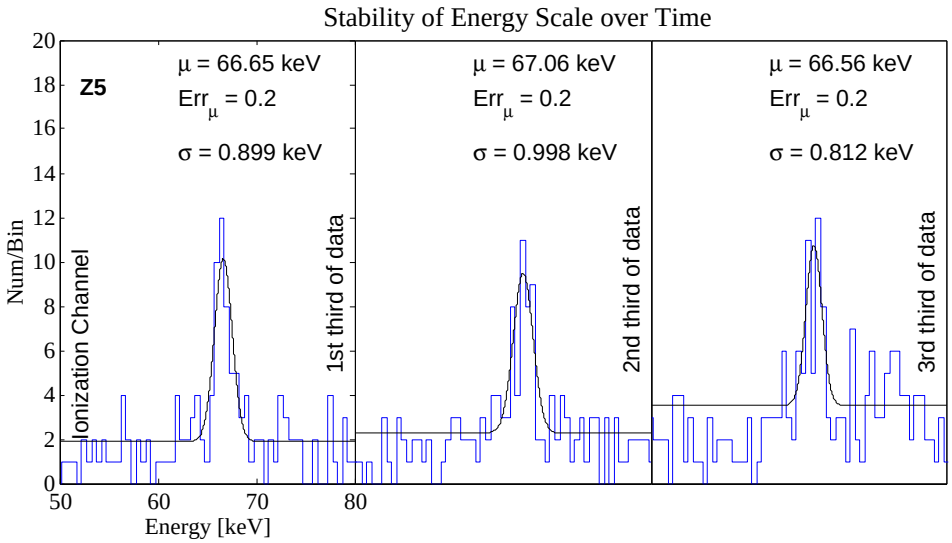

Figure 6.42: Stability of the ionization energy scales at 67 keV. The figure shows behavior of the ionization channel over three roughly equal periods. The fitted position of the peaks are listed at the top of each panel.

The Electron Recoil Band

Monitoring the stability of the electron and nuclear recoil yield bands is central to maintaining the high level of discrimination required to perform the WIMP search. Figure 6.43 shows the behavior of the mean of the electron recoil band, averaged in the range $40 < E_r < 60$, over the timescale of the run, with each point corresponding to a period of $\sim$ five days. With the exception of one period in which the noise in one of the detectors (Z4) increased slightly, the electron recoil band shows good stability over time.

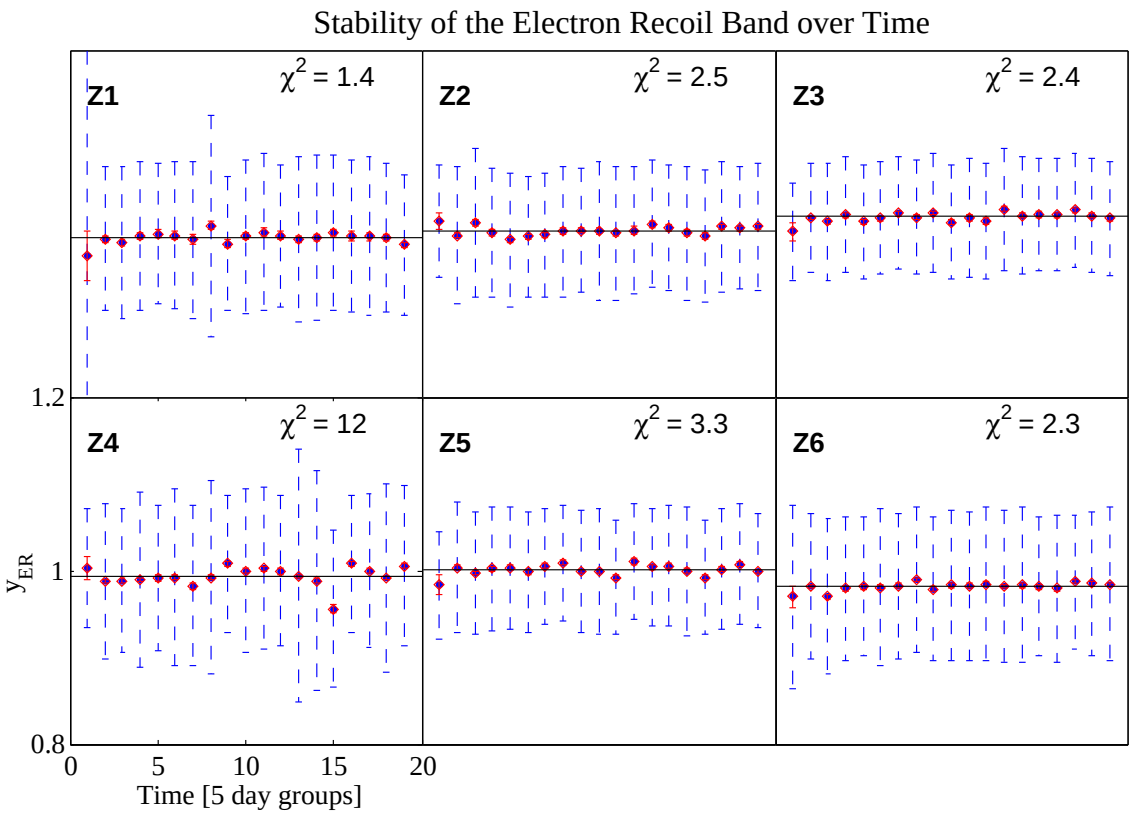

Figure 6.43: Stability of the electron recoil band. The circles and solid error bars correspond to the average electron recoil yield in the range $40 < E_r < 60$. The dashed error bars correspond to the 1σ width of the band. With the exception of one point in detector Z4 the data shows good stability over time.

Baseline Noise

A quantity that is relevant to the stability of the yield bands and the discrimination parameters is the baseline noise in the various channels. Figure 6.44 shows the variation of the ionization baseline noise over time for both the inner (solid line) and outer (dashed line) electrodes. None of the detectors exhibit a measurable trend.

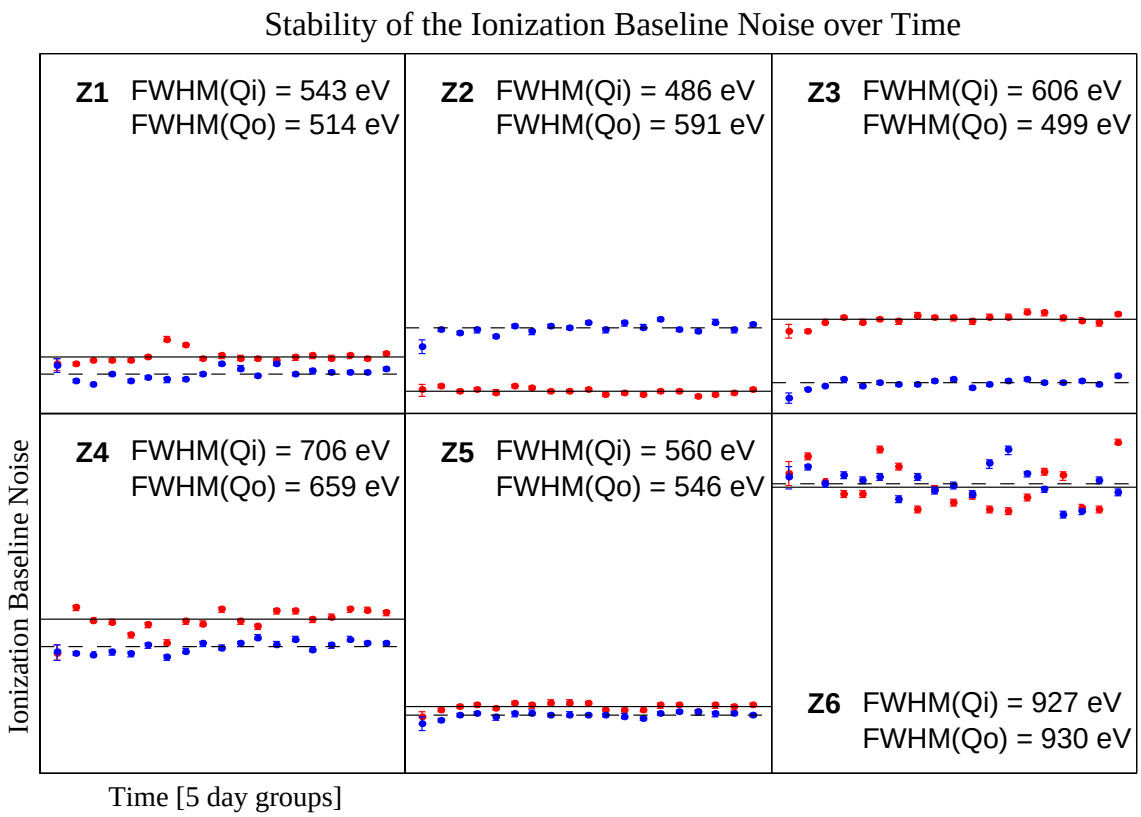

Figure 6.44: Stability of the ionization baseline noise. The ionization baseline noise, averaged over time slices of ~ 5 days, is compared to the average value (horizontal lines). No significant trend in the noise is observed over time. The solid (dashed) lines correspond to the inner (outer) electrode. The values of the noise mean are indicated at the top of each panel.

Muon Coincident Neutron Rate

It would be extremely desirable to perform a similar analysis as described above for the nuclear recoil band. This is not possible, however, due to the very small number of nuclear recoil scatters. A good handle on the behavior of the nuclear recoil band, however, can be obtained by considering the total rate of events observed as a function of time. Figure 6.45 shows variation in the rate of nuclear recoils, quoted in number of observed events per detector per day, with time. A χ^2 comparison of the rate, averaged over a $\sim$ five day period, with the total run average (shown as the horizontal lines) indicates that both the single scatter (solid error bars) and multiple scatter (dashed error bars) rates are consistent with a constant value.

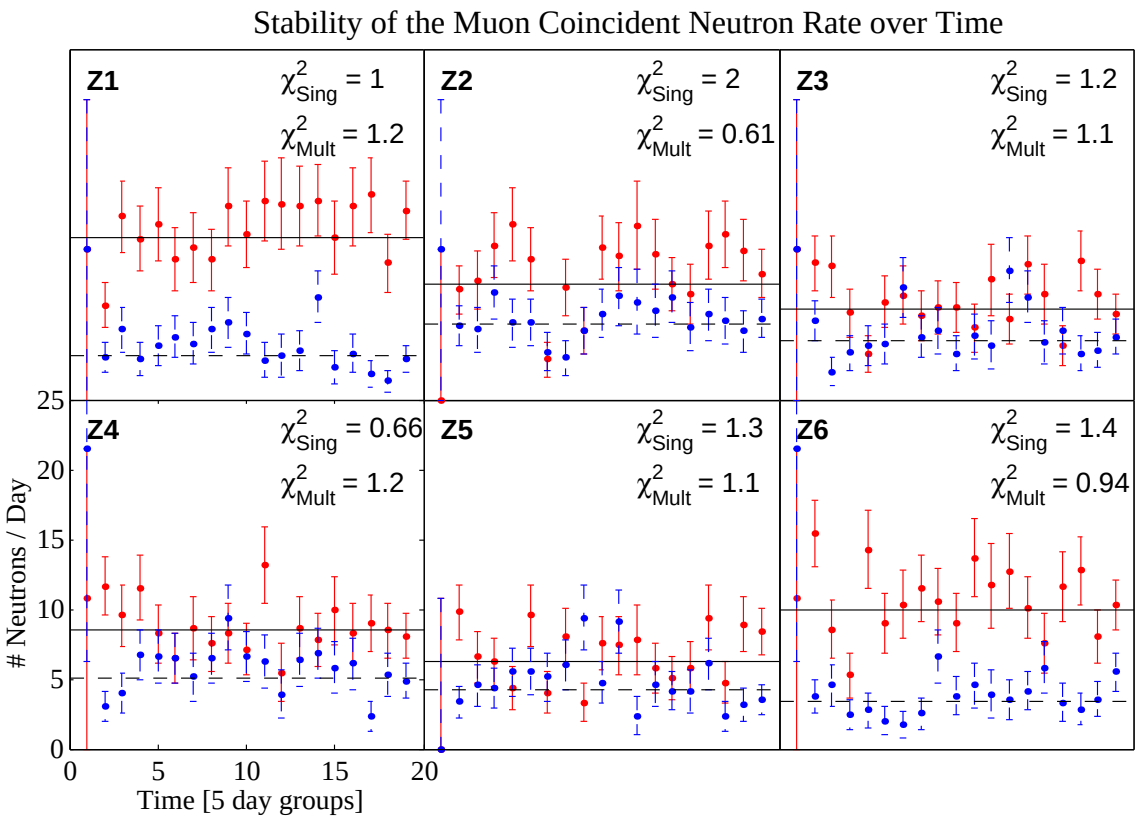

Figure 6.45: Stability of the muon coincident neutron rate. The muon coincident neutron rate, averaged over time slices of ~ 5 days, is compared to the average rate (horizontal lines). All detectors have a χ^2 of ~ 1, consistent with a time independent rate. The solid lines correspond to the singles neutron rate, and the dashed lines correspond to the multiples rate.

Chapter 7

Contamination Levels

As mentioned in chapter 5, significant effort is put into insulating the detectors from the natural environmental radioactivity to a level which allows a Dark Matter search to proceed. With the mechanism for shielding external backgrounds well established, the onus is shifted toward minimizing the amount of radiation originating within the shield. Of primary concern are the detectors themselves and the materials immediately surrounding them. The internal backgrounds can be divided into the following two categories:

- Surface contamination : These backgrounds are due to the accumulation of radionucleides on the surface of the detectors or the immediately surrounding material from the environment in which the detectors are fabricated, stored, or tested. Examples of such background sources include ^{210}Pb, ^{14}C, and ^{40}K.

- Bulk contamination : The method by which the detector crystals are grown precludes the majority of backgrounds that do not arise from isotopes of Ge or Si. However, cosmogenically created radioisotopes will begin to accumulate within the bulk of the crystals during any periods in which the detectors are exposed to the high cosmic ray flux above ground. Some such background may

even be continuously produced by the neutron flux at the shallow SUF site[1], or by the periodic neutron calibrations.

7.1 Surface Contamination

I will briefly describe some of the more notorious radioisotopes, due to the nature of their decay products and long half-lives, and the conclusion that can be inferred about them from the current Dark Matter run at SUF.

^{14}C With a half-life of 5730 years, any ^{14}C contamination will provide a constant background source throughout the time span of the experiment. ^{14}C undergoes beta decay, resulting in a spectrum with an energy mean of 50.1 keV, and an end-point at 156 keV.

^{210}Pb Environmental ^{222}Rn decays into ^{210}Pb, via four intermediate daughters, within $\sim$4 days. Several of these decays involve a high energy α particle, which could result in the recoiling nucleus being implanted in the detector with depths of up to several μm. ^{210}Pb has a half-life of 22 years, long enough to provide a nearly constant background throughout the time span of the experiment. It may be possible to observe the expected $\sim$5% per year decrease in rate, thus providing a handle for identifying such contamination. ^{210}Pb also undergoes beta decay, with an energy mean of 6.2 keV, and an end-point of 63.5 keV.

^{40}K This isotope has a half-life of 1.3×10^9 years. Its dominant decay mode is beta decay with an end-point energy of 1.3 MeV. While energy depositions of this magnitude are outside the interesting WIMP search range, the betas have enough energy to pair produce and could lead to secondary particles, betas and gammas, with sufficiently low energy to fall within the region of interest.

[1] At rates $\sim$100 times lower than if the experiment were running at the surface.

The common feature of these three radioisotopes is the production of low energy βs, a background which results in surface electron recoils. All of these backgrounds are sufficiently long lived that they will not decay on the time scale of the experiment.

7.1.1 ^{210}Pb

There exists several handles for estimating and measuring the amount of ^{210}Pb deposited on the surface of the detectors. Measurements of ^{222}Rn concentration and the time spent by the detectors at various locations, combined with a model for ^{210}Pb plate-out on the surface [66] leads to an estimate of ^{210}Pb concentration on the detectors' surfaces. The low background data in Run 21, on the other hand, allows for a direct measurement of the rate of two components of the ^{210}Pb decay chain : the 5.3 MeV α particles and the recoiling nuclei from the decay of ^{210}Po as well as the βs from the decay of ^{210}Pb. Figure 7.1 shows the measured β spectra as well as a Monte Carlo simulation [66] of the ^{210}Pb decay spectrum. A limit on the amount of ^{210}Pb is determined by matching the Monte Carlo spectra to the data in the region just above 20 keV, chosen because the efficiency of the β cut (as defined in section 6.4) decreases rapidly beyond this point.

Similarly, measuring the rate of 5 MeV α particles incident on the detectors leads to a determination of the amount of ^{210}Pb. Figure 7.2 shows the distribution of these events in a 2D plot, as well as their recoil spectrum. The location of this population, well below the main electron recoil band is a result of the shallow penetration depth of the α particles, and is the primary feature by which they are identified.

The results of the three above-mentioned methods are shown in Figure 7.3. Given the uncertainties on the measurements of $\sim$ a factor of 2, there appears to be reasonable agreement between the three measurements. The systematically higher measurement, based on the β rate from the data is attributable to the presence of β sources other than ^{210}Pb. ^{210}Bi, a β emitter that is present in the ^{210}Pb decay chain may partially or fully account for the discrepancy in the measured β rate.

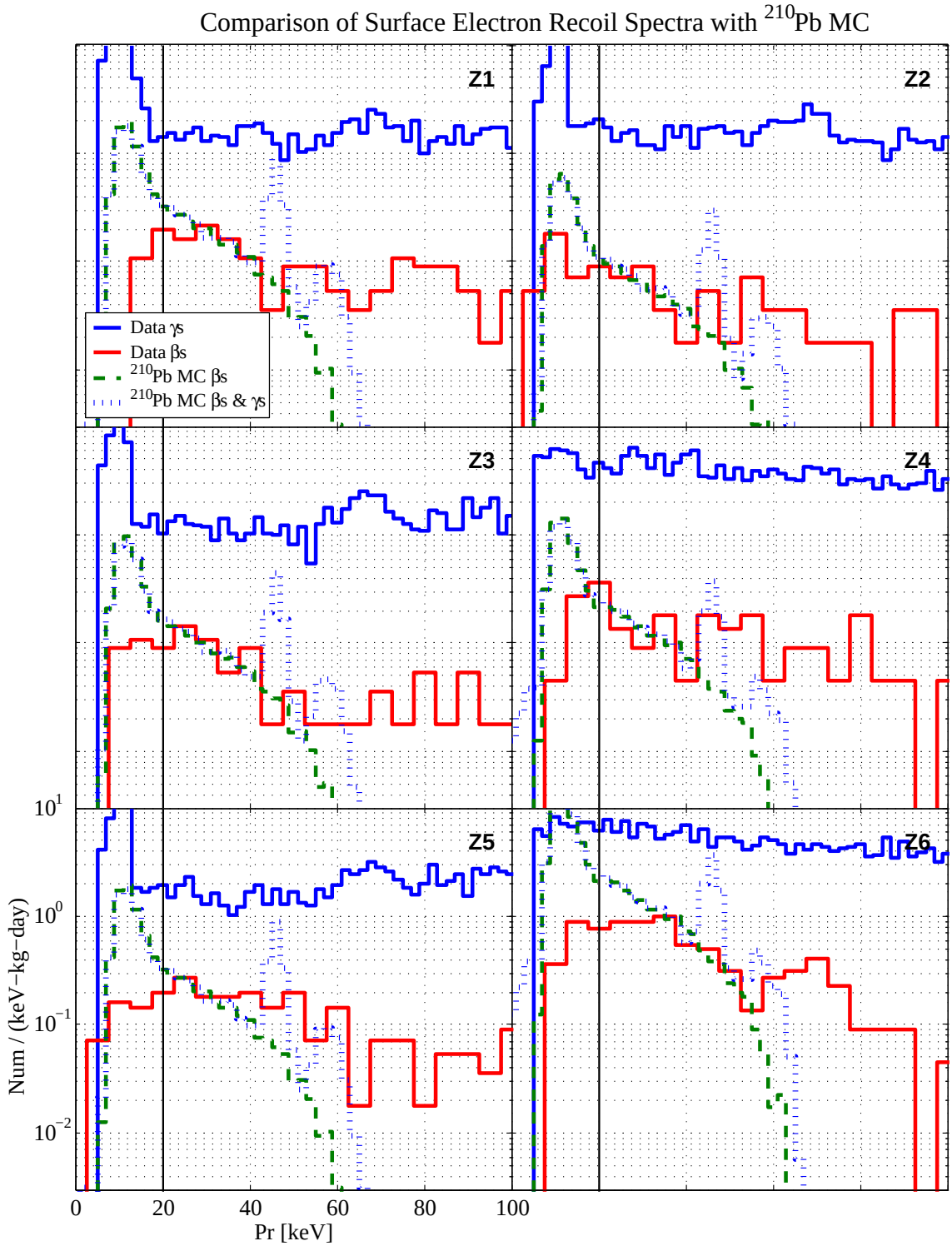

Figure 7.1: Comparison of β spectra between data and ^{210}Pb Monte Carlo simulation. The coarsely (finely) binned solid line is the muon anticoincident β (γ) rate, while the dashed (dotted) line corresponds to the Monte Carlo β (γ) rate. Monte Carlo simulation data from [66].

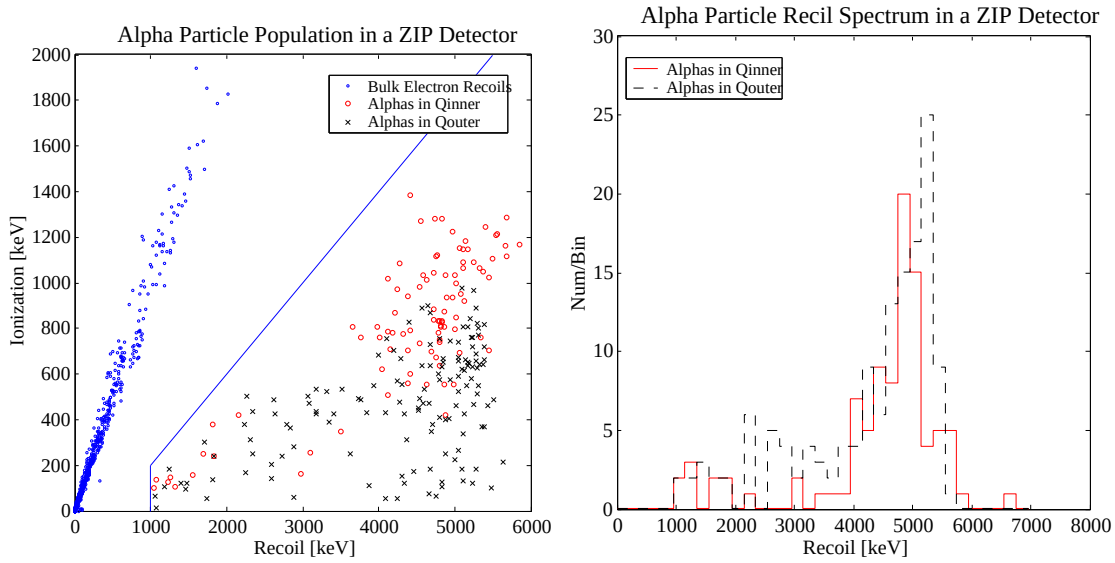

(a) (b)

Figure 7.2: 2D plot (a) and recoil histogram (b) of α particles in the low background data. α particles in the inner (outer) electrodes, denoted by circles (crosses), are identified as events with recoil energies $> 1\,\mathrm{MeV}$ and a suppressed ionization signal. The electron recoil band is seen as a line with a slope of one. Figures taken from [68].

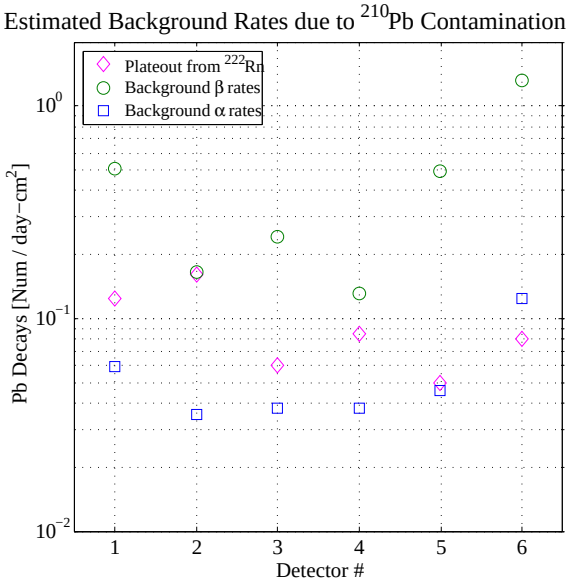

Figure 7.3: Comparison of ^{210}Pb background rate estimates. The diamond symbols indicate the ^{210}Pb rate based on calculation of Pb plate-out and environmental Rn concentrations, while the circles and squares are based on the measures β and α rates in the data. Due to various currently unknown efficiencies, the rates may reasonably vary within a factor of 2. The three measurements appear to be in fair agreement, with the higher rate based on the β data attributable to sources other than ^{210}Pb.

7.1.2 ^{14}C

Figure 7.4 shows the background β spectrum compared to a ^{14}C Monte Carlo simulation [66]. There exists strong evidence that one of the Si detectors (Z6) was contaminated with ^{14}C in the course of testing. A primary concern, therefore, is to determine whether that contamination appears on other detectors via one of two mechanisms : ^{14}C atoms from the surface of Z6 leave that detector and attach themselves to other detectors when the Ice Box is placed under vacuum; or the other detectors acquire the ^{14}C from the same contamination source as Z6. The spectra in detectors Z5 and Z6 are suggestive of a ^{14}C source. One issue of concern, however, is the efficiency of the β band definition at high energy; as the more energetic βs are able to penetrate deeper into the crystal they eventually cease to be surface recoils. At that point is becomes becomes impossible to identify the component of electron recoils due to βs from the overwhelmingly larger γ rate ($\sim$ 100$\times$ larger).

The presence of events above 156 keV in most of the detectors hints at another β source. ^{40}K and ^{210}Bi are both possibilities, however, Monte Carlo simulations are required to quantify any possible contamination.

7.2 Bulk Contamination

Interactions between the hadronic component of cosmic-rays and Ge result in the creation of ^{68}Ge and ^{65}Zn isotopes. The decay chains of these isotopes are shown in Figure 7.5. Both of these decays chains have a half-life of $\sim$1 year, meaning that a significant fraction of the isotopes would have decayed between the end of detector fabrication and the beginning of a low background run[2]. Although both decay chains result in low energy gammas ($\sim$10 keV), electron recoil discrimination remains sufficiently high at that energy to reduce the possibility of such backgrounds being mistaken for nuclear recoils.

[2]Assuming that in the meantime the detectors are stored underground in order to avoid further activation.

Interaction of neutrons (both thermal and high energy) with the Ge detectors result in the creation of ^{71}Ge and ^{73m}Ge isotopes. The sources of the neutrons are muon interactions within the shield (as described in chapter 5), and the ^{252}Cf calibrations. The muon induced neutrons, however, will be suppressed by several orders of magnitude at the Soudan deep site. As shown in Figure 7.6, these Ge isotopes result in 10 keV x-rays and 67 keV gammas.

Figure 7.7 shows the time evolution of the low energy x-rays in a Ge detector. With a time baseline of $\sim$100 days this data set in only beginning to be sensitive to the long lived ^{68}Ge isotopes. With data from longer exposures it will be possible to deconvolute the contribution of the various isotopes to the low energy background rates.

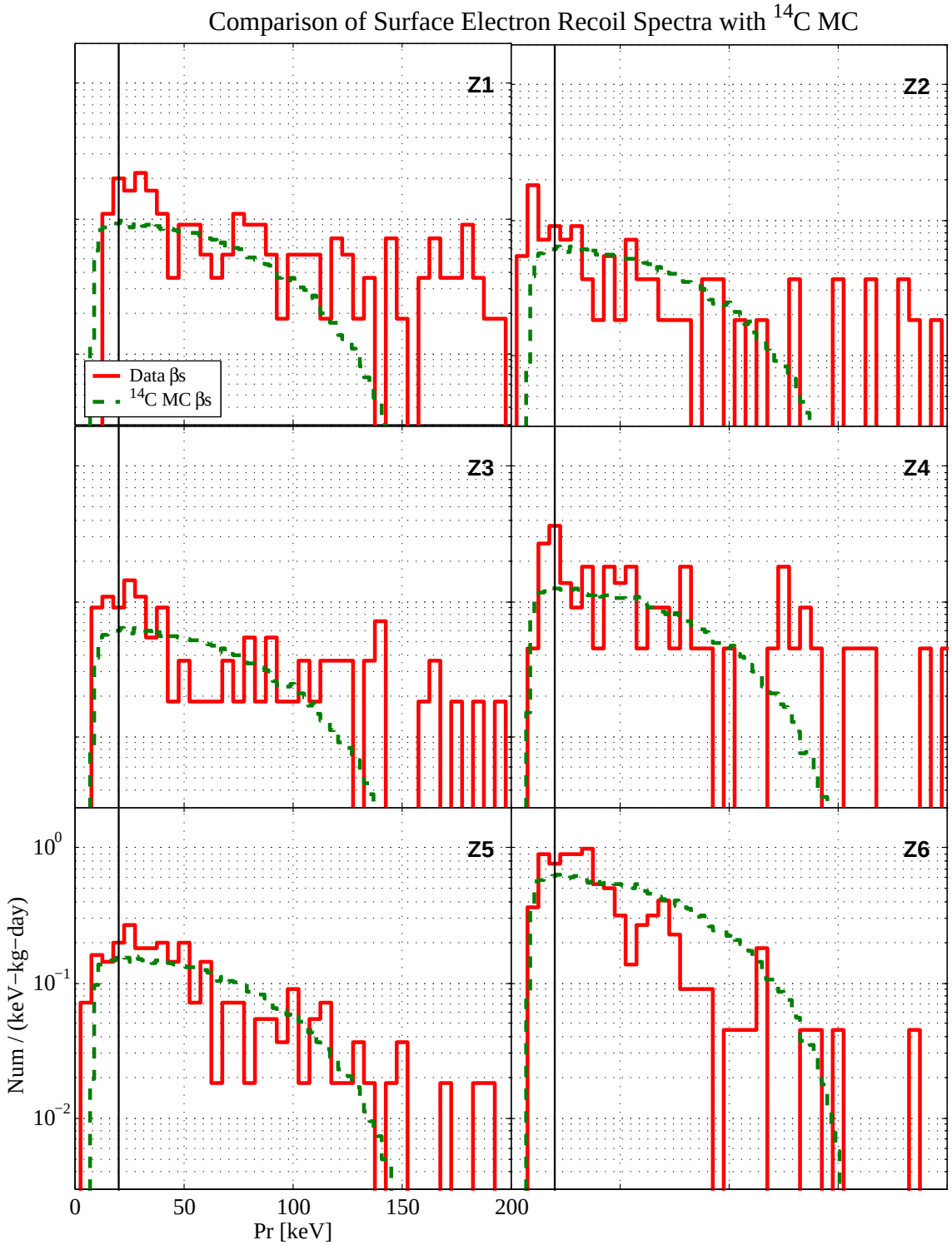

Figure 7.4: Comparison of β spectra between data and ^{14}C Monte Carlo simulation. The solid line is the muon anticoincident β spectrum, while the dashed line corresponds to the Monte Carlo β spectrum. Data from detectors Z5 and Z6 is suggestive of ^{14}C contamination. The presence of events above 156 keV in most of the detectors also hints at another β source, possibly ^{40}K. Monte Carlo simulation data from [66].

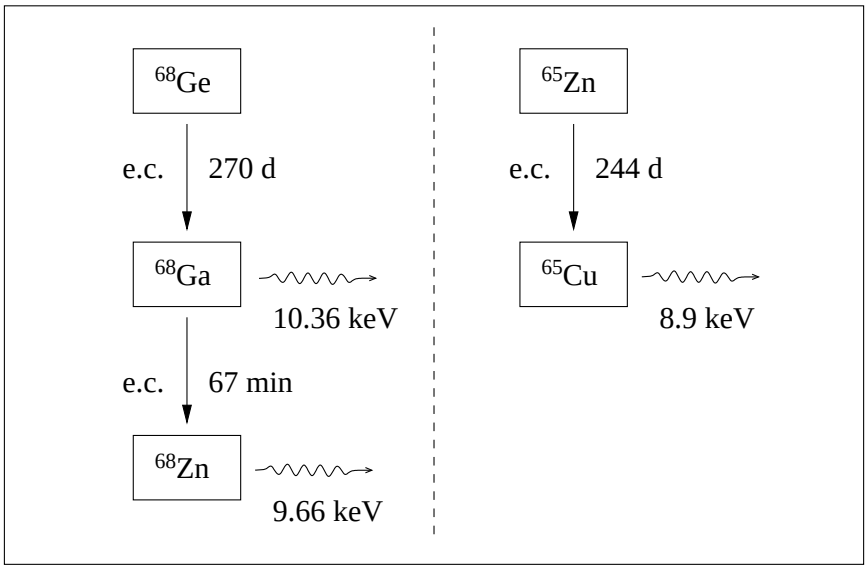

Figure 7.5: Radioisotopes created by cosmogenic activation in Ge. Both decays chains have a half-life of ~ 1 year and result in low energy x-rays.

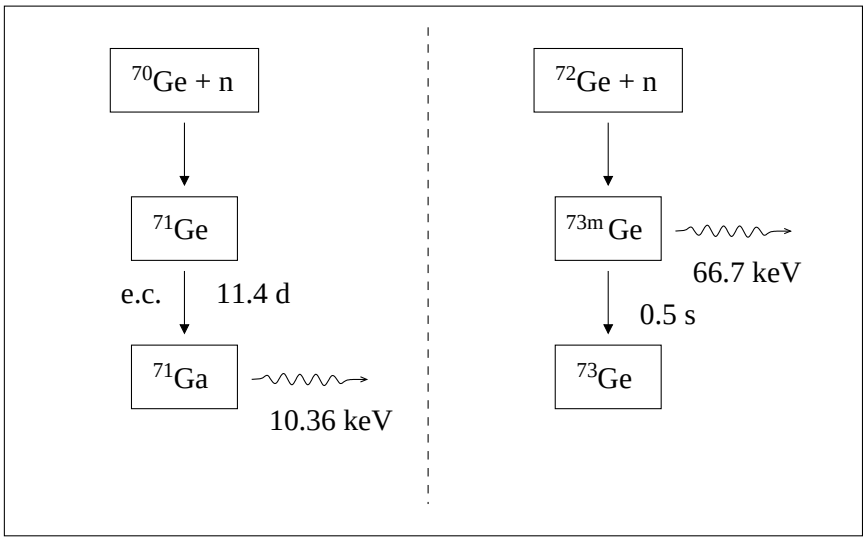

Figure 7.6: Radioisotopes created by thermal and high-energy neutron activation in Ge. The decay chains are short-lived on the timescale of the experiment.

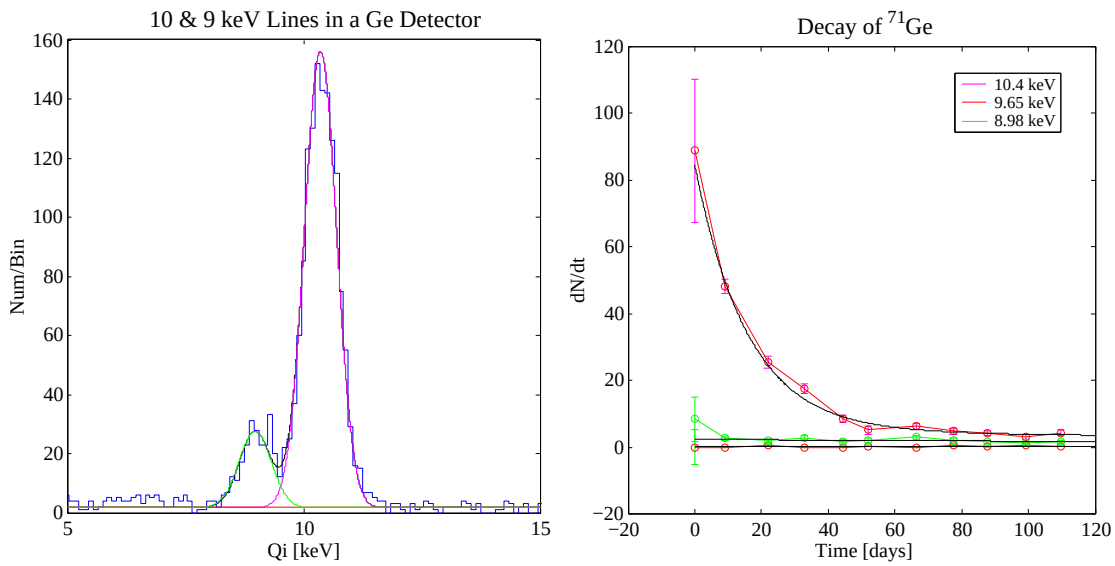

(a) (b)

Figure 7.7: Observation of the 11.4 day half-life of ^{71}Ge. Panel (a) shows the total 10.4 keV signal over the entire run. The amplitude of the 10.4 keV signal is plotted as a function of time (b) revealing the characteristic decay shape.

Chapter 8

Low Background Data

In this chapter I will present the Dark Matter data, taken over ~ 100 days, leading to the determination of the WIMP exclusion limits in the mass – cross-section parameter space.

8.1 Defining the Data Set

Although the initial refrigerator cooldown for Run 21 began in July of 2001, a series of calibrations, followed by a refrigerator failure delayed the onset of the *Low Background* data set until mid-December 2001. Since then, data taking in the low background mode proceeded without interruption until the beginning of April 2002, with the exception of one week in February in which a ^{60}Co calibration was performed. The data set is known as the *3 V* data set based on the value of the ionization voltage bias[1]. A two week period at the end of December 2001 was taken with an ionization voltage bias of 6 V to allow a comparison between the two configurations and provide input for the decision of which voltage to begin with. This data will be excluded from

[1] Although the run was labeled by the name 3 V, not all the detectors were biased with this value. The ionization voltage bias for the four Ge detectors was in fact 3 V, while for the two Si detectors it was 3.8 V.

the current analysis, but will be included with the rest of the 6 V data that is being taken since the month of April 2002.

The 3 V data set under consideration, therefore, consisted of a total of 93 real days, corresponding to 65.1 live days and a total of 4.7 million events. Figure 8.1 shows a plot of the accumulated livetime as a function of elapsed (real) time. With the exception of the two periods during which the 3 V data was not taken, the slope is very close to 0.72, the expected value based on the trigger rate and DAQ dead time.

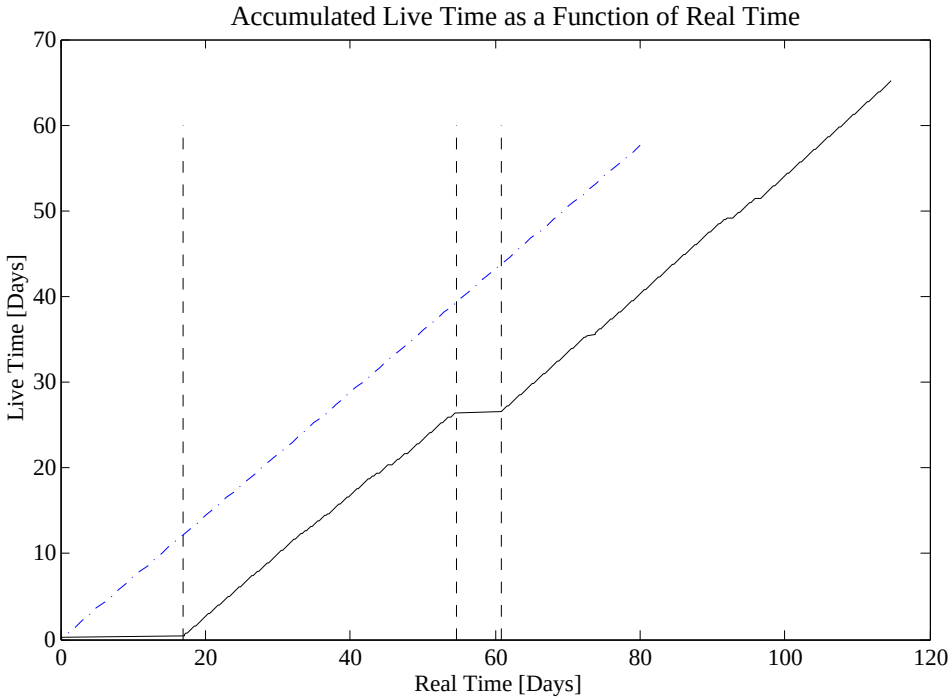

Figure 8.1: Accumulated livetime as a function of elapsed time for the 3V data set.

8.2 Muon Coincident Data

Of the 4.7 million recorded events, 3.6 million are coincident with activity in the muon veto, as defined in section 6.5 and Figure 6.38. Figure 8.2 shows the yield

distributions as a function of recoil energy for the six detectors. In addition to the dominating electron recoil band, a population of events is clearly seen within the nuclear recoil band.

Figures 8.3, 8.4, and 8.5 shows the recoil energy spectra of the bulk electron, nuclear, and surface electron recoils respectively. The muon coincident electron recoil rates are consistent with those measured in previous runs. The nuclear recoil rates, on the other hand, are suppressed by a factor of ~ 3, with respect to previous runs. The suppression is due to the polyethylene neutron moderator that was added prior to the beginning of Run 21. Monte Carlo predictions [69] of the nuclear recoil rate suppression are consistent with the measured value [70]. The muon coincident nuclear recoils are an important measure of the detector stability as shown is section 6.6.

Muon coincident surface electron recoils are more likely to be due to interactions in the surface layers of the detectors or to betas generated within the volume of the tower rather than due to detector surface backgrounds [2]. This population of events provides an additional data set in which to study the correlation between risetime and yield for surface electron recoils.

[2]Event rates due to surface backgrounds, and thus uncorrelated with the muon veto, are suppressed severely by requiring coincidence with a muon. Such backgrounds will appear, instead, in the muon anticoincident data set.

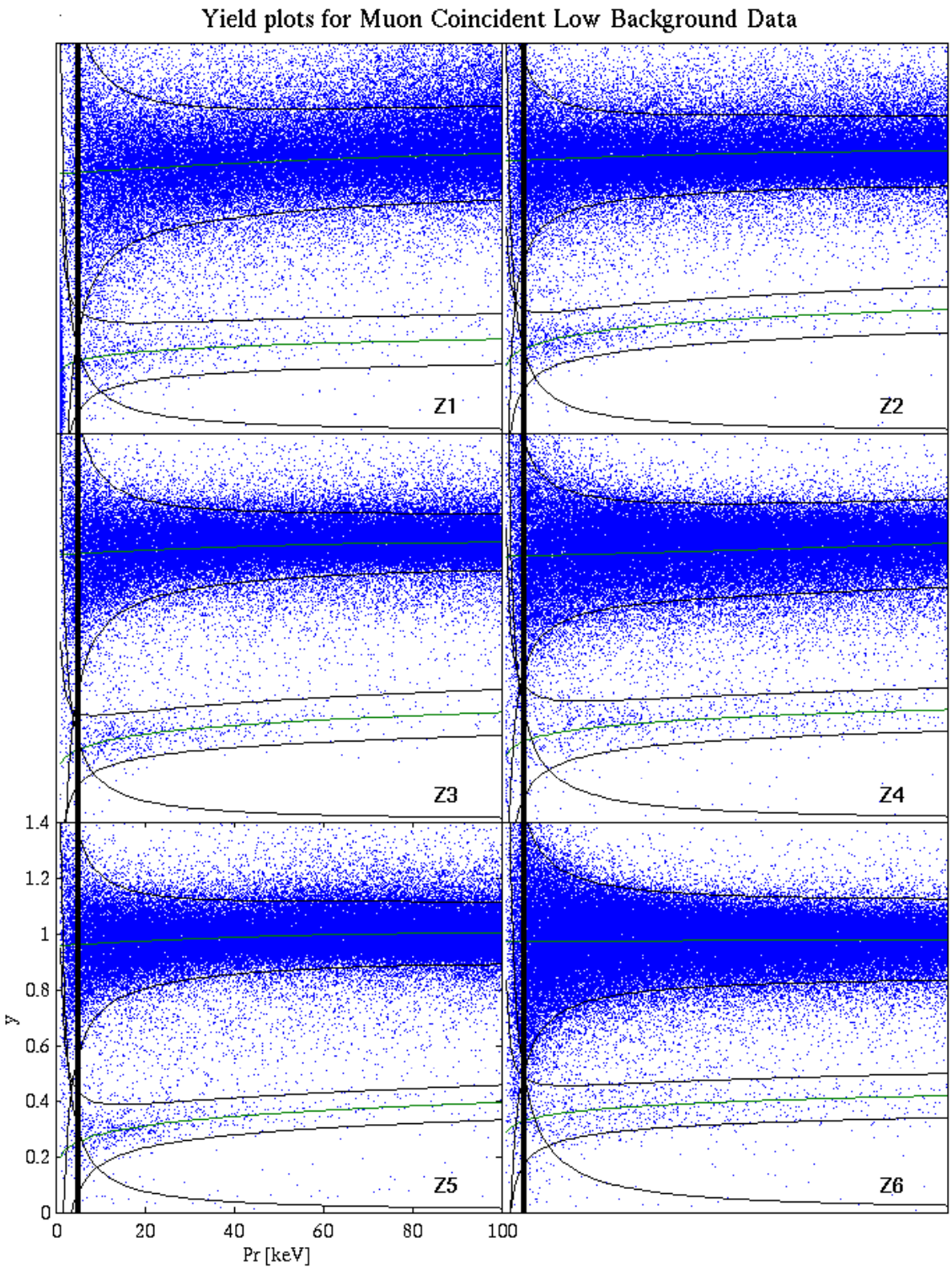

Figure 8.2: y plot of the muon coincident low background data.

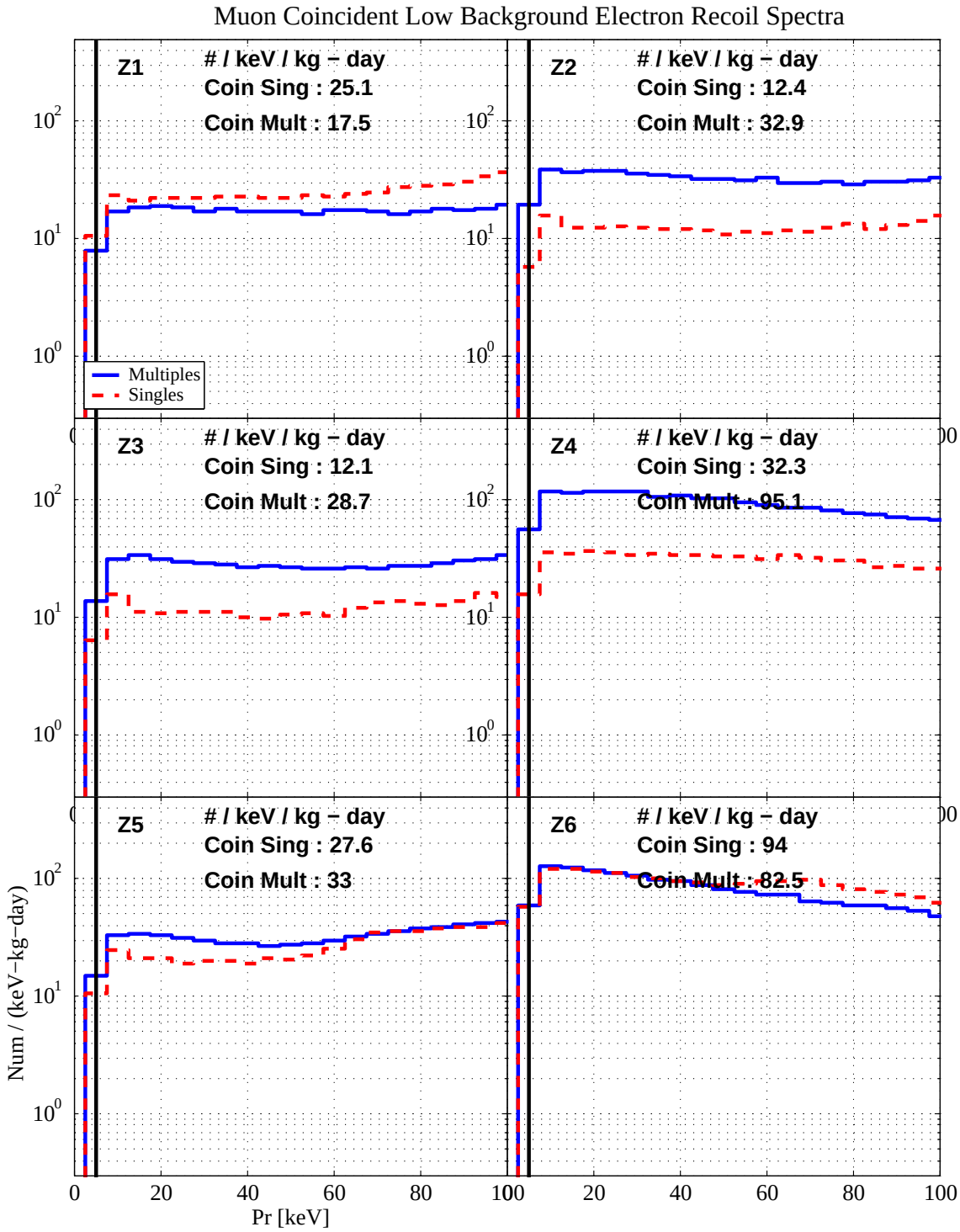

Figure 8.3: Muon coincident bulk electron recoil spectra. The dashed (solid) histogram corresponds to single (multiple) scatter events. The average rates, in units of events/keV-kg-day are indicated at the top of each panel.

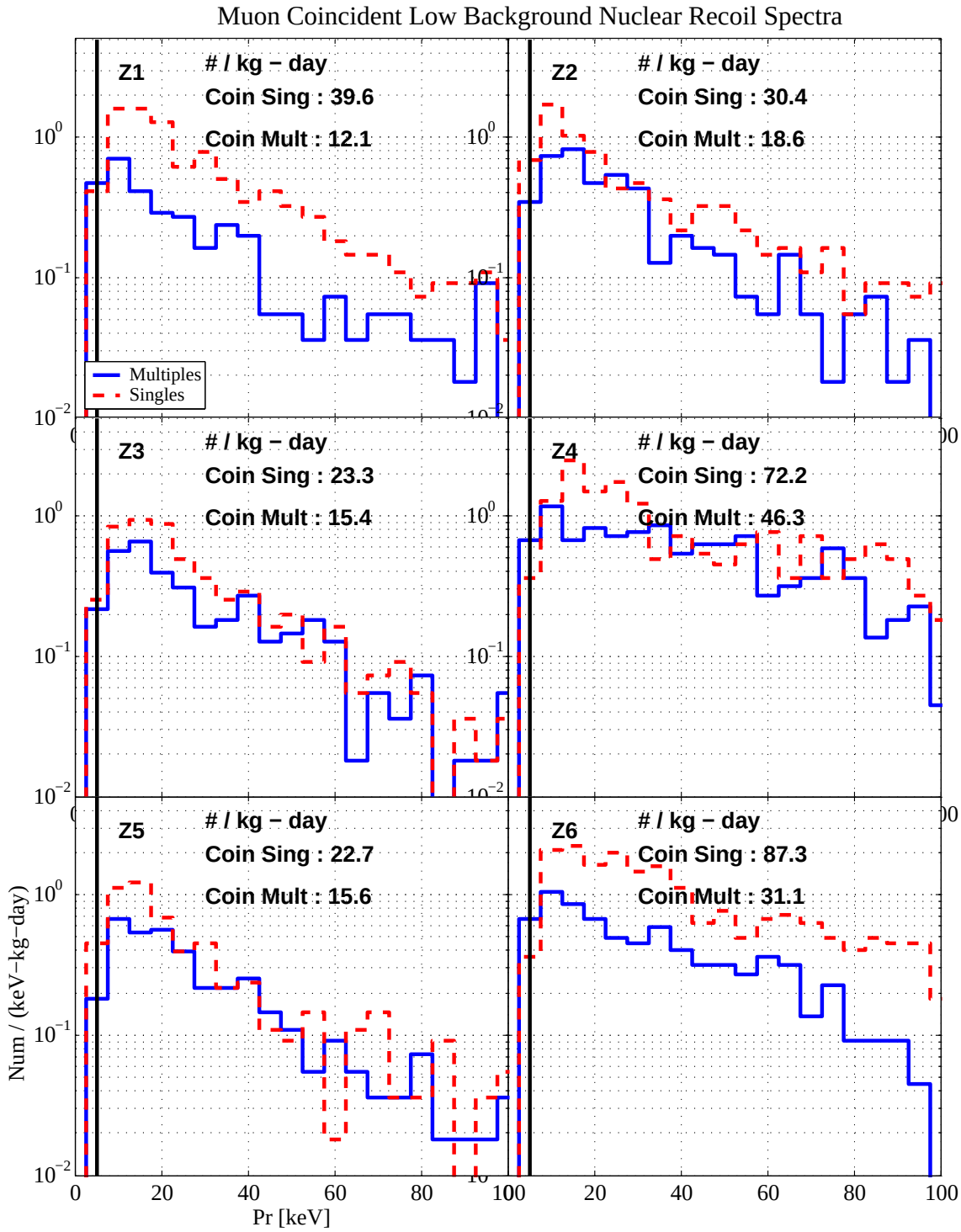

Figure 8.4: Muon coincident nuclear recoil spectra. The dashed (solid) histogram corresponds to single (multiple) scatter events. The average rates, in units of events/keV-kg-day are indicated at the top of each panel.

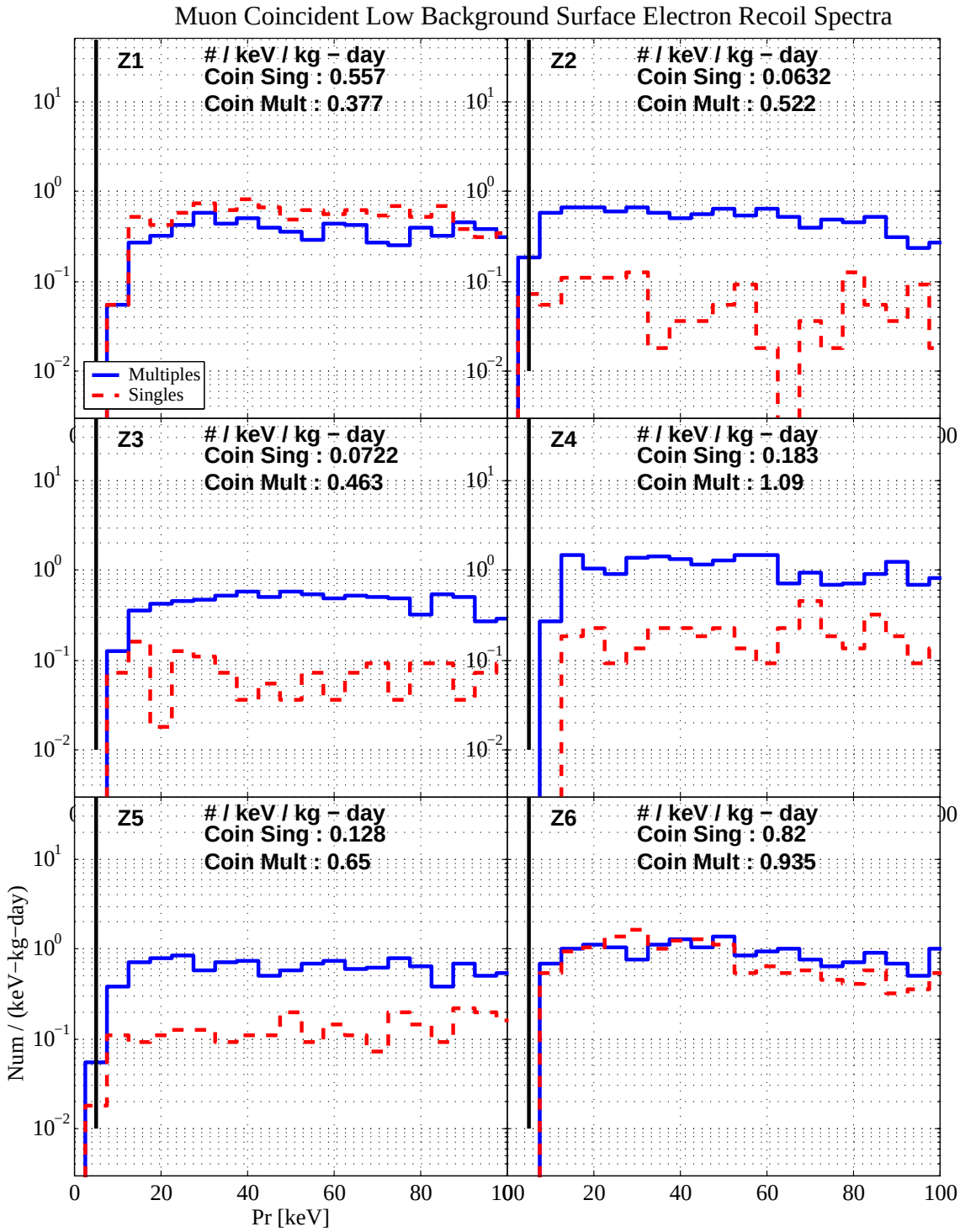

Figure 8.5: Muon coincident surface electron recoil spectra. The dashed (solid) histogram corresponds to single (multiple) scatter events. The average rates, in units of events/keV-kg-day are indicated at the top of each panel.

8.3 Muon Anticoincident Data

The yield distribution of the muon anticoincident data set is shown in Figure 8.6. Figures 8.7, 8.9, and 8.8 show the recoil energy spectra of the bulk electron, nuclear, and surface electron recoils respectively.

8.3.1 Gammas & Betas

Figures 8.7 and 8.8 shows the recoil energy spectra of the bulk and surface electron recoils respectively. Based on the electron recoil rejection (Table 6.5) and the measured muon anticoincident electron recoil rates the expected leakage into the nuclear recoil band is expected to be < 1 event for most of the detectors. The expected number of bulk electron recoils leaking into the nuclear recoil band is given in Table 8.1 for the entire energy range (5-500 keV) as well as for low and high energy ranges, 5-30 keV and 30–100 keV respectively. Also shown in Table 8.1 is the expected number of surface electron recoils leaking into the nuclear recoil band based on the method described in section 6.4.

8.3.2 Anticoincident Nuclear Recoils

Figure 8.9 shows the nuclear recoil spectra for the muon anticoincident data set, without the application of the risetime cut. The number of observed nuclear recoils in Z2–Z5 cannot be accounted for by possible electron leakage. The measured nuclear recoil rate is roughly a factor of two lower than that measured in previous runs and is compatible with the expected effect of the added polyethylene moderator. Z1 shows a very high rate at low recoil which drops off quickly above 20 keV. The excess of events at low recoil, compared with other Ge ZIPs, is due to the misidentification of a fraction of muon coincident Z1 recoils as being muon anticoincident. This effect is explained in section 8.4. The high rate seen in Z6 is consistent with β leakage into

	Detector					
Energy Bin	Z1	Z2	Z3	Z4	Z5	Z6
Gammas						
5-30	2.4	0.14	0.28	0.33	0.078	1.05
30-100	0.66	0.081	0.18	0.29	0.070	0.78
5-100	2.7	0.14	0.36	0.49	0.72	1.71
Betas without risetime cut						
5-20	33	0.44	0.11	0.47	0.56	5.6
20-40	1.0	0.70	0.55	0.0	1.3	4.5
40-60	0.63	0.25	0.37	0.39	0.90	1.8
60-100	1.3	0.0	0.50	0.0	1.6	2.3
Betas with risetime cut						
5-20	4.0	0.0	0.06	0.0	0.11	0.51
20-40	0.0	0.0	0.18	0.0	0.64	0.17
40-60	0.06	0.0	0.0	0.0	0.23	0.18
60-100	0.15	0.0	0.0	0.0	0.54	0.15

Table 8.1: Expected number of bulk and surface electron recoil leaking into the nuclear recoil band. The top section of the table (gammas) lists the 90% CL maximum number of bulk electron recoils that are expected to appear in the nuclear recoil band. The risetime cut was not used in this estimate. The second and third section lists the expected number of surface electron recoils (without and with the risetime cut) as determined by the method described in section 6.4.

the nuclear recoil band (section 8.4) although estimates of β leakage such as the one shown in Table 8.1 appear to misestimate the rate.

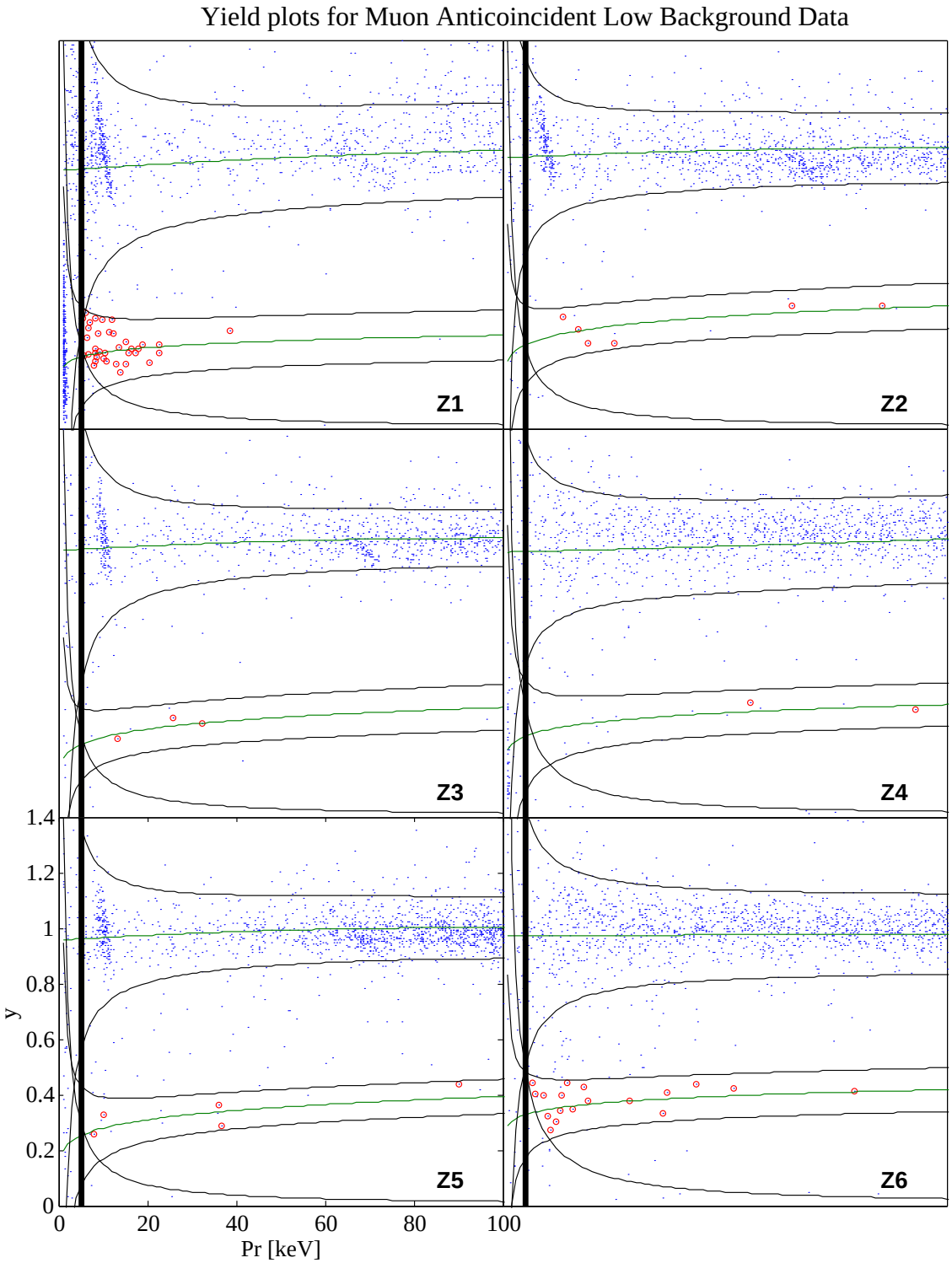

Figure 8.6: y plot of the muon anticoincident low background data. Single scatter nuclear recoils passing all cuts, including the risetime cut, are highlighted with small circles.

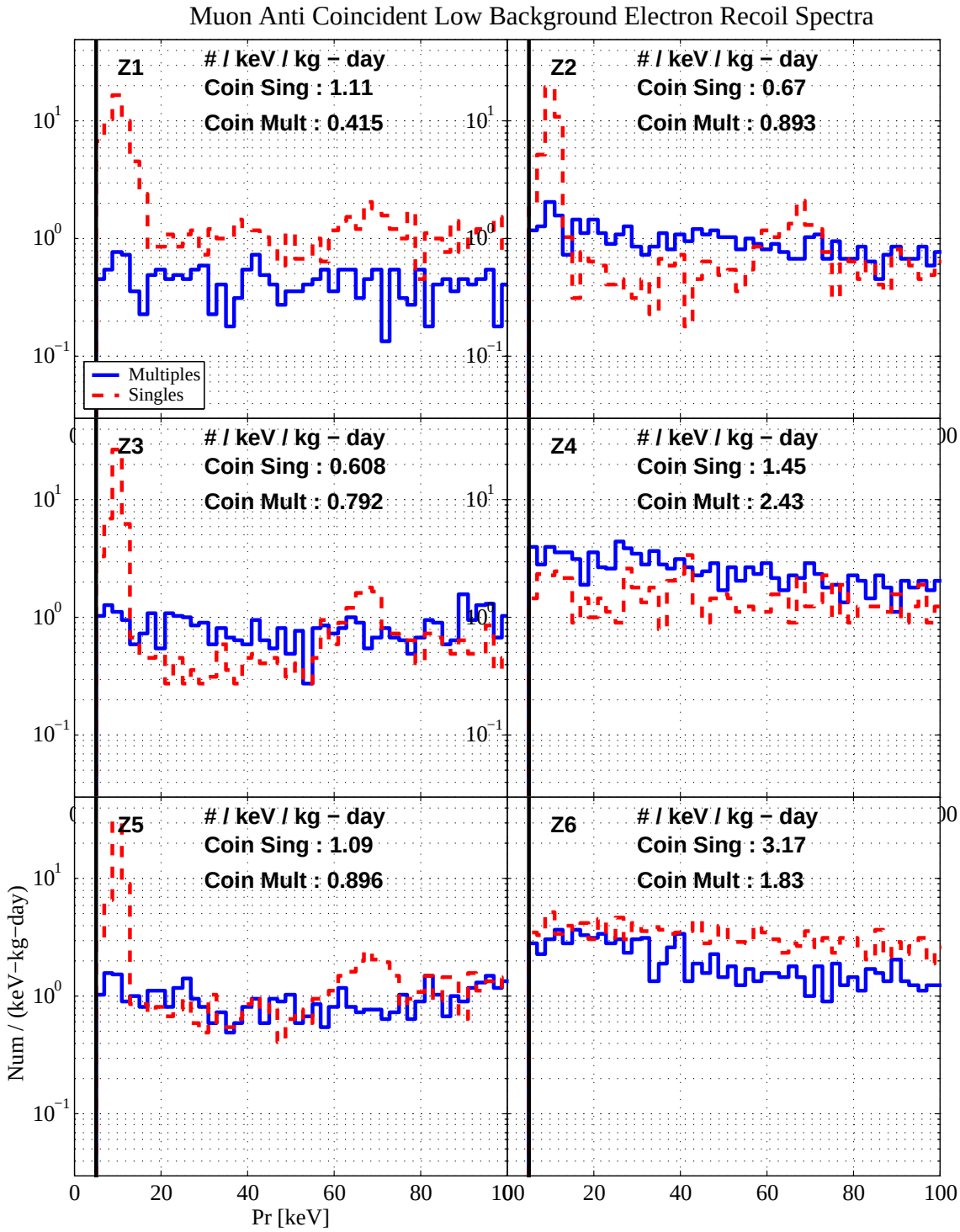

Figure 8.7: Muon anticoincident bulk electron recoil spectra. The dashed (solid) histogram corresponds to single (multiple) scatter events. The average rates, in units of events/keV-kg-day are indicated at the top of each panel.

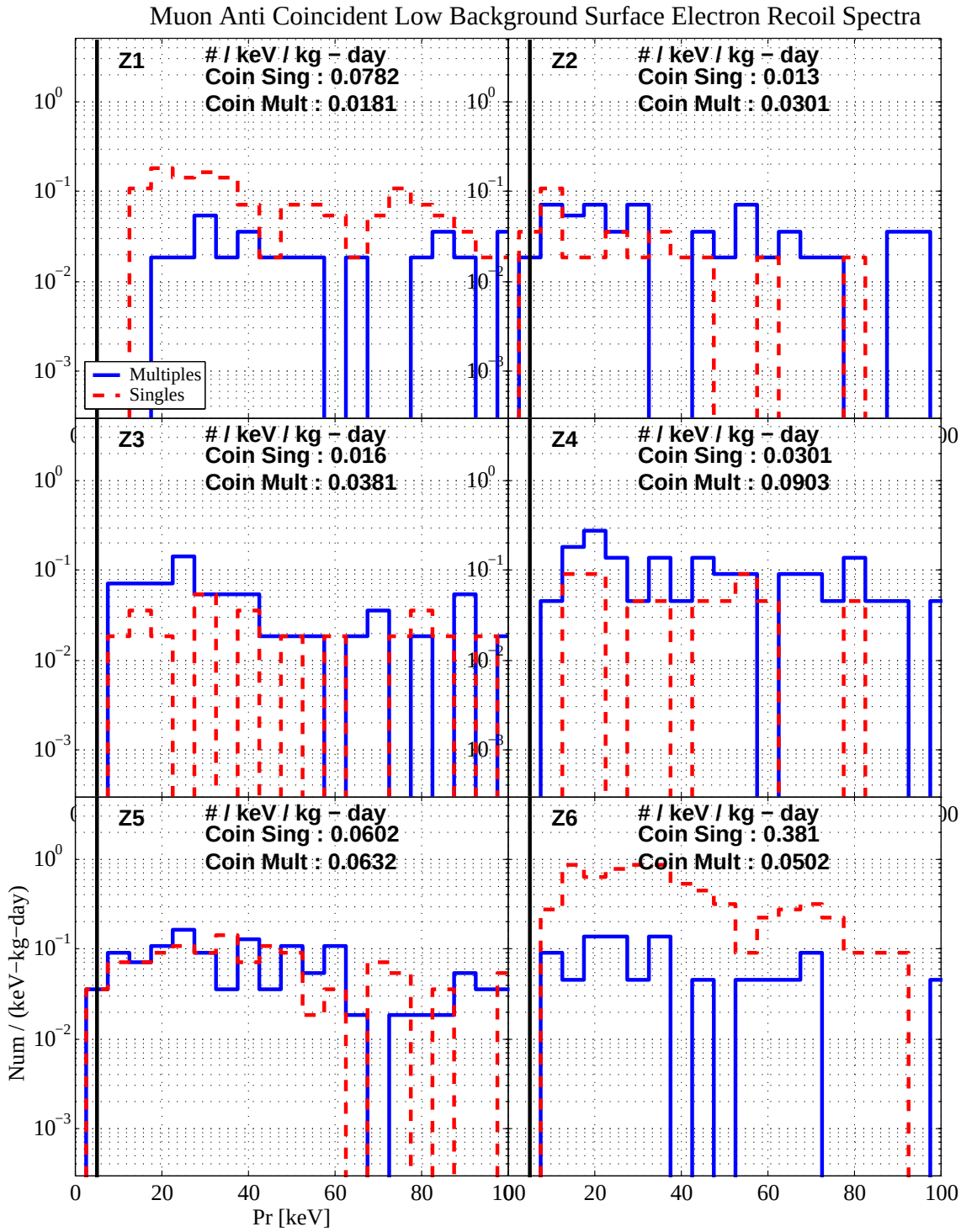

Figure 8.8: Muon anticoincident surface electron recoil spectra. The dashed (solid) histogram corresponds to single (multiple) scatter events. The average rates, in units of events/keV-kg-day are indicated at the top of each panel.

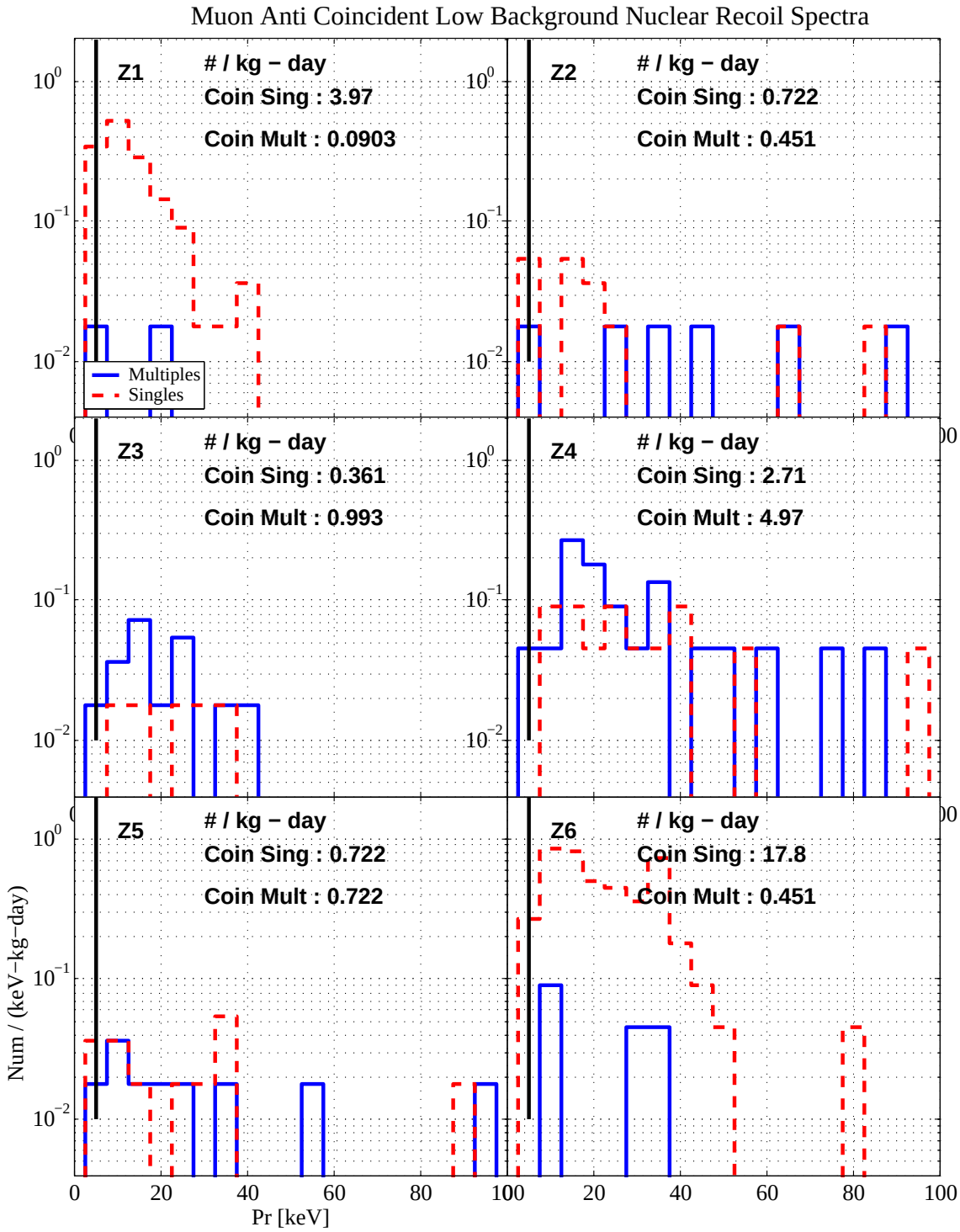

Figure 8.9: Muon anticoincident nuclear recoil spectra. The dashed (solid) histogram corresponds to single (multiple) scatter events. The average rates, in units of events/keV-kg-day are indicated at the top of each panel.

8.4 Statistical Tests

In order to determine whether the muon anticoincident nuclear recoils were consistent with a potential WIMP signal or a veto anticoincident neutron background, Kolmogorov-Smirnov tests were performed on a number of event parameters. The Kolmogorov-Smirnov (KS) test consists of comparing the cumulative distribution function (CDF) of the data with that of the hypothetical event source. The result returned by the KS test is the probability that a random set of events drawn from the hypothetical distribution is in worst disagreement than the data. In general, data distributions with KS values as low as 5% may be interpreted as being consistent with the hypothetical distribution since the data is still within 3σ of the expected distribution.

The parameters for which the KS test was performed are listed below

Time to Previous Veto Hit This is the parameter that is used to determine whether an event is coincident or anticoincident with a muon. For events that are anticoincident and uncorrelated with muons, the expected distribution of the time between the event and the most recent muon is an exponential, whose slope is determined by the average muon rate.

y^* This parameter is based on the standard yield parameter (y). y^* is defined as

$$y^* = \frac{y - y_{nr}}{\sigma_{nr}} \tag{8.1}$$

where y_{nr} is the energy dependent mean of the nuclear recoil band and σ_{nr} is the energy dependent width. The distribution of y^*, for actual nuclear recoils, then becomes a Gaussian with a mean of 0, a 1σ width of 1, with no energy dependence.

Livetime This is a measure of the livetime, since the beginning of the data run, prior to each event. It is expected that the data are uniformly distributed in

this parameter, and any apparent structure would suggest sporadic or periodic bursts of events.

x, y These parameters are the reconstructed x and y interaction positions within the detectors. There is no a priori known distribution function for these parameters, however, it is possible to apply the KS test between a data set (the muon anticoincident events) and a calibration set (the muon coincident events).

The KS test was applied to data both with and without the application of the risetime cut. This was done in an attempt to determine the presence of and influence of β contamination in the distributions of the above parameters.

Figure 8.10 shows the muon veto time CDF (circles and crosses) along with an exponential CDF as expected for an uncorrelated event distribution. Detectors Z2–Z6 shows excellent agreement with being uncorrelated with muons in the veto. Events in Z1, however, show a strong correlation with muons, as seen by the sharp peak at small times. This correlation is examined as a function of recoil energy (as shown in Figure 8.11). The data's correlation with muons is seen to decrease and finally disappear as the recoil energy threshold is increased from 5 keV to 25 keV. The explanation of this phenomena lies in Z1's large T_c gradient. Although the phonon response can be corrected offline (as described in section 6.2), this correction is not available for the online trigger. Consequently, there is a large spread in the time between an interaction and the time the phonon pulse surpasses the triggering threshold for events occurring in Z1, with the phenomena being more significant at low energies. The large *trigger time jitter* results in some muon coincident events appearing to be anticoincident (as defined by the muon anticoincidence cut). Trigger time jitter, due to variation in the phonon pulses, can be avoided by using a muon coincidence cut based on the time between the ionization pulse and the muon veto with such an approach being adopted for future analyses.

The y^* CDF for all six detectors are shown in Figure 8.12. Data from Z1–Z4 are consistent a normally distributed y^*, both with and without the use of the risetime cut, although for all four detectors, the data with the risetime cut is systematically in

better agreement with the expected CDF than the data without the risetime cut. This trend may suggest the presence of a small component due to non nuclear recoil events, such as low yield betas, although no definitive claim can be made. The situation is different for Z5 and Z6. The result of the KS test for Z6 data without a risetime cut is $6.6 \times 10^{-5}\%$, indicating that the data is highly inconsistent with a Gaussian distribution. Examining Figure 8.12 closely, however, shows that the distribution of low y^* events ($y^* < 0$) for Z6 appears to be in good agreement with a Gaussian distribution. Events with $y^* > 0$, however, appear peaked at $y^* \sim 2$. This strong evidence of a population low yield betas leaking into the nuclear recoil band is not altogether surprising since it is known that the surfaces of Z6 are contaminated with betas. However, the analysis of Z6 supports the interpretation of the Z5 KS results as being consistent with a small component of betas leaking into the nuclear recoil band.

The distribution of the livetime parameter is shown in Figure 8.13. There appears to be no evidence for a departure from a random distribution of livetimes for any of the detectors. Table 8.2 list the results of the KS tests for the aforementioned parameters as well as for the x,y distribution of the events.

	Detector					
KS Test	Z1	Z2	Z3	Z4	Z5	Z6
Time to Previous Veto	1^{-21}	92.6	32.2	99.6	18.3	21.9
	1^{-13}	81.6	78.2	97.8	16.1	81.1
y^*	22.4	19.6	41.1	27.0	2.41	7×10^{-5}
	64.1	77.9	59.5	60.9	4.38	31.7
Livetime	82.4	55.7	17.4	7.27	81.3	41.2
	85.8	60.7	9.55	22.5	78.4	54
x	0.0255	30.0	72.2	39.5	83.0	57.1
	43.2	51.1	86.1	90.8	99.6	40.2
y	18.0	8.9	14.1	42.0	6.86	2.2
	77.1	9.1	82.2	15.9	39.3	13.0

Table 8.2: Kolmogorov-Smirnov test of the distribution of various parameters. The two rows quoted for each variable correspond to data without (with) applying the risetime cut.

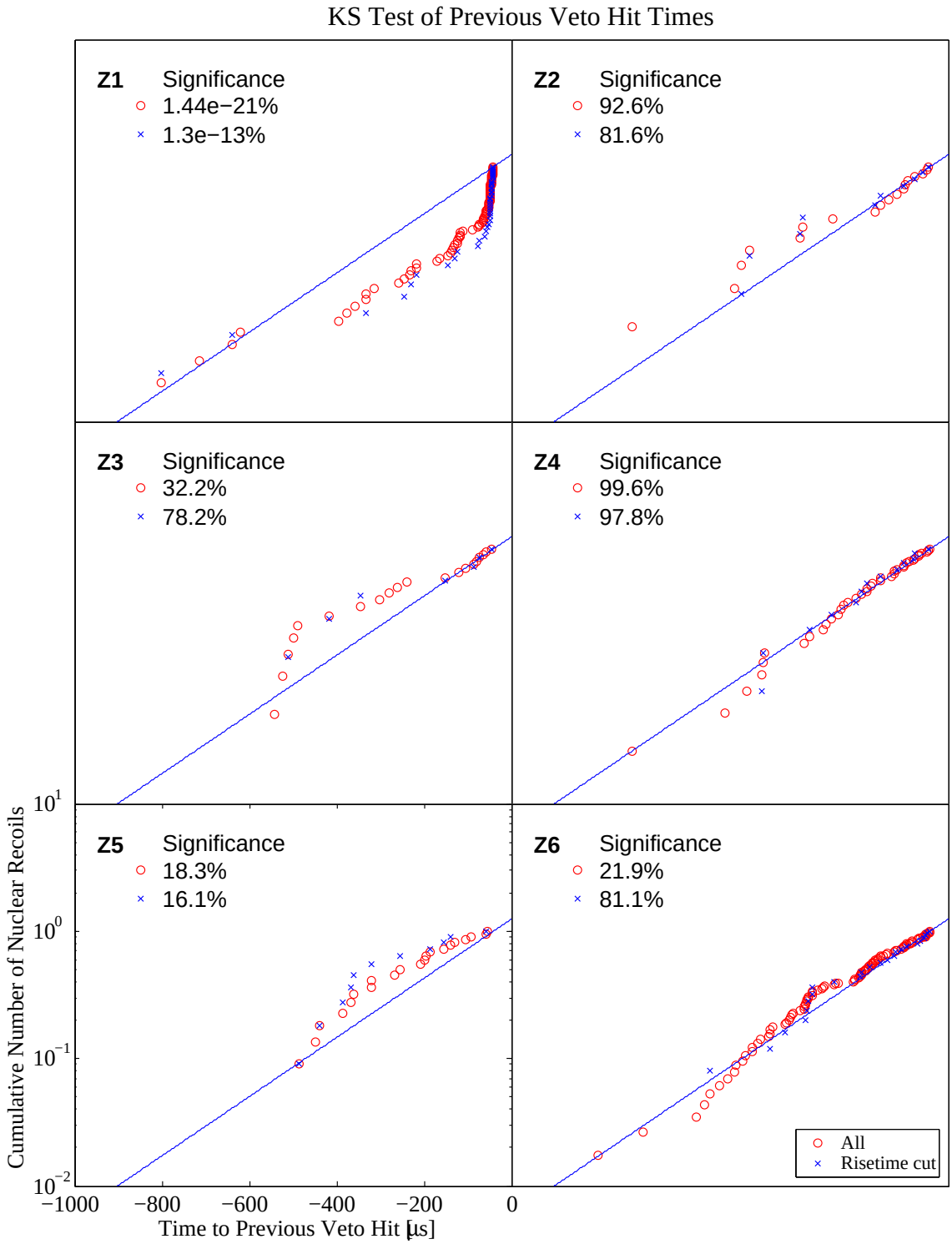

Figure 8.10: Kolmogorov-Smirnov test of the veto time distributions. With the exception of Z1, the events appear uncorrelated with the muon veto for all the detectors.

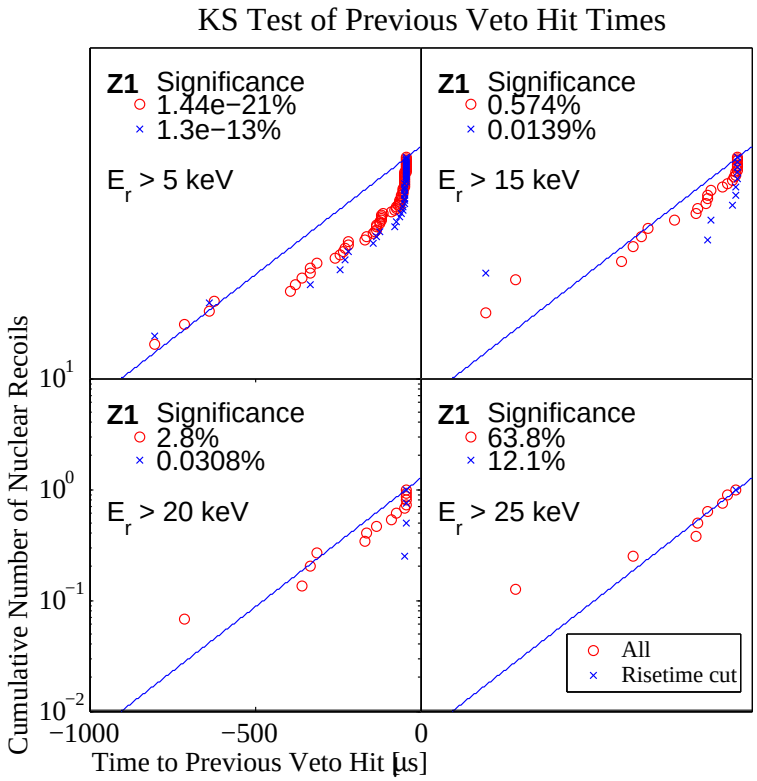

Figure 8.11: Kolmogorov-Smirnov test of the veto time distributions for Z1. As the energy threshold is increased the events become less correlated with the muon veto. This indicates the variation in the phonon pulse risetimes is quite significant for events with $E_r < 25\,\mathrm{keV}$.

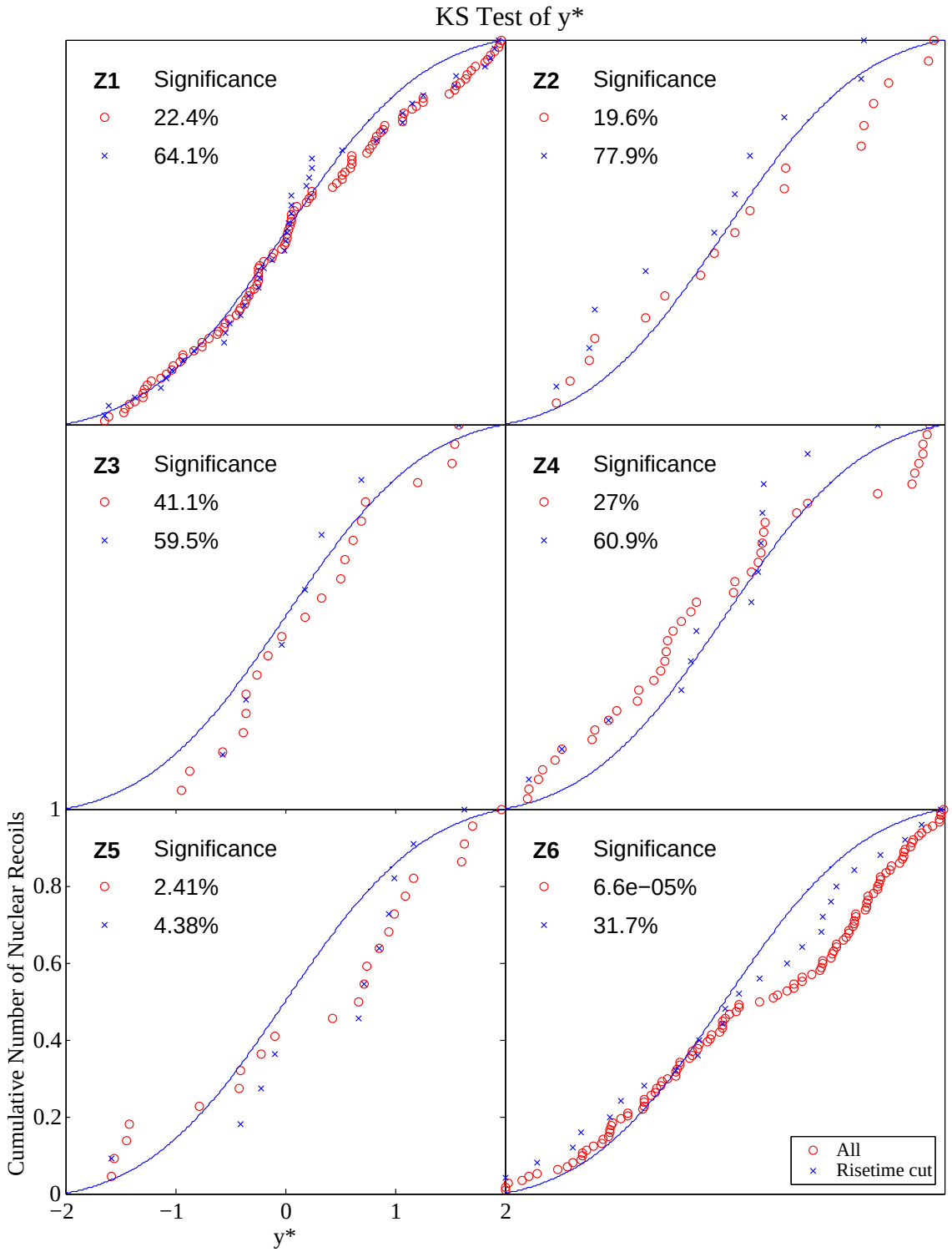

Figure 8.12: Kolmogorov-Smirnov test of the y^* distributions. Nuclear recoil events in Z1–Z5 are normally distributed in y^* with a mean of 0 and a standard deviation of 1. Z6 on the other hand, deviates strongly for values of $y^* > 0$ as a result of the large β rate leaking into the nuclear recoil band.

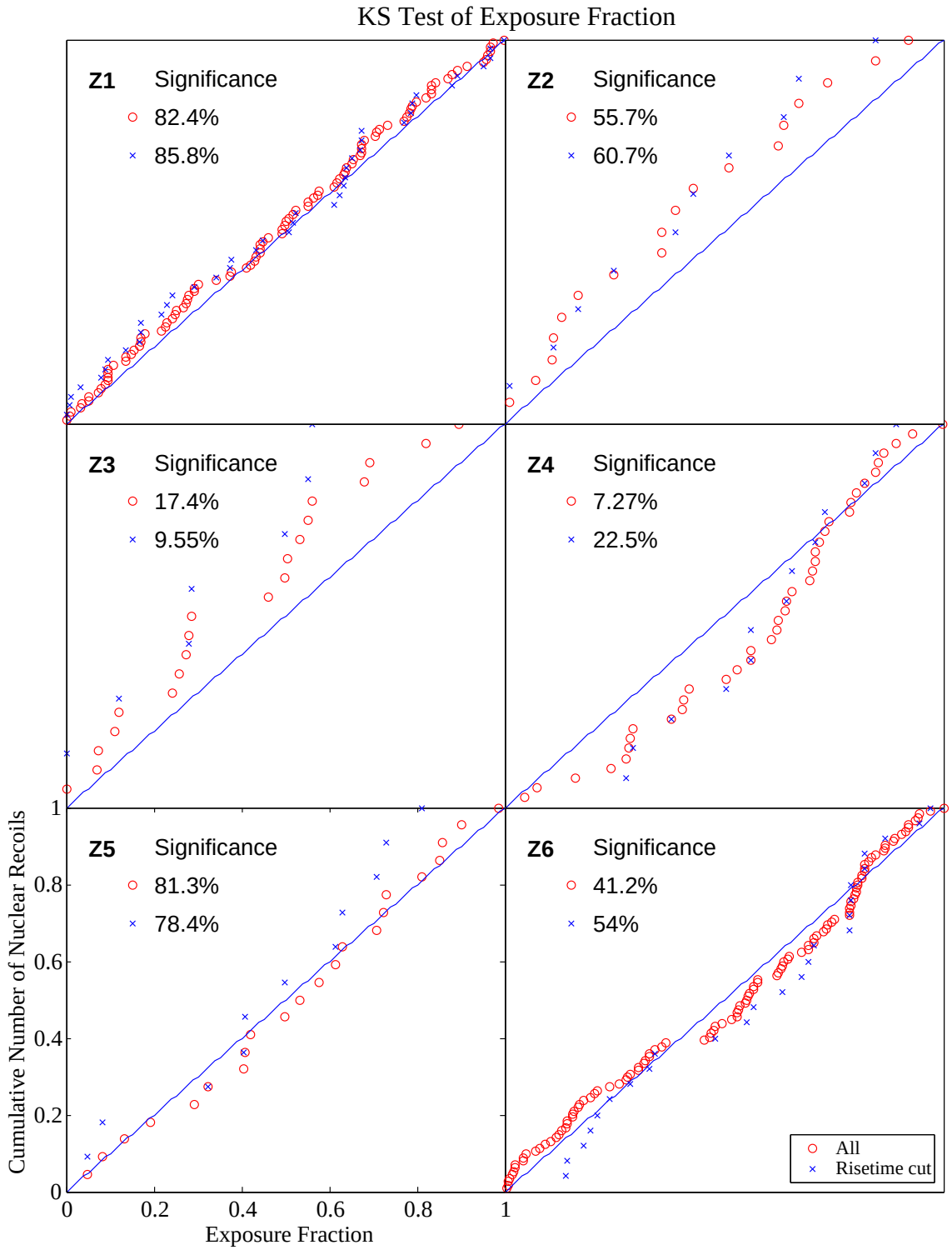

Figure 8.13: Kolmogorov-Smirnov test of the cumulative livetime distribution. All events appear uniformly distributed in livetime.

8.5 Determining the WIMP Exclusion Limit

Any possible WIMP signal will appear in the single scatter muon anticoincident nuclear recoil data set. However, there exists a background with the same signature. Neutrons created in the rock of the tunnel, may penetrate the shield and scatter in a detector while leaving no signal in the plastic scintillator by which they can be vetoed. Understanding the contribution of this background, referred to as *external neutrons*, to the measured nuclear recoil rate is important in determining the WIMP mass – cross-section exclusion limit. For the purposes of determining the limit, detector Z6 was excluded from the analysis due to the high rate of β contamination. In addition, the phonon recoil threshold for Z1 was raised to 20 keV, instead of 5 keV. The resulting efficiency for single scatter nuclear recoils in Ge is shown in Figure 8.14. Convolving this efficiency with the observed single scatter nuclear recoil spectrum yields a result consistent with a Monte Carlo simulation of external neutrons [71] as shown in Figure 8.15. A Kolmogorov-Smirnov test of the observed nuclear recoil spectrum and what is expected due to external neutrons yields 49%, indicating a high degree of compatibility.

The measured nuclear recoil rate in Si ZIPs, as well as the rate of multiply scattered nuclear recoils in Ge and Si can be used to determine the number of single scatter nuclear recoils due to external neutrons. Figure 8.16 shows the expected relative rates of multiple scatter in all detectors, single scatter in Si, and single scatters in Ge ZIPs. The Monte Carlo predictions [69] are normalized to the measured single scatter rate in Ge, and show excellent agreement with the data strongly supporting the hypothesis that the observed muon anticoincident nuclear recoils are due to external neutrons. The resulting WIMP mass – cross-section upper limit is shown in Figure 8.17.

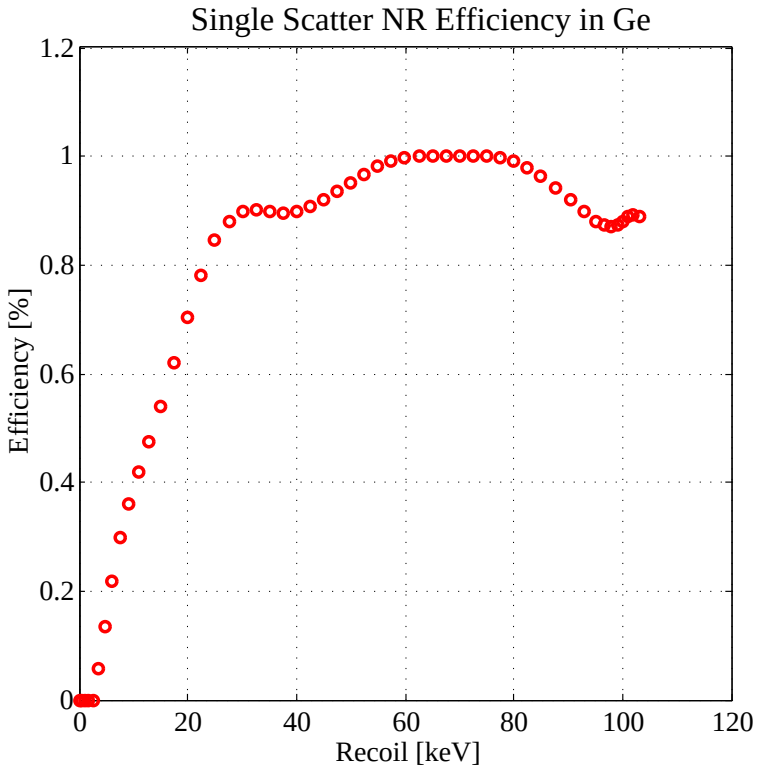

Figure 8.14: Single scatter nuclear recoil efficiency in Ge ZIPs. The efficiency, normalized to a maximum of 1 corresponds to a total exposure of 27.3 kg-days and takes into account the 20 keV recoil threshold used for Z1.

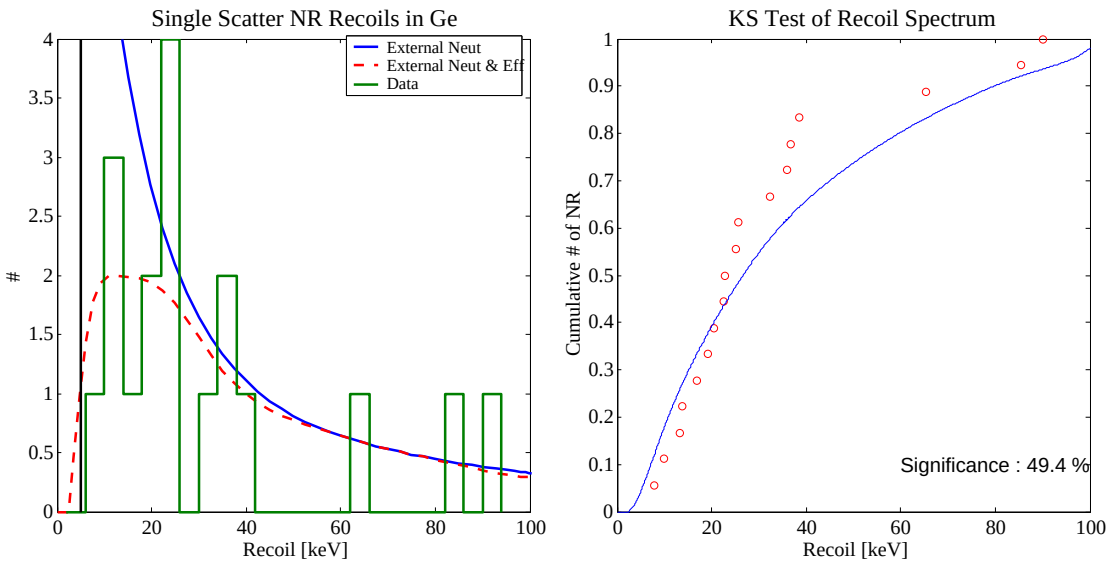

(a) (b)

Figure 8.15: Comparison of the single scatter nuclear recoil spectrum in Ge ZIPs with the external neutron Monte Carlo spectrum [71] before (solid line) and after (dashed line) the application of the nuclear recoil detection efficiency (a). A Kolmogorov-Smirnov test of the measured and Monte Carlo spectra yields 45% (b).

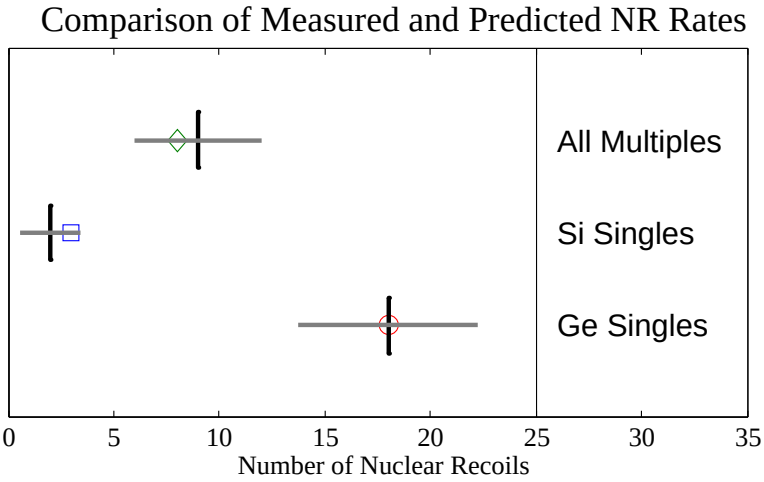

Figure 8.16: Comparison of Monte Carlo predictions [69] (symbols) for the rate of multiple scatters, single scatters in Si, and single scatters in Ge with data (crosses). The Monte Carlo results are normalized to the rate of Ge single scatters and the width of the crosses correspond to the Poisson error on the observed number of events.

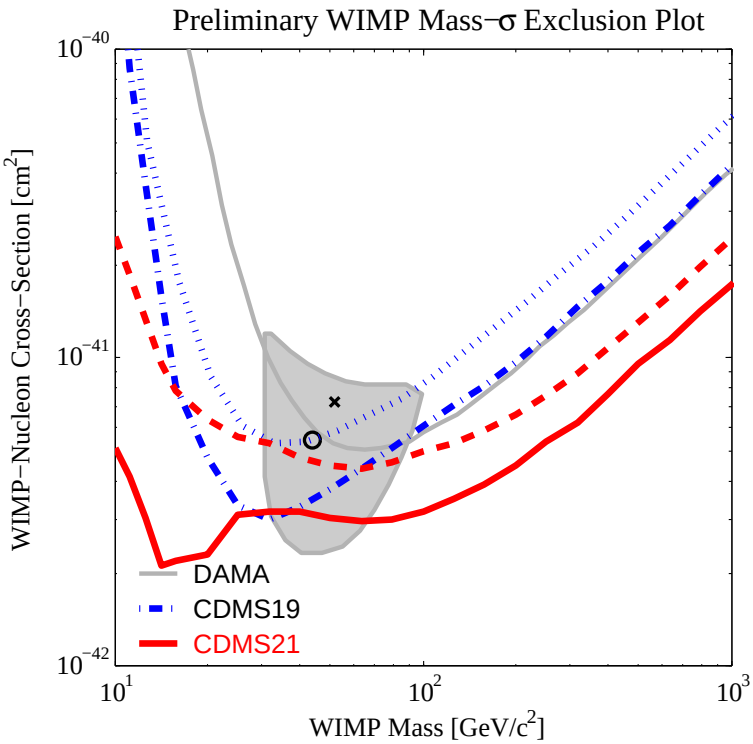

Figure 8.17: WIMP mass – cross-section exclusion plots. This result is based on the 3V data set taken during Run 21. The solid line is the result of Run 21 obtained by subtracting the contribution of the external neutrons from the nuclear recoil rate, while the dashed line is the result if all of the nuclear recoils are assumed to be of unknown origin. The dash-dotted and dotted lines are the equivalent results from Run 19. Also shown is the DAMA exclusion limit (light solid line) and detection claim (filled region). Figure taken from [69]

Chapter 9

Conclusion

During the past few years the development of ZIP detectors has led to full scale production of the ZIPs required for the CDMS II experiment. Run 21 highlighted the capabilities of these detectors, such as sub- keV energy resolution, bulk electron recoil discrimination of 99.99% between 5 and 100 keV, and surface electron recoil discrimination of better than 98% using a combination of yield and risetime information. Measurements of the background interaction rates seen by the six detectors of Tower 1, combined with the discrimination capabilities resulted in the Dark Matter limit shown in Figure 8.17. The installation of the Tower 1 detectors at the Soudan deep site, however, is required to take full advantages of the detectors' capabilities and extend the sensitivity of the CDMS II experiments to regions of WIMP parameter space where a number of SUSY models may be verified or refuted. In fact recent results from the Muon g-2 collaboration [72] indicate the possible existence of WIMPs with cross-sections that may be within the reach of direct detection experiments within the next few years. The future of the CDMS experiment promises to be an exciting one with lots of good science to appear in future theses.

Appendix A

Calculation of the Quasiparticle Collection Efficiency

This appendix contains the Matlab code used to calculate the quasiparticle collection efficiency as a function of Al fin length. The function `Coll_fix` takes as an argument the number of TESs in a (5 mm)^2 cell and returns two vectors containing the Al fin lengths (`lvec`) and their respective quasiparticle collection efficiencies (`Coll_vec`). The rest of the listed function are called from within `Coll_fix`.

```
Coll_fix.m :

function [lvec , Coll_vec] = Coll_fix(Nsens)

  %For 360 micron this Al

  lf = [20 40 60 80 100 120 140 160 180 200 220 240 260 280 ...
300 320 340 360 380 400 420 450 500 550 600 650 700 ...
750 800 850 900 950 1000];
```

```
  AbsQP = [0.9981 0.9944 0.9887 0.9811 0.9718 0.9609 0.9485 0.9347 ...
0.9197 0.9033 0.8856 0.8664 0.8456 0.8233 0.7999 0.7756 0.7507 ...
0.7257 0.7009 0.6764 0.6526 0.6182 0.5656 0.5190 0.4782 0.4427 ...
0.4116 0.3844 0.3605 0.3394 0.3206 0.3037 0.2885];

  lvec = lf;
  Coll_vec = (NumQP(lf,Nsens).*AbsQP);

  %----------------------

function ans = AbsQP(lfin)

  ldiff = 360;
  ans = (ldiff./lfin).*(1-exp(-lfin./ldiff));

  %-----------------------

function ans = NumQP(lfin,Nsens)

  lambda = 0.3;
  ans = ((1-alpha(lfin,Nsens).^10)./(1-alpha(lfin,Nsens))).* ...
              (efin(lfin,Nsens)*lambda);

  %------------------------

function ans = alpha(lfin,Nsens)

  lambda = 0.3;
  egrid = 0.2;
  deadarea = 1368000;atot = 5000*4900;
```

```
  edead = deadarea/atot;

  ans = (1- lambda*(efin(lfin,Nsens) + edead))*(1 - lambda*egrid);

  %--------------------------

function ans = efin(lfin,Nsens)

  Atot = 5000*4900;
  wfin = 50; Nfins = 11;

  ans = Nsens*Nfins*lfin*wfin/Atot;

  %-----------------
```

Appendix B

Simulating IV Curves

This appendix contains the Matlab code used to simulate IV curves. The script `TES` is the top level script which calls the various other listed functions. Simulation input parameters are found in `Relements.m`.

`TES.m` :

```
% Calculates IbIs Curves and signal to noise for a given TES

clear all; clc
clf

%1- Initialize the various parameters

init

% Calculate some properties
```

```
  %Vs=[0.1:0.5:40]*1e-6;
  Vs=[0.1:0.3:60]*1e-6 * 0.5; %% The last number sets the resolution . kinda
  Vs=[0.1:0.3:60]*1e-6 * 0.4;
  P=[];T=[];R=[];ssn=[];

  [Peq,Req,Ib,Is,In2] = IbIs(Rmatrix,Tb,E,Rb,Vs,ph_par,W,d,L,Leff);
  sn = SigNoise(In2,Req,Rb,Vs);

  %%Now to cheat a little and put in Is such that it snaps :

  P = [P Peq']; %T = [T Teq'];
  R = [R Req']; %ssn = [ssn sn'];
  I = [Ib];
  V = [Vs];
  Is = [Is];

  %Make plots

  ppower(Ib,P,R);

%-----------------------------------------------

init.m :

  % Inital Tc and base Temp;
  Tc = 0.080; Tb = 0.040; %K

  %Bias resistor
  Rb = 0.020; % Ohm

  %Power Dissipation constant : P = EV(T^5 - T^5)
```

```
  E = 2.8e-9;% W/K^5/um^3;

  %TES Characteristics
  d = 0.04;% 40nm W thickness
  L = 250; Leff=1.2*L; % microns %% You should try Leff=1.15L
  W = 1;

  %Total resistance, and hence resistivity, I'll leave
  %to the Relements matrix
  Relements
  elementTc = Rmatrix(:,3);

  %Phase separation Variables :

  %Heat conduction down the line
  Kn=(2e-8./(Rmatrix(:,1)*d).*elementTc/4); % rho = R/sq*d =
                                            % (Rmatrix(:,1)*d
  Ks=Kn/3;
  Kb=(E*d)*(elementTc.^5 - Tb^5) ./ (elementTc - Tb);

  etan = sqrt(d*Kn./Kb);
  etas = sqrt(d*Ks./Kb);

  ph_par=[Kb,Ks,Kn,etas,etan];

%-----------------------------------------------

Relements.m :

  %- An array of resistive elements with different Tc's width's etc
  %
```

```
  %   Rsq | w | Tc | Num | Ph
  %    .    .    .    .    .
  %    .    .    .    .    .
  %
  % Rsq = Resistance per square for 40nm thick W
  %
  % Num = Number of elements with this property. This should be a
  %             multiplicative term.
  % Ph = whether it'll phase separate: 1=yes; 0=no.
  %

  re1 = [5.0, 0.005, 0.080, 168, 1]; % mOhm / mK / mK
  re2 = [5.0, 0.005, 0.090, 308, 1];
  re3 = [5.0, 0.005, 0.100, 364, 1];
  re4 = [5.0, 0.005, 0.115, 196, 1];
  %re5 = [5.0, 0.005, 0.115, 4*28, 1];

  Tb = 0.045;
  %Power Dissipation constant : P = EV(T^5 - T^5)
  E = 1.8e-9;% W/K^5/um^3;
  W = 0.7;

  Rmatrix = [re1;re2;re3;re4];%re5];

%-----------------------------------------------

IbIs.m :


  %
  % function [Peq,Teq] = findBias()
```

```
%
% Calculates the equilibrium Power and Temperature for a given Ib
%

function [Peq_tot,Req_tot,Ib,Is,In2] =
                    IbIs(Rmatrix,Tb,E,Rb,Vs,ph_par,W,d,L,Leff)

%% Rmatrix containes [R/square TransitionWidth Tc
%%                                   ElementWeighting PhaseSep]
%% Tb : Tbase of the fridge (in K)
%% E  : (Sigma) Power dissipation constant ~ 2.8e-9 W/K^5/um^3
%% Rb : Bias Resistor (20 mOhm)
%% Vs : Input sensor bias voltage array
%% ph_par : Contains the parameters required to do the phase
%%          separation calculation
%% W/d/L  : Physical dimensions of the TESs
%% Leff   : Effective L for the purposes of phase separation

  kill=0;

  Peq_tot = zeros(1,length(Vs));
  Teq_tot = zeros(1,length(Vs));

  Rn = Rmatrix(:,1)*L/W;
  w  = Rmatrix(:,2);
  Tc = Rmatrix(:,3);
  ph_sep = Rmatrix(:,5);

  Kb=ph_par(:,1);
  Ks=ph_par(:,2);
  Kn=ph_par(:,3);
```

```
  etas =ph_par(:,4);
  etan =ph_par(:,5);

  for ii=1:length(Vs)
    nelements = size(Rmatrix,1); % Number of TES 'zones' with
                                 % different (Tc) parameters

    Peq = zeros(1,nelements);
    Teq = zeros(1,nelements);
    Req = zeros(1,nelements);

    for jj=1:nelements;
      if(ph_sep(jj))  % i.e. if there is phase separation
ro = Rn(jj)*W*d/L;
par = [Kb(jj) Ks(jj) Kn(jj) W d ro Rn(jj) Tc(jj) Tb L Leff ...
                   etas(jj) etan(jj) Vs(ii)];
[Req(jj)] = findBias_PhSep(par);
Peq(jj)=Vs(ii)^2/Req(jj);
Peq(jj)=Peq(jj)*Rmatrix(jj,4);
Teq(jj)=Tc(jj);
if(Rmatrix(jj,4)==0)
  Req(jj)=Inf;
else
  Req(jj)=Req(jj)/Rmatrix(jj,4);
end

      else % if there is no phase separation, i.e. plain old TES

k=E*(W*L*d); % Power dissipation constant scaled to the volume of
                     % the TES
[Peq(jj),Teq(jj)] = ...
```

```
    findBias_Plain(Rn(jj),w(jj),Tc(jj),Tb,k,Vs(ii));
Peq(jj)=Peq(jj)*Rmatrix(jj,4); % Weigh the power by the number of
                                        % TES elements at that Tc
if(Rmatrix(jj,4)==0)
  Req(jj)=Inf;
else
  Req(jj)=Rs(Teq(jj),w(jj),Rn(jj),Tc(jj))./Rmatrix(jj,4);
end
      end
    end %% of loop over the Tc zones (i.e. nelements)

    Rparasitic=0; %%% Should feed it in as an input parameter
    Rcircuit = Rparasitic+Rb;

%    for jj=1:nelements
%      %find the parallel resistance
%      Rparallel = Req; Rparallel(jj)=[]; % <- Remove the jj'th
%                                % resistor from the calculation
%
%      if(length(Rparallel)==0)
% Rpar_tot = Inf;
%      else
% if(sum(1./Rparallel)==0)
%   Rpar_tot = Inf;
% else
%   Rpar_tot  = 1./sum((1./Rparallel));
% end
%      end
%    end
%      in2(jj)=Inoise_e(Req(jj),Rpar_tot,Rcircuit,Teq(jj));
```

```
      Peq_tot(ii) = sum(Peq);
      Is(ii) = sum(Vs(ii)./Req);
      Req_tot(ii) = Vs(ii)/Is(ii);

      bandwidth=[10e-6,200e-6];  %risetime = 10us -> falltime = 200 us
      In2(ii) = Inoise(mean(Teq),Req_tot(ii),Rcircuit,bandwidth) ;
      Ib(ii) = (Req_tot(ii)/Rb + 1)*Is(ii);
    end %of Vs loop

%-----------------------------------------------
```

findBias_Plain.m :

```
  %
  % function [Peq,Teq] = findBias()
  %
  % Calculates the equilibrium Power and Temperature for a given Ib
  %

  function [Peq,Teq] = findBias_Plain(Rn,w,Tc,Tfr,k,Vs)

  %- Find the bias point for a range of Vb's

    defaultopt = optimset('display','final','TolX',eps); %% This is used
                                                %to suppress the VERY
                                                %annoying
                                                %grandfather warnings

    par = [Rn,w,Tc,Tfr,k,Vs];
    x1 = Tc-2*w+0.000001;x2=200/1000;
```

```
    Teq = fzero('power_Plain',[x1 x2],defaultopt,par);
    Peq = k*((Teq^5 - Tfr^5));

%-----------------------------------------------

findBias_PhSep.m :

  %
  % function [Veq,Req] = findBias()
  %
  % Calculates the equilibrium Power and Temperature for a given Ib
  %

  function [Req] = findBias_PhSep(par)

    defaultopt = optimset('display','final','TolX',eps); %% This is used
                                                %to suppress the VERY
                                                %annoying
                                                %grandfather warnings
    Kb = par(1);
    Ks = par(2);
    Kn = par(3);
    W  = par(4);
    d  = par(5);
    ro = par(6);
    Rn = par(7);
    Tc = par(8);
    Tb = par(9);
    L    = par(10);
    Leff = par(11);
    etas = par(12);
```

```
    etan = par(13);
    Vin  = par(14);

    x1 = 0.001;x2=L/2; % microns

    if(power_PhSep(x2,par)>0)
      x0=L/2;
    else
      x0 = fzero('power_PhSep',[x1 x2],defaultopt,par);
      i0 = sqrt(Kb*W^2*d*(Tc-Tb)/ro*(1+sqrt(Ks/Kn)* ...
                  tanh(Leff/2/etas-x0/etas)./tanh(x0/etan)));
    end

    %Veq = (2*x0/L)*Rn.*i0;
    Req = (2*x0/L)*Rn;

%-----------------------------------------------

power_Plain.m :

  %
  %   function [ans] = fz(T);
  %
  %   ans = Pcool - Pjoule;

  function ans = power_Plain(T,par);

    Rn = par(1);
    w  = par(2);
    Tc = par(3);
    Tfr= par(4);
```

```
    k  = par(5);
    Vs = par(6);

    Pcool = k*(T.^5 - Tfr^5);
    Pcool(T<=Tfr)=0;

    Vss = Vs*ones(1,length(T));
    Pjoule(T>=(Tc-2*w)) = Vss(T>=(Tc-2*w)).^2./ ...
                  Rs(T(T>=(Tc-2*w)),w,Rn,Tc);
    Pjoule(T<(Tc-2*w)) = 0;

    ans = Pjoule - Pcool;

%---------------------------------------------
```

power_PhSep.m :

```
  %
  %   function [ans] = fz2(T);
  %
  %   ans = Vin - Vsen

  function ans = power_PhSep(x0,par);

    Kb = par(1);
    Ks = par(2);
    Kn = par(3);
    W  = par(4);
    d  = par(5);
    ro = par(6);
    Rn = par(7);
```

```
    Tc = par(8);
    Tb = par(9);
    L    = par(10);
    Leff = par(11);
    etas = par(12);
    etan = par(13);
    Vin  = par(14);

    Isen = sqrt(Kb*W^2*d*(Tc-Tb)/ro*(1+sqrt(Ks/Kn)* ...
        tanh(Leff/2/etas-x0/etas)./tanh(x0/etan)));

    Vsen=(2*x0/L)*Rn.*Isen;

    ans = Vin - Vsen;

%-----------------------------------------------

Rs.m :

  %
  %   function [Res]=Rs(T,w,Rn,Tc);
  %
  %   ans = (Rn/2)*(tanh((T-Tc)/w)+1);
  %

  function ans = Rs(T,w,Rn,Tc);

    ans = (Rn/2).*(tanh(5./w .* (T-Tc)) + 1);

%-----------------------------------------------
```

SigNoise.m :

```
  %
  %   function ans=SigNoise(Rb,Ib,Ts,Rs);
  %
  %   ans = sig./noise;
  %   sig = 1./Vbias;
  %   noise = Inoise(Ts,Rs,Rb);

  function ans = SigNoise(In2,Req,Rb,Vs);

    k = 1.38e-23; % J/K Boltzmann's constant
    bandwidth = [10e-6,200e-6];  %risetime = 10us -> falltime = 200 us
    bw = 1/bandwidth(1)-1/bandwidth(2);
    Tb = 0.600; % K

    sig = 1./Vs; sig(sig<=0)=0;  % kinda simplistic at this point

    nbias2 = (4*k*Tb./Rb).*(Rb./(Req + Rb)).^2;
    ntot2 = nbias2+In2;
    ntot = sqrt(ntot2*bw);

    ans = sig./ntot;

%----------------------------------------------
```

Inoise.m :

```
  %
  %   function ans=Inoise(Ts,Rs,Tb);
  %
```

```
  function ans = Inoise(Ts,Rs,Rb,bw)

    k = 1.38e-23; % J/K Boltzmann's constant
    a = 100; %alpha
    n = 5;
    tau = 100e-6; %100 microsec
    w=[1/bw(2):10:1/bw(1)];

    if(Rs>0)
      ns2 = (4*k*Ts./Rs).*(Rs./(Rs + Rb)).^2;
      nph2= (4*k*Ts./Rs).*(n^2/a^2 + w.^2*tau^2)./(1 + w.^2*tau^2) + ...
  (4*k*Ts./Rs).*(n/2)./(1 + w.^2*tau^2);
    else
      ns2 = 0;nph2=0;
    end

    nph2 = sum(nph2);
    ans = ns2+nph2;


%-----------------------------------------------

ppower.m :

  %  function ans = ibisplot(filename,detname,fignum,outfile)

  function ans = ppower(ib,P,R)

    % Input Arguments :
    %  Make the 3 plots ...
```

```
    msize=8;

    %  P = [fliplr(P') P'];
    %  ib = [-fliplr(ib) ib];

    Pnormal = (ib*0.02/(0.02+max(R))).^2*max(R);

    plot(ib*1e6,P*1e12,'b.',ib*1e6,Pnormal*1e12,'r.', ...
                                 'markersize',msize-2);
    set(gca,'fontsize',10);
    grid on;
    ylabel('P[pW]');
    xlabel('W Bias Current [\muA]');
    %  vline(detbias,'r');

    printme=0;
    if (printme)
     figure(fignum)
     orient tall
     eval(['print ' outfile 'ibis.eps -f' int2str(fignum) ' -depsc2']);
     eval(['print ' outfile 'rvst.eps -f' int2str(fignum+1) ' -depsc2']);
    end

%-----------------------------------------------

ibisplot.m :

  %  function ans = ibisplot(filename,detname,fignum,outfile)

  function ans = ibisplot(P,R,ib,Is,T,name,outfile)
```

```
% Input Arguments :

if (nargin==6) % i.e. if outfile is provided
  printme = 1;
  msize=2;
else
  printme=0;
  msize=8;
end

sensor = name;
fignum=2;

%  Make the 3 plots ...

P = [fliplr(P') P'];
R = [fliplr(R') R'];
ib = [-fliplr(ib) ib];
Is = [-fliplr(Is) Is];

%-- Determine Range
xmax = max(ib*1e6);
xmax=1000;
y1max = max(Is(ib<1e-3)*1e6*1.1);
y2max = max(R(ib<1e-3)*1.1);
y2min = -y2max/10;
y3max = max(P*1e12*1.1);
y3min = -y3max/10;

g1 = (log10(xmax));
```

```
g2 = floor(g1);
grmax = floor(10^(g1-g2))*10^g2;
grpitch = 10^g2;
gridx = [-grmax:grpitch:grmax];
gridx = [-grmax:2*grpitch:grmax];


figure(fignum);
subplot(3,1,1);
plot(ib*1e6,Is*1e6,'markersize',msize);
set(gca,'fontsize',16);   %Can't get it to work at the start
title(['TES Characterisitcs: 'sensor]);   %
axis([-xmax xmax -y1max y1max]);
set(gca,'fontsize',10);
ylabel('I[\muA]');
grid on;
set(gca,'XTick',gridx);
%  vline(detbias,'r');

% grid on;

subplot(3,1,2);
plot(ib*1e6,R,'markersize',msize);
axis([-xmax xmax y2min y2max]);
set(gca,'fontsize',10);
grid on;
set(gca,'XTick',gridx);
ylabel('R[\Omega]');
grid on;
%  vline(detbias,'r');
```

```
    Pnormal = (ib*0.02/(0.02+max(R))).^2*max(R);

    subplot(3,1,3);
    %plot(ib*1e6,P*1e12,'markersize',msize);
    plot(ib*1e6,P*1e12,'b.',ib*1e6,Pnormal*1e12,'r.','markersize',msize);
    axis([-xmax xmax y3min y3max]);
    set(gca,'XTick',gridx);
    set(gca,'fontsize',10);
    grid on;
    ylabel('P[pW]');
    xlabel('W Bias Current [\muA]');
    %  vline(detbias,'r');

    %figure(fignum+1)
    %plot(abs(T)*1000,R,'.');
    %axis([45 165 -.5 max(R)+0.5]);
    %set(gca,'fontsize',16);
    %title(['R(' sensor ') vs. T']);
    %xlabel('T [mK]');
    %ylabel('R [\Omega]');

    if (printme)
      figure(fignum)
      orient tall
      eval(['print '  outfile 'ibis.eps -f' int2str(fignum) ' -depsc2']);
      eval(['print '  outfile 'rvst.eps -f' int2str(fignum+1) ' -depsc2']);
    end

%-----------------------------------------------
```

Bibliography

[1] E. E. Kolb and M. S. Turner. *The Early Universe*. Addison-Wesley, 1990.

[2] P. J. E. Peebles. *Principles of Physical Cosmolgy*. Princeton University Press, 1993.

[3] J. A. Peacock. *Cosmological Physics*. Cambridge University Press, 1999.

[4] W. L. Freedman *et al*. Final results from the hubble space telescope key project to measure the hubble constant. *Astrophysical Journal*, 553:47–72, 2001.

[5] P. de Bernardis *et al*. Multiple peaks in the angular power spectrum of the cosmic microwave background: Significance and consequences for cosmology. *Astrophysical Journal*, 564:559–566, 2002.

[6] R. Stompor *et al*. Cosmological implications of the maxima-1 high-resolution cosmic microwave background anisotropy measurement. *Astrophysical Journal, Letters*, 561:L7–L10, 2002.

[7] C. Pryke *et al*. Cosmological parameter extraction from the first season of observations with the degree angular scale interferometer. *Astrophysical Journal*, 568:46–51, 2002.

[8] A. V. Filippenko and A. G. Riess. Evidence from type ia supernovae for an accelerating universe. In *AIP Conference Proceedings*, volume 540, pages 227–246, 2000.

[9] W. Percival *et al.* The 2df galaxy redshift survey: the power spectrum and the matter content of the universe. *Monthly Notices of the Royal Astronomical Society*, 327:1297–1306, 2001.

[10] P. Coles and G. F. R. Ellis. *Is the Universe Open or Closed.* Cambridge University Press, 1997.

[11] N. A. Bahcall, L. M. Lubin, and V. Dorman. Where is the dark matter? *Astrophysical Journal, Letters*, 447:L81–L85, 1995.

[12] P. Salucci and M. Persic. Dark matter halos around galaxies. In *Astronomical Society of the Pacific Conference Series*, volume 117, pages 1–27, 1997.

[13] R. G. Carlberg. Galaxy cluster virial masses and omega. *Astrophysical Journal*, 462:32–49, 1996.

[14] A.E. Evrard, C.A. Metzler, and J.F. Navarro. Mass estimates of x-ray clusters. *Astrophysical Journal*, 469:494–507, 1996.

[15] G. Girardi *et al.* Optical mass estimates of galaxy clusters. *Astrophysical Journal*, 505:74–95, 1998.

[16] T. P. Walker *et al.* Primordial nucleosynthesis redux. *Astrophysical Journal*, 376:51–69, 1991.

[17] C. J. Copi *et al.* Big-bang nucleosynthesis and the baryon density of the universe. *Science*, 267:192–199, 1995.

[18] D. Tytler *et al.* Review of big bang nucleosynthesis and primordial abundances. *Physica Scripta Volume T*, T85:12–31, 2000.

[19] M. S. Turner and J. A. Tyson. Cosmology at the millennium. *Reviews of Modern Physics*, 71:S145–S164, 1999.

[20] O. Elgaroy *et al.* A new upper limit on the total neutrino mass from the 2df galaxy redshift survey. arXiv:astro-ph/0204152 to appear in PRL.

[21] S. J. Asztalos *et al.* Experimental constraints on the axion dark matter halo density. *Astrophysical Journal, Letters*, 571:L27–L30, 2002.

[22] G. Jungman, M. Kamionkowski, and K. Griest. Supersymmetric dark matter. *Physics Reports*, 267:195–373, 1996.

[23] J.D. Lewin and P.F. Smith. Review of mathematics, numerical factors, and corrections for dark matter experiments based on elastic nuclear recoil. *Astroparticle Physics*, 6:87–112, 1996.

[24] S. Golwala. *Exclusion Limits on the WIMP-Nucleon Elastic-Scattering Cross Section from the Cryogenic Dark Matter Search.* PhD thesis, University of California at Berkeley, 2000.

[25] L. Baudis *et al.* New limits on dark-matter weakly interacting particles from the heidelberg-moscow experiment. *Physical Review D*, 59:022001/1–5, 1999.

[26] R. Gaitskell *et al.* The statistics of background rejection in direct detection experiments for dark matter. *Nuclear Physics B, Proceedings Supplements*, 51B:279–283, 1996.

[27] R. Bernabei *et al.* Search for wimp annual modulation signature: results from dama/nai-3 and dama/nai-4 and the global combined analysis. *Physics Letters B*, 480:23–31, 2000.

[28] R. J. Gaitskell and V. Mandic. Dark matter tools working group limit plotter. http://dmtools.berkeley.edu/limitplots.

[29] S. Hart *et al.* to appear in Sources and Detection of Dark Matter and Dark Energy in the Universe, 2002.

[30] F. Probst *et al.* Results of cresst phase i. *Nuclear Physics B, Proceedings Supplements*, 110:67–69, 2002.

[31] M. Bravin *et al.* Simultaneous measurement of phonons and scintillation light for active background rejection in the cresst experiment. *Nuclear Instruments and Methods in Physics Research A*, 444:323–326, 2000.

[32] A. Benoit *et al.* Improved exclusion limits from the edelweiss wimp search, 2002. Sumbitted to Physics Letters B, astro-ph/0206271.

[33] A. Benoit *et al.* First results of the edelweiss wimp search using a 320 g heat-and-ionization ge detector. *Physics Letters B*, 513:15–22, 2001.

[34] H. Wang *et al.* to appear in Sources and Detection of Dark Matter and Dark Energy in the Universe, 2002.

[35] T. J. Sumner *et al.* Zeplin-iii: A two-phase xenon dark matter detector. In *The Identification of Dark Matter*, pages 452–456. World Scientific, 2000.

[36] D. Cline. Zeplin iv: A one ton ultimate wimp detector. astro-ph/0111098.

[37] C. J. Martoff *et al.* Suppressing drift chamber diffusion without magnetic field. *Nuclear Instruments and Metods A*, 440:355–359, 2000.

[38] N. Boukhira *et al.* Search for dark matter with the picasso experiment. *Nuclear Physics B, Proceedings Supplements*, 110:103–105, 2002.

[39] A. Habig *et al.* An indirect search for wimps with super-kamiokande, 2001. Proceedings of ICRC 2001, arXiv:hep-ex/0106024.

[40] R. Abusaidi *et al.* Exclusion limits on the wimp-nucleon cross section from the cryogenic dark matter search. *Physical Review Letters*, 84:5699–5703, 2000.

[41] B. L. Dougherty. Measurements of ionization produces in silicon crytals by low-energy silicon atoms. *Physical Review A*, 45:2104–2107, 1992.

[42] G. Gerbier *et al.* Measurements of ionization of slow silicon nuclei in silicon for the calibration of a silicon dark-matter detector. *Physical Review D*, 42:3211–3214, 1990.

[43] J. Lindhard *et al. Mat. Fys. Medd. Dan. Selsk*, 33:10, 1963.

[44] B. A. Young, B. Cabrera, and A. T. Lee. Observation of ballistic phonons in silicon crystals induced by alpha particles. *Physical Review Letters*, 64:2795–2798, 1990.

[45] P. N. Luke. Voltage-assisted calorimetric ionization detector. *Journal of Applied Physics*, 64:6858–6860, 1988.

[46] R. M. Clarke, T. Saab, P. L. Brink, P. Colling, S. W. Nam, A. K. Davies, B. Cabrera, J. Hellmig, R. J. Gaitskell, M. B. Crisler, S. Eichblatt, and B. A. Young. Enhanced ballistic phonon producation for surface events in a cryogenic silicon detector. *Applied Physics Letters*, 76:2958–2960, 2000.

[47] S. Nam. *Development of Phonon-Mediated Cryogenic Particle Detectors with Electron and Nuclear Recoil Discrimination*. PhD thesis, Stanford University, 1998.

[48] R. Clarke. *An Athermal Phonon Mediated Dark Matter Detector with Surface Event Discrimination*. PhD thesis, Stanford University, 1999.

[49] T. Saab, R. M. Clarke, B. Cabrera, R. A. Abusaidi, and R. J. Gaitskell. Design of qet phonon sensors for the cdms zip detectors. *Nuclear Instruments and Methods A*, 444:300–303, 2000.

[50] K. Irwin. *Phonon-Mediated Particle Detection Using Superconducting Tungsten Transition-Edge Sensors*. PhD thesis, Stanford University, 1990.

[51] K. D. Irwin *et al.* A self-biasing cryogenic particle detector utilizing electrothermal feedback and a squid readout. *IEEE Transactions on Applied Superconductivity*, 5:2690–2693, 1995.

[52] A. J. Miller. *Development of a Broadband Optical Spectrophotometer Using Superconducting Transition-edge Sensors*. PhD thesis, Stanford University, 2001.

[53] M. L. Roukes, M. R. Freeman, R. S. Germain, and R.C. Richardson. Hot electrons and energy transport in metals at millikelvin temperatures. *Physical Review Letters*, 55(4):422–425, 1985.

[54] M. E. Huber, P. A. Neil, R. G. Benson, D. A. Burns, A. F. Corey, C. S. Flynn, Y. Kitaygorodskaya, O. Massihzadeh, J. M. Martinis, and G. C. Hilton. Dc squid

series array amplifiers with 120 mhz bandwidth (corrected). *IEEE Transactions on Applied Superconductivity*, 11:4048–4053, June 2001.

[55] B. Young, T. Saab, B. Cabrera, J. J. Cross, and R. A. Abusaidi. Tc tuning of tungsten transition edge sensors using iron implantation. *Journal of Applied Physics*, 86(6975):1–2, 1999.

[56] A. A. Abrikosiv and L. P. Gor'kov. *Soviet Physics JETP*, 12:1243, 1961.

[57] W. A. Roushen and J. Rouvalds. Susceptibility and order parameter for a superconductor with coupl ed magnetic impurities. *Physical Review B*, 3(5):2929, 1985.

[58] P. L. Brink *et al.* Determination of the tc distribution for 1000 transition edge sensors. In *AIP Conference Proceedings*, volume 605, pages 529–532, 2002.

[59] B. Cabrera. Design considerations for tes and qet sensors. *Nuclear Instruments and Method A*, 444:304–307, 2000.

[60] W. J. Skopol, M. R. Beasley, and M. Tinkam. Self-heating hotspots in superconducting thin-film microbridges. *Journal of Applied Physics*, 45:4054–4066, 1974.

[61] T. Shutt *et al.* A solution to the dead-layer problem in ionization and phonon-based dark matter detectors. *Nuclear Instruments and Method A*, 444:340–344, 2000.

[62] D. Abrams *et al.* Exclusion limits on the wimp-nucleon cross section from the cryogenic dark matter search, 2002. arXiv:astro-ph/0203500, submitted to Physical Review D.

[63] T. Perera. *The Limiting Background in a Dark Matter Search at Shallow Depth.* PhD thesis, Case Western Reserve University, 2002.

[64] A. J. Da Silva. *Development of a Low Background Environment for the Cryogenic Dark Matter Search.* PhD thesis, The University of British Columbia, 1996.

[65] A. Sonnenschein. *A search for Weakly Interacting Massive Particles with Low Temperature Detectors Capable of Simultaneously Measuring Ionization and Heat*. PhD thesis, University of California at Santa Barbara, 1999.

[66] Laura Baudis. private communication.

[67] Richard Gaitskell. private communication.

[68] Walter Ogburn. private communication.

[69] Richard Schnee. private communication.

[70] D. Abrams *et al.* Exclusion limits on the wimp-nucleon cross-section from the cryogenic dark matter search, 2002. Submitted to Physical Review D.

[71] Sharmila Kamat. private communication.

[72] G. W. Bennett *et al.* Measurement of the positive muon anomalous magnetic moment to 0.7 ppm, 2001. arXiv:hep-ex/0208001, submitted to Physical Review Letters.